

# **PROCESSING, STRUCTURING, AND SWITCHING OF MICROPOROUS POLYMERS**

vorgelegt von  
Diplom-Chemiker

DANIEL BECKER

geboren in Berlin

von der Fakultät II – Mathematik und Naturwissenschaften

der Technischen Universität Berlin

zur Erlangung des akademischen Grades

Doktor der Naturwissenschaften  
Dr. rer. nat.

genehmigte Dissertation

Promotionsausschuss:

Vorsitzender: Prof. Dr. rer. nat. Thomas Friedrich

Gutachter: Prof. Dr. rer. nat. Arne Thomas

Gutachter: Prof. Neil B. McKeown

Tag der wissenschaftlichen Aussprache: 17. Februar 2017

Berlin 2017







Ich will entwerfen, unter welchen  
neuen Zügen der Despotismus sich  
in der Welt einstellen könnte: Ich sehe  
eine unübersehbare Menge  
ähnlicher und gleicher Menschen, die  
sich rastlos um sich selbst drehen, um  
sich kleine und gewöhnliche Freuden  
zu verschaffen, die ihr Herz ausfüllen.  
Jeder von ihnen ist ganz auf sich  
zurückgezogen, dem Schicksal aller  
anderen gegenüber wie unbeteiligt:  
seine Kinder und seine besonderen  
Freunde sind für ihn die ganze  
Menschheit; was seine übrigen  
Mitbürger angeht, so ist er zwar bei  
ihnen, aber er sieht diese nicht; er  
berührt sie, aber er spürt sie nicht; er  
lebt nur in sich und für sich selbst.

◆ Alexis de Tocqueville, 1840 ◆



# Danksagung

Zu Beginn dieser Abhandlung ist es mein Privileg, all denjenigen zu danken, die direkt oder indirekt auf vielfältige Weise zu der Fertigstellung dieser Dissertation beigetragen haben.

Die Anfertigung dieser Arbeit ermöglichte Prof. Arne Thomas, der mir eine Position in seiner Arbeitsgruppe an der Technischen Universität Berlin bereitstellte. Darüber hinaus fungierte er als Ideengeber in zahlreichen Situationen und wusste sowohl bei praktischen wie auch theoretischen Fragestellungen weiterzuhelfen. Gleichzeitig verlieh er mir während meiner Forschung ausreichend Freiraum, um eigene Ideen zu entwickeln und diesen nachzugehen, insbesondere was das Thema über lichtresponsive poröse Materialien betrifft.

Meinen Dank erfahren ebenfalls Prof. Thomas Friedrich für die Übernahme des Prüfungsvorsitzes der wissenschaftlichen Aussprache sowie Prof. Neil McKeown für die Erstellung des Zweitgutachtens über diese Dissertation.

Mein Dank für die Durchführung verschiedener Analysen richtet sich an Christina Eichenauer für Sorptions- und thermogravimetrische Messungen, Maria Unterweger für Röntgendiffraktometrie, Samantha Voges sowie Dr. Jan-Dirk Epping für manuelle nuklearmagnetische resonanzspektroskopische (NMR) Analysen inklusive Diskussion der Ergebnisse, Marlies Gräwert für gelpermeationschromatografische Untersuchungen und ebenso Dr. Maria Schlangen-Ahl und Marc Griffel für massenspektrometrische Messungen. Matthias Trunk, Dr. Sabrina Fischer und Dr. Kamalakannan Kailasam verdienen ebenso Erwähnung für die Aufnahme von Festkörper-NMR Spektren. Von großer Bedeutung für diese Arbeit, und wiedergegeben im ersten Kapitel, sind sekundärelektronenmikroskopische Aufnahmen, durchgeführt von Prof. Anna Fischer, Martin Rohloff, Axel Heilemann sowie Dr. Amandine Guiet. Erstere und Letztere waren zusätzlich eine große Hilfe bei der Bestimmung der Kryptonsorption an Polymerfilmen. Ebenso gilt meine Anerkennung Nina Heidary für die Durchführung oberflächenverstärkter infrarotabsorptionsspektroskopischer Messungen, die zu wichtigen Erkenntnissen bei der Bindung eines Polymerfilms an eine Goldoberfläche führten. Nora Konnertz und Dr. Martin Böhning gilt mein Dank für die Durchführung von Gaspermeationsmessungen, auf die im dritten Kapitel eingegangen wird.

Keinesfalls unerwähnt bleiben sollen die schnell in die Tat umgesetzten und von Einfallsreichtum geprägten Dienste von Glasbläser Carsten Hirschfeld. Gedankt sei auch Harald Link für die schnelle und unkomplizierte Bearbeitung von Anliegen jedweder Art im BA-Gebäude. Anfragen rund um mechanische Arbeiten stellten die werkstatterfahrenen Hände von Peter Schnepfmüller vor keinerlei Probleme und wurden dementsprechend rasch und zuverlässig erledigt.

Weitere Anerkennung gebührt Dr. Jérôme Roeser, der durch enormes Fachwissen glänzt und zu diversen Denkanstößen verhalf. Außerdem erklärte er sich bereit, das Manuskript Korrektur zu lesen. Dr. Johannes Schmidt wird für die Einsichten, insbesondere in die Theorie und Praxis der Sorptionsanalytik, sowie für die fruchtbare Kooperation, die Teile des dritten Kapitels umfasst, gedankt.

Nicolas Chaoui, Matthias Trunk, Dr. Ali Yassin und Dr. Hakan Bildirir gilt mein Dank für einen wissenschaftlich wertvollen Ideenaustausch. Neben den zuvor genannten Personen, sorgten vor allem auch Anne Svilarov (geb. Sobotta), Sophie Kücken, Dr. Peter „G.S.D.“ Döhlert, Daniel „Danyo“ Hagemeyer, Thomas Langenhahn, Dr. Robin White, Dr. Sabrina Fischer, Dr. Elham Baktash, Dr. Kamalakannan Kailasam sowie Oussama Yahiaoui für eine sehr angenehme und von Momenten aufheiternder Natur durchsetzte Arbeitsatmosphäre, die es vermochte, eine durchaus positive Grundstimmung zu zeitigen.

Ohne die kompetente bürokratische Unterstützung von Anne Svilarov hätten sich viele Dinge ungleich komplizierter gestaltet. Als unermüdliche Assistentin von Prof. Thomas konnte sie bei unzähligen Gelegenheiten durch zielstrebige und gründliche Arbeit organisatorischen Stress lindern und präsentierte dabei ein unerschöpfliches Maß an Geduld und Verständnis. Diese Aufgabe wurde im letzten Abschnitt der Doktorarbeit von Svetlana Barg übernommen, die diese Verantwortung ebenso ernst nimmt.

Da es von großer Wichtigkeit ist, über den Tellerrand hinauszublicken und auch Interesse für Themen außerhalb der eigenen Hauptbeschäftigung zu zeigen, danke ich Dr. Rafael Schiwon, Sticky, Filla sowie Friederike Geiger für wertvolle Diskussionen und Erfahrungen rund um Politik, Geostrategie, Tanz, Fotografie und Philosophie.

Familienseitiger Dank entfällt vor allem auf meine Eltern Elke „Mutti“ und Detlef „Papa“ Becker sowie meine Schwester Sabrina, die in meiner frühen Zeit nicht müde wurden, meinen ständigen Wissensdurst nach schlicht allem nach bestem Wissen zu stillen. Geringfügig weniger geduldige Eltern und Geschwister hätten kapituliert und damit in diesen formativen Jahren möglicherweise einen Zustand intellektueller Apathie in mir induziert, mit der wahrscheinlichen Konsequenz, dass diese Doktorarbeit nie verfasst worden wäre.

# Acknowledgements

At the beginning of this dissertation, it is my privilege to say thanks to all those who directly or indirectly contributed in various ways to the completion of this doctoral thesis.

The compilation of this work was afforded by Prof. Arne Thomas, who provided me with a position in his group at Technische Universität Berlin. Moreover, he acted as a source of ideas in numerous situations and knew how to give helpful advice on issues of practical and theoretical nature. At the same time, in conducting my research he granted me latitude large enough to conceive and develop my own concepts especially with an eye towards the topic on light-responsive porous materials.

I am also indebted to Prof. Thomas Friedrich for assuming the chairmanship of my doctoral examination and Prof. Neil McKeown for offering the second opinion on this thesis.

My thanks for countless analyses is dedicated to Christina Eichenauer for sorption- and thermogravimetric measurements, Maria Unterweger for X-ray diffractometry, Samantha Voges as well as Jan-Dirk Epping, PhD, for manual nuclear magnetic resonance (NMR) analyses including the discussion of the results, Marlies Gräwert for gel permeation chromatographic investigations, and Maria Schlangen-Ahl, PhD, and Marc Griffel for mass spectroscopic measurements. Matthias Trunk, Sabrina Fischer, PhD., and Kamalakannan Kailasam, PhD, also merit acknowledgement for the recording of solid state NMR spectra. Of high significance for this work, and presented in the first chapter, were secondary electron micrographs, conducted by Prof. Anna Fischer, Martin Rohloff, Axel Heilemann and Amandine Guiet, PhD. Prof. Fischer and Dr Guiet were, in addition, a great help with the acquisition of krypton sorption results on polymer films. My gratitude is also devoted to Nina Heidary for the operation of surface enhanced infrared absorption spectroscopic analytics leading to important insights into the binding of a polymer film to a gold surface. Nora Konnertz und Martin Böhning, PhD, receive thanks for gas permeation measurements, which are dealt with in the third chapter.

Credits have to be given to glass blower Carsten Hirschfeld, whose services were not only completed in a timely fashion but also bespoke a high degree of ingenuity. Thanks also to Harald Link

for the prompt and uncomplicated handling of requests of all kinds in the BA building. Requests regarding mechanical issues never posed a serious challenge to the experienced hands of Peter Schnepfmüller and were thusly executed swiftly and reliably.

Further gratitude is claimed by Jérôme Roeser, PhD, who can call his own a plethora of knowledge about the subject matter and was able to stimulate new directions of thought. Furthermore, he took on the task of proofreading the manuscript. Johannes Schmidt, PhD, is thanked for the insights especially into theory and praxis of sorption analytics as well as for the fruitful cooperation that materialised in parts of the third chapter.

Nicolas Chaoui, Matthias Trunk, Ali Yassin, PhD, and Hakan Bildirir, PhD, receive thanks for a scientifically worthwhile exchange of ideas. Apart from the just mentioned individuals, did Anne Svilarov, née Sobotta, Sophie Kücken, Peter „G.S.D.“ Döhlert, PhD, Daniel „Danyo“ Hagemeyer, Thomas Langenhahn, Robin White, PhD, Sabrina Fischer, PhD, Elham Baktash, PhD, Kamalakannan Kailasam, PhD, and Oussama Yahiaoui care for a pleasant working atmosphere interspersed with cheerful moments that were able to generate a very positive prevailing mood.

Without the competent bureaucratic support by Anne Svilarov, things would have been much more complicated. An indefatigable assistant to Professor Thomas, she alleviated bureaucratic pressure on countless occasions by assiduous and thorough work with a display of inexhaustible patience and understanding. In the final period of my work, this task has been handed over to Svetlana Barg, who takes this responsibility just as seriously.

As it is of utter importance to always show an open mind for things lying outside the own field of occupation it is my pleasure to have met Rafael Schiwon, PhD, Sticky, Filla, as well as Friederike Geiger through which I was able to gather valuable experiences by means of discussing or engaging in topics like politics, geostrategy, dancing, photography, and philosophy.

Finally, I am immeasurably indebted to my parents Elke “Mutti” and Detlef “Papa” Becker as well as my sister Sabrina, all of which in my early years have not given up on the task of answering my torrent of questions about just everything. Slightly less patient parents and siblings might have capitulated and thus possibly induced in myself in these formative years a state of intellectual apathy, the ramification of which might very well have been that this doctoral thesis would not have come to fruition at all.

# Zusammenfassung

Diese Arbeit enthält Ergebnisse aus drei verschiedenen Themengebieten, die unabhängig voneinander zu betrachten sind. Der gemeinsame Nenner dieser Themen beläuft sich auf das Konzept von Porosität. Während die Forschung des ersten Kapitels darauf abzielt, neue Methoden zu entwickeln, um gemeinhin unprozessierbare Polymere als dünne Filme herstellen zu können, werden im zweiten Kapitel Versuche beschrieben, Mikroporosität mit Mesoporosität zu infiltrieren, um Systeme mit hierarchisch organisierter Porenstruktur zu erhalten. Das finale Kapitel legt dar, wie auf Porosität innerhalb eines Systems dergestalt Einfluss genommen werden kann, dass sie unter Zuhilfenahme von elektromagnetischer Strahlung spezifischer Wellenlänge geändert, das heißt geschaltet werden kann.

## KAPITEL 1 ♦ FILME

Mikroporöse Polymernetzwerke (MPNs) werden, wenn sie zwei- oder dreidimensionalen Bindungsmustern gehorchen, üblicherweise als unlösliche und damit unprozessierbare Feststoffe erhalten. In dieser Arbeit wurde die grundlegende chemische Struktur von den Polymeren PPN-6 und CMP-1 unberührt gelassen. Stattdessen war es das Ziel diese Polymere in eine Morphologie zu bringen, die einem Film gleicht. Erreicht wurde dies durch die Bereitstellung einer Oberfläche, die funktionelle Gruppen aufweist, die an der Polymerisationsreaktion zur Herstellung der Polymere teilnehmen können.

Es wird gezeigt, dass PPN-6 *via* Yamamoto Kreuzkupplungsreaktion auf einen mit einer SAM (selbstassemblierte Monolage) versehenen goldbeschichteten Siliziumwafer raufpolymerisiert werden konnte. Der erhaltene Polymerfilm weist zwei unterschiedliche Regime auf: zunächst eine sehr homogene initiale Lage, die sich direkt an und von der Oberfläche bildet und mit Dicken von Dutzenden Nanometern aufwartet. Auf dieser initialen Lage formt sich eine weitere Schicht, die irreguläre Agglomeration von Polymerkugeln zeigt, die sich in Lösung vorgeformt haben, um dann von der homogenen Schicht durch terminale reaktive funktionelle Gruppen fixiert zu werden. Sowohl die Dicke der initialen Lage als auch das Ausmaß der Agglomeration auf dieser, konnten in

großem Maße durch den Prozessparameter Reaktionszeit beeinflusst werden. Darüber hinaus wurde gezeigt, dass vorherige SAM-Funktionalisierung von essentieller Wichtigkeit ist, um eine stabile, d.h. kovalente Anbindung des Films an die Oberfläche zu gewährleisten.

Die Anwendbarkeit des entwickelten Konzepts konnte durch erfolgreiche Adaptierung auf das Polymer CMP-1 erweitert werden. Mithilfe der Sonogashira-Hagihara Kreuzkupplungsreaktion wurden CMP-1 Filme auf Goldsubstraten hergestellt. Die Dicken dieser Filme sind vergleichbar mit denen der PPN-6 Filme und sind ebenso abhängig von der Reaktionszeit. Im Gegensatz zu PPN-6 Beschichtungen präsentieren sich CMP-1 Filme weniger homogen mit stärkerer Neigung zu partikulärem Wachstum auf dem initialen Film. Auf Grund der Fähigkeit von Alkylgruppen mit Gold in Wechselwirkung zu treten, zeigte sich, dass vorherige SAM-Funktionalisierung im Falle der CMP-1 Filme keine Voraussetzung ist, da auch entsprechende Blindproben Polymerbeschichtung aufweisen.

## KAPITEL 2 ♦ SILIKA

Das Ziel eines porösen Materials mit hierarchisch organisierter Porenstruktur wurde mittels Infiltration von SBA-15 artigem Silika mit mikroporösem PPN-6 verfolgt. Nachfolgende Auflösung des Silikatemplats sollte PPN-6 liefern, das ein mesoporöses Porenregime eingearbeitet hat. Leider jedoch schlugen alle Versuche das Silika—ob unbehandelt, hydrophobisiert oder funktionalisiert—zu infiltrieren fehl, sodass die Bildung eines mikro-/mesoporösen organischen Polymers scheiterte.

## KAPITEL 3 ♦ LICHT

Die Einführung von Lichtresponsivität in mikroporöse Materialien bestimmt das finale Kapitel. Diarylethene (DAEs) und Azobenzene (Azos) wurden als konstitutive Struktureinheiten in Polymere intrinsischer Mikroporosität (PIMs) inkorporiert. Die erhaltenen DAE-PIM und Azo-PIM sind mikroporös, reversibel responsiv auf Lichtstimuli und—von hoher Wichtigkeit für die Prozessierung—löslich in organischen Lösemitteln, insbesondere THF. Die Oberfläche von DAE-PIM von beinahe  $400 \text{ m}^2 \cdot \text{g}^{-1}$  wurde durch Isomerisierung—Zyklisierung und Zykloreversion—der DAE-Einheiten verändert. Die Isomerisierung konnte sowohl in UV-vis als auch in NMR Untersuchungen verfolgt und auch im Festkörper bewerkstelligt werden. In Kombination mit Matrimid (MI) wurden freistehende Membranen als Kompositmaterial DAE-PIM@MI produziert, in denen die DAE Einheiten ihr Isomerisierungspotential beibehalten. Eingesetzt in Gasdiffusionsexperimenten, konnte auf Gasdiffusivität und -permeabilität dieser Membranen, auf Grund unterschiedlicher Eigenschaften des offenen und geschlossenen Zustandes der DAE-Einheiten, durch Lichteinstrahlung Einfluss genommen werden.

Auch Azo-PIM wurde als permanent mikroporös und lichtresponsiv charakterisiert. Die innere Oberfläche entwickelt sich in starker Abhängigkeit zu der Anzahl durchgeführter Umfällungen und erreicht mindestens  $305 \text{ m}^2 \cdot \text{g}^{-1}$ . Verschiedene Wellenlängen konnten eingesetzt werden, um (*E*) → (*Z*) und (*Z*) → (*E*) Isomerisierung zu erzielen. Die Reversibilität in Kombination mit der Ermüdungsbeständigkeit des Materials ist bei Azo-PIM stärker ausgeprägt als bei DAE-PIM.

# Summary

This work presents results from three different topics that stand independent from each other. If one wants to find a common denominator connecting all these topics it might be porosity. Whereas the work described in the first chapter aimed at devising new methodologies to allow nominally unprocessable polymers assume film-like morphologies, the second chapter elaborates on attempts to infuse microporosity with mesoporosity as to obtain a hierarchically organised porous system. The final chapter sets out to show that porosity within a system is not destined to be an unalterable property but can be changed upon exposure to specific wavelength of electromagnetic radiation.

## CHAPTER 1 ♦ FILMS

Microporous polymer networks (MPNs) when adhering to a two- or three dimensional connection pattern are usually obtained as insoluble thus unprocessable solids. In this work, the basic structure of well-known networks—PPN-6 and CMP-1—was left untouched. Instead, it was aimed at compelling those polymers to adopt a film-like morphology by providing a surface that exposes functional groups to partake in the polymerisation reaction utilised for the polymer's creation.

It is shown, that *via* Yamamoto cross-coupling reaction PPN-6 could be polymerised onto a SAM-functionalised (self-assembled monolayer) gold coated silicon wafer. The obtained polymer film shows two distinct regimes: a very homogeneous initial layer that forms bottom-up directly from the surface and exhibits thicknesses of several dozen nanometre with an additional layer atop that displays irregular agglomeration of polymer particles that have pre-formed in solution and where scavenged by the first layer *via* terminal reactive groups. The thickness of the initial layer as well as the extent of agglomerate growth on top, were found to be commensurate with reaction time thus allowing very roughly to adjust both these parameters. In addition, it is shown that prior SAM-functionalisation is essential to yield firmly, *i.e.* covalently attached films.

The scope of the developed approach was broadened by successful adaptation to CMP-1 relying on Sonogashira-Hagihara cross-coupling reaction to form films of CMP-1 on gold substrates. The films show thicknesses comparable to PPN-6 films. Likewise, the thickness is dependent on reaction

time. In contrast to PPN-6 coatings, CMP-1 films appear to be less homogeneous with a higher proclivity to exhibit particulate agglomerates atop the initial film. Moreover, owing to the ability of alkyne groups to interact with gold, it was figured out that prior SAM-functionalisation in the case of CMP-1 films is not necessary as blank samples did display polymer coating as well after having been present in the polymerisation reaction.

## CHAPTER 2 ♦ SILICA

In order to obtain a porous material with hierarchically organised pore structure, mesoporous SBA-15-like silica was sought to be infiltrated by microporous PPN-6. Subsequent digestion of the silica template was expected to yield PPN-6 with a mesoporous pore regime imprinted on the nominally microporous PPN-6. However, all attempts at infiltrating the silica—comprising utilisation of pristine, hydrophobised, and functionalised silica surfaces—were to no avail and consequently the anticipated formation of a micro-/mesoporous organic polymer did not materialise.

## CHAPTER 3 ♦ LIGHT

Introduction of light-responsiveness into microporous materials governs the final chapter. Diarylethenes (DAEs) and azobenzenes (Azos) were rendered constituent part of a polymer of intrinsic microporosity (PIM). Acquired DAE-PIM and Azo-PIM are shown to be microporous, responsive to light stimuli in a reversible manner, and—very important with respect to processing—soluble in common organic solvents, in particular THF. DAE-PIM's apparent surface area of approximately  $400 \text{ m}^2 \cdot \text{g}^{-1}$  could be altered by means of isomerisation of DAE entities, that is cyclisation yielding the closed and cycloreversion yielding the open state. The isomerisation events can be traced in UV-vis as well as NMR spectroscopy. Owing to DAE's unique properties, isomerisation was also achieved in solid state as either film or powder. In conjunction with Matrimid (MI), free-standing membranes were produced as composite material DAE-PIM@MI, in which DAE moieties retain their ability to isomerise. These membranes were employed in gas diffusion experiments and it is shown that gas diffusivity as well as gas permeability can be switched by light due to different properties of the open and the closed state of the DAE units.

Azo-PIM was likewise shown to exhibit both permanent microporosity and light-responsiveness. Its apparent surface area is influenced by the number of precipitation cycles and amounts to at least  $305 \text{ m}^2 \cdot \text{g}^{-1}$ . Different wavelengths could be applied to trigger (*E*) → (*Z*) and (*Z*) → (*E*) isomerisation and reversibility in combination with fatigue resistance is higher in the case of Azo-PIM as compared to DAE-PIM.

# OUTLINE

<b><u>INTRODUCTION</u></b>	1
POROUS MATERIALS IN THE MODERN AGES	4
POROUS ORGANICS   INTRODUCTION	5
POROUS ORGANICS   SYNTHESIS	6
SURFACE AREA   AN IMPORTANT FEATURE	10
SURFACE AREA   THE THEORY BEHIND	12
PORE VOLUME	14
PORE SIZE AND PORE SIZE DISTRIBUTION	15
TYPES OF ISOTHERMS	16
HYSTERESIS PHENOMENA	17
OTHER TECHNIQUES	19
SCOPE OF THESIS	20
<b><u>CHAPTER 1 ♦ FILMS</u></b>	
MICROPOROUS POLYMER FILMS ON GOLD ELECTRODES	21
RESULTS AND DISCUSSION	
PPN-6   A FILM ON GOLD   PART ONE	23
CONCLUSION	33
CMP-1   A FILM ON GOLD   PART TWO	35
CONCLUSION	45
<b><u>CHAPTER 2 ♦ SILICA</u></b>	
TEMPLATED POROSITY	47
RESULTS AND DISCUSSION	
SILICA   PRISTINE	49
SILICA   PRISTINE   PPN-6	51
SILICA   FUNCTIONALISATION WITH HEXAMETHYLDISILAZANE (HMDS)	53
SILICA   HMDS   PPN-6	54
SILICA   FUNCTIONALISATION WITH PARABROMOPHENYLTRIMETHOXSILANE (PBPTMOS)	55
SILICA   PBPTMOS   PPN-6	57
CONCLUSION	59
<b><u>CHAPTER 3 ♦ LIGHT</u></b>	
PHOTOCHROMISM	61
AZOBENZENES	63
DIARYLETHENES	65
LIGHT-SWITCHABLE MICROPOROUS STRUCTURES	70
DAE-POLYMER   3D	72
RESULTS AND DISCUSSION	
DAE-CMP	74
CONCLUSION	81

DAE AND AZO-POLYMERS   1D	83
RESULTS AND DISCUSSION	
DAE-PIM	84
CONCLUSION	91
AZO-PIM	92
CONCLUSION	98
<b>APPENDIX</b>	<b>101</b>
<b>EXPERIMENTAL PART</b>	
INSTRUMENTATION	116
MATERIALS	118
GENERAL PROCEDURE FOR SAM FORMATION	119
GENERAL PROCEDURE FOR FILM FORMATION	119
MONOLITHIC SBA-15-TYPE SILICA	120
FUNCTIONALISATION WITH HMDS	120
FUNCTIONALISATION WITH PBPTMOS	121
PPN-6 FORMATION   WET-APPROACH	121
PPN-6 FORMATION   DRY-APPROACH	121
SYNTHESIS OF TETRAKIS(4-BROMOPHENYL)METHANE	121
SYNTHESIS OF 4-IODOTHIOPHENOL	122
SYNTHESIS OF PPN-6 FILMS	123
SYNTHESIS OF CMP-1 FILMS	123
SYNTHESIS OF 3,5-DIBROMO-2-METHYLTHIOPHENE	124
SYNTHESIS OF 3-BROMO-2-METHYL-5-TRIMETHYLSILYLTHIOPHENE	124
SYNTHESIS OF 1,2-BIS(2'-METHYL-5'-TRIMETHYLSILYLTHIEN-3'-YL)HEXAFLUOROCYCLOPENT-1-ENE	125
SYNTHESIS OF 1,2-BIS(5'-IODO-2'-METHYLTHIEN-3'-YL)HEXAFLUOROCYCLOPENT-1-ENE	126
SYNTHESIS OF DAE-CMP	126
SYNTHESIS OF 2,2'-BIS(4,4,5,5-TETRAMETHYL-1,3,2-DIOXABOROLAN-2-YL)-9,9'-SPIROBIFLUORENE	127
SYNTHESIS OF DAE-PIM	127
SYNTHESIS OF 3,3',4,4'-TETRAFLUOROAZOBENZENE	128
SYNTHESIS OF AZO-PIM	129
<b>ABBREVIATIONS</b>	<b>131</b>
<b>LITERATURE REFERENCES</b>	<b>135</b>



# INTRODUCTION

What remains when you dismantle something entirely? Imagine you hold in your hand a sophisticated piece of handcraft such as a mechanical wrist watch and start to strip off its parts cogwheel by cogwheel, screw by screw, and all the other minute components. What you will end up with is, of course, nothing. As unspectacular as this might seem, very useful items have been conceived out of this *nothing* by transforming it into a void. Picture, for example, *nothing* being held firmly and isolated between two glass panels and a thermally insulating window is obtained. Or try to confine that *nothing* by erecting walls all through it and you will end up with something like a sponge thereby turning *nothing* into voids that can soak in and store water.

A kitchen sponge is a good starting point when approaching the topic of this thesis. A sponge is composed of a series of voids—henceforth called *pores*—between the material walls and in the case of a sponge for domiciliary use these pores are visible to the eye. However, shrinking the pores in a Gedankenexperiment to a volume that can accommodate only one thousand molecules of dinitrogen  $N_2$  (hereafter referred to as nitrogen for simplicity) leads to pore dimensions of the type discussed throughout this thesis.

A basic consideration in the discussion of porosity is that the internal surface area (SA), *i.e.* the area of the aforesaid walls that confine as well as separate the pores, will increase as the average size of a pore decreases. Since pore walls cannot be infinitely thin, the overall pore volume is also reduced. This can be understood *via* the visualisation of an ordinary room that is divided by a wall. There will be two more surfaces provided by the dividing wall hence more wallpaper to bring onto every wall to make it a lovely room ( $\rightarrow$  higher SA) with a concomitant need to remove items of furniture that are now too big to fit into either of the two compartments ( $\rightarrow$  lower pore size). In addition, as the wall must be of a known thickness, the overall volume of the two compartments will be lower than the volume of the initially undivided room (**Figure 1**).

In terms of research, a significant amount of effort has been devoted to the synthesis and characterisation of porous materials. Conventionally, they are classified according to their pore size as macro-, meso-, and microporous, defined as materials with pore diameters of  $> 50$  nm, 50 to 2 nm,

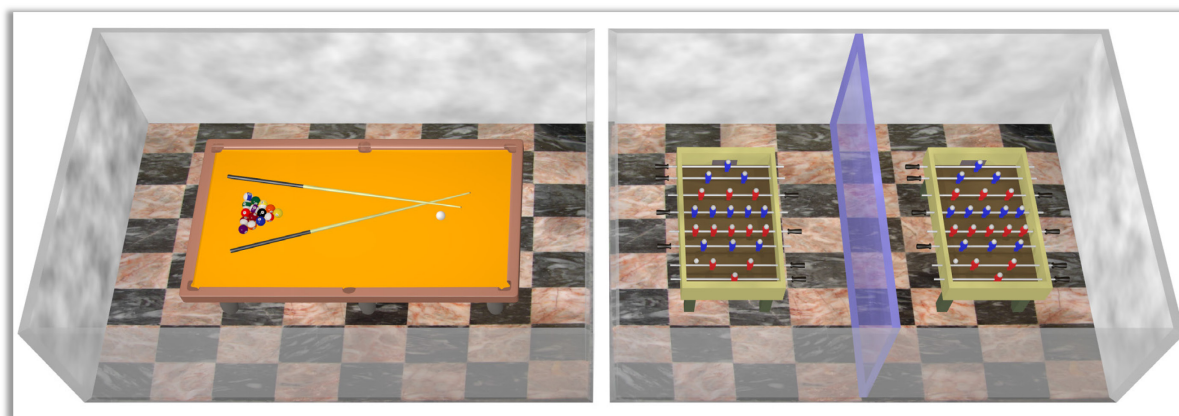


**Figure 1.** Simplification of the observation of an increase in surface area (two additional walls) with a concomitant decrease in pore size (voluminous furniture needs to be replaced by smaller one). As the wall that divides up a pore cannot be infinitely thin, the overall pore volume decreases as well (illustration).

and  $< 2$  nm, respectively.<sup>[1]</sup> **Figure 2** provides an overview of materials constituting these classes, which comprise purely inorganic, organic-inorganic hybrid, and purely organic materials. It is important to note that porous materials often feature contributions from all three pore size domains to their overall porosity.

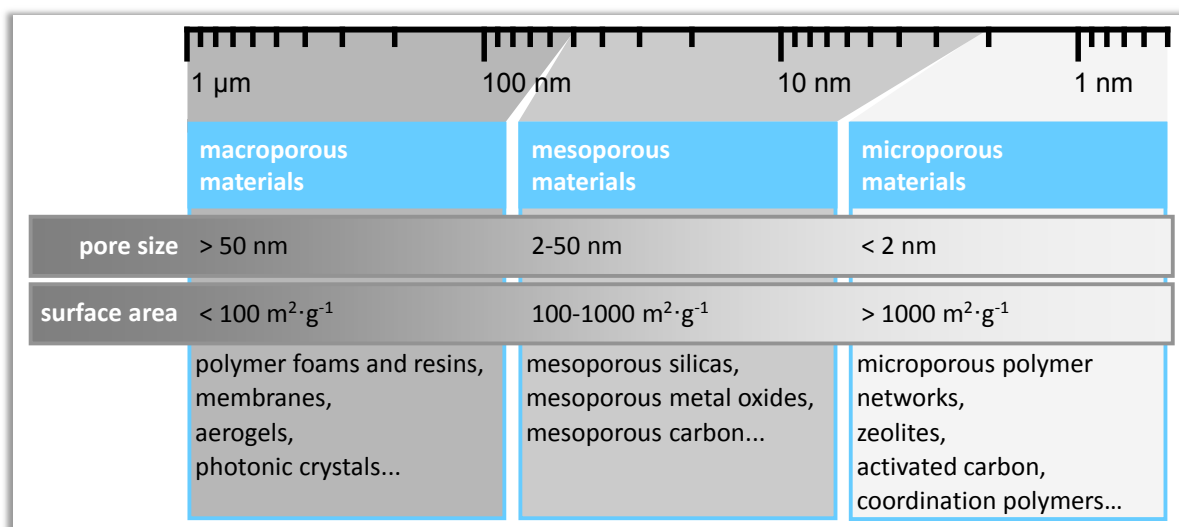


**Figure 2.** Overview of pore sizes from macro- to microporous materials.

Porous materials in general have been known for thousands of years and were used millennia ago by the Egyptians, who in *ca.* 1500 BC used gypsum as a construction material or charcoal to purify water by exploiting its high surface/contact area imparted to the material by its porous nature.<sup>[2]</sup> However, a scientific foundation for the investigation of porosity is not to be found until the advent of the 18<sup>th</sup> century when in 1717 James Jurin published his findings regarding the relationship between the height to which water rises in a capillary to the tube's diameter.<sup>[3]</sup> All but ninety years later, Thomas Young published 'An Essay on the Cohesion of Fluids' where he elaborated on the formation of contact angles of fluids on surfaces.<sup>[4]</sup> His descriptive treatise was put

into mathematical terms by Pierre Simon de Laplace in 1805 yielding the Young-Laplace-equation that relates the pressure above a phase boundary to the radius of that boundary.<sup>[5]</sup> Advancing those ideas and combining the aforementioned discoveries, in 1871 William Thomson (later Lord Kelvin) issued a paper presenting the Kelvin-equation that allowed calculation of the required vapour pressure for condensation of a gas in a capillary of known radius.<sup>[6]</sup> The inverse approach—calculating the capillary’s radius from known vapour pressure—is a method, in a rough approximation, used currently to calculate pore size. Due to its importance and forthcoming reference to it the Kelvin equation is presented as Eq 1:

	for droplets	for cavities
(Eq. 1)	$\ln \frac{p}{p_0} = + \frac{2\sigma V_m}{rRT}$	$\ln \frac{p}{p_0} = - \frac{2\sigma V_m}{rRT}$

Where  $p$  = actual vapour pressure,  $p_0$  = saturation vapour pressure for a given compound at a specific temperature  $T$ ,  $\sigma$  = surface tension,  $V_m$  = molar volume of the liquid,  $r$  = radius of the meniscus, and  $R$  = universal gas constant. These formulations of the equation assume a droplet or cavity of spherical shape. The essence of the Kelvin equation is that the smaller the radius of a droplet, the higher its vapour pressure, *i.e.* the easier it evaporates. To stabilise such a small droplet, the outside pressure needs to be raised to values above the standard vapour pressure (saturation vapour pressure) of the respective substance or, in other words, a small droplet is only stable under over-saturated conditions. On the other hand, the opposite is true for cavities, which is why in this case the term of the equation is preceded by a minus sign. The vapour pressure in a cavity is smaller than the respective saturation vapour pressure of a given substance. The cavity tends to collapse/implode when the outside pressure is not lowered to values below the saturation vapour pressure or, more simply, a cavity is only stable in an under-saturated environment. The latter aspect is very important when, on pages to come, a phenomenon is described that is known as capillary condensation.

Interestingly, if only these principles had been at work, there would have been no possibility for the formation of clouds in the sky. For as soon as enough water molecules assemble to form a condensed phase embodied in a minute droplet, the inherent vapour pressure of that droplet is enormously high causing it to explode instantaneously. Fortuitously, there is cloud formation and the solution to this apparent paradox is accounted for either by fluctuations, which are always present and lead to a deviation from equilibrium conditions allowing larger droplets to form, or by condensation seeds such as dust particles that serve as nucleation sites.<sup>[7-8]</sup>

After this brief synopsis of the theoretical foundations for porosity analysis and surface area determination, which will be dealt with in more detail at a later stage, a concise survey of important porous materials in the modern ages is presented.

---

## POROUS MATERIALS IN THE MODERN AGES

It is understood, for reasons discussed below, that inorganic materials can be rendered porous more easily than organic compounds. As a result, the first materials targeted for porosity were of inorganic fabric. A widely used porous material is activated carbon (AC). At the beginning of the 20<sup>th</sup> century carbonaceous precursors were combined with metal halides. Carbon dioxide or steam served as oxidising agent producing the activated carbon after carbonisation of the precursors at high temperatures (> 600 °C). Continuing progress has led to the development of activated carbons with astoundingly high surface areas exceeding 3000 m<sup>2</sup>·g<sup>-1</sup> in the 1970s with AMOCO (American Oil Company) employing aromatic precursors and chemical activation with potassium hydroxide.<sup>[2]</sup> These high-SA materials are capable of adsorbing copious amounts of gaseous or other compounds and can serve as catalyst supports enhancing reaction yield by virtue of an increase in catalyst loading, dispersion, and accessibility to catalytic sites. The high SA allows of fine catalyst dispersion inside the porous structure that is much more pronounced than could ever be achieved by solely grinding bulk catalyst. Furthermore, the combination of an insoluble support material with a catalytically active species generates a material referred to as *heterogeneous catalyst* providing the obvious advantage of easy removal of the catalyst material from the reaction mixture by filtration for reuse. This leads to minimised catalyst cost and increased product purity, two implications of paramount importance to industry.

Another ubiquitously employed porous material is porous silica. As early as 1911, Richard Zsigmondy reported on the inner structure of silicic acid gels and proposed an interconnected pore system. In addition, he calculated the pore diameter to be 5 µm.<sup>[9]</sup> Materials with exceptionally low densities as low as 0.02 g·cm<sup>-3</sup> were synthesised as aerogels in 1931 by Samuel Kistler.<sup>[10]</sup> Those materials feature remarkably low thermal conductivity and are thus ideally suited to serve as thermally insulating layers.

An important characteristic of the aforementioned ACs and porous silicas is their amorphous structure. In contrast, zeolites (Greek for *boiling stones*) are perhaps the archetypical microporous materials exhibiting a high degree of structural order that renders them crystalline. Zeolites can be found in nature most prominently as aluminium silicates, though rare examples incorporate beryllium, zinc or boron instead of aluminium or phosphorus instead of silicon. Understanding their porous structure was pioneered by Richard Barrer who in 1938 published a seminal work on their sorption behaviour.<sup>[11]</sup> Zeolites can also be accessed synthetically. A breakthrough was achieved in 1972 by Mobil Oil scientists with the synthesis of ZSM-5 (Zeolite Socony Mobil-5; Socony: Standard Oil Company of New York), a zeolite consisting of AlO<sub>4</sub> and SiO<sub>4</sub> tetrahedra.<sup>[12]</sup> Other elements have been implemented since. For example, phosphorus has substituted silicon to produce aluminium phosphates (ALPOs). Addition of phosphorus to aluminium silicates led to the formation of silicon aluminium phosphates (SAPOs).

In 1992, Kresge and co-workers at Mobil attempted to produce mesoporous materials with a comparable high degree of order as presented by the aforesaid zeolites, thus broadening the range of possible applications and/or improve performance. Mesopores are larger than micropores and

enable improved mass transfer and diffusion properties of reactants/products *e.g.* in catalysis. Kresge *et al.* focused on siliceous systems and MCM-41 is perhaps the most acclaimed member of this new family of mesoporous materials, often referred to as *mesoporous molecular sieves*.<sup>[13]</sup> Synthesised *via* a surfactant mediated template approach, hexagonally ordered cylindrical pores were obtained after calcination of the condensed silica to remove the porogenic surfactant. It is noteworthy that, whilst a system of ordered mesopores was achieved, the resulting material does not exhibit a long-range order as is typical for zeolites. The very material itself, *i.e.* the walls, consists of amorphous silica that has been compelled to assume an ordered structure by the micellar templating approach.

The previous paragraph disclosed general strategies for generating porosity within a material. Chemical activation for example was used to impart porosity to carbonaceous precursors yielding AC. Another approach is based on templating and used in synthesis of mesoporous silica. This methodology is very versatile as it allows of varying structures with different pore sizes to be imposed on siliceous precursors. A drawback, however, is the need to dispose of the template entirely in order to obtain the desired structure. Means to achieve this are calcination, washing/extraction, or template digestion by etching or microwaves. Templating can be categorised into hard and soft templating depending on the nature of the template. The former approach employs inorganic templates whereas the latter exploits organic counterparts. Soft templating for example was used in the aforementioned synthesis of MCM-41. A further categorisation can be made by distinguishing between *exo* and *endo* templating. In the former the template surrounds polymer precursors whereas in the latter the template is surrounded by polymer precursors.<sup>[14]</sup> Another and totally different approach to obtain porous materials is scaffolding, which can be imagined as building up a molecular scaffold piece by piece without the need for a template. This strategy relies on thermodynamically governed reaction pathways of reversible nature as to ensure that a crystalline structure evolves exhibiting voids between struts and nodes. That approach has been successfully employed in the realms of inorganic/organic hybrid and also purely organic materials such as ,respectively, porous coordination polymers (PCPs) aka metal organic frameworks (MOFs) and covalent organic frameworks (COFs).<sup>[15]</sup>

## **POROUS ORGANICS | INTRODUCTION**

The molecules described in this treatise are, mainly, of organic nature. Extensive research efforts have been devoted to imparting porosity to organic systems. Organic molecules have an innate propensity to be soft. This is in stark contrast to inorganic frameworks such as zeolites. Due to their hardness, zeolites can easily build up pores of permanent nature. Organic molecules/polymers tend to collapse upon solvent removal thereby packing space-efficiently, *i.e.* with no voids in between the molecules or chains hence there are no pores to be found. The idea, then, is to forestall space-efficient packing by carefully employing monomers that polymerise into a structure that cannot pack efficiently after solvent removal. This can be achieved by monomers with three-dimensional

geometry but also planar ones that together with bulky moieties form a structure that cannot pack space-efficiently. In this scenario steric repulsion will inevitably lead to the creation of pores (**Figure 3**).

But why undertake such a resource- and time-demanding endeavour in the first place when there are, as described, highly porous materials in stock? For one, the extent to which target structures can be tailored *via* organic synthesis according to the desired application is simply unparalleled and not available in the realm of inorganic materials. Another incentive is to obtain materials that are lightweight and exhibit low densities, thus to eliminate the need for metals inside the structure as metals contribute significantly to overall mass and in so doing reduce specific surface area values by merely raising the mass. Although total surface area values might be comparable or even higher, when it comes to integration of the materials into some sort of appliance, especially one that is conceived to be mobile, the weight factor plays a crucial role.

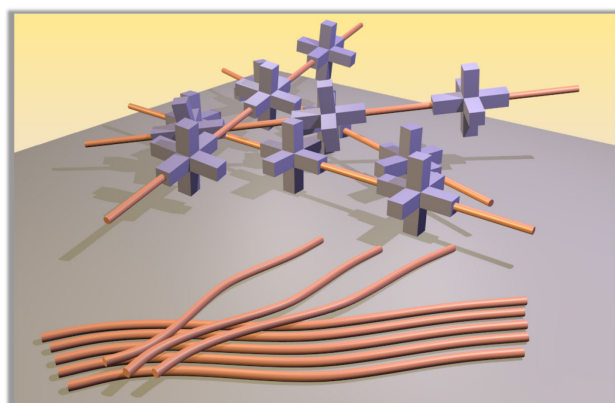


**Figure 3.** The illustration shows unbranched polymer chains that will pack space-efficiently when lacking bulky moieties (foreground). Backdrop shows creation of void space between polymer chains due to steric hindrance of cumbersome nodes. Created using the Blender™ 3D software; see end of Appendix for further information.

Moreover, metals might pose environmental problems on grounds of low biodegradability and/or toxicity issues. Finally, materials devoid of metals are generally cheaper since light elements such as carbon and oxygen can be found in abundance on our planet whereas metals, save for iron and aluminium, are much scarcer, which is particularly true for noble metals. This, of course, becomes apparent when recalling that for the creation of the elements our universe tells a story of nuclear fusion and not fission. That course of events draws a picture of bottom-up synthesis of all elements placing light elements at the very start. Having thus justified the research into organic porous materials, a chronological overview of that kind of compounds is provided.

## POROUS ORGANICS | SYNTHESIS

In 1974, Davankov *et al.* described that cross-linking of ordinary polystyrene chains yields ‘macronet isoporous gels’ that in spite of not being regarded as permanently porous displayed pronounced swelling behaviour and consequently could accommodate considerable amounts of gas or

solvents.<sup>[16]</sup> For this to work, cross-linking must be extensive and the name of this polymer class gives a hint of that: hyper cross-linked polymers (HCPs).<sup>[17]</sup>

In 1990, Robson *et al.* reported on an 'unusual material' formed from tetrakis(4-cyanophenyl)-methane and a copper(I) salt that was crystalline and had two-thirds of its volume occupied by liquid as deduced from single crystal XRD.<sup>[18]</sup> This seminal work describes porous coordination polymers (PCPs) as hybrid materials, *i.e.* a material containing both organic (linker) and inorganic (metal nodes) components. PCPs were thoroughly investigated in the course of that decade and led Yaghi *et al.* to publish new results in that field in 1995.<sup>[19-23]</sup> For reasons undisclosed, he was not content with the already existing and well-established designation (P)CP and introduced a new one: metal organic framework (MOF). In succession, MOF-5 was described in 1999 as a crystalline material with Zn<sub>4</sub>O nodes joined together by 1,4-benzenedicarboxylate (BDC) linkers and despite increased mass by incorporated metal it could compete with the extraordinary high specific surface areas found in activated carbons. After optimisation of the conditions used for preparation and activation, MOF-5 was reported to exhibit a specific surface area of 3800 m<sup>2</sup>·g<sup>-1</sup>, applying the theory of Brunauer, Emmett, and Teller (BET).<sup>[24-26]</sup> It should be noted that there is an ongoing but seemingly dwindling debate over the appropriateness of the designation *MOF* in spite of its prompt acceptance within the community of chemists and material scientists.<sup>[27]</sup> Over the ensuing years, different nodes and linkers have been utilised leading to systems with ever increasing BET surface areas such as MIL-101 (Matériaux Institute Lavoisier-101, chromium nodes, 1,4-BDC linkers, SA<sub>BET</sub> = 4100 m<sup>2</sup>·g<sup>-1</sup>)<sup>[28]</sup>, UMCM-2 (University of Michigan Crystalline Material-2, zinc nodes, thieno[3,2-b]thiophene-2,5-dicarboxylate and 1,3,5-tris(4'-carboxyphenyl)benzene linkers, SA<sub>BET</sub> = 5200 m<sup>2</sup>·g<sup>-1</sup>),<sup>[29]</sup> and NU-110E (Northwestern University-110-Experimental, copper nodes, 1,3,5-tris(((1,3-carboxylic acid-5-(4-ethynyl)phenyl))-ethynyl)phenyl)-benzene linkers, SA<sub>BET</sub> = 7140 m<sup>2</sup>·g<sup>-1</sup>)<sup>[30]</sup> with the highest ever reported apparent BET surface area for a porous solid. These kinds of compounds are highly crystalline and usually obtained in solvothermal reactions under inert gas at elevated temperature and pressure in order to establish reversibility and ensure the thermodynamically most stable product to be formed. That being said, the very first PCP by Robson *et al.* was obtained in ambient conditions without precautionary measures regarding exclusion of air.<sup>[18]</sup>

In 2004, McKeown *et al.* developed polymers of intrinsic microporosity (PIMs).<sup>[31]</sup> These are one-dimensional polymers the porosity of which is not derived from spatiality as in HCPs and MOFs. Rather, the polymer chains are formally linear but not geometrically straight and display kinks in each repeating unit due to thoughtful choice of monomers such as spirobifluorene, spirobiindane, or binaphthyl. Due to a contorted structure these chains although loose cannot pack space-efficiently as described earlier and illustrated in **Figure 3**. A remarkable property of PIMs as porous materials is that they can be soluble in common organic solvents, a trait that will be capitalised on later in this thesis. Being soluble allows the processing of PIMs into films or membranes. On the other hand, the feature of low dimensionality, the very reason for solubility, restricts those systems in terms of achievable SA<sub>BET</sub> values with PIM-1 already being one of the more porous examples with 850 m<sup>2</sup>·g<sup>-1</sup>. Also, the individual polymer chains pack randomly thus giving rise to amorphous materials.

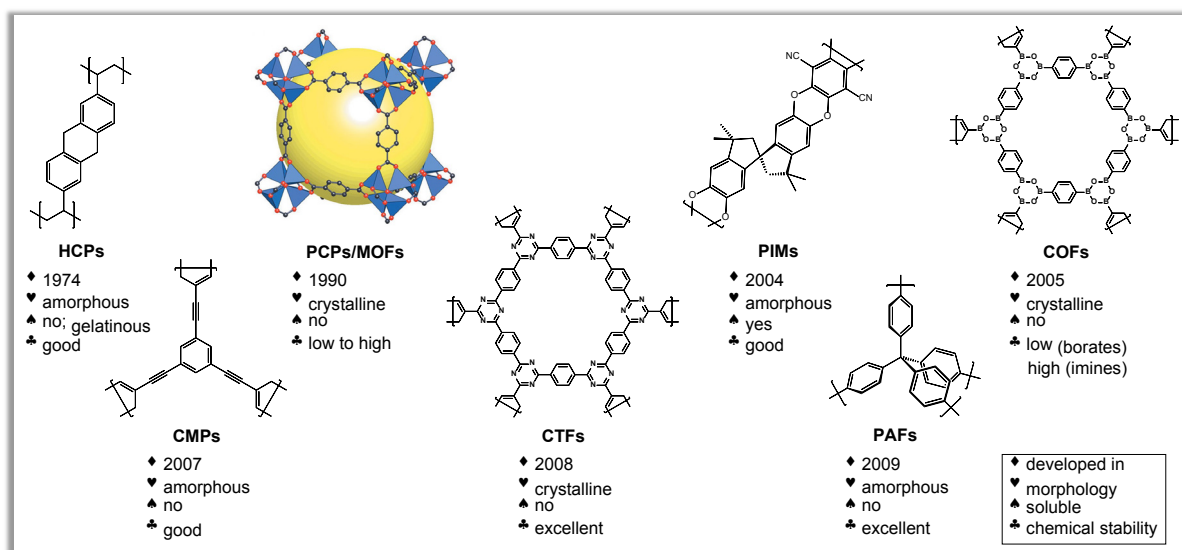


**Figure 4.** Landmark microporous polymers and basic information. Structures shown are: a hyper cross-linked polystyrene network, MOF-5, PIM-1, COF-1, CMP-1, CTF-1, and PAF-1 aka PPN-6; picture for MOF taken from reference 24).

The first all-organic ordered frameworks were presented by Yaghi *et al.* in 2005.<sup>[32]</sup> Covalent organic frameworks COF-1 and COF-5 were formed, respectively, from self-condensation reaction of 1,4-phenylenediboric acid and co-condensation reaction of the aforementioned with 2,3,6,7,10,11-hexahydroxytriphenylene and exhibited specific  $SA_{\text{BET}}$  of 711 and 1590  $\text{m}^2 \cdot \text{g}^{-1}$ , respectively. COFs exploit the same bond forming principle as MOFs inasmuch as the bonds between monomer units are formed reversibly allowing thermodynamics to govern the process which in turn yields highly crystalline materials. The structures of the first examples of COFs were defined by stacking of two-dimensional sheets in a staggered (COF-1) or eclipsed (COF-5) fashion. To attain higher SAs, three-dimensionality had to be implemented and drawing on findings from Galoppini *et al.*, Yaghi and co-workers synthesised 3D COFs such as COF-103 *via* self-condensation of tetrahedral tetrakis(4-(dihydroxyboryl)phenyl)silane presenting a specific  $SA_{\text{BET}}$  of 4210  $\text{m}^2 \cdot \text{g}^{-1}$ .<sup>[33-34]</sup> The first COFs were formed by boroxine (COF-1) and boronate ester (COF-5) formation, a bonding pattern that suffers from instability under ambient conditions as boron-oxygen bonds are highly susceptible to hydrolysis. Stability could be improved<sup>[35]</sup> by exploitation of imine (COF-300)<sup>[35]</sup> and hydrazone (COF-42, COF-43)<sup>[36]</sup> linkages between monomer units.<sup>[37-39]</sup>

Another class of microporous organic polymers was presented in 2007 when Cooper and co-workers synthesised conjugated microporous polymers (CMPs) featuring conjugation of  $\pi$ -electrons between two nodes.<sup>[40]</sup> Owing to their kinetically governed bond formation *via* palladium-catalysed Sonogashira-Hagihara C–C cross-coupling reaction, these materials do not develop an ordered arrangement of nodes and struts and are amorphous. CMPs are usually obtained in an A-B-type polymerisation reaction, *i.e.* from two monomer species. The synthetic details, however, are still a matter of concern especially regarding the employed equivalents of each monomer as well as the amount of catalyst. The first report on CMPs states a BET surface area of 834  $\text{m}^2 \cdot \text{g}^{-1}$  for CMP-1. In this work CMP-1 could be obtained with a  $SA_{\text{BET}}$  of 1538  $\text{m}^2 \cdot \text{g}^{-1}$  by employing a protocol

different from the original recipe.<sup>[41]</sup> In literature reports using the original protocol, various monomers have been employed and similar to what was observed for COFs it was found that three-dimensional tetrahedral monomers yield polymers with the highest SAs. For example, tetrakis(4-iodophenyl)methane in combination with 1,4-diethynylbenzene gives rise to polymer E1 with an  $SA_{\text{BET}}$  of  $1213 \text{ m}^2 \cdot \text{g}^{-1}$ .<sup>[42]</sup> As is inevitable for polymers with high molar masses, CMPs are not soluble. Nevertheless, synthesis can be designed such as to lower the dimensionality of the resulting polymer and introduce solubility-mediating groups as was achieved in so-called soluble CMPs (SCMPs).<sup>[43]</sup>

In a similar vein to COF synthesis, Thomas *et al.* introduced covalent triazine-based frameworks (CTFs) in 2008 relying on reversible bond formation.<sup>[44]</sup> In sharp contrast to COFs, however, CTFs display astonishing chemical robustness while likewise showing crystallinity albeit to a somewhat smaller extent. The structures of COF-1 and CTF-1 show an identical structural pattern and  $SA_{\text{BET}}$  for CTF-1 ( $791 \text{ m}^2 \cdot \text{g}^{-1}$ ) is of comparable magnitude as the one reported for COF-1 ( $711 \text{ m}^2 \cdot \text{g}^{-1}$ ). It was observed that the amount of zinc(II) chloride, serving at the same time as solvent and catalyst, exerts a great influence on the obtained products with higher surface areas achieved when more  $\text{ZnCl}_2$  was employed though at the expense of crystallinity. Due to the high nitrogen content, CTFs are comprehensively decorated with Lewis-basic sites making those materials potential solid catalysts with CTF-1 showing activity in the synthesis of cyclic carbonates.<sup>[45]</sup> Likewise, to a large extent CTF materials possess structural fragments that mimic bipyridine units that in turn provide coordination sites for *e.g.*  $\text{Pt}^{2+}$ . This was exploited to heterogenise the molecular Periana catalyst by virtue of an insoluble porous polymer.<sup>[46]</sup>

In 2009, a benchmark polymer was synthesised by Zhu *et al.* capitalising on findings from Thomas and co-workers that introduced nickel-catalysed Yamamoto C–C cross-coupling reactions for polymerisation of halogenated monomers.<sup>[47-48]</sup> Porous aromatic framework-1 (PAF-1), the homo-polymer derived from tetrakis(4-bromophenyl)methane, exhibited sky-rocketing  $5600 \text{ m}^2 \cdot \text{g}^{-1}$  boosting it into the realm of high surface area MOFs, thereby refuting once and for all any notion of crystallinity as the *sine qua non* for high surface area values. However, the naming *framework* is misleading as the material is amorphous.<sup>[49]</sup> *Network* instead is a more appropriate designation. Two years later, Zhou *et al.* developed an improved synthesis for PAF-1 and named their material porous polymer network-6 (PPN-6).<sup>[50]</sup> Substitution of silicon for carbon at the centre of the monomer led to PPN-4 with a yet higher  $SA_{\text{BET}}$  of  $6461 \text{ m}^2 \cdot \text{g}^{-1}$ . In terms of morphology—crystalline vs. amorphous—these examples make utterly clear the importance of whether a reaction proceeds *via* reversible (thermodynamic control) or irreversible (kinetic control) pathways. For a similar tetrahedral monomer was employed in the reversible formation of crystalline COF-103 whereas irreversibly generated PPN-4, though highly porous, is amorphous. The consistently higher SA in both cases of the silicon analogue (PPN-4 and COF-103) as compared to its carbon counterpart (PPN-6 and COF-102) is explained by the more expanded geometry of the monomer unit with silicon at the centre. An important benefit of PAFs/PPNs as compared to MOFs comes with the former material's vastly enhanced physicochemical stability; a consequence of robust covalent bonds rather than coordination bonds as in MOFs.

The hitherto mentioned systems display porosity as a result of linking together countless monomer units to a polymer that cannot pack space-efficiently due to stiff constituents thereby creating voids in between struts and nodes. However, it was shown that discrete organic molecules can be designed such as to achieve the same by forestalling space-efficient packing of individual molecules. This phenomenon was discovered a couple of decades ago when in 1976 Barrer *et al.* reported on the adsorption behaviour of Dianin's compound that itself is a more or less flat molecule but crystallises to form a six-membered ring from six Dianin's molecules held together by hydrogen bonds.<sup>[51]</sup> Ever since, much progress has been made and the modern pioneers in this subject are to be found in the groups of Mastalerz and Cooper contributing greatly to this area, with the former providing important insights into chemical and tectonical peculiarities<sup>[52]</sup> and the latter combining those and other findings.<sup>[53]</sup> In 2009, Cooper *et al.* published a series of organic cages formed from condensation reactions of 1,3,5-triformylbenzene and various amines to produce materials that proved porous by nitrogen sorption with BET surface areas of up to  $624 \text{ m}^2 \cdot \text{g}^{-1}$ .<sup>[54]</sup> Utilisation of different chemistry and skillful exploitation of hydrogen bonding patterns allowed Mastalerz and co-workers to obtain porous molecular organic crystals with a staggering  $\text{SA}_{\text{BET}}$  of  $2796 \text{ m}^2 \cdot \text{g}^{-1}$ .<sup>[55]</sup> These two concepts differ in the manner in which the pores are formed. Whereas Cooper *et al.* synthesised molecules that themselves contain a pore hence show *endo-porosity*, the aforementioned example by Mastalerz *et al.* relies on pore formation between discrete molecules upon targeted aggregation by hydrogen bonding hence show *exo-porosity*, as mentioned in the introductory example of Dianin's compound. Nonetheless, Mastalerz is also highly engaged in endo-porous molecules.<sup>[56-57]</sup>

**Figure 4** summarises the described microporous organic polymers (MOPs) but excludes the recently described porous cages as molecular compounds. MOP is a catch-all phrase for the various systems that have been developed though excluding PCPs/MOFs due to their partly inorganic nature.

## SURFACE AREA | AN IMPORTANT FEATURE

One of the most crucial parameters related to the characterisation of porous materials is the already mentioned surface area, which will be used here to describe the accessible surface area, *i.e.* surfaces inside the material that are accessible to probe molecules. For this to take place, the pores must not be closed but open as to allow molecules or atoms to enter and exit. To make comparison between different materials feasible, total SAs are converted into specific SAs by dividing total SA by sample weight. As can be drawn from **Figure 2**, microporous materials can exhibit SAs that exceed  $1000 \text{ m}^2 \cdot \text{g}^{-1}$  and for this reason are most obviously very suitable for the following applications.

### *Gas storage*

In the light of a highly sought-after clean alternative to fossil fuels,  $\text{H}_2$  storage has become a topic of paramount importance to many researchers. The goal is to store  $\text{H}_2$  in an energy- and cost-efficient

manner, for example within a powder adsorbent rather than by means of compression of H<sub>2</sub> gas in an appropriate storage vessel. Apart from a high SA, binding enthalpy is another decisive factor to ensure high gas uptake. A trade-off, therefore, has to be found between sufficiently strong binding of the H<sub>2</sub> inside the material and an energy-efficient and reversible release upon *e.g.* heating.<sup>[58-59]</sup> A material that performs well in this context is PPN-4 taking up 8.34 wt.% (77 K, 55 bar)<sup>[60]</sup> of H<sub>2</sub> and exceeding the revised, and drastically reduced, target value issued by the U.S. Department of Energy (DOE) of 5.5 % by 2015.<sup>[61]</sup> However, PPN-4 only performs well at cryogenic temperature under elevated pressure. For a system to be energy- and therefore cost-efficient it has to work near 298 K under pressures close to 1 bar. There is thus far no material synthesised that can meet such performance targets. Operation at near ambient temperature has been partially achieved by the material PT4AC, showing an H<sub>2</sub> uptake of 0.5 wt.% (298 K, 70 bar)<sup>[62]</sup>, a mere fraction of the DOE target value.

In addition to H<sub>2</sub>, microporous materials are also intended to serve as adsorbents for other gases including methane, an alternative to fossil fuels, or carbon dioxide in the context of an envisaged carbon dioxide capture and storage/utilisation (CCS/U) infrastructure. The polymer COP-1 exhibits a high CO<sub>2</sub> uptake of 127.6 mmol·g<sup>-1</sup> (318 K, 200 bar) at high pressure and elevated temperature but shows mediocre performance at ambient conditions with only 1.4 mmol·g<sup>-1</sup> (298 K, 1 bar)<sup>[63]</sup> that lies in the same region as the value for PAF-1 of 1.1 mmol·g<sup>-1</sup> (298 K, 1.013 bar).<sup>[58,64]</sup> Interestingly, COP-1 exhibits a slightly higher CO<sub>2</sub> uptake despite its vastly inferior specific SA<sub>BET</sub> of 168 m<sup>2</sup>·g<sup>-1</sup> as compared to 5600 m<sup>2</sup>·g<sup>-1</sup> for PAF-1. This demonstrates the importance of heteroatoms inside a structure to interact with carbon dioxide as COP-1 is bedecked with nitrogen atoms whereas PAF-1 incorporates none.

### *Gas separation*

For a substance to separate a mixed gas feed it must show a propensity to accommodate one gas more preferentially than the other. For this to happen the material can be designed with functional groups that allow of preferred interaction with only one gas in the feed. A typical example is incorporation of amine groups into the structure of a porous polymer to enhance its affinity to carbon dioxide, which shows a strong interaction between the electron-deficient carbon and the lone-pair providing nitrogen.<sup>[65-68]</sup>

### *Heterogeneous catalysis*

Most representatives of microporous materials are insoluble in common solvents. The reason for that is their high degree of polymerisation with the corollary of an enormous molecular weight. This inherent feature poses a problem in terms of processability. On the other hand, being insoluble enables such materials to be employed as catalyst support or catalyst in their own right to perform heterogeneous catalysis that offers easy recovery and recyclability of the catalyst thereby facilitating purification of the product. This can save financial resources and decide whether or not a process is economically viable.<sup>[69-70]</sup>

### *Organic electronics*

Microporous organic polymers have found application in organic electronic devices, in particular organic solar cells. A dominant approach for organic photovoltaics is the so-called bulk hetero junction (BHJ) where donor and acceptor phases are randomly mixed. For successful operation, a solar cell must provide for the generation of excitons, *i.e.* electron-hole pairs, upon absorption of photons. Subsequently, the exciton is to be split and the electron separated from the hole. This process is only favoured when taking place at a so-called p-n-junction, which is a rather inorganic term and usually related to inorganic semiconductors that have been p- and n-doped. However, the basic concept, *mutatis mutandis*, is absolutely legitimate in the world of organic molecules. Then, n-doped and p-doped are referred to as electron acceptor, *i.e.* exhibiting a low-energetic LUMO (lowest unoccupied molecular orbital), and electron donor, *i.e.* with a high-energetic HOMO (highest occupied molecular orbital), respectively. Now, the space where exciton separation can take place is exactly at the donor-acceptor interface and there where the walls are thin and the space is vast, microporous materials offer a unique environment for exciton separation to take place in an efficient and widespread manner. To put it differently, microporous materials themselves constitute an outright interface and have nearly no matter buried in bulk. A feasible approach is to infiltrate a microporous network that plays the role of the donor with an acceptor such as phenyl-C<sub>61</sub>-butyric acid methyl ester (PC<sub>61</sub>BM) that is universally used as acceptor molecule.<sup>[71]</sup> Alternatively, a MOP can be designed such as to comprise both donor and acceptor moieties.<sup>[72]</sup>

### **SURFACE AREA | THE THEORY BEHIND**

As mentioned earlier, surface area is one of the most important properties of a porous material. The most commonly used method to assess surface area is based on the theory of Brunauer, Emmett, and Teller (BET) formulated in 1938.<sup>[26]</sup> Their concept was an extension of Langmuir's theory on adsorption.<sup>[73]</sup> Whereas the latter is restricted to monolayer adsorption, the BET theory takes into account multilayer adsorption and is therefore more in agreement with reality. Both approaches, however, are based on flat, uniform, and chemically homogeneous surfaces. Yet, surfaces provided by microporous materials deviate far from this ideal and are mostly amorphous, irregularly formed, and typically highly curved, necessary features to generate high surface areas by micropores. Other shortcomings of the BET model especially regarding microporous systems became apparent and were summarised together with amendments by Rouquerol *et al.* so that the BET concept is still employed to determine surface area values.<sup>[74-76]</sup> The BET theory is most typically applied to volumetric nitrogen sorption. This method is based on providing nitrogen in very small doses to the sample starting under high vacuum conditions and measuring whether or not the pressure inside the probe cell rises. When the sample adsorbs nitrogen, those adsorbed nitrogen molecules cannot contribute to a pressure gain inside the cell. The nitrogen volume necessary to stimulate a pressure gain is then measured step by step. The higher the SA of the sample, the more nitrogen it can accommodate, hence more nitrogen is necessary to induce a pressure increase in the probe cell. Due

to the high vapour pressure of nitrogen at ambient conditions, the entire measurement has to be carried out at low temperatures in order to lower the vapour pressure of nitrogen. The alternative to measure, say, at room temperature and apply extremely high pressures in order to compel nitrogen into the pores and reach condensation, is not feasible due to nitrogen's supercritical behaviour above 126 K implying that it cannot be liquefied above that temperature, let alone at room temperature. For this reason, nitrogen sorption experiments are carried out at 77 K, cooled by liquid nitrogen. The isotherm is recorded up to a relative pressure  $p/p_0$  of unity where condensation of the probe gas occurs, because the probe gas nitrogen is cooled with liquid nitrogen.

For the determination of SA, it is expedient to use the BET equation in its linearised formulation:

$$(Eq. 2) \quad \frac{p}{n^a(p_0 - p)} = \frac{1}{n_m^a C} + \frac{(C - 1)}{n_m^a C} \cdot \frac{p}{p_0} \quad \text{with} \quad C = \exp\left(\frac{h_1 - h_l}{RT}\right)$$

$$y = I + S \cdot x$$

Eq. 2 relates the amount of gas adsorbed  $n^a$  at relative pressure  $p/p_0$  to the monolayer capacity  $n_m^a$ . The BET constant  $C$  is related to enthalpy of adsorption of the first layer of adsorbate ( $h_1$ ) as well as of the following layers ( $h_l$ ). In the generic formulation of a linear equation below the BET equation  $y$  and  $x$  denote function value and variable, respectively,  $I$  denotes y-intercept, and  $S$  stands for slope of the graph. From the linear form, both the BET constant and monolayer capacity can be obtained via Eq. 3:

$$(Eq. 3) \quad C = 1 + \frac{S}{I} \quad \text{and} \quad n_m^a = \frac{1}{S + I}$$

Where the monolayer capacity  $n_m^a$  expresses how much gas (in moles) is adsorbed in a fully occupied monolayer. In conjunction with Avogadro's constant  $L$  and the geometrical area that one adsorbate molecule occupies  $a_m$  (0.162 nm<sup>2</sup> for N<sub>2</sub> at 77 K) total surface area is given by Eq. 4:

$$(Eq. 4) \quad SA_{total} = n_m^a \cdot L \cdot a_m$$

To enable a comparison between different materials and exclude the factor of weight, total SA values are divided by sample mass and values are given in m<sup>2</sup>·g<sup>-1</sup> according to Eq. 5:

$$(Eq. 5) \quad SA = \frac{SA_{total}}{m}$$

To obtain a linear BET graph, attention has to be paid to what points of the isotherm are taken into account. It was observed that values taken in the  $p/p_0$  range of 0.05 to 0.30 yield a linear BET graph.<sup>[77]</sup> But this range was established based predominantly on the characterisation of mesoporous systems. Due to cooperative effects, micropores are filled with gas at much lower

pressures than is the case for larger pores. The Kelvin equation predicts that the point where a liquid is in thermodynamic equilibrium with its vapour will be reached earlier in more pronouncedly curved spaces. As a result, micropores are filled at lower relative pressures than larger pores. The inevitable consequence is that monolayer formation is completed at lower pressures. Thus, for microporous systems to assess the moment correctly when a monolayer is completed, *i.e.* to determine monolayer capacity, the threshold has to be set to lower values of  $p/p_0$  by one order of magnitude: 0.005 to 0.030.<sup>[75-76]</sup> To aggravate the problem, a BET curve can exhibit more than one linear region. To facilitate the decision for the correct five points to choose, Rouquerol *et al.* established so-called consistency criteria.<sup>[74]</sup> Firstly, from the Rouquerol plot  $n^a(p_0 - p)$  vs.  $p/p_0$  only values should be considered for BET analysis that lie on the branch with a positive slope, *i.e.* the maximum value and values to the left that not necessarily need to be subsequent. Secondly, the y-intercept of the linear BET graph should be positive which in turn yields a positive value for the BET constant that itself is only meaningful when larger than zero.

## PORE VOLUME

Apart from surface area, another descriptive parameter for porous materials is pore volume ( $V_{\text{pore}}$ ). As schematically depicted in **Figure 1**, pore volume decreases with increasing surface area. To assess  $V_{\text{pore}}$ , it is essential to know how much adsorbate the sample can accommodate in total. Therefore, a point close to saturation pressure needs to be taken from the isotherm to calculate  $V_{\text{pore}}$ , for at this point it can be argued that the pores are entirely filled with liquid adsorbate. Attention has to be paid in the event of a steep increase of adsorbed volume at the end of the isotherm. This pattern commonly reflects textural porosity and/or macropores present in the sample. Textural porosity is derived from agglomeration of once independent particles thereby creating void interstitial space in between particles that might be misconstrued as meso- or macropores. In this case, a point has to be chosen that lies well below the saturation pressure but still in the region of the isotherm with a moderate slope. The value that is displayed as ordinate is the volume of nitrogen adsorbed  $V_{\text{ads}}$  and needs to be transferred into volume of liquid nitrogen  $V_{\text{liq}}$  (Eq. 6):

$$(Eq. 6) \quad V_{\text{liq}} = V_{\text{ads}} \cdot \frac{P_a V_m}{RT}$$

Where  $P_a$  = ambient pressure ( $1 \cdot 10^{-5}$  Pa),  $T$  = ambient temperature (273.15 K),  $R$  = universal gas constant ( $8.3144 \text{ J} \cdot \text{mol}^{-1} \cdot \text{K}^{-1}$ ), and  $V_m$  = molar volume of liquid adsorbate ( $34.7 \cdot 10^{-6} \text{ m}^3 \cdot \text{mol}^{-1}$  for nitrogen). When all the constant values are entered, a formula is obtained that makes feasible a convenient assessment of pore volume  $V_{\text{liq}}$  for any given isotherm point  $V_{\text{ads}}$  according to Eq 7:

$$(Eq. 7) \quad V_{\text{liq}} = V_{\text{ads}} \cdot \frac{1.5}{1000}$$

## PORE SIZE AND PORE SIZE DISTRIBUTION

Pore size and its associated distribution are also important parameters especially for the classification of a material as micro-, meso-, or macroporous and to what extent it contains pores of one or the other domain. The Kelvin equation is the starting point for the assessment of pore size since it relates required vapour pressure for condensation inside a tube to the known radius of that tube. Exploiting the inverse approach makes feasible the calculation of the Kelvin radius of the tube, that is to say Kelvin pore radius  $r_K$ , from known relative vapour pressure (Eq. 8):

$$(Eq. 8) \quad r_K = -\frac{2\sigma V_m}{RT \ln(p/p_0)}$$

Where,  $\sigma$  = surface tension ( $8.85 \cdot 10^{-3} \text{ J} \cdot \text{m}^{-2}$  for nitrogen at 77 K),  $V_m$  = molar volume of liquid adsorbate ( $34.7 \cdot 10^{-6} \text{ m}^3 \cdot \text{mol}^{-1}$  for nitrogen),  $R$  = universal gas constant ( $8.3144 \text{ J} \cdot \text{mol}^{-1} \cdot \text{K}^{-1}$ ), and  $T$  = boiling point of nitrogen (77 K). Insertion of constant values, introduction of a factor of  $10^{10}$  for conversion from metre to angstrom as well as a conversion factor from a natural to a common logarithm, and finally multiplying the term by -1 lead to a simplified expression (Eq. 9):

$$(Eq. 9) \quad r_K(\text{\AA}) = \frac{4.17}{\log(p_0/p)}$$

A caveat needs to be introduced here. The Kelvin radius describes the radius of a pore at a relative pressure where condensation occurs. Yet, before condensation occurs some adsorbate has already formed on the inner walls of the pore. Likewise, during desorption a certain amount of adsorbate remains at the pore walls after evaporation takes place. Obviously, this phenomenon has to be considered for both the adsorption and desorption branch and leads to underestimation of pore size when solely relying on  $r_K$ . To alleviate this inaccuracy, the mentioned adsorbate layer needs to be accounted for by determination of its thickness so that the actual pore radius is obtained as Eq. 10:

$$(Eq. 10) \quad r = r_K + t$$

Several approaches have been proposed to determine the statistical thickness  $t$  of a monolayer of an adsorbed film such as the methods of Halsey,<sup>[78]</sup> de Boer,<sup>[79]</sup> or the carbon black method,<sup>[80]</sup> which will not be dealt with in more detail here.

Along with pore size, it is important to know how many different pore sizes are present within a sample and what share from the overall pore volume these different pores domains claim. This is reflected in the so-called pore size distribution (PSD) that basically relates the amount of adsorbed or desorbed volume of adsorptive to the pore size. Various approaches have been developed to tackle this issue such as the method proposed by Barrett, Joyner, and Halenda (BJH) that describes

the determination of pore radii by assessment of how much liquid adsorbate is desorbed at a certain relative pressure starting from  $p/p_0 = 1$ , basically employing the Kelvin equation.<sup>[81]</sup> Later advancement led to formulation of the DH-method by Dollimore and Heal.<sup>[82]</sup> However, these early classical macroscopic approaches have shown to be inaccurate in handling of pores smaller than median mesopores (< 10 nm) resulting in an underestimation of pore size. For reasons discussed below, in small pores additional forces also emerge from adsorbate-adsorbate interaction and have to be taken into account. To overcome the deficiencies, approaches based on density-functional-theory (DFT) have been developed, which more accurately describe the sorption and phase behaviour of fluids in extremely constrained/confined spaces. In a nutshell, DFT methods compare the experimentally obtained isotherm with a set (kernel) of model isotherms each representative of a pore system with a specific pore size and assigns each of these model isotherms a factor that reflects to what extent the respective model isotherm is contained in the experimentally obtained isotherm. As the PSD of each model isotherm is known, the experimental isotherm can be assigned a pore size distribution as a mélange of model PSDs.

## TYPES OF ISOTHERMS

In the nanometer domain things behave very differently from what is experienced in the macroscopic world. There are effects that are noticeable only in the nanoscopic world. Filling a micropore (diameter < 2 nm) with nitrogen necessitates far less pressure of gas than is required to fill a meso- or macropore. This is because in a pore of such small dimensions nitrogen molecules will interact with the pore walls and the other nitrogen molecules much more strongly than is the case in bigger pores yielding forces that help to hold the molecules inside. As those forces are less evident in or even absent from meso- and macropores, the applied pressure or, for that matter, the number of gas molecules/atoms per volume fraction, needs to be higher in those bigger pores in order to compel the gas to enter and stay inside.

The shape of the recorded isotherm already gives a fingerprint of the pore system behind. As mentioned above, micropores will be filled with gas at appreciably lower relative pressures than larger pores. This behaviour is reflected in the shape of the isotherm exhibiting a very steep increase of adsorbed volume right in the beginning at low  $p/p_0$  values. According to IUPAC recommendations, this kind of isotherm is designated as type I (**Figure 5, left**).<sup>[77]</sup> Samples that are exclusively microporous will show an extended and near-flat plateau region after micropore filling has been completed, *i.e.* that there is no significant external surface area to be covered with adsorbate at higher relative pressures. Unrestricted monolayer-multilayer formation cannot take place in micropores because their restricted volume does not allow of multilayer formation hence micropores are just filled up by small amounts of adsorptive, so-called *micropore filling*.

A type II isotherm is produced by non-porous or macroporous materials. The initial steep increase typical for type I isotherms is absent and adsorption is governed by unrestricted monolayer-multilayer formation. The knee of a type II isotherm is referred to as *point B* and is an indication of

the complete formation of a statistical monolayer whence multilayer formation proceeds. It should be noted that multilayer formation usually starts before a complete monolayer is formed.

Type III isotherms can be observed when adsorbate-adsorbate interactions dwarf adsorbate-adsorbent interactions. This type of isotherm is rather rare. Isotherm types I, II, and III are fully reversible, *i.e.* the desorption branch—evolving after saturation pressure of  $p/p_0 = 1$  has been reached—follows the exact same trace of the adsorption branch.

The most striking feature of type IV isotherms is their non-reversibility. Other than that, they resemble type II isotherms in terms of monolayer-multilayer formation. Conversely, at a certain point, multilayer formation gives way to so-called capillary condensation manifesting itself in a near-vertical slope of the isotherm. The formation of a plateau towards saturation pressure suggests the absence of macropores.

Type V isotherms initially show a similarity to type III inasmuch as adsorbate-adsorbate interactions play an important role. To their end they are reminiscent of type IV isotherms meaning that they are likewise not reversible and exhibit hysteresis.

Type VI isotherms are reversible and again show unrestricted monolayer-multilayer formation as is the case for type II. However, their stepwise evolution is indicative of multilayer formation by subsequent monolayers. This kind of behaviour is displayed by non-porous, uniform surfaces.

## HYSTERESIS PHENOMENA

When desorption does not follow the path described by the adsorption branch of the isotherm, a phenomenon is present that is referred to as *hysteresis*. Hysteresis can assume different shapes (**Figure 5, right**). As described above, hysteresis necessitates that the adsorbate occupies energy states that are different during adsorption and desorption. Hysteresis H1 and H4 are considered the two extreme cases between which H2 and H3 evolve. The near-vertical desorption of H1 tends to be exhibited by samples with well-defined cylindrical pores or specimens containing agglomerates or spheres of monodisperse radius assembled in regular arrays. As such they present a narrow pore size distribution leading to desorption at one specific value of relative pressure. H2-like hysteresis is ascribed to systems of multiple pore diameters whereas H3-like hysteresis is attributed to materials featuring plate-shaped particles that promote formation of slit-shaped pores. The latter is true for H4 as well, with the initial part of the isotherm being different in demonstrating the presence of micropores. Dashed lines (**Figure 5, right**) exemplify low pressure hysteresis that is usually encountered in soft porous materials such as MOPs and is caused by swelling of the organic and non-rigid structures. Swelling causes the compounds to alter their structure during the measurement thereby forestalling a point of closure of desorption and adsorption branch. In such a case, analysis is severely hampered.

The reasons for hysteresis are a matter of intense debate and can be manifold.<sup>[83-84]</sup> One explanation features the phenomenon of capillary condensation that is found in mesopores. During initial multilayer formation according to unrestricted monolayer-multilayer formation and visualised

by a moderate but steady positive slope after point B has been passed, adsorbate molecules of opposite sites get in closer proximity. When the distance is small enough, adsorbate-adsorbate interactions come into effect and supplement adsorbate-adsorptive interactions whereupon a concave meniscus is formed. This gives rise to abrupt pore filling by liquefaction of incoming adsorptive even at conditions of substantial under-saturation, *i.e.* at  $p/p_0 < 1$ , and is visualised by a near-vertical slope of the isotherm. Due to the additional adsorbate-adsorbate interactions (capillary forces) the molecules assume an energetically more favourable state. During desorption the pore is emptied *via* a receding meniscus as opposed to adsorption that is initially governed by unrestricted multilayer formation. That is the reason why adsorbate molecules refuse to enter the gas phase during desorption to a certain point and lower relative pressures need to be applied than were necessary for adsorption. Capillary condensation predominantly occurs in pores that are not of

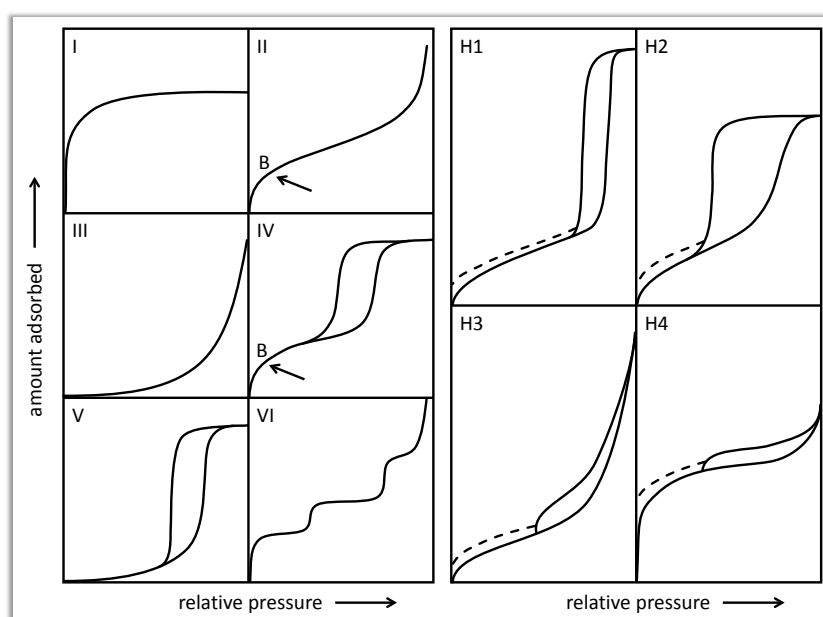


**Figure 5.** Types of isotherms (left) and hysteresis (right) as classified by IUPAC (reproduced from reference 77).

ideal cylindrical shape but consist of a main body that encompasses most of the volume and an entrance/neck that is of smaller diameter, so-called ink-bottle pores (*i.e.* type II/H2 isotherms). Generally, the smaller the diameter of the entrance, the lower  $p/p_0$  at which sudden desorption is observed. This is predicted by the Kelvin equation, which stipulates that the relative pressure required to form a concave meniscus is lower for smaller diameters. This means that under-saturation can be more pronounced to form a concave meniscus when the diameter is smaller. There is, however, a lower limit of abrupt desorption due to physical properties of the adsorptive, the so-called tensile strength effect. That effect causes a cavity to implode due to overwhelming surface tension that cannot be sustained by no matter how small a radius of the meniscus. In the case of nitrogen at 77 K the lowest relative pressure at which desorption is observed lies between 0.40 and 0.45.

Complementary reasoning for the occurrence of hysteresis is provided by network models that deal with so-called pore-blocking (percolation) effects and cavitation phenomena.<sup>[85-87]</sup> Pore-blocking is assumed to take place in pores with wide body and narrow neck, as described above. Although the wide body would empty at higher relative pressure, evaporation of its contents is kinetically obstructed by the narrow entrance which itself is filled with adsorbate that requires lower  $p/p_0$  to be emptied. Thus, the wide pore body remains filled until the neck is emptied. When that has been achieved, the entire contents of the body evaporate at once causing the isotherm to plummet almost vertically. The other phenomenon is called cavitation and considered to occur in pores with necks of yet smaller diameters than is the case for pore-blocking. In that instance the adsorbate inside the neck demands such low a relative pressure that the contents of the wide body, which is very eager to evaporate at much higher relative pressure, cannot be held in check and starts to evaporate irrespective of the neck still being filled. This happens at a relative pressure higher than required for emptying the neck and proceeds *via* cavitation, *i.e.* gas bubbles formed in the pore body diffuse through the neck that is still filled with liquid adsorbate. As a result, the pore body will be emptied whereas the neck is still filled. The neck then starts to release its adsorbate when the respective  $p/p_0$  is reached.

## OTHER TECHNIQUES

The preceding discussion focused on volumetric nitrogen sorption at 77 K. Nevertheless, other gases have found application in sorption analysis as well. Additionally, techniques other than gas sorption have been proven useful and this section is to elucidate some of them without any claim to be exhaustive.

Carbon dioxide sorption analysis performed typically at 273/298 K, is particularly appropriate for the characterisation of materials containing very small pores, so-called ultra micropores with diameters below 0.7 nm that are not accessible to nitrogen. A further benefit is less demanding requirements for machinery as measurements can be conducted at near room temperature and under less pronounced vacuum. In addition, owing to the relatively high temperature of measurement the gas has higher thermal thus kinetic energy, a circumstance that diminishes diffusion problems and allows the diffusion rate equilibrium to be reached much faster. Thus, analysis time is greatly reduced by approximately a factor of 10 as compared to nitrogen sorption, leading to CO<sub>2</sub> sorption analysis runs of a few hours at most.

Krypton sorption at 77 K is well-suited for very small sample masses or, for that matter, samples with very small surface areas. The reason for this is the vastly enhanced sensitivity of the probe system caused by an immensely different saturation pressure of nitrogen and krypton at 77 K that for nitrogen amounts to 760 Torr and for krypton to 2.6 Torr in a subcooled state. As a result, at given relative pressure and volume of probe cell, the ratio of dosed probe gas to adsorbed probe gas will be a lot larger for nitrogen meaning that in relation to the amount of gas adsorbed much more probe gas remains in the cell above the porous sample in the case of nitrogen as compared to

krypton. Thus, the pressure change inside the cell will be small and hard to measure for nitrogen whereas it is large for krypton. For that reason, samples with small surface areas can induce a larger hence more reliably measurable change in pressure when probed with krypton as compared to nitrogen.

The aforementioned methods can be applied for assessment of very small pores but they falter and eventually fail to produce results when bigger pores are to be investigated. Macropores with diameters above 50 nm cannot be probed by volumetric gas sorption. Instead, mercury intrusion porosimetry is used for pores with diameters from 0.04  $\mu\text{m}$  to 400  $\mu\text{m}$ . The smaller a cavity, the larger the required pressure to fill it with mercury hence the applied pressure gives rise to assessment of pore size.

More exotic techniques for investigation of porosity are small and wide angle X-ray scattering (SAXS/WAXS) and positron annihilation lifetime spectroscopy (PALS). Common to these methods is their ability to penetrate not only open but also closed pores.

## **SCOPE OF THESIS**

Chapter 1 expounds findings concerning the development and synthesis of new morphologies of microporous organic polymers. It will be shown that it is possible to produce microporous polymers in a film-like morphology as opposed to the conventionally obtained powder. This was achieved for both PPN-6 (aka PAF-1) and CMP-1.

Chapter 2 presents research into templating approaches aimed at the introduction of mesoporosity into a microporous system. This was attempted by infiltration of mesoporous silica with precursor molecules for a microporous polymer.

Chapter 3 describes results regarding the infusion of microporous systems with the intriguing properties of light responsive molecules. It will be shown that it was possible to create structures that are both microporous and reversibly light responsive and that changes in gas sorption and other properties can be triggered by light stimuli.

Each of these chapters comprises an introduction to its respective topic followed by a presentation of the obtained results and associated discussion to be concluded by summarising remarks in tandem with an outlook. These three main chapters are succeeded by an Appendix that presents details of certain calculations and deliberations as well as additional plots all of which are referred to within the main text and help to follow the author's line of argument. The Appendix is succeeded by the Experimental Part containing details of analytical methods and syntheses protocols. The final pages of the thesis are dedicated to a list of abbreviations used throughout this work and a compilation of literature references.

# CHAPTER 1

## FILMS

### MICROPOROUS POLYMER FILMS ON GOLD ELECTRODES

Microporous polymer networks (MPNs) have become an intensely investigated research field due to their unique ability to combine advantages of porous materials with the tunable functionality inherent to organic molecules.<sup>[15]</sup> Introduction of various functional groups into the backbone of MPNs has led to applications in catalysis,<sup>[45-46,69-70,88-89]</sup> energy conversion/storage,<sup>[90-93]</sup> and gas sorption<sup>[58-59,94-95]</sup> and separation.<sup>[96-98]</sup> Versatility of applications for MPNs was recently enhanced by exploring their usefulness in organic electronic devices.<sup>[71,99-101]</sup> Common to most MPNs is their insolubility in any solvent caused by a high degree of cross-linking tantamount to high molecular weight. A lack of solubility is indeed advantageous in regard to heterogeneous catalysis. However, for applications such as membranes, catalytically active coatings, functionalised nanoparticles, and in particular organic electronics such as organic light emitting diodes or organic photovoltaics, it is essential to obtain microporous polymers as thin films.

Different strategies have been pursued to reach that goal. One way to circumvent pronounced cross-linking is to use compounds that yield polymers of lower dimensionality as achieved in PIM synthesis and described earlier.<sup>[31]</sup> That approach was extended to conjugated dendrimers and soluble CMPs (sCMPs)<sup>[43]</sup> as well as MPN nanoparticles,<sup>[102]</sup> which likewise were processable from solution. Further improvement was attained by the design of novel organic cages, soluble in many solvents and advantageously self-aggregating into porous crystals after solvent removal.<sup>[54,56]</sup> In some cases, surfaces provided during synthesis served as nucleation site onto which polymers were deposited.<sup>[71,103-105]</sup> For example, Götzhäuser *et al.* produced free-standing but non-porous membranes of polymer carpets,<sup>[106]</sup> which were fabricated based on earlier findings on cross-linking of SAMs.<sup>[107-109]</sup> More recently, Dichtel *et al.* reported on COF-5 assembled, yet not covalently, on graphene.<sup>[103]</sup> In a related manner, Bein *et al.* attached a thienothiophene-based COF to an ITO

electrode.<sup>[71]</sup> As a further means to form polymer films, electro-polymerisation has been employed necessitating electro-polymerisable tectons.<sup>[110-112]</sup> Although this approach allows of a very defined growth of films, it suffers from decisive drawbacks. It is limited in scope due to reliance on electro-polymerisable monomers. In addition, this technique usually shows an innate propensity for inclusion of impurities in the polymer films due to entrapment of electrolyte during synthesis that cannot be disposed of. This has severe detrimental effects on electronic properties.<sup>[113-114]</sup>

In the aforementioned approaches the polymer/electrode interface is not well controlled and it can be assumed that films are attached to the surfaces solely by dispersion forces, thus potentially prone to electrode/surface detachment. This would certainly be advantageous in case free-standing films or membranes are aimed at. However, for other applications such as electrocatalysis or organic electronics, formation of stable films on electrodes is an indispensable requirement. To that end, methodologies have been developed that enable more control over attachment of films to electrodes. Early attempts employed MOFs<sup>[115-120]</sup> that the groups of Fischer and Bein compelled to assume film-like morphology *via* bonding to a self-assembled monolayer (SAM) yielding so-called surface bonded MOFs (surMOFs). Other procedures aimed at formation of films of amorphous all-organic polymers on SAM-functionalised substrates by covalent binding.<sup>[121]</sup>



**Figure 6.** Concept of film formation on gold surfaces. Only SAM-functionalised substrates are able to bind a polymer film covalently whereas blank samples remain unaffected (left, illustration). For the proof of concept experiments, tetrakis(4-bromophenyl)methane (TBPM) was chosen as monomer to yield PPN-6 as film covalently bonded to a SAM bearing a halogen substituent as functional group that can partake in the polymerisation reaction (right, X = I or Br). Conditions for Yamamoto reaction were as follows: 1.00 eq. TBPM ( $c = 5.2 \text{ mmol}\cdot\text{l}^{-1}$ ), 4.60 eq. 2,2'-bipyridyl, 4.63 eq. bis(1,5-cyclooctadiene)nickel(0), 4.66 eq. 1,5-cyclooctadiene in a volumetric 1:1 mixture of dry DMF and dry THF at room temperature for time periods of 18 min to 20 h.

In this work, a bottom-up approach is embarked upon to grow a network onto a flat substrate (**Figure 6**). In this way, it is desired to create coatings of microporous polymers that heretofore were only accessible as insoluble powders with no prospect of processability. Furthermore, unambiguous spectroscopic and macroscopic evidence will be delivered to show that SAM-functionalisation is essential for firm attachment of the film to the substrate in the case of PPN-6 coatings. The substrate of choice is gold because it is a superior electrode and amenable to modification by a SAM that served as bond-mediating group. Modifying the gold surface with a SAM bearing accessible halogen groups allows of a polymerisation reaction to be carried out that involves the halogen substituent. Since the SAM itself is covalently bonded to the gold, the formed polymer is also connected to the

surface in a covalent fashion provided that the monomer species reacts with the exposed functional groups of the SAM. As it is desirable to have the SAM influence the system to as small an extent as possible while creating a connection between the surface and the polymer that features electronic conjugation, 4-bromothiophenol was opted for to function as SAM-forming molecule and is a commercially available, cheap candidate.

## RESULTS AND DISCUSSION

### PPN-6 | A FILM ON GOLD | PART ONE <sup>[122]</sup>

The first set of experiments was designed as proof of concept and aimed at establishing a methodology for the growth of microporous polymer films onto an electrode. It was clear from the outset that the films will contain very little mass of substance rendering investigation of porosity by sorption methods difficult. For this reason, the polymer of choice to grow on the surface is PPN-6, which is known to exhibit a high specific surface area. In 2009, Thomas *et al.* reported the first porous polymer synthesised by Yamamoto cross-coupling reaction.<sup>[48]</sup> In the same year, Zhu *et al.* applied this reaction scheme to the tetrahedral monomer tetrakis(4-bromophenyl)methane yielding PAF-1 with reported surface areas of 5600 and 7100 m<sup>2</sup>·g<sup>-1</sup> applying either BET or Langmuir theory, respectively.<sup>[47]</sup> The synthetic protocol for PAF-1 was later improved by Zhou *et al.* and PAF-1 was renamed PPN-6 in the process.<sup>[50]</sup> For practical reasons, the here applied protocol resembles that of Zhou *et al.* and the designation PPN-6 will therefore be maintained throughout this thesis.

The following excerpt provides a succinct description of the experimental procedure. For a more in-depth account, the interested reader is kindly referred to the experimental part at the end of this dissertation.

Gold coated silicon wafer pieces approximately the size of 1 × 4 cm were cleaned with piranha solution before being immersed in an ethanolic solution of either 4-bromothiophenol or 4-iodothiophenol for SAM-functionalisation following established procedures.<sup>[123-124]</sup> The as-functionalised wafer pieces were then subjected to a Yamamoto-type Ullmann cross-coupling reaction solution according to the PPN-6 protocol that avoids elevated temperatures thus reducing the danger of SAM desorption.<sup>[124]</sup> Substrates were subjected to the solution from atop thereby forestalling any mechanical stress induced by the stirrer. After varying amounts of time the reaction was quenched by careful addition of aqueous hydrochloric acid. The chief amount of polymer formed during the reaction precipitated as bulk powder. However, it could already be judged visually at this stage that a layer of polymer did also form on the substrates. After the reaction, the silicon pieces adopted a dull look in the region that was immersed in the reaction mixture whereas that part of the surface that was not submerged remained unaltered, *i.e.* utterly shiny. Bulk and wafer pieces were treated similarly in terms of washing and Soxhlet extraction.

Before any discussion of the formed films can begin, it is wise beforehand to confirm the identity of the produced bulk powder as PPN-6 by applying various techniques. Elemental analysis revealed

atomic composition with acceptable accuracy: calculated (found) for  $C_{25}H_{16}$  in m-%: C 94.90 (92.70), H 5.10 (6.18). IR spectra (**Figure 7**) of formed bulk polymer reveal the disappearance of typical C-Br signals at 509 and 532  $cm^{-1}$  ( $\delta CBr$ ). Solid state  $^{13}C\{^1H\}$  CP/MAS NMR (rotation frequency 10 kHz) exhibits five signals, as expected (**Figure 8, left**). Four signals appear in the aromatic region at 143.9, 137.3, 128.8, and 123.0 ppm and one signal at 62.2 ppm that can be ascribed to the  $sp^3$ -hybridised carbon central to every tetraphenylmethane repeating unit. At 27.7 ppm, an additional signal protrudes the side band and originates from residual THF.

Nitrogen sorption experiments were conducted at 77 K (**Figure 8, right**). The determined BET surface area amounts to  $2977\text{ m}^2\cdot\text{g}^{-1}$ , a very high value in itself but appreciably lower than the benchmark value of  $5600\text{ m}^2\cdot\text{g}^{-1}$  reported by Zhu *et al.* for PAF-1<sup>[47]</sup> and also lower than the value of  $4023\text{ m}^2\cdot\text{g}^{-1}$  published by Zhou *et al.* for PPN-6.<sup>[50]</sup> After the identity of the bulk polymer has been conclusively established as PPN-6, investigation of the formed films ensues.

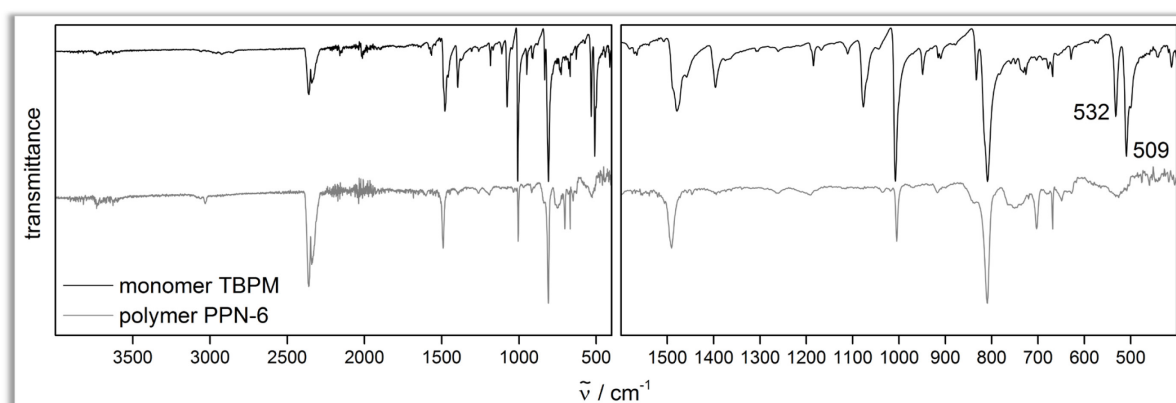


**Figure 7.** ATR-FTIR spectra of monomer tetrakis(4-bromophenyl)methane (TBPM, black line) and bulk polymer PPN-6 (grey line). Disappearance of the labelled signals is indicative of loss of bromine, hence polymer formation. Plots are stacked along the ordinate axis.

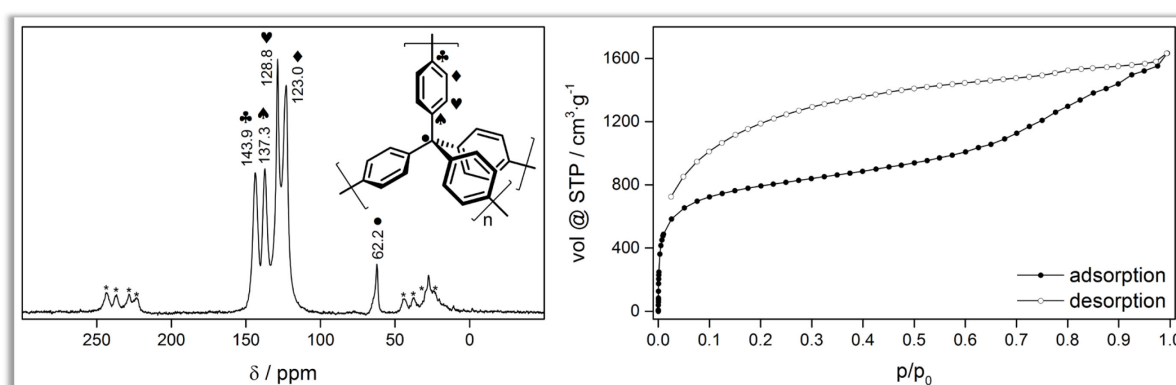


**Figure 8.** Solid state  $^{13}C\{^1H\}$  CP/MAS NMR spectrum (left,  $v_{rot} = 10\text{ kHz}$ , spinning sidebands are marked with an asterisk) and isotherm derived from nitrogen sorption at 77 K of bulk polymer PPN-6 that was formed during the reaction (right).

One main objective of this work is to prove the necessity of the SAM for covalent hence firm binding of the polymer film to the substrate. An appropriate means of demonstration is to employ blank wafer pieces next to SAM-functionalised substrates in the very same reaction (**Figure 6**). Those

blanks have been cleaned in piranha solution, too, but not been subjected to SAM-functionalisation. Indeed, in most experiments, the blank samples came out of the reaction as they entered the reactor, *i.e.* clean and shiny, with no polymer layer attached. However, in some cases although the blank sample did not expose any bond-mediating groups at its surface, it did exhibit a layer of polymer after the reaction (see **Figure 9, right-hand side**). In those instances the blank substrate seems to have served merely as nucleation site for nascent polymer. To verify whether or not a SAM is indispensable to attach a polymer layer firmly onto a gold substrate both the blank and the SAM-covered specimens were immersed in THF overnight without stirring whereupon only the blank sample showed detachment of the polymer film upon rinsing with THF. This confirms that the polymer film was not covalently bonded to the substrate. The SAM-covered sample resisted thorough rinsing *via* pipette and retained the polymer film. After the swelling procedure, the film on the SAM-functionalised sample exhibited cracks. This observation is in line with a polymer film that suffered from structural strain caused by swelling and drying. To further substantiate the claim that



**Figure 9.** Left-hand side: Photographs of as-purchased gold coated silicon wafer (a), a SAM-functionalised sample (b), and blank sample (c) the latter two of which were subjected to the PPN-6 polymerisation reaction. Middle to right-hand side: Photographs of SAM-functionalised gold wafer with grown polymer film PPN-6 before (middle) and after (right) swelling and rinsing with THF. For comparison, one of the rare occasions with a polymer film deposited on a non-functionalised (blank) gold wafer is shown under the same treatment showing removal of the polymer film after rinsing with THF. To increase the visibility of cracks after and also prove their absence before this procedure, SAM-pictures have been graphically edited (sharpness set to 100 %, colour saturation set to 400 % in MS Powerpoint 2010).

the polymer film binds in a covalent fashion to the surface of the substrate, a technique has been employed that is capable of elucidating processes at surfaces: surface enhanced infrared absorption spectroscopy (SEIRAS). A silicon single crystal is covered with a layer of gold by electrochemical deposition and placed at the bottom of a probe cell. Within the probe cell, formation of the SAM was studied first and subsequently the entire PPN-6 procedure was carried out within the cell. The gold film is nanostructured and serves both as SAM-functionalised surface and as IR signal amplifier. SEIRAS is sensitive to surfaces and relies on a local amplification of the incident electric field around small metal islands. Since signal enhancement arises from excitation of surface plasmon polaritons, the effect promptly fades away with increasing distance from the surface and is observable only up to approximately 8 nm, which is very suitable to study mono and multilayer formation.<sup>[125]</sup> SEIRAS

allows to monitor SAM formation on gold and the covalent binding of the first layers of monomer to the SAM.

In **Figure 10, left** successful formation of the SAM by covalent attachment of 4-bromothiophenol to gold can be witnessed. The characteristic S–H stretching band  $\nu(\text{SH})$  at around  $2580\text{ cm}^{-1}$  is absent already shortly after incubation suggesting complete consumption of thiol groups in the reaction with gold.<sup>[126-128]</sup> In addition, the typical vibrational modes of benzene were detected at 1466 and

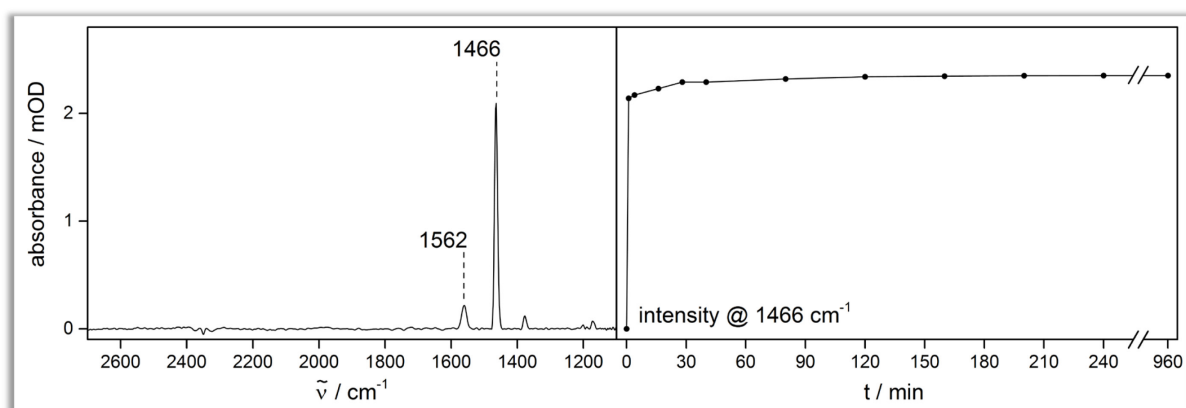


**Figure 10.** SEIRA spectrum of SAM formation of 4-bromothiophenol on gold recorded minutes after incubation (left) and the evolution over time of the most intense signal at  $1466\text{ cm}^{-1}$  (right).

$1560\text{ cm}^{-1}$ . The first denotes the C–H in-plane bending and C–C asymmetric stretching mode, the second indicates the C–C symmetric stretching mode.<sup>[127]</sup> To examine the evolution of the spectrum the most intensive aromatic band at  $1466\text{ cm}^{-1}$  was chosen as a marker for monolayer formation on the gold surface. **Figure 10, right** displays two distinct regimes with a primary process related to a completed SAM adsorption within the first 30 minutes and an additional, slight but continuous increase in intensity over the remaining 16 hours. The secondary process can be attributed to rearrangements of thiol molecules. Therefore, a longer incubation time of SAM solution onto the gold surface is assumed to lead to a more homogeneous monolayer formation. Subsequent removal

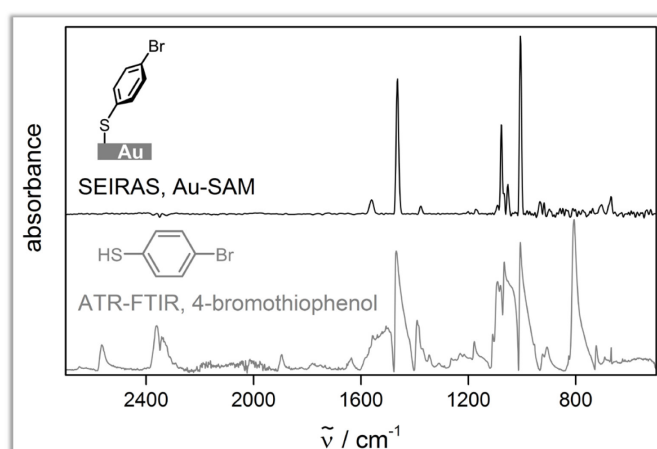


**Figure 11.** Comparison between SEIRA and ATR-FTIR spectra. The latter shows the spectrum of 4-bromothiophenol that was employed for SAM-formation. The ATR-FTIR spectrum features more signals than the SEIRA spectrum since it does not impose the selection rule inherent to SEIRAS. Plots are stacked along ordinate axis.

of the SAM-containing solution and several rinsing cycles with ethanol did not affect the overall band intensities, indicating strong binding of thiol to the gold surface *via* covalent Au–S bonds. Moreover, no remaining S–H modes could be detected. The fact that the SEIRA spectrum in **Figure 10, left** looks rather neat can be ascribed to the selection rule innate to SEIRAS. Only those vibrations are enhanced that upon IR excitation display a change in dipole moment with a predominantly perpendicular orientation to the surface while vibrations parallel to the surface remain unamplified.<sup>[129-133]</sup> **Figure 11** shows a comparison between a SEIRA and a bulk ATR-FTIR spectrum that makes clear how the selection rule manifests itself. Furthermore, at around  $2580\text{ cm}^{-1}$  the aforementioned typical  $\nu(\text{SH})$  can be observed in the ATR-FTIR bulk spectrum of 4-bromothiophenol. It should be noted that below  $1000\text{ cm}^{-1}$  SEIRAS does not deliver reliable results since the silicon single crystal itself starts to absorb in that region.

After verification of successful SAM formation, Yamamoto polymerisation reaction was carried out within the SEIRAS probe cell to record spectra derived directly from the surface involving only the first layers of monomer thus giving direct proof whether or not the SAM is involved covalently in the process of PPN-6 film growth. Indeed, a shift in the wavenumbers of the two characteristic vibrational modes at  $1466$  and  $1560\text{ cm}^{-1}$  could be observed. **Figure 12, left** shows spectra before (A) and after (B) Yamamoto cross-coupling reaction and careful rinsing of the SEIRAS cell. For clarity, the

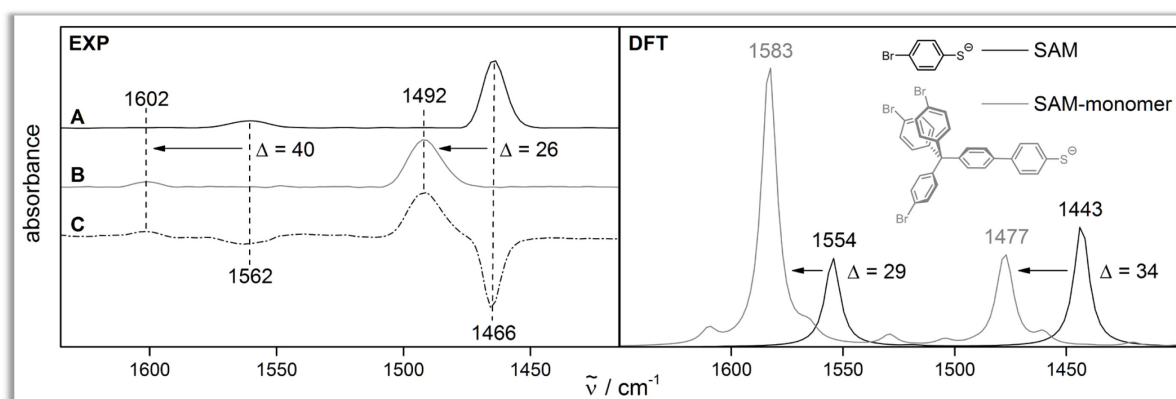


**Figure 12.** Left: SEIRA spectra of the SAM recorded in equilibrium after 16 hours (A), subsequent to the Yamamoto coupling reaction (B), and difference spectrum B minus A (C). In C positive bands are related to the emerging polymer matrix, negative bands are characteristic for consumed (incorporated) SAM. Plots are stacked along ordinate axis. Right: DFT calculated IR absorption spectra for model compounds mimicking the SAM and a SAM molecule that has reacted with one monomer unit.

respective difference spectrum obtained by subtracting the spectrum recorded before from the spectrum recorded after the polymerisation reaction is plotted as well (**Figure 12, C**). In the difference spectrum the characteristic bands of the aromatic  $\nu(\text{CC})$  stretching at  $1562$  and  $1466\text{ cm}^{-1}$  decrease while new bands at  $1602$  and  $1492\text{ cm}^{-1}$  appear. These significant band shifts of  $40$  and  $26\text{ cm}^{-1}$  to higher wavenumbers are a good indication for the ongoing reaction consuming the bromine functionalities of the SAM. Thus, it can be argued that new C–C bonds are formed between the aromatic ring of the SAM and the phenyl groups of tetrakis(4-bromophenyl)methane under cleavage of the bromine end groups of the SAM. Notably, comparable shifts of  $29$  and  $34\text{ cm}^{-1}$  to

higher wavenumbers are predicted by DFT calculations for the  $\nu(\text{CC})$  vibrations of a molecular model system composed of one 4-bromothiophenol molecule linked to one monomer unit in vacuum (**Figure 12, right**). It is concluded that film formation is indeed initiated at the bromine-terminated surface, resulting in a covalent attachment of the PPN-6 film to the gold electrode. **Figure 13** provides the geometrically optimised structures (in vacuum on the BP86/6-31g\* level using Gaussian 09) of the model compounds that were employed in the calculations.

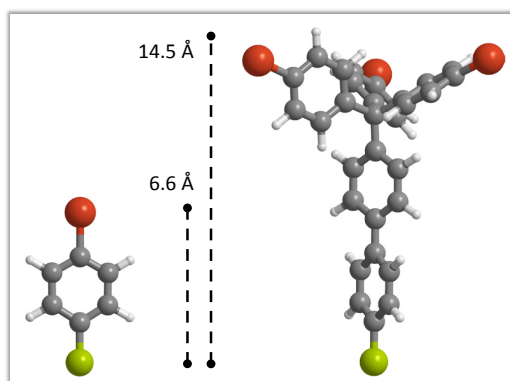


**Figure 13.** Geometrically optimised 3D structures of the SAM molecule 4-bromothiophenolate before reaction (left) and coupled to one monomer unit (right) as employed in DFT calculations (carbon: dark grey, hydrogen: light grey, sulphur: yellow, bromine: red). It can be seen that the penetration depth of SEIRAS of approximately 8 nm is well suited to observe most importantly the first but also subsequent layers. This is even more valid when recalling that SAM molecules are usually bent towards the surface.

The yet presented data show that SAM functionalisation is an indispensable prerequisite for firm attachment of the PPN-6 film to the substrate for in this fashion the polymer is bonded covalently to the gold *via* the intermediary SAM. Alongside spectroscopic records, focus was set on more illustrative results. By virtue of secondary electron microscopy (SEM) information on the nanoscopic morphology of the film was gathered. **Figure 14** presents SEM micrographs with increasing magnification. For better visibility **Figure 14 a)** shows an area of the sample where the polymer film only partially covers the gold surface. The polymer film is very smooth and homogeneous. However, some larger particles are also found to be located on top of the polymer film. This becomes even more apparent in cross-section SEM pictures. **Figure 14 b)-f)** portrays cross-sections of the polymer films. The films are very homogeneous up to a thickness where the spatial limit for the primary growth process, which starts directly at the surface, is reached. It is assumed that this polymer layer is formed by polymerisation of monomers in solution with the bromophenyl moieties exposed by the SAM on the gold surface. On top of this dense polymer layer, a second open polymer layer with a thickness of about 5  $\mu\text{m}$  did form and consists of agglomerates of polymer spheres. It can be reasoned that these polymer particles had been pre-formed in solution and subsequently bound to the homogeneous primary polymer layer *via* terminal bromine groups. **Figure 14 e)** clearly shows the primary polymer layer and a polymer particle bound to it.

To further corroborate the importance of a self-assembled monolayer, SAM-functionalised and blank samples both of which received identical treatment in terms of polymerisation reaction and

subsequent swelling procedures, have been inspected by SEM. As was mentioned earlier and can be reviewed in **Figure 9**, only the blank sample displayed detachment of polymer film after THF treatment whereas the SAM-functionalised sample clung to its polymer film and only suffered from crack formation. SEM micrographs prove that the film is still firmly attached to the SAM-

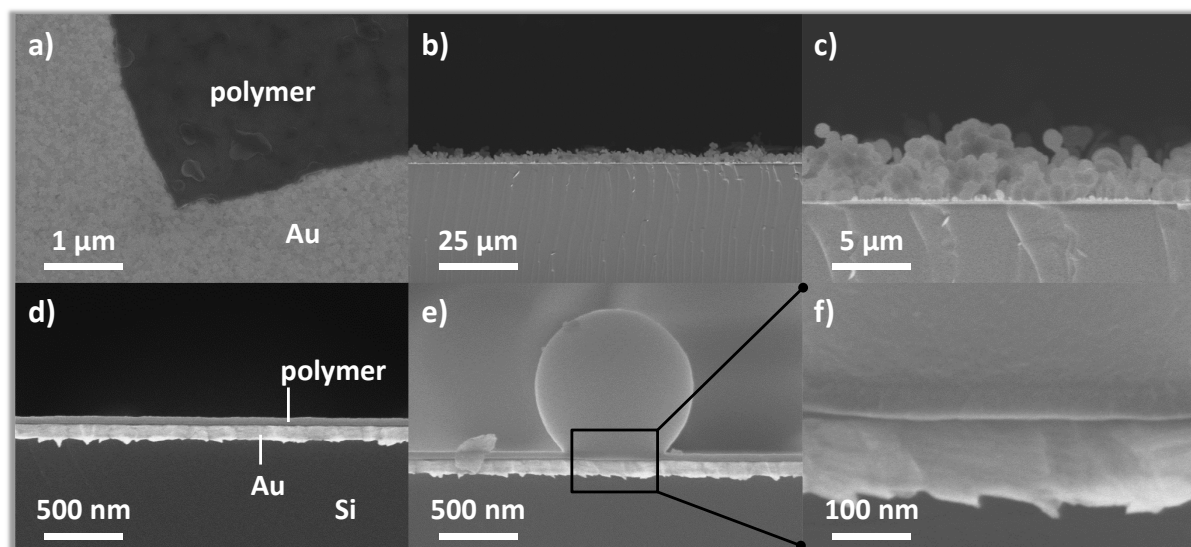


**Figure 14.** SEM micrographs of a PPN-6 film grown on a gold substrate *via* Yamamoto cross-coupling reaction after 20 h reaction time. Top-view (a) and cross-section (b-f) micrographs showing increasing magnification from b to f. The primary layer of homogeneous film can clearly be seen (d) as well as particulate growth of polymer spheres atop (b and c).

functionalised substrate (**Figure 15 a**). This is supported by EDX line and spot scans that confirm the presence of carbon. A spot scan was conducted to compensate for insufficient resolution during the line scan as can be witnessed by the mere meagre increase in intensity of the carbon signal well within the polymer layer. Spot scan, affirmatively, reveals the carbonaceous nature of the film as well as of the polymer midget that grew onto the homogeneous layer with the values for the three spots being (in atom-% carbon) 96 (spot 1), 76 (spot 2), and 6 (spot 3) thereby demonstrating that spot scan is far more adept at this task than line scan. **Figure 15 b**) shows an SEM cross-section micrograph from a blank sample from which the formed film was removed *via* swelling in and rinsing with THF. It is obvious that no film resides on the gold layer after the swelling procedure as is confirmed by an EDX line scan that supplements the visible proof of the absence of carbon. The slight increase in the carbon count (yellow curve) can be attributed to carbon impurities apparently residing on the gold layer.

The produced polymer layer is indeed very smooth and of very homogeneous thickness. However, as can be observed in **Figure 14 b**) and **c**) on top of the primary layer a massive layer of particulate nature can be found. The natural step forward in the thinking process was to figure out whether or not it is possible by means of varying reaction times to influence the extent of that agglomeration. The premise is that the shorter the reaction time, the smaller the magnitude of agglomerate growth, which would prove the hypothesis correct that the formation of a homogeneous film is the primary process hence occurring first followed by attachment of

pre-formed particles from solution. The employed reaction times equaled 18 and 50 min. After 18 min, a thin, homogeneous polymer film can be observed on the gold substrate. On top of this film a few larger particles can already be spotted that become more numerous as the reaction proceeds.

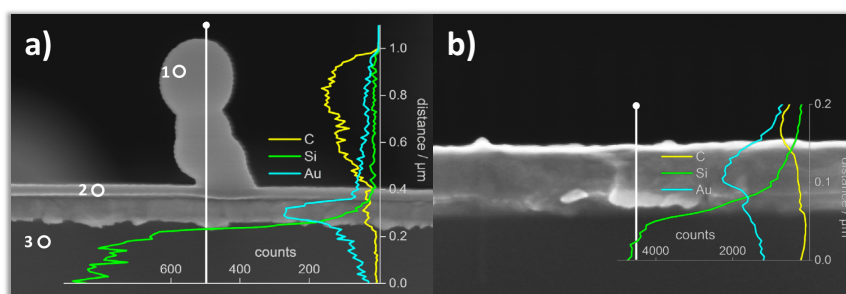


**Figure 15.** SEM cross-section micrographs with superimposed results from EDX line scan analyses of SAM-functionalised gold with polymer grown atop (a) and blank sample after polymer layer was detached by swelling and rinsing (b). In a) spot scans complement line scan analysis. Vertical white lines indicate the path of the line scan.

After 20 h, a second, open layer of agglomerated particles is formed (**Figure 16**). These results buttress the notion that agglomerate growth happens after smooth film formation. Moreover, it was investigated how reaction time influences the thickness of the film. The assumption, naturally, is

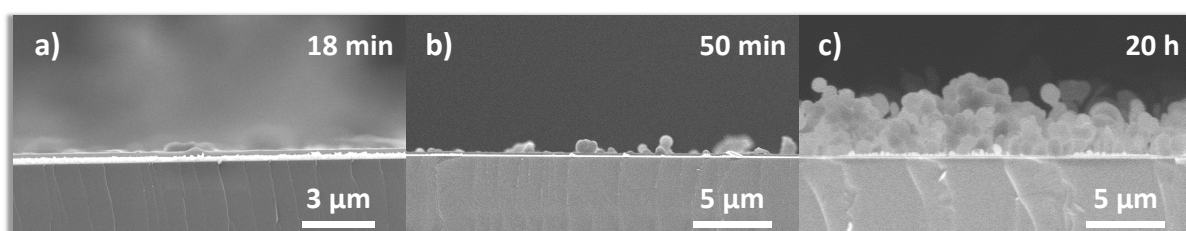


**Figure 16.** SEM cross-section micrographs of samples that have been subjected to Yamamoto cross-coupling reaction for varying periods of time. An enhanced formation of a second, particulate layer atop the homogeneous polymer film with increasing reaction time is obvious.

that the shorter the reaction time, the less thick the film will become. **Figure 17** portrays SEM cross-section micrographs to disclose film thickness from samples with different reaction times alongside top-view images to reinforce the observation of less particulate growth with shorter reaction time. The experiments show that film thickness can be tuned to some extent depending on the reaction time. This outcome might prove valuable when considering applications in which the polymer film serves as molecular sieve with meshes in the nanometer domain. Diffusion of molecules to the electrode will take longer with increasing film thickness.

As mentioned at the beginning of the chapter, it was expected that the produced films contain only a very small mass of polymer thus rendering sorption analysis challenging. In fact, although polymer was definitely attached to the samples as could be seen by eye and SEM, it was not possible to measure a mass gain even on a five digit high precision balance. Nevertheless, various samples have been combined and measured at once to increase the available mass. The thusly measured samples exhibited a covered surface of 16.9 cm<sup>2</sup>. As a result, a 5-point krypton sorption

measurement could be obtained (**Figure 18**). As the overall sample mass was still too low to be obtained by simple weighing, the measured surface area cannot be calculated as gravimetric surface area (a value usually presented for bulk porous materials), but is related to the provided substrate surface. It should further be noted that the given film morphology—a thin, dense and homogeneous

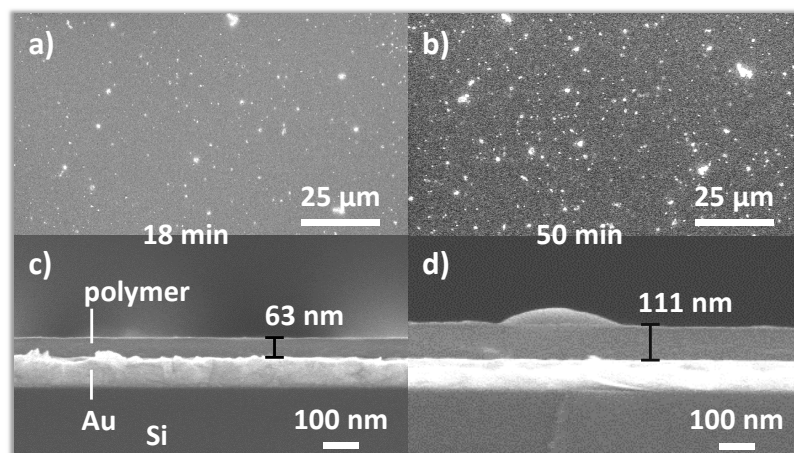


**Figure 17.** Top-view images (a and b) to underline the dependence of agglomerate density on reaction time and cross-section micrographs (c and d) to reveal that reaction time influences film thickness as well.

polymer layer plus a thicker polymer layer consisting of aggregated polymer particles—obstructs any meaningful estimation of applied sample mass using film thickness since an estimation of overall density of such films is stricken with high inaccuracy. From krypton sorption measurement a surface area of  $67.5 \text{ cm}^2 \cdot \text{cm}^{-2}$  sample area could be calculated. This supports the assumption of a porous polymer film on the coated substrate. Due to aforesaid reasons, the unavailability of both sample weight and sample density, a valid BET analysis cannot be applied to the sorption measurement. This notwithstanding, a BET plot for the points of the measurement meeting the criteria recommended by Rouquerol *et al.*,<sup>[74]</sup> marked grey in **Figure 18**, already shows porosity with reasonable values for

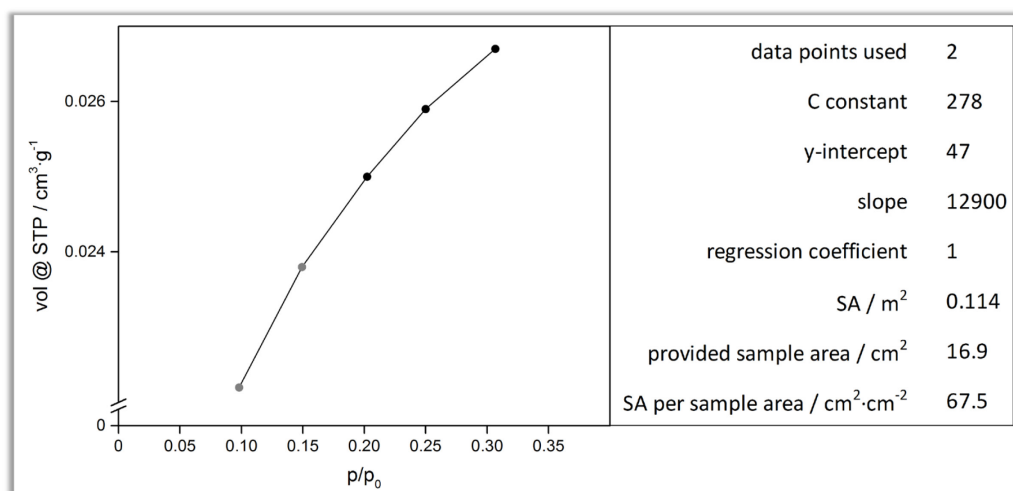


**Figure 18.** Left half shows the recorded data points from Krypton sorption measurement at 87 K. The points of grey colour were the only applicable to BET analysis the result of which is summarised in the table on the right-hand side.

BET constant  $C$  and  $y$ -intercept. The author is aware that this procedure is not recommendable for conducting a proper BET analysis. However, in the light of the restrictions imposed by the film-like nature of the substrate it is still deemed sufficient to qualitatively verify that porosity is present.

Two different molecules were employed for SAM functionalisation: 4-bromothiophenol and 4-iodothiophenol. The idea behind this was to figure out whether the different reactivity of the two halogen atoms in metal mediated cross-coupling reactions translates into a detectable variation in the process of film formation. In the experiments conducted in this work, there always occurs a competition between film formation and bulk polymerisation. Because the goal was to grow a film onto a substrate it was investigated whether surface reaction can be favoured over bulk reaction. Obviously, this can only show any effect in binding of the very first layer of monomer molecules because it is a homomolecular reaction and after the first layer has been established all exposed functional groups are alike. Iodine is far more reactive than bromine but the effect of higher reactivity should be most pronounced at short reaction times. It can be reasoned that prolonged reaction times will redeem any initial advance in kinetics of one sort of SAM over the other. Polymer covered substrates with either bromine or iodine bearing SAMs were analysed *via* SEM in regard to polymer film thickness probing multiple sites of each substrate to get a mean value. After 18 min, bromine and iodine SAM substrates exhibited a mean polymer film thickness of  $61 \pm 10$  and  $64 \pm 8$  nm, respectively. After 50 min, these figures change to  $134 \pm 14$  and  $166 \pm 11$  nm for bromine and iodine SAM-functionalised substrates, respectively. Apparently there is a difference in film thickness depending on the nature of the functional group exposed by the SAM. It should be noted that for the sake of comparability each experiment (18 and 50 min) accommodated two substrates, one with bromine-SAM and one with iodine-SAM within the same reaction vessel, thus subjected to the same exact polymerisation reaction. The obtained results do not show significant differences in film growth on either bromine- or iodine-terminated SAMs. Quite contrarily to the initial assumption, a more noticeable difference is observed for longer-term samples (50 min) but overall a clear relationship between the nature of the SAM and ensuing film growth cannot be proposed at this point of the investigation.

To conclude this section, an alternative experimental setup is introduced that allowed of a substantial reduction of employed substances. This setup similarly guarantees that no mechanical stress is imposed on the substrates, which are placed with their back on a support such as a glass slide used in optical microscopy. The exposed faces of the substrates are then treated with a few drops of reaction mixture. If applied carefully and not too excessively, surface tension of a DMF/THF blend will prevent the reaction mixture from spilling over the fringes. In this way, a confined reaction space is generated that requires only minute amounts of reactants. Naturally, stirring is not possible in such a setup due to which homogeneous dispersion of reactants within the droplet is thwarted. Accordingly, the obtained films were rather inhomogeneous (**Figure 19 c**). The PPN-6 protocol plays into the cards of this approach. For the reaction proceeding at room temperature greatly facilitates the setup. It is recommended to conduct this kind of experiments inside a glove box as establishment of an inert atmosphere using Schlenk technique proves difficult in this case. Although

the reaction was conducted at room temperature and the reaction vessel sealed as good as possible, a slow but steady evaporation process could not be forestalled. This led to changes in concentration as well as solubility within the droplet thereby detrimentally affecting the reaction itself as well as film formation. Provision of a tangible amount of solvent mixture, in composition identical to the used reaction solvent, at the bottom of the reaction vessel to establish a saturated atmosphere could not compensate for evaporation. Eventually, film formation could be observed on the

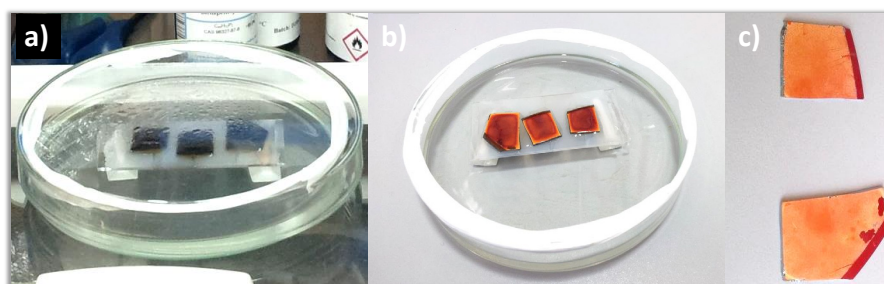


**Figure 19.** Photographs of droplet setup during reaction (a), after reaction (b), and substrates after work-up (c). A petri dish serves as enclosed reaction vessel the bottom of which is covered with a layer of solvent mixture resembling the reaction solvent in order to provide a saturated atmosphere thereby slowing down evaporation. In c) a rather inhomogeneous covering of the substrates with polymer can be witnessed. The two blank spots (bottom sample in c), are caused by mechanical stress during handling with forceps.

the substrates but surprisingly also on substrates that were blanks, *i.e.* that did not bear a SAM. In contrast to the experiments with hanging blank substrates, on which film formation took place, the films on the droplet blank samples could not be detached by swelling in THF. This phenomenon might find an explanation in the circumstance that uneven distribution of reactants within the droplet exacerbated by an evaporation process led to a situation in which the polymer was literally stamped onto the substrates. This scenario is reminiscent of the proceedings described on upcoming pages where tethering of CMP-1 to an electrode is recounted.

In consideration of inconclusive film formation regarding homogeneity of films along with the circumstance that film formation did take place on blank samples as well this approach was abandoned. However, improvements in setup such as real tight sealing to further avoid evaporation as well as application of larger amounts of reaction mixture to provide a more homogeneous reaction environment might prove this concept useful. On the other hand, enhancing the employed volume of reaction mixture diminishes the one big trait this methodology benefits from that is to reduce the amount of reactants.

## CONCLUSION

The presented results demonstrate that the proof of concept was successful. Gold coated substrates have been covered with polymer film in a reaction that also yielded bulk polymer that could be subjected to standard analytical methods thereby confirming the desired target structure of the bulk. In so doing, the chemical nature of the grown film was also confirmed since the substrate was

present in the same exact reaction. Moreover, it could be shown that film thickness as well as particulate growth atop the homogeneous film could be controlled to some extent by varying the reaction time. An additional insight into the porous nature of PPN-6 is portrayed in **Figure 20**. Nitrogen sorption isotherms of PPN-6 samples obtained after varying reaction times differ considerably with higher surface area values being achieved for longer reaction times. This can be fathomed when imagining that, although precipitate is formed already after minutes, at longer reaction times nascent polymer particles will be cross-linked much more extensively thereby creating more pores leading to higher surface area values. The initial choice for PPN-6 was based on

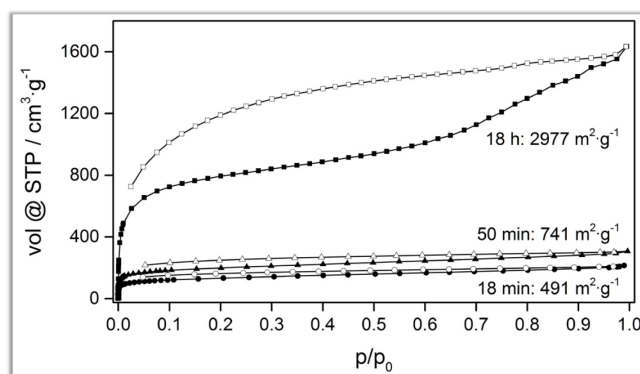


**Figure 20.** Isotherms derived from nitrogen sorption at 77 K of three PPN-6 samples after varying reaction times (solid symbols: adsorption, empty symbols: desorption).

the assumption that the polymer films exhibit very small mass of polymer. This was indeed the case as encountered during sorption experiments of the films. Nevertheless, krypton sorption revealed the porous nature of the films.

Electrodes coated with PPN-6 might be useful in applications where the polymer can serve as molecular sieve to allow only molecules of an appropriate size to reach the electrode. Furthermore, the ability to tune the thickness of the film can prove valuable when diffusion length and -time need to be adjusted since thicker films exact a higher diffusion time from the agent molecules. In addition, the aforementioned possible applications can be envisaged to be expanded to polymers with different parameters such as pore size to allow larger or smaller molecules to pass to the electrode. Also, polymers could be potentially used that have been functionalised either post synthetically or *via* employment of functionalised monomers.

To broaden the scope of possible applications for the presented film growing method it is advisable to employ different polymers. Especially, exploiting the very nature of the substrate as being a superb electrode leads to the idea of employing polymers that show a higher degree of conjugation of  $\pi$ -electrons than PPN-6. To that end, CMP-1 was chosen as candidate to render the approach more versatile.

## CMP-1 | A FILM ON GOLD | PART TWO

Since their development *via* Sonogashira-Hagihara palladium catalysed cross-coupling reaction in 2007, CMPs have been studied extensively in respect to the scope of monomers to employ as well as reaction conditions to apply.<sup>[40,134-136]</sup> Moreover, their potential application in organic electronics has been studied since, making it extremely interesting to fabricate those polymers as a thin film on an electrode.<sup>[90,137-138]</sup> It is noteworthy that the vast majority of literature on CMPs describes a fifty percent excess of ethynyl to halogen functional groups—an unusual ratio adopted due to empirical criteria as this was shown to yield materials with enhanced surface areas.<sup>[139]</sup> This might be due to inconsistent quality of the educt 1,3,5-triethynylbenzene. In this work, however, the educt was purified by chromatographic filtration and used in a quantity that reflects a one to one ratio of ethynyl- to halogen-groups.

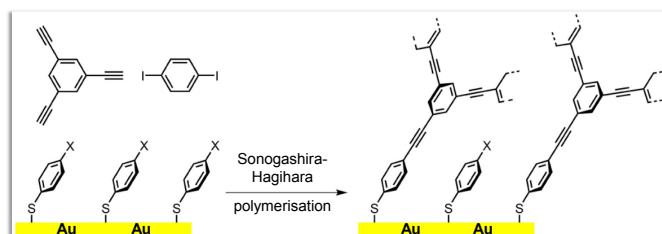


**Figure 21.** Sketch of film formation of CMP-1 on SAM-functionalised gold electrodes (X = I or Br) *via* palladium catalysed Sonogashira-Hagihara cross-coupling reaction according to the following reaction conditions: 1.00 eq. p-diiodobenzene ( $c = 0.0056 \text{ mol}\cdot\text{l}^{-1}$ ), 0.67 eq. 1,3,5-triethynylbenzene, 0.013 eq. tetrakis(triphenylphosphine)palladium(0) in a volumetric 2:1 mixture of dry DMF and dry TEA at  $80^\circ\text{C}$  for time periods of 25 min to 19 h.

During CMP-1 synthesis it is customarily observed that the polymer forms within a timeframe of minutes or even seconds depending in particular on the type of halogen functionality employed. Moreover, the product occupies the entire volume of the reaction vessel; a phenomenon that is not beneficial to smooth film formation. For this reason, first attempts in the present work made use of the lowest yet reported concentration of p-diiodobenzene of  $0.066 \text{ mol}\cdot\text{l}^{-1}$ .<sup>[134]</sup> In addition, to slow down polymer formation and thus enhance the chance of a smooth film growth, early experiments employed the brominated rather than the iodinated monomer due to the former's lower reactivity. Still, as can be perceived in **Figure 22 a)** even at this low a concentration the reaction vial got filled up with polymer. This, naturally, leads to problems in terms of reaction environment, for under such circumstances the reaction might enter a stage where both an even thermal conductivity as well as a uniform diffusion of monomers are severely impeded. Also, and more important for this work, since the substrates are in such close proximity to and virtually engulfed in polymer, smooth film formation can be assumed to be frustrated unlike in a liquid environment. Indeed, **Figure 22 c)** gives an idea of how unevenly films are formed on the substrates. It is not even safe to assure that those films have been formed bottom-up, as desired, or merely got stamped onto the substrates from all-surrounding polymer. The obtained bulk polymer was washed and Soxhlet extracted from methanol as routinely done for CMPs and according to nitrogen sorption at 77 K exhibited a BET

surface area of  $796 \text{ m}^2 \cdot \text{g}^{-1}$ , which is inferior to the literature value of  $870 \text{ m}^2 \cdot \text{g}^{-1}$  for CMP-1 using the same concentration.<sup>[134]</sup> Moreover, although bulk material was Soxhlet extracted, its yield amounted to 207 % insinuating massive amounts of impurities. The macroscopic appearance offers an image of inhomogeneous composition. The consequence of this outcome was to abandon the classical

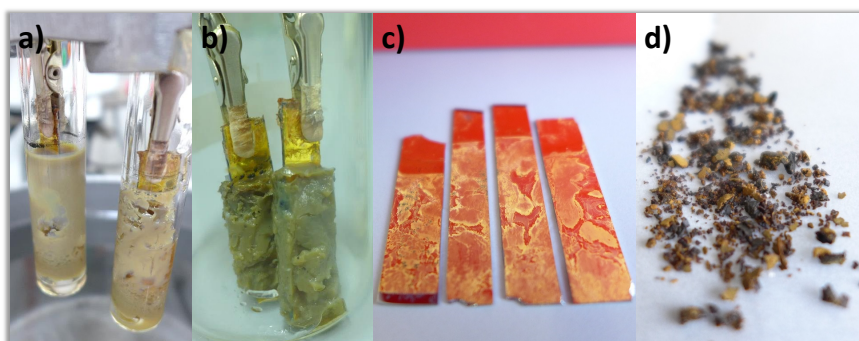


**Figure 22.** Photographs of CMP-1 reaction when finished (a), substrates engulfed in polymer as withdrawn from reaction vessel (b), substrates where excess polymer has been removed (c), and bulk polymer after washing, Soxhlet extraction, and vacuum drying (d).

approach and embark on a methodology that avoids the formed polymer demanding such an enormous space within the reaction vessel. The most influential parameter in this regard is concentration that was accordingly further reduced to nearly homeopathic amounts. In the new reaction protocol the concentration of p-dihalobenzene was set to  $0.0056 \text{ mol} \cdot \text{l}^{-1}$ . This time, p-diiodobenzene was employed. In addition, no copper(I) iodide was used and the amount of catalyst was reduced to 0.013 eq. with p-diiodobenzene defining 1.0 eq. However, the decisive feature in this case to ensure a liquid reaction environment is the decrease in concentration. It is emphasised that except for the low concentration these reaction conditions were adapted from a recently optimised protocol developed in our laboratory that yielded CMP-1 with improved structural integrity and enhanced porosity.<sup>[41]</sup> In spite of the fact that the more reactive iodo monomer has been used, there was no prompt and overwhelming formation of polymer. Quite the opposite was true with the reaction solution remaining colourless and clear for the first 10 min (**Figure 23**). Then, a slight yellow tinge arose and governed the next 15 min. Finally, after 25 min, the

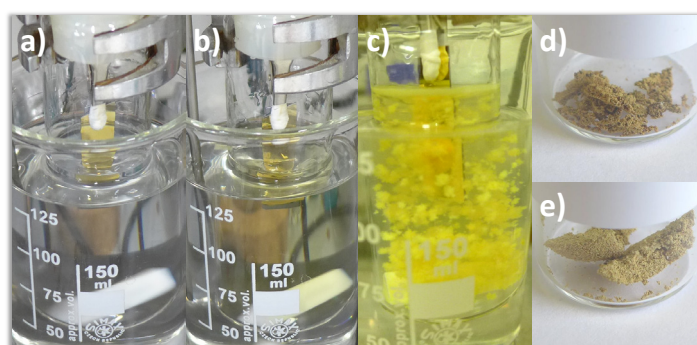


**Figure 23.** Photographs of CMP-1 synthesis during the first 10 min (a), the ensuing 15 min (b), and precipitated polymer after 35 min already forming bigger agglomerates in c). Pictures in d) and e) show bulk polymer washed and dried after reaction times of 35 min (d) and 19 h (e).

solution turned turbid and very gentle precipitation of yellow flakes could be observed. The flakes grew slightly in size but what is more important they did not aggregate to pile up but kept stirring so that the substrates were surrounded by liquid medium for the entire time of the reaction. As such, it could be guaranteed that the reaction proceeded entirely in solution or at the very least in dispersion and that films grown on the substrates did develop bottom-up, as desired. As in the previously described experiments, substrates with SAMs bearing either bromine or iodine were employed. Since p-diiodobenzene was used as linker it was considered worthwhile to use an iodine bearing SAM for a more or less equal reactivity of the surface compared to bulk reaction in solution. Nonetheless, both bromine and iodine SAM-functionalised gold substrates did exhibit a film after the reaction proceeded for 25 min at the least (**Figure 24 b) and c**). In case the substrates were withdrawn before that time *i.e.* within the initial phase during which the solution turned yellow but no precipitation was observed just yet, neither substrate was coated with polymer. This is illustrated in **Figure 24 a)** that features two substrates obtained from an experiment analogous to the one shown in the previous **Figure 23**. This finding suggests that the process of film growth at the surface is not favoured over polymerisation in solution to form bulk CMP-1. In the applied experimental

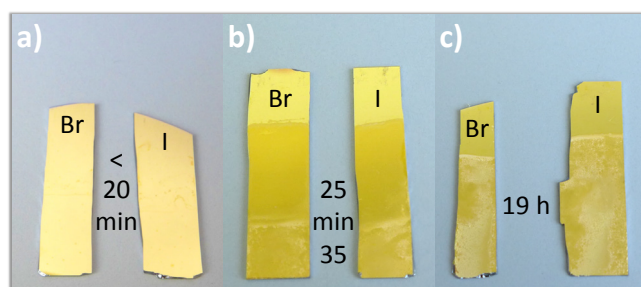


**Figure 24.** Photographs of gold substrates that were withdrawn after varying time intervals from a CMP-1 polymerisation reaction. Sub-short-term experiments (a) yield no covering of either specimen. Short-term trials (b, 25 min) gave rise to much more homogeneous films than long-term trials (c). But already after 35 min homogeneity is adversely affected in comparison to a 25 min sample.

setup the substrates were immersed into the reaction solution from atop *via* a metal wire that pierced through a septum in order to control depth of immersion. In this way it was possible to withdraw the substrates to a certain extent in order to stop the reaction for the upper part whereas the lower part of the substrate remained immersed. In this manner, substrates as presented in **Figure 24 b)** could be obtained.

To verify that the films on the substrates were in fact CMP-1, the bulk material acquired in the reactions was analysed. Firstly, the two batches, short-term (35 min) and long-term (19 h), differ in colour with the long-term CMP-1 exhibiting a brighter hue leaning to beige whereas the short-term sample is of brown colour. Results from elemental analysis differ as well and show a slightly better overall conformity to theoretical values for the long-term sample: calculated (found short-term CMP-1; found long-term CMP-1) for  $C_{21}H_9$  in m-%: C 96.53 (87.71; 92.53), H 3.47 (3.41; 3.71).

The mentioned difference in colour could be caused by a more pronounced conjugation of  $\pi$ -electrons within the long-term sample triggered by more comprehensively consumed functional

groups. This claim can be substantiated by solid state  $^{13}\text{C}\{^1\text{H}\}$  CP/MAS NMR spectra (**Figure 25**). *Prima facie*, the two samples do not differ noticeably except for signal to noise ratio. Both yield similar signals at (numbers in brackets for long-term sample) 134.4 (134.6), 128.0 (128.1), and 120.8 (121.1) ppm for aromatic carbons and 87.4 (87.5) ppm for ethynyl carbons. There is, however, one

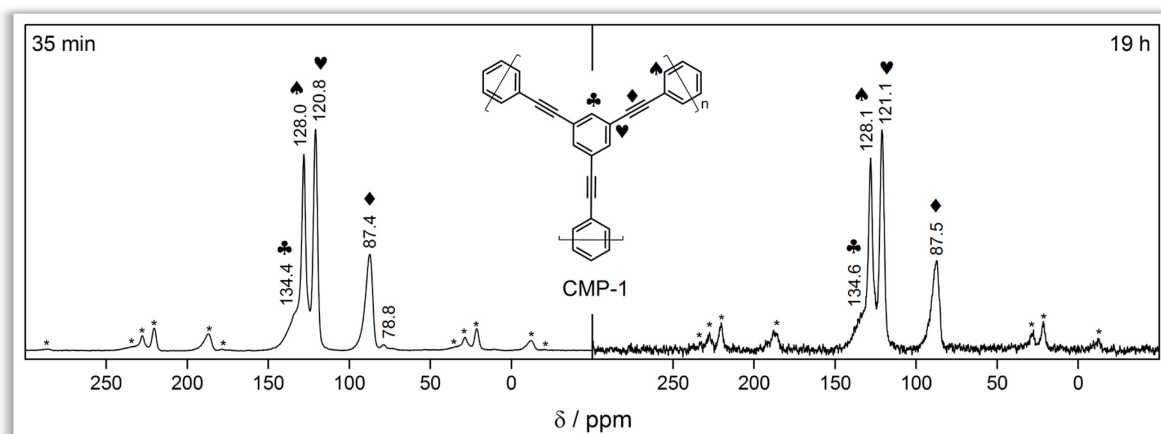


**Figure 25.** Solid state  $^{13}\text{C}\{^1\text{H}\}$  CP/MAS NMR spectra of both short-term and long-term CMP-1 trials ( $v_{\text{rot}} = 10$  kHz, spinning sidebands are marked with an asterisk).

signal present only in the short-term sample at 78.8 ppm that can be assigned to terminal ethynyl carbons of unreacted ethynyl groups. The short-term sample seems to suffer from a higher degree of unreacted ethynyl groups (see Appendix **Figure A1**), a circumstance that supports the notion of diminished conjugation of  $\pi$ -electrons.

To further investigate the structure of the obtained CMP-1 samples, ATR-FTIR investigations have been conducted. Short-term as well as long-term sample have been compared to both of the employed educts 1,3,5-triethynylbenzene and 1,4-diiodobenzene. In this manner, congruent and differing signals can be spotted easily. **Figure 26** reveals that the typical alkyne C–H stretching vibration mode at  $3277\text{ cm}^{-1}$  is absent from the spectra of both CMP-1 specimens. On the other

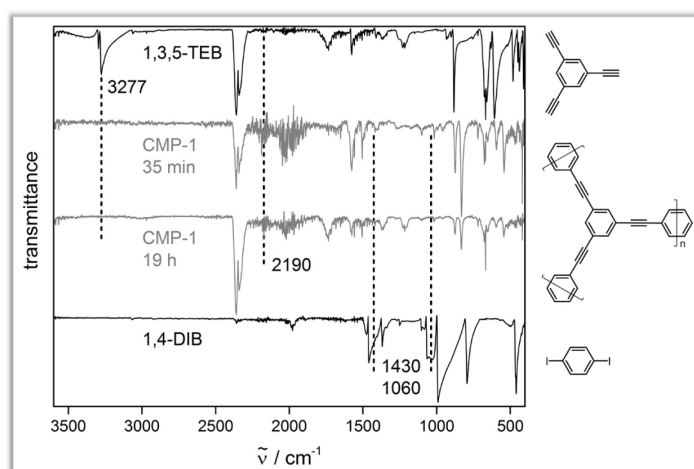


**Figure 26.** ATR-FTIR spectra from CMP-1 samples (grey) and both educts 1,3,5-triethynyl-benzene (top black) and 1,4-diiodobenzene (bottom black). Plots are stacked along ordinate axis.

hand, a vibration mode, which is lacking in the educt 1,3,5-triethynylbenzene, appears, albeit only weakly and submerged in noise, in the CMP-1 spectra at  $2190\text{ cm}^{-1}$  and can be assigned to  $\text{C}\equiv\text{C}$  stretching mode of disubstituted alkyne. Furthermore, characteristic signals hailing from the second starting material 1,4-diiodobenzene at  $1430$  and  $1060\text{ cm}^{-1}$  can be deemed absent from the CMP-1 long-term sample but slight traces of this educt can be found in the CMP-1 short-term sample again indicating a less complete conversion hence more unreacted end groups strengthening the notion of reduced conjugation of  $\pi$ -electrons. It is noteworthy, though, that traces of 1,4-diiodobenzene can be spotted whereas the spectra are completely devoid of residual signals from 1,3,5-triethynylbenzene, although the latter's presence is clearly revealed in the NMR spectrum at least of short-term CMP-1.

The basic idea for the very low concentration applied in the reaction was to avoid the substrates from being engulfed in polymer and ensure smooth film formation. As a concomitant feature, the reaction was allowed to proceed as solution/dispersion-based reaction in contrast to typical CMP-1 synthesis. This circumstance in conjunction with the other altered parameters applied in this work and adopted from reference 41 are apparently conducive to enhanced structural integrity of the polymer especially at short reaction times as can be witnessed by means of nitrogen sorption. The obtained surface area values exceed comparative figures from a study on the influence of concentration on surface area values by far.<sup>[134]</sup> In that study, a decrease in concentration was accompanied by a steady decline in surface area dropping from  $956$  to  $870\text{ m}^2\cdot\text{g}^{-1}$  for *p*-diiodobenzene concentrations of  $0.666\text{ mol}\cdot\text{l}^{-1}$  and  $0.066\text{ mol}\cdot\text{l}^{-1}$ , respectively. Apart from the concentration of *p*-diiodobenzene other experimental parameters differed likewise in the literature study: (notes in brackets for parameters in this work) ethynyl/iodine molar ratio of 1.5 (1.0), usage of copper(I) iodide (none), toluene/TEA volumetric ratio of 1:1 (DMF/TEA volumetric ratio of 2:1), tetrakis(triphenylphosphine)palladium(0) mol-% of 4.3 (1.3), and finally, reaction time of 72 h (35 min and 19 h). Conversely, two crucial characteristics are identical: reaction temperature of  $80\text{ }^\circ\text{C}$  and employment of iodinated benzene as linker rather than their brominated brethren. These latter two factors play an important role in terms of reactivity and reaction progress. Giving credit to the vastly reduced reaction time makes the upcoming values even more astounding. Nitrogen sorption experiments revealed BET surface areas of  $1423$  and  $1538\text{ m}^2\cdot\text{g}^{-1}$  for 35 min CMP-1 and 19 h CMP-1, respectively (**Figure 27**). These values surpass the aforesaid figure of  $870\text{ m}^2\cdot\text{g}^{-1}$  by a staggering 64 and 77 %. Considering the trend disclosed in the literature study suggesting lower surface areas for reduced concentrations these results, obtained with a concentration of only a twelfth of the reference value, are even more striking. Another feature unveiled by these outcomes regards an apparent difference between CMP-1 and PPN-6 formation. As can be assessed from **Figure 20**, PPN-6 requires long reaction times to accomplish high surface area values while CMP-1 seems to reach its apex within a little more than half an hour. A finding that suggests that the palladium-catalysed Sonogashira-Hagihara reaction for CMPs reaches full conversion a great deal faster than the nickel-mediated Yamamoto cross-coupling reaction for PPNs using stoichiometric amounts of nickel. However, a caveat needs to be issued on the nature of functional groups in both cases. Whereas

CMP-1 synthesis employed an iodinated compound, the PPN-6 protocol made use of a brominated species of less reactivity. In addition, other experimental parameters differ as well most importantly reaction temperature that was set to 80 °C for CMP-1 and left at room temperature for PPN-6 synthesis.

As can be drawn from **Figure 27**, not only surface areas exceed the reported value. Surface area contributed from micropores is also higher and reaches 1343 and 1318  $\text{m}^2\cdot\text{g}^{-1}$  for short-term and

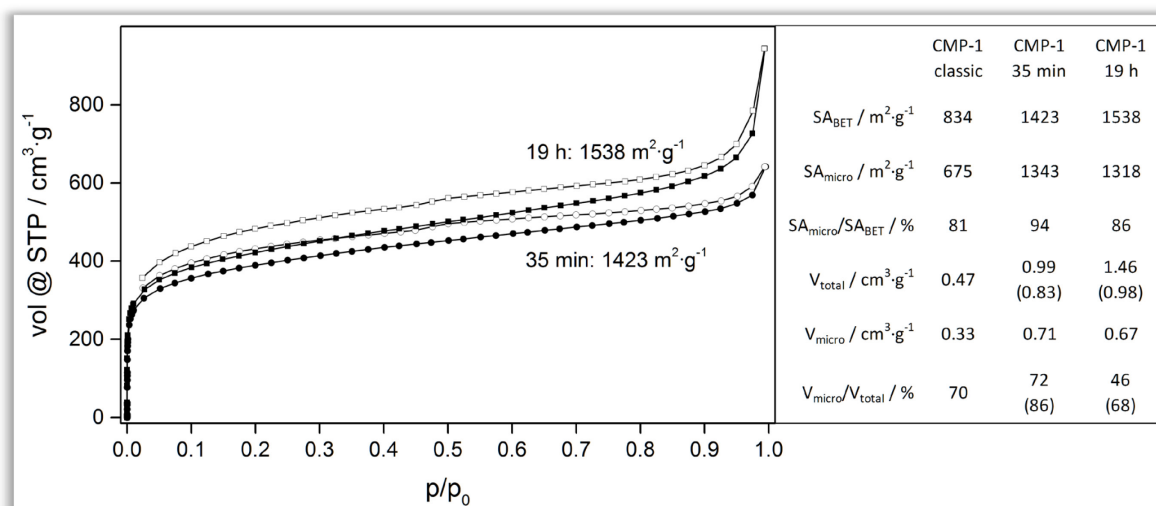


**Figure 27.** Isotherms derived from nitrogen sorption at 77 K for short-term and long-term CMP-1 trials (solid symbols: adsorption, empty symbols: desorption). Additional information provides comparison to CMP-1, obtained *via* the classical synthetic route (values originate from reference 40).  $SA_{\text{BET}}$  calculated from nitrogen adsorption branch using BET method; micropore SA calculated from nitrogen adsorption branch using t-plot method; total pore volume derived at  $p/p_0 = 0.99$  (values in brackets obtained at  $p/p_0 = 0.92$  for short-term and 0.93 for long-term),  $V_{\text{micro}}$  derived from t-plot method using Halsey equation.

long-term experiment, respectively, compared to  $675 \text{ m}^2\cdot\text{g}^{-1}$  reported in literature. Moreover, the share of microporous surface area in total surface area is increased, too. Overall pore volume is nearly twice as high but it has to be mentioned that the isotherms obtained in this work are of different shape. Whereas Cooper *et al.* acquired near-perfect type I isotherms the graphs obtained here show a steeper, steady increase after micropore filling has been completed. Furthermore, approaching saturation pressure the isotherms in **Figure 27** exhibit a steep increase in gas uptake indicative of macropore presence and/or textural porosity. This is intensified for the long-term trial and is plausible since longer reaction times allow the system to cross-link more comprehensively thereby creating structures of higher dimensions. That circumstance necessitated different points to be applied in calculation of total pore volume. The neat numbers in the table in **Figure 27** are the results obtained by emulating the analysis reported by Cooper *et al.* with total pore volume calculated at  $p/p_0 = 0.99$  while numbers in brackets were acquired by applying lower relative pressure values that can still be considered to lie on the segment of the adsorption branch with a constant slope. Even so, total pore volume amounts to 0.83 and 0.98  $\text{cm}^3\cdot\text{g}^{-1}$  for short-term and long-term trial, respectively, which dwarfs the value of 0.47  $\text{cm}^3\cdot\text{g}^{-1}$  for conventional CMP-1. Pore volume provided by micropores is at least twice as high as the reported value, yielding a share of

micropore volume in total pore volume of 72 and 46 % for short-term and long-term trial, respectively, when related to a total pore volume at  $p/p_0 = 0.99$ . Using total pore volume derived from lower  $p/p_0$  values, micropore volume ratio becomes yet higher than or comparable to the value of 70 % for classical CMP-1.

An interesting observation comes to the fore when comparing short-term and long-term experiment amongst themselves. Both micropore surface area and micropore volume are slightly lower for the long-term sample which is surprising considering the irreversibility of the Sonogashira-Hagihara cross-coupling reaction defying cleavage of a bond once formed. Thus, any micropore once formed stays a micropore and will not be broken up again. Either the discerned difference, which is indeed quite small, lies within the error margin or, alternatively, interpenetration can serve as a line of reasoning. Longer reaction times undoubtedly increase the likelihood of interpenetration that can lead to a reduction in both accessible micropore surface area and micropore volume.

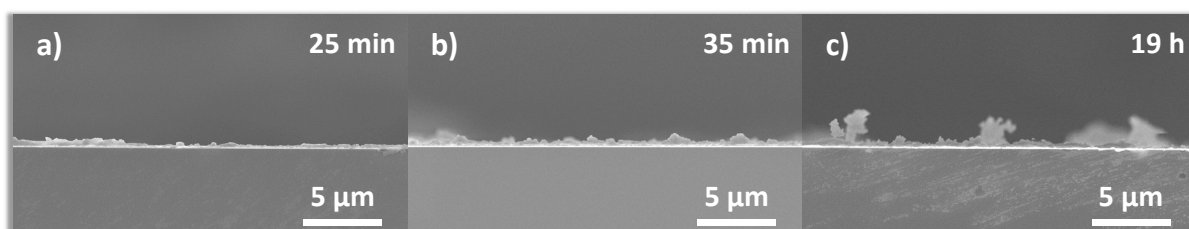


**Figure 28.** SEM cross-section micrographs from substrates that have been subjected to CMP-1 polymerisation reaction for varying amounts of time.

Following the identification of the formed bulk polymer as CMP-1, more graphic results were sought by means of SEM in conjunction with EDX analysis. The circumstance of more pronounced film growth with enhanced reaction time is supported by cross-section micrographs that show more polymer residing on those substrates that have been subjected to the reaction for longer periods of time (**Figure 28**). This finding is also reflected in top-view images that show an increased amount of polymer agglomerates for the long-term sample. Likewise, the thickness of the homogeneous film increases with enhanced reaction time (**Figure 29**). The analysis of multiple sites of a short-term and

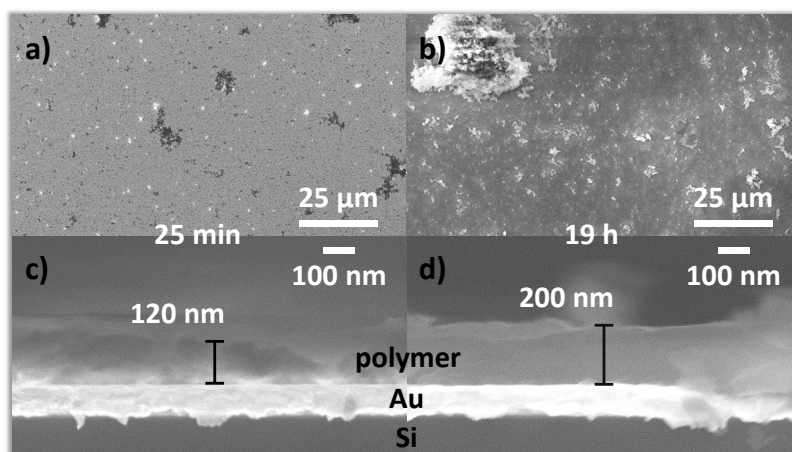


**Figure 29.** Top-view (a and b) and cross-section (c and d) SEM micrographs from CMP-1 coated substrates.

a long-term sample showed average values for film thickness of  $132 \pm 24$  nm and  $239 \pm 61$  nm, respectively; figures that lie within the same region as those obtained for PPN-6 films that amount to around 60 and 150 nm for a short-term (18 min) and a long-term (50 min) sample, respectively. The overall higher values for CMP-1 films can be attributed to faster reaction progress during CMP-1 formation. Although the long-term samples should not be used to arrive at this conclusion due to vastly differing durations that the substrates were subjected to the reactions (19 h for CMP-1 films vs. 50 min for PPN-6 films), reaction times of the short term samples match sufficiently well and allow of a direct comparison of the obtained film thicknesses.

One main aspect of the previous chapter on PPN-6 films on gold electrodes was to prove the SAM indispensable for covalent attachment of the polymer film. Similar experiments were conducted for CMP-1 films. A blank sample was immersed in the reaction mixture adjacent to a SAM-functionalised sample. After 19 h, both substrates were covered with polymer. Ensuing swelling of the substrates in THF overnight produced a different result than obtained for blanks covered with PPN-6 films. Whereas PPN-6 was easily removed *via* rinsing after swelling (*cf.* **Figure 9**), CMP 1 films clung to the non-functionalised substrate no matter how harsh the sample was rinsed *via* pipette (**Figure 30**).

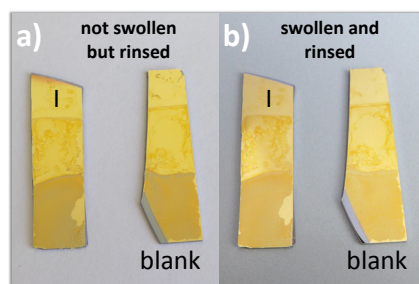


**Figure 30.** Photographs of CMP-1 films on gold substrates after 19 h reaction time that have been functionalised with an iodine-terminated SAM (a) and subjected to reaction without prior SAM functionalisation (b). Both SAM-functionalised and blank sample retain their polymer film after swelling.

EDX line scans performed on cross-section specimens confirm the carbonaceous nature of the film residing on the blank sample. These results are complemented by line scans from short-term (25 min) and sub-short-term (20 min) samples (**Figure 31**). To recapitulate briefly, the sub-short-term sample was withdrawn from the reaction mixture when the solution already displayed a yellow tinge

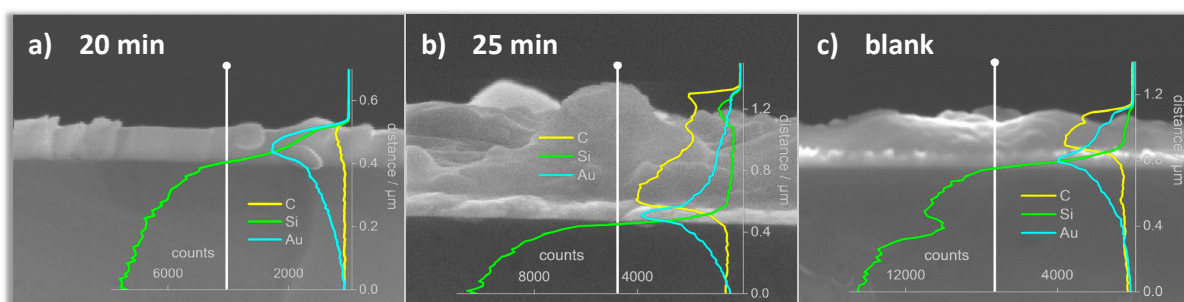


**Figure 31.** EDX line scan results superimposed onto SEM cross-section micrographs from sub-short-term (a), short-term (b), and blank samples (c).

but not yet precipitate. Five minutes later into the reaction, precipitation was obvious and at that point in time short-term samples were obtained. The sub-short-term sample's apparent lack of an attached polymer film (*cf.* photographs in **Figure 24**) is verified by SEM examination as is the presence of carbon within the film atop the short-term sample.

The key to rationalise the observation of a polymer layer forming on top of a blank sample lies within the different monomers employed. PPN-6 synthesis consumes tetrakis(4-bromophenyl)-methane, a molecule that is unimpressed by the presence of gold. CMP-1 formation, on the other hand, utilises 1,4-diiodobenzene as well as 1,3,5-triethynylbenzene in a Sonogashira-Hagihara cross-coupling reaction. It has been established that gold can be substituted for copper in that kind of cross-coupling reaction and serve as alkyne activating agent.<sup>[140-142]</sup> Moreover, gold was attributed a yet more prominent role in that it can supplant palladium as catalyst altogether. This, however, is a subject of debate juxtaposing claims that it is actually residual palladium traces that perform the catalysis and not gold itself<sup>[143]</sup> with others that contest this view and maintain that gold is indeed active on its own provided that it is not molecularly dispersed in gold complexes but present in a clustered form, that is to say nanoparticles.<sup>[144]</sup> The latter view is reinforced by studies focusing on the active sites as well as experiments conducted in vacuum where the occurrence of any homogeneity, *i.e.* leaching of catalyst can be ruled out.<sup>[145-146]</sup> Whatever the real skills of gold in that environment, suffice it to say that in any event it does interact with the alkyne and this creates a scenario in which a blank sample, *i.e.* a pristine gold covered substrate can induce polymer formation to take place directly at the surface. That being said, when drawing a picture of gold acting as co-catalyst, supplanting copper, or catalyst, supplanting palladium, one has to bear in mind that in neither case gold is entitled to get a hold of the reaction product after the catalytic cycle has been completed. For as is essential to catalysts, gold would provide a reactive centre for bringing together reactants but after the reaction has taken place, the product is cleaved off of the gold. This means that the potential of gold for serving as catalyst would favour the reaction to take place directly at the surface but it would not lead to covalent attachment of the polymer film to the substrate. For this to occur, another peculiarity of gold has to be accounted for.

The previous chapter dealt with PPN-6 films covalently attached to gold electrodes *via* a SAM and capitalised on gold's property to form gold-sulphur bonds for thiol-based SAM formation. Yet, thiols are not the only molecules interacting with gold in that manner. It was shown that nitrile and isonitrile groups do so as well *via* exploitation of the high electron density within the triple bond between carbon and nitrogen.<sup>[147-149]</sup> More importantly, not the nitrogen but the triple bond is responsible for this behaviour, so much so that alkynes are also candidates for SAM formation on a gold surface.<sup>[150-152]</sup> In this work, one of the employed reactants is 1,3,5-triethynylbenzene that is potentially prone to strong interaction with a gold surface. Owing to its trifold functionality, the monomer could form a SAM on gold while still exposing reactive groups that can partake in the polymerisation reaction thus prompting the polymer film to stick to the surface in a covalent fashion.

To elucidate whether or not interactions between ethynyl groups and the gold surface are detectable in the system described herein, UV-vis reflection and Raman spectroscopic experiments were conducted. UV-vis reflectance measurements were operated on a gold wafer after it has been subjected to a solution of 1,3,5-TEB as sole component under otherwise conditions that pertained during the actual polymerisation reaction. The idea was to detect absorption of electromagnetic radiation by a possibly formed SAM of 1,3,5-TEB. However, no conclusive evidence could be gathered as to whether the anticipated monolayer had formed. Comparison with a blank sample, *i.e.* a pristine gold wafer showed no significant difference in the spectra of the supposedly SAM-covered specimen. Such an outcome was not completely unexpected as UV-vis absorption of 1,3,5-TEB is not particularly strong and thus challenging for the study of systems with such low a concentration of analyte.

More appropriate in that regard are surface-enhanced Raman spectroscopy (SERS) and surface-enhanced IR absorption spectroscopy (SEIRAS). The latter, however, cannot be employed to detect the possible formation of a sulphur-gold bond as the silicon single crystal used in SEIRAS itself absorbs in the energetic region that accommodates the absorption signal of said bond. In principle, SEIRAS could be used to probe the absence of the vibrational mode effected by the terminal carbon-hydrogen bond, an observation that would be tantamount to the formation of a sulphur-gold bond. However, seeing that the analyte molecule 1,3,5-TEB has more than one ethynyl group at least one of which remains intact after assumed SAM formation renders SEIRAS inappropriate eventually. As a result, SERS was performed on the utilised gold-coated silicon wafers to detect a potentially created sulphur-gold bond. The results were as unsatisfying as those from UV-vis experiments insofar as no significant deviation from the baseline could be observed after exposure of the gold surface to 1,3,5-TEB treatment. However, these negative, or rather neutral, results should not be treated as cogent evidence that SAM formation had not taken place. To be sure, positive results would have proven SAM formation real but it has to be kept in mind that the probed system consists of a monolayer of analyte molecule and as such approaches the realm of single molecule spectroscopy. The concentration of analyte might just have been too minuscule to be detected by the described techniques. After all, SAM formation with triple bond motifs in general and ethynyl groups in particular is a reported fact as described above. By and large, gold substrates are well-suited systems to be probed by SERS. Nevertheless, their plasmonic resonance depends strongly on the roughness and morphology of the film. It is entirely possible that for example the roughness of the purchased gold-coated silicon wafers that were employed in the polymerisation reactions and the SAM-formation experiments is not sufficiently pronounced or otherwise inadequate as to induce an enhancement of the Raman signal that would give proof of a formed sulphur-gold bond.

An interesting phenomenon can be witnessed when taking a closer look at the blank substrate employed in the polymerisation reaction. From the very beginning, the purchased silicon wafer was not entirely covered with gold but exhibited some sites devoid of gold coating thus presenting the bare silicon. As can be surmised from **Figure 30**, where the gold-free fringe can be found in the bottom left edge of the blank sample, the polymer film does not cover that very part of the

substrate although the wafer piece was immersed in the reaction solution in its entirety. A low-magnification SEM micrograph in **Figure 32, left** allows an unequivocal judgement that the polymer layer sharply avoids traversing the pure silicon and remains within the area covered with gold. This occurrence suggests that in this environment only gold is susceptible to the formation of a SAM

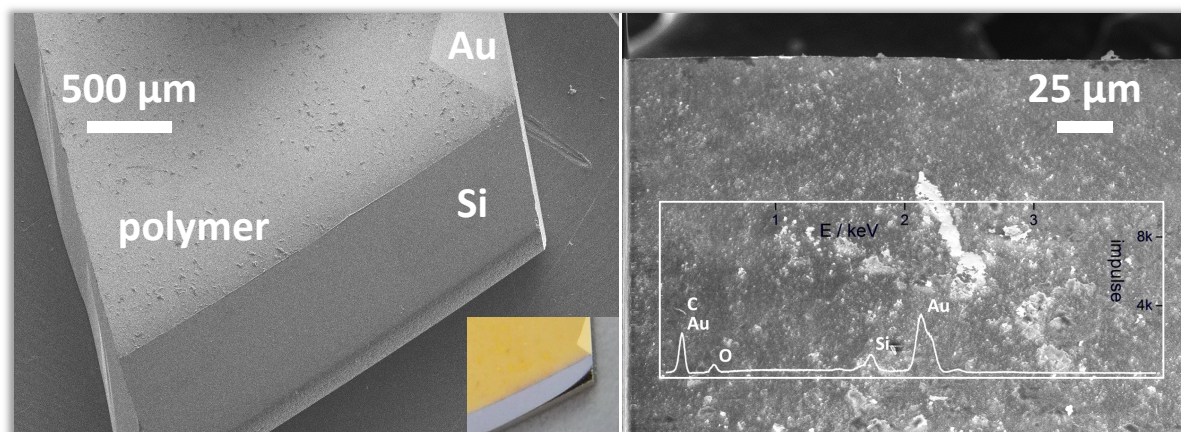


**Figure 32.** Top-view SEM micrographs and EDX area scan of blank sample confirm the presence of a polymer layer on top of the gold coating. The inset in the left picture shows a photograph of the measured sample, the SEM image of which is depicted in the larger frame, and reveals also optically that the silicon wafer piece exhibits an area that does not bear a gold coating. The polymer layer was probed by EDX area scan (right; the plot itself covers the actually probed region) disclosing the carbonaceous nature of the film.

by 1,3,5-TEB molecules whereas silicon is not. In addition, **Figure 32, right** shows an EDX area scan that again confirms the presence of carbon within the polymer layer. Owing to the high penetration depth of the probe beam, the chemical composition of underlying strata is also recorded.

## CONCLUSION

The herein developed methodology that was initially used to yield PPN-6 films on gold substrates could be adapted to the synthesis of a conjugated microporous polymer leading to the formation of CMP-1 films on gold. In stark contrast to PPN-6, for which it was shown that prior SAM functionalisation of the gold surface is vital for a covalent attachment of polymer films, CMP-1 films were also obtained on blank, *i.e.* unfunctionalised substrates. This peculiarity is caused by the nature of employed 1,3,5-triethynylbenzene that, through its ethynyl groups, does interact with gold surfaces and can form a SAM of its own thus serving as both monomer and bond-mediating group. However, such behaviour cannot be assumed to be equally applicable to other alkyne monomer species utilised in CMP synthesis. Accordingly, the obtained results regarding successful formation of CMP-1 films on gold substrates that have been functionalised with a SAM in advance (4-bromothiophenol or 4-iodothiophenol) are highlighted here as a means to form films of CMPs that incorporate monomers with no tendency to SAM formation.



# CHAPTER 2

## SILICA

### TEMPLATED POROSITY

The advent of mesoporous silica with ordered pore structure at the beginning of the 1990s heralded new opportunities for porous materials.<sup>[13,153-154]</sup> In particular, with the development of MCM-41 the world of material science witnessed an expansion of available pore systems of ordered nature from microporous zeolites to mesoporous silica. As defined by IUPAC convention, mesopores have diameters of 2 to 50 nm and are thus far bigger than micropores with diameters of less than 2 nm.<sup>[1]</sup> This enhancement in size of the pore interior has been made use of as confined reaction space and catalyst support in heterogeneous catalysis with higher diffusion rates of educts and products alike as compared to microporous systems. In addition, mesoporous silica has found use in drug delivery as well as templating approaches. For instance, the hexagonally ordered mesoporous channels of SBA-15 (Santa Barbara-15) can be infiltrated with metal salt precursors.<sup>[155-156]</sup> High thermal stability of silica permits calcination of the infiltrated system allowing the precursor to convert to a metal oxide that mimics the negative shape of the template. As a result, porous metal oxides can be obtained in defined shapes that can prove advantageous to semiconductor performance. Likewise, an exact replica of the silica template, *i.e.* the positive form can also be obtained by using the negative mould as template. The templating approach can moreover be used to obtain so-called (inverse) opals also known as photonic crystals.<sup>[157-160]</sup> Although not meso- but macroporous, and therefore somewhat extraneous to this topic these structures are extremely intriguing as they feature periodically aligned spheres (opal) or cavities (inverse opal) comparable in size to the wavelengths of visible electromagnetic radiation. This property endows the material with waveguide capability with potential application in envisaged quantum computers.<sup>[161-162]</sup>

The goal of this work was to obtain a microporous network with imprinted mesoporosity derived from a siliceous template. To this end, it was devised to infiltrate mesopores of a silica monolith with the monomers used in PPN-6 synthesis. The employed silica should be devoid of significant microporosity as in an intermediate stage of the process a successful infiltration was sought to be proven by the presence of microporosity provided by formed PPN-6. Moreover, many possible silica precursors were considered inappropriate for the approach, namely those that are available as powder only. The reason springs from practical considerations. It is very hard to separate powder of potentially infiltrated silica from bulk polymer that has been formed in excess. This in turn makes sorption analysis of the silica pointless since microporosity will certainly be detected but not due to polymer inside the silica but rather as a result of excess polymer. Another aspect regards the nature of porosity within the prospective template. In principle two different types of pore architecture can be conceived. One in which the pores are interconnected as is the case in so-called worm-like pore systems and another that exhibits pores lacking significant interconnection and can thus be treated as isolated from each other. These two situations will lead to different outcomes. After infiltration and decomposition of the template, an interconnected pore system will yield a monolithic since interconnected negative shape whereas a pore system consisting of isolated pores will give rise to isolated *e.g.* rods of the anticipated material (**Figure 33**).

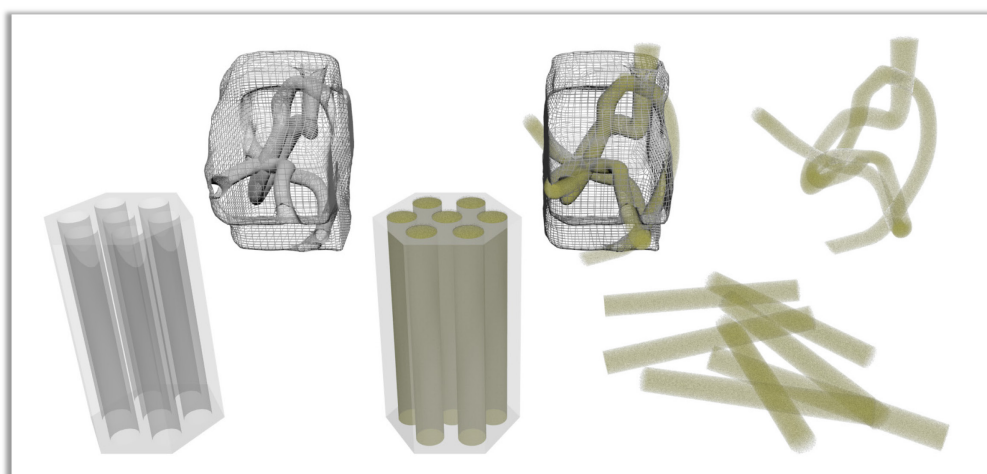


**Figure 33.** Illustration of the influence the pore system has on the templated polymer. Foreground shows an idealised micropore-free SBA-15 structure featuring a hexagonally ordered pore system with no interconnection between the pores before infiltration (left), infiltrated with PPN-6 (middle), and the polymer obtained after the template has been dissolved (right). Backdrop shows a silica template with a worm-like, *i.e.* interconnected pore system neat (left), infiltrated (middle), and polymer after template-removal (right).

For this reason, a worm-like pore system within the template might be desired as it provides the necessary structural interconnectivity to obtain a polymer with an interstitial regime of mesoporous voids between polymer chains as a result of the templating process. Different siliceous materials exhibiting worm-like pore systems have been reported. For example, KIT-6 (Korean institute of technology-6) features a mesostructure with  $Ia\bar{3}d$  symmetry as does MCM-48.<sup>[13,154,163-164]</sup>  $Pm\bar{3}n$  symmetry can be found in SBA-1<sup>[165-166]</sup> whereas SBA-16<sup>[156]</sup> as well as FDU-1 (Fudan university-1)<sup>[167]</sup>

incorporate pore systems of  $Im\bar{3}m$  symmetry, which is not innocuously referred to as ‘the plumber’s nightmare.’<sup>[168]</sup> The pore system of FDU-12 features  $Fm\bar{3}m$  symmetry.

Conversely, materials such as SBA-15 display hexagonally arranged mesopores ( $P6mm$ -symmetry) that if isolated from each other could be expected to lead to isolated polymer rods of, in this case, PPN-6. Comparably thick pore walls in SBA materials (3.1 to 6.4 nm for SBA-15)<sup>[155]</sup> as compared to *e.g.* MCM materials (0.6 to 1.2 nm for MCM-41)<sup>[169]</sup> are a decisive feature as the expected mesoporosity that PPN-6 should be infused with hails from the portion of the template that is not occupied by polymer, that is to say the walls of the silica.<sup>[170]</sup> Moreover, SBA-15 is not exclusively mesoporous but contains microporosity within the walls, a circumstance subject to numerous studies.<sup>[171-179]</sup> However, whether or not those microporous channels are sufficiently spacious to accommodate the rather formidable zoo of compounds required in the synthesis of PPN-6 and are thus able to interlock the polymer rods that are anticipated to form inside the cylindrical mesopores, remains to be seen.

## RESULTS AND DISCUSSION

### SILICA | PRISTINE

In the light of the aforesaid predicament of the impossibility to separate excess polymer from the supposedly infiltrated silica template when relying on silica in form of powder, it was imperative to employ a monolithic template. This requirement ruled out the use of worm-like siliceous materials as these are not available in monolithic form. However, it was possible to identify a protocol reported in literature for the synthesis of monolithic silica exhibiting a structure akin to SBA-15.<sup>[180]</sup> The procedure utilises an ethanolic solution of the triblock copolymer Pluronic-123 (P-123) as templating agent and tetraethyl orthosilicate (TEOS) as silicon source. The novelty of this protocol by Zhao *et al.* comes with the step where the already solidified gel is covered with a layer of paraffin oil before ageing at elevated temperatures commences. This is reported to prevent formation of cracks within the solid due to structural strain by shrinkage of the siliceous block. **Figure 34** portrays the result typically obtained in this work and shows that the reproduction of the protocol from Zhao *et al.* did work to some extent albeit crack formation could not be forestalled as successfully as was achieved in the literature account. Nevertheless, as the main goal was to obtain silica chunks of



**Figure 34.** Photographs of a monolithic silica chunk after ageing at room temperature (left) and after subsequent ageing at 60 °C. Crack formation progresses during ageing at elevated temperatures diminishing the structural integrity of the monolith that eventually fell into pieces. A one euro coin serves as scale.

tangible size rather than powder the silica synthesis is considered successful. After all, a monolith of the size depicted in **Figure 34** would have to be crushed into smaller pieces in any event lest application of the silica in the envisaged experiments is obstructed. The aged samples were washed clean from excess paraffin oil and subjected to calcination (550 °C for 6 h) for template removal and the formation of porosity. Upon calcination a considerable mass loss of 63.2 % was detected. Thermogravimetric analysis (TGA) of an aged sample showed a comparable mass loss of 63.4 % (**Figure A2**). The obtained calcined silica was proven to be porous by volumetric nitrogen sorption yielding a  $S_{\text{A}_{\text{BET}}}$  of  $446 \text{ m}^2 \cdot \text{g}^{-1}$ . NLDFT calculation revealed a narrow PSD with a single pore domain centred around a pore diameter of 4.9 nm and a cumulative pore volume of  $0.46 \text{ cm}^3 \cdot \text{g}^{-1}$  (**Figure 35**).

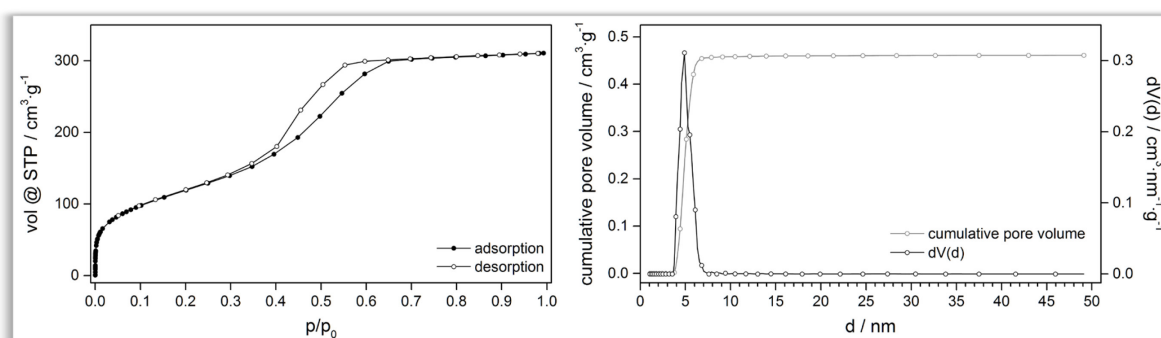


**Figure 35.** Isotherm obtained from nitrogen sorption at 77 K (left) and plot of NLDFT results for both cumulative pore volume and PSD (right).

Notably, albeit the isotherm displays an uptake at low relative pressures, NLDFT calculations show no contributions from micropores to either pore volume or surface area thus characterising this material bereft of microporosity, as desired. The shape of the isotherm reflects type IV and shows mesopore filling after point B has been passed before levelling off towards saturation pressure clearly suggesting the absence of macropores or textural porosity. During desorption, hysteresis is evident.

The degree of structural order was evaluated by powder X-ray diffraction (PXRD) (**Figure 36**). An aged sample, *i.e.* before calcination, shows a weak reflex at  $0.97^\circ 2\theta$  as shoulder adjacent to the primary X-ray beam, which translates into an interplanar distance of 9.1 nm employing Bragg's law.

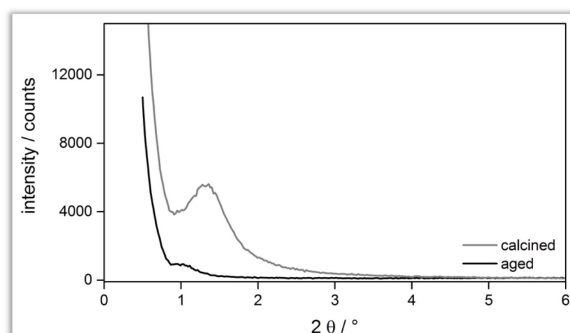


**Figure 36.** PXRD patterns obtained from an aged (black curve) and a calcined (grey curve) sample. The aged sample shows a very weak signal at  $0.97^\circ 2\theta$ . After calcination, this reflex is shifted to  $1.3^\circ 2\theta$ .

This reflex is commonly assigned to the reflection off of the (100) lattice plane. The low intensity of the signal is arguably caused by the low contrast provided by the specimen. At this stage the silica was still infiltrated with block-copolymer P-123, *i.e.* the pores were not empty resulting in only a small difference in the mass densities of the siliceous material and its pores-to-be. Calcination triggers the generation of porosity by decomposition and eventual expulsion of P-123 with a concomitant contraction of the structure occasioning the (100) reflex to appear at  $1.3^\circ 2\theta$ , which is indicative of an interplanar distance of 6.7 nm. In addition to the (100) reflex, (P)XRD patterns of SBA-15 materials commonly also show the (110) and (200) reflections at around  $1.4^\circ 2\theta$  and  $1.7^\circ 2\theta$ , respectively. Those are usually observed with very low intensity indeed but their conspicuous absence here suggests a low degree of crystalline order.

### SILICA | PRISTINE | PPN-6

First attempts at infiltration of silica with a microporous polymer employed calcined silica without further treatment other than vacuum drying prior to polymerisation runs. Generally, under inert atmosphere a flame-dried glass vial was charged with the reactants required in PPN-6 synthesis (see Chapter 1 or Experimental Part for details) save for the monomer tetrakis(4-bromophenyl)methane lest polymerisation commences before template is present. It was ensured that all components got dissolved before the silica chunks were added in an amount that guaranteed all template pieces being properly immersed in and surrounded by reaction solution. The system was given a few minutes to let the silica chunks get properly soaked with the medium. Only at this point was the reaction solution complemented by addition of monomer in a dissolved state to ensure and facilitate a homogeneous distribution of all components.

After the reaction was completed, silica pieces were recovered and worked-up by means of washing, Soxhlet extraction, and ensuing drying in vacuum. After the silica template was subjected to the polymerisation reaction, according to nitrogen sorption analysis an increase in  $SA_{\text{BET}}$  could be detected. Assuming that possibly not the entire pore interior was filled with polymer, the supposedly infiltrated silica was employed in the same kind of polymerisation reaction yet a second time to monitor if a further increase in surface area is observed. As a result, however, a decline in SA was detected yielding a value that lies between the figures for pristine silica and the sample that partook in the polymerisation only once (**Figure 37**). Moreover, the isotherm did not assume a significantly different shape after polymerisation, an unanticipated outcome when considering that, if successful, the mesopores will be occupied by a microporous polymer with no apparent mesoporosity remaining. Thus, an increase in the low relative pressure region as well as a diminution of hysteresis, which reflects the typical pattern for mesoporous systems, can be expected.

In addition, TGA showed no mass loss that reaches the expected value of 8.4 % assumed to be observed in case of decomposition of a polymer formed quantitatively inside the whole space of the mesoporous channels (see Appendix Comment A for TGA and calculation). More importantly, the sample subjected to the polymerisation reaction twice showed a lower mass loss as compared to the

specimen employed only once, a result utterly unexpected when assuming infiltration had been successful. On the other hand, the seemingly higher polymer content of the sample employed only once accords with results obtained from nitrogen sorption that ascribe a higher  $SA_{\text{BET}}$  to that very sample as compared to the one that had been subjected to polymerisation twice.

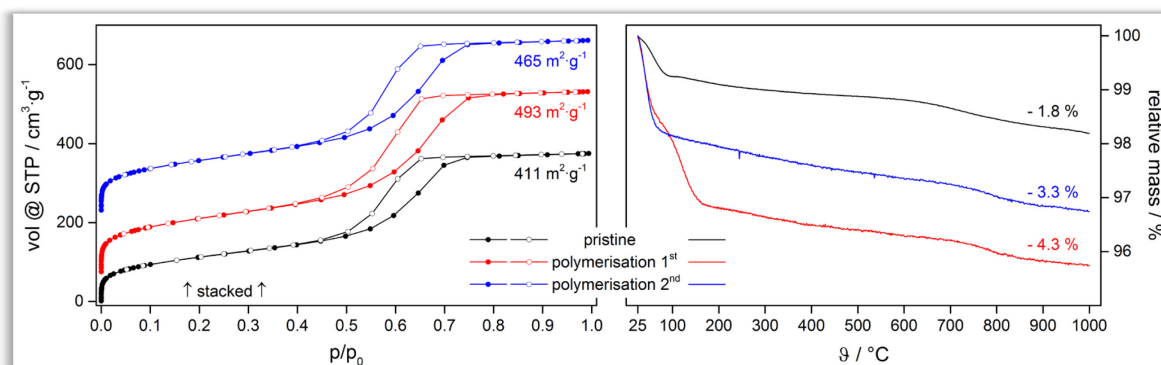


**Figure 37.** Isotherms derived from nitrogen sorption at 77 K (left-hand side) and TGA plots (right-hand side) for a pristine silica sample after calcination (black curves), ensuing first (red curves) and second (blue curves) polymerisation reaction. For better visibility red and blue isotherms are stacked along the ordinate axis; solid symbols: adsorption, empty symbols: desorption.

In order to ascertain whether or not the structural pattern of the template was successfully imprinted on the polymer PPN-6, the silica was removed by virtue of etching with an aqueous solution of ammonium hydrogen difluoride ( $\text{NH}_4\text{HF}_2$ ). Inconveniently, although a very tangible amount of several hundreds of milligrammes of polymer was expected to be revealed the concrete obtained quantity was far too less to be collected. In fact, it appeared as if almost no polymer remained. Thus, analysis of the polymer was impossible.

In the light of this, it might be conceivable that the infiltration itself did not progress as assumed in the first place. The detected increase in  $SA_{\text{BET}}$  of the supposedly infiltrated silica after the first and second polymerisation runs as compared to the pristine sample might then be ascribed to excess polymer attached to the silica but not actually residing inside its porous system. Although it was endeavoured to avoid such an outcome by multiple washing steps its materialisation cannot be ruled out. This line of argument, moreover, helps to explain why  $SA_{\text{BET}}$  of the sample subjected to the polymerisation twice was lower than the value of the sample that underwent this procedure only once. For if it premised that indeed excess polymer is responsible for the gain in  $SA_{\text{BET}}$ , this increase can be interpreted as a rather erratic event than as a systematically caused incident. As such, a lower  $SA_{\text{BET}}$  value after the second polymerisation can be attributed to a lower amount of excess polymer present in or on the specimen.

An alternative explanation is based on the possibility of polymer inside the pores being washed out during the first and the second polymerisation run. This explanation, however, is conceded less probability as it is hard to understand why polymer inside the pores should get washed out in a second run during which, subsequent washing steps included, an environment is created that exactly resembles the conditions that led to the infiltration in the first run.

## SILICA | FUNCTIONALISATION WITH HEXAMETHYLDISILAZANE (HMDS)

The question then arises what might have foiled successful formation of polymer inside the siliceous structure. As possible reason for the failed attempt to form PPN-6 inside the silica, the chemical structure of the template was singled out. Here, silica was formed by condensation reaction of TEOS in acidified ethanol. Naturally, the condensation reaction cannot consume the entire supply of hydroxy groups provided by the hydrolysed TEOS. A reasonable amount of unreacted hydroxyls will remain at the silica-air phase boundary, *i.e.* the surface, rendering the formed silica hydrophilic. This peculiarity gives rise to an incompatibility in polarity between the template and the reagents used in PPN-6 synthesis since the latter are hydrophobic. The polymerisation reaction itself did indeed proceed as could be judged from bulk polymer that formed in trials following the wet-approach (more details on that later). Unsuccessful infiltration then might have been thwarted by a template that, due to its hydrophilic surface, did not allow reagents to enter its porous system.

The issue of polarity incompatibility posed by the hydrophilic surface of the silica was addressed by virtue of surface functionalisation. A possible strategy is to decrease or eliminate the hydrophilic character of the silica by functionalisation with hexamethyldisilazane (HMDS), which transforms terminal hydroxy groups to trimethylsiloxanes rendering the surface hydrophobic in the process. The success of functionalisation was monitored by an increase in sample weight of 8.3 % with respect to the final mass, *i.e.* the mass obtained after functionalisation.

TGA revealed a mass loss of 4.7 % for the functionalised sample (**Figure 38, right red curve and Figure A3**). *Prima facie*, TGA does not confirm the mass increase determined by simple weighing. But one has to bear in mind how the surface is altered by HMDS treatment. Hydrogen is substituted by trimethylsilyl (TMS) groups. The latter are only partially susceptible to thermal decomposition and subsequent expulsion from the system, which represents the *modus operandi* of a TGA machine. In other words, by HMDS functionalisation groups are introduced into the system that will not entirely be removed during a TGA run. Assuming that only the methyl groups are expunged from the surface with the newly introduced silicon atoms remaining firm in place even at 1000 °C, the observed mass

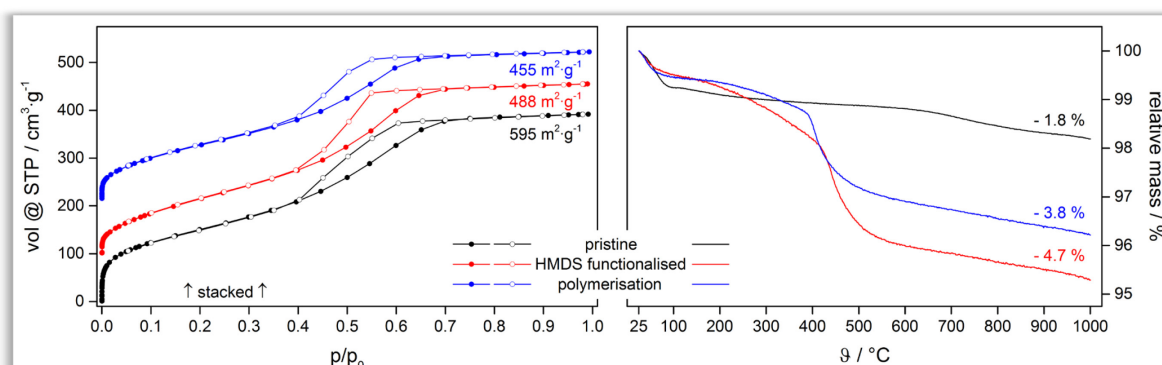


**Figure 38.** Isotherms derived from nitrogen sorption at 77 K (left-hand side) and TGA plots (right-hand side) for a pristine silica sample after calcination (black curves), ensuing functionalisation with HMDS (red curves) and subsequent polymerisation reaction (blue curves). For better visibility red and blue isotherms are stacked along the ordinate axis; solid symbols: adsorption, empty symbols: desorption.

loss of 4.7 % during TGA has to be set into relation to the mass gain of 8.3 %. As a result, the former constitutes 56.6 % of the latter. Affirmatively, in theory a mass loss of 59.1 % is predicted in case three methyl groups per TMS unit are jettisoned when put into relation to the mass increase observed for the transformation of a hydroxyl to a trimethylsiloxane group (see Appendix Comment B for TGA and calculation).

To assess how comprehensive functionalisation was the added TMS groups have to be set into relation to the number of silanol groups presented by the silica. According to a publication quantifying silanol sites in various mesoporous ordered siliceous systems, SBA-15 exhibits 1.7 hydroxy groups per square nanometre that are accessible to HMDS.<sup>[181]</sup> In conjunction with the observed mass gain a fairly high degree of functionalisation of 0.74 can be determined (see Appendix Comment C for calculation). This means that nearly three quarters of all accessible hydroxy groups have been transformed into trimethylsiloxanes.

Substituting trimethylsilyl for hydrogen not only alters the surface chemistry of the silica but also changes its gas sorption properties. As TMS groups are profoundly more bulky, a decrease in gas uptake is expected. Indeed, nitrogen sorption at 77 K shows a specific  $S_{A_{BET}}$  for the HMDS treated sample of  $488 \text{ m}^2 \cdot \text{g}^{-1}$ , considerably less than the value of  $595 \text{ m}^2 \cdot \text{g}^{-1}$  for the pristine, *i.e.* calcined sample (**Figure 38, left** red and black curve, respectively). Allowing for the mass increase induced by functionalisation of 9.0 or 8.3 % with regard to initial, *i.e.* mass available before functionalisation, or final mass, respectively, a specific  $S_{A_{BET}}$  of  $546 \text{ m}^2 \cdot \text{g}^{-1}$  has been expected, if only gravimetric influences had been at work. This shows that the surface area is indeed affected by bulky residents in the porous structure. Concomitantly, according to NLDFT calculations pore volume decreases from  $0.58$  to  $0.53 \text{ cm}^3 \cdot \text{g}^{-1}$  in the course of the functionalisation process.

### SILICA | HMDS | PPN-6

With the surface of the silica rendered hydrophobic it was employed in a polymerisation reaction of the kind described above with the objective to form PPN-6 inside the pore system. Again, investigation of porosity and combustible components drew a bleak picture that suggested that the infiltration of the silica was unsuccessful. Nitrogen sorption showed a decrease in  $S_{A_{BET}}$  culminating in  $455 \text{ m}^2 \cdot \text{g}^{-1}$  for the HMDS-functionalised sample that has been subjected to polymerisation (**Figure 38**). However, provided that the pores are infiltrated with highly microporous PPN-6, an increase in surface area is anticipated. Moreover, as was the case with the unfunctionalised sample subjected to polymerisation, the shape of the isotherm still bears testimony to the presence of a mesopores indicating that infiltration was fruitless.

In addition, TGA showed that the mass loss after the polymerisation run is actually lower than it was before amounting to 3.8 % as compared to 4.7 % for the HMDS-functionalised sample. The expected value lies around 12.6 % (see Appendix Comment D for calculation). These two results, lower  $S_{A_{BET}}$  and lower mass loss, are indeed hard to fathom when supposing that polymerisation had just not taken place. In such an event the initially employed template material should remain

unaffected and give identical results in both surface area and mass loss as compared to a specimen probed before functionalisation.

Solid state CP/MAS NMR investigations of the supposedly infiltrated silica buttresses the notion that infiltration was unsuccessful in showing no signals whatsoever that would confirm the presence of PPN-6 inside the siliceous template (**Figure 39**).

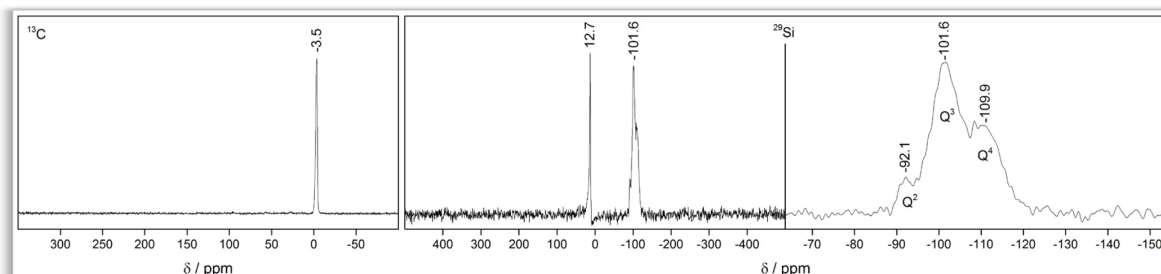


**Figure 39.** Solid state CP/MAS NMR spectra ( $v_{\text{rot}} = 10$  kHz) from a HMDS-functionalised sample that has been subjected to PPN-6 polymerisation reaction.  $^{13}\text{C}\{^1\text{H}\}$  (left) and  $^{29}\text{Si}\{^1\text{H}\}$  (middle to right) spectra show that no polymer is found inside the template. Carbon NMR gives rise to only one signal at -3.5 ppm hailing from the methyl moieties of the trimethylsiloxane units. The respective silicon atom of that group begets the signal at 12.7 ppm in the silicon NMR. Therein, the multiplet at around 102 ppm is magnified in the spectrum to the right with  $\text{Q}^2$ ,  $\text{Q}^3$ , and  $\text{Q}^4$  denoting  $\text{Si}(\text{OSi})_2(\text{OH})_2$ ,  $\text{Si}(\text{OSi})_3(\text{OH})$ , and  $\text{Si}(\text{OSi})_4$  species, respectively.<sup>[181]</sup>

Upon removal of the silica template *via* treatment with  $\text{NH}_4\text{HF}_{2(\text{aq})}$  no polymer was found to be left over, a finding that confirms on a macroscopic level what has been suggested by analytical investigations. If infiltration had worked satisfactorily, a mass of several hundreds of milligrammes would have been uncovered upon template removal (see Appendix Comment D).

### SILICA | FUNCTIONALISATION WITH PARABROMOPHENYLTRIMETHOXYSILANE (PBPTMOS)

After it was soundly established that infiltration of the silica template has failed, emphasis was put on how to increase the likelihood of polymerisation to take place inside the pores. The previous approach entailed alteration of the surface properties with the aim to decrease hydrophilicity as to enhance the probability of polymerisation to take place inside the pores. However, the introduced HMDS groups remain passive in the sense that they do not react with incoming reagents due to which that methodology does not actively foster polymerisation inside the pores. To promote such a scenario the silica surface was functionalised with a molecule that can actively partake in the PPN-6 reaction. Parabromophenyltrimethoxysilane (PBPTMOS) was chosen as suitable candidate to decorate the pore walls. A condensation reaction between the molecule's methoxy and the silica's hydroxy groups under release of methanol leads to covalent attachment of a parabromophenylsiloxane moiety to the surface leaving the brominated phenyl ring exposed to incoming reagents. Advantageously, at the same time the surface's hydrophilicity is diminished as well. **Figure 40** shows a graphical abstract of the envisaged surface alteration in juxtaposition with the earlier described method involving functionalisation with HMDS.

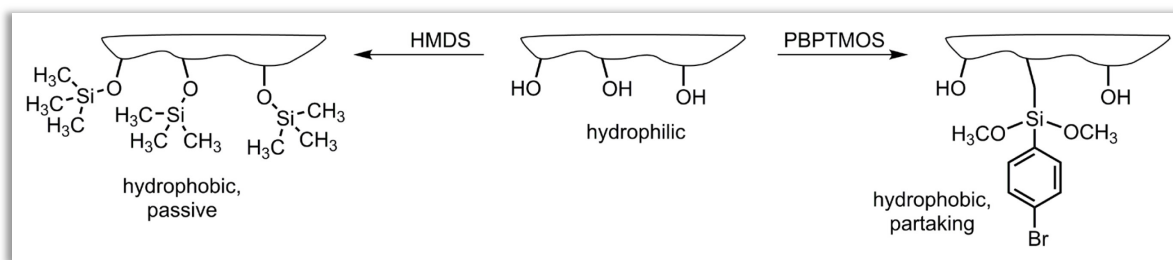


**Figure 40.** Sketch of surface functionalisation employing either HMDS in order to solely decrease hydrophilicity of the surface or PBPTMOS to decorate the surface with moieties that participate in the polymerisation reaction of PPN-6 and, in addition, render the surface hydrophobic.

The functionalisation with PBPTMOS yielded an increase in sample weight of 17.5 % with respect to the final mass, *i.e.* the mass obtained after functionalisation. The employed molar amount of PBPTMOS was 16.7 mmol and the observed mass increase amounted to 3.6608 g. Presupposing different condensation events, these numbers help to identify whether condensation occurred one-, two-, or three-fold. Eventually, a one-fold condensation with two remaining methoxy groups per PBPTMOS unit is the most likely event (see Appendix Comment E for discussion thereof).

During TGA a total mass loss of 16.1 % was recorded. Again, that result cannot be taken at face value as what was true for the functionalisation process *via* HMDS is applicable here as well. The introduced groups will not be expelled in their entirety with the silicon atoms remaining unaffected by combustion. Consequently, the mass loss observed during TGA has to be set into relation to the mass gain of 17.5 % caused by functionalisation. As a result, the mass loss constitutes 92.0 % of the mass increase. Theoretical considerations to reinforce this experimentally obtained ratio need to take into account different condensation events. However, with the aforesaid reckoning favouring a one-fold condensation it is reasonable to apply these conditions first. Indeed, the result closest to the experimental finding is obtained when assuming a one-fold condensation reaction with a theoretical ratio for mass loss during TGA to mass gain through functionalisation of 89.0 %, somewhat below the experimentally obtained value of 92.0 % but still in good agreement (see Appendix Comment F for TGA and calculation).

The degree of functionalisation was determined to be 0.63 (see Appendix Comment G) assuming an amount of hydroxy groups present at the surface of 1.7 groups per square nanometre, identical to what has been applied in the respective assessment for the HMDS-functionalised sample. That amount of available hydroxy groups, however, was established for hydroxyls accessible to HMDS, a smaller molecule than PBPTMOS. Nevertheless, due to the absence of a more appropriate data it is considered a valid parameter to use for the purpose at hand. Moreover, if a correction was to be applied, the value of 1.7 groups per square nanometre is to be reduced since in this context it is reasonable to argue that the number of accessible hydroxyls is lower for a bigger molecule as compared to a smaller one. This, in turn, leads to a higher degree of functionalisation by decreasing the denominator in the fraction while keeping the numerator unchanged.

Functionalisation with PBPTMOS implies that the pores of the silica accommodate bulky entities. As a result, both porosity and surface area are expected to decrease. However, BET analysis of the isotherms derived from nitrogen sorption at 77 K shows that  $SA_{\text{BET}}$  remains virtually unaltered with

486 and 487  $\text{m}^2\cdot\text{g}^{-1}$  for pristine and PBPTMOS-functionalised samples, respectively (**Figure 42**, left). Taking into account the mass gain of 21.3 or 17.5 % with regard to initial, *i.e.* mass available before functionalisation, or final mass, respectively, the obtained result seems inconsistent with theory. Assuming only mass affects surface area, a  $\text{SA}_{\text{BET}}$  of 401  $\text{m}^2\cdot\text{g}^{-1}$  is calculated to be the maximum. A value below this calculated figure could be explained by pore blocking effected by cumbersome entities. Clearly, the measured  $\text{SA}_{\text{BET}}$  surpasses the theoretical maximum, a circumstance that cannot be explained in the context of this investigation as it is highly unlikely that the introduced PBPTMOS groups enable the system to accommodate more gas than before functionalisation.

### SILICA | PBPTMOS | PPN-6

Apart from the variation in functional groups attached to the surface another aspect was paid attention to. The question as to where the PPN-6 formation does actually take place was identified as one of the problems encountered during the experiments. In the previously described attempts, the monolithic chunks of the silica template were properly immersed in an excess of reaction medium, a configuration designated *wet-approach* in hindsight. However, in such a reaction scheme competition as to where the polymerisation takes place could not be ruled out. This, theoretically, can create a situation in which most or even the entire polymerisation takes place within the surplus liquid reaction medium leaving the silica unaffected and possibly empty. To frustrate the occurrence of such an event, a second methodology was adopted. According to the *dry-approach*, an excess of reaction medium was circumvented and only as much reaction medium applied as necessary to impregnate the silica pieces (**Figure 41**). The PBPTMOS-functionalised silica was employed in PPN-6



**Figure 41.** Photograph of reaction vials set up according to either wet-approach (left) or dry-approach (right).

polymerisation batches following either the wet- or dry-approach. Results from nitrogen sorption analysis and TGA do suggest a difference between these two protocols indeed. However, when compared to the reference plot, *i.e.* the isotherm obtained for PBPTMOS-functionalised silica exhibiting a  $\text{SA}_{\text{BET}}$  of 487  $\text{m}^2\cdot\text{g}^{-1}$ , the polymerisation samples produce figures slightly above and below this value with 502 and 479  $\text{m}^2\cdot\text{g}^{-1}$ , for batches from wet- and dry-approach, respectively.

TGA disclosed mass losses of 14.5 and 13.6 % for wet- and dry-approach samples, respectively (**Figure 42**, right). These values are lower than the figure of 16.1 % obtained for the PBPTMOS-functionalised sample, a result that is anomalous albeit not as straightforwardly as it might seem. If polymerisation and tethering of the polymer to the surface was successful, the bromine atom is

sacrificed in the course of the reaction thereby in fact reducing the mass inside the pores at least to a certain extent. That extent is determined by the nature of the motif that is tethered to the surface. In this case, a tetraphenylmethane (TPM) moiety is coupled to the phenyl ring of the surface bonded PBPTMOS. Assuming an ideal reaction progress, *i.e.* all PBPTMOS anchor sites react to an individual TPM unit and these TPMs bear no residual bromine atoms, a mass decrease can only occur when the added TPM is more lightweight than the sacrificed bromine atom. This, however, is not the case with the former putting approximately four times as much mass onto the balance than the latter. Moreover, the ideal conditions outlined above will not be met in reality and most probably not all PBPTMOS units will react and the attached TPM units will certainly bear residual bromine functionalities in addition to the fact that more than a monolayer of TPM is attached. These factors all favour an increase in the mass of the matter present inside the pores. Thus, with not even the most benign assumptions sanctioning a reduced mass loss after polymerisation, the eventual conclusion is that it is indeed anomalous to observe a diminished mass loss for the samples that have been subjected to polymerisation trials.

Furthermore, the observed values for the polymerisation experiments following the wet- and dry-approach do not reach the calculated mass loss of 16.6 % based on the provided sample mass and pore volume of the siliceous template (see Appendix Comment H for calculation).

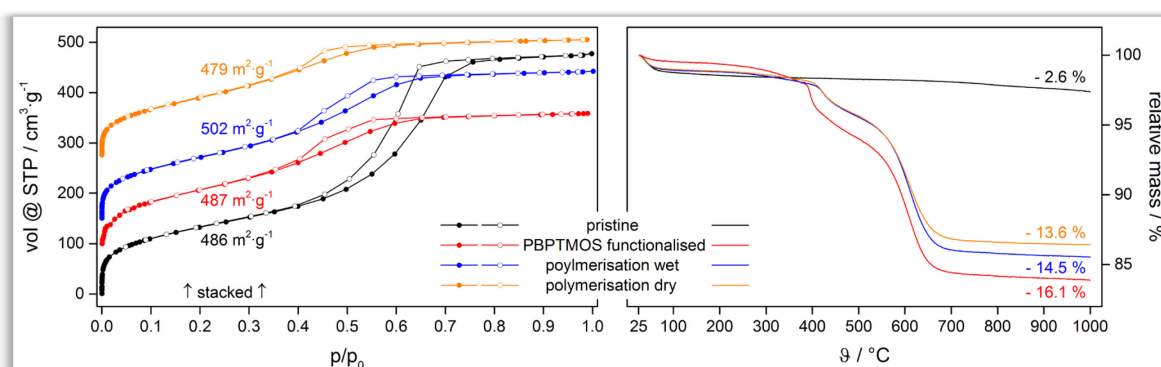


**Figure 42.** Isotherms derived from nitrogen sorption at 77 K (left-hand side) and TGA plots (right-hand side) for a pristine silica sample after calcination (black curves), ensuing functionalisation with PBPTMOS (red curves) and subsequent polymerisation reaction following either wet (blue curves) or dry (orange curves) approach. For better visibility red, blue, and orange isotherms are stacked along the ordinate axis; solid symbols: adsorption, empty symbols: desorption.

To lay bare the polymer possibly residing in the pores, the silica was etched away by means of  $\text{NH}_4\text{HF}_2(\text{aq})$  treatment. However, as was observed and described above for the polymerisation attempts employing either unfunctionalised or HMDS-functionalised silica the process revealed no amount of polymer to speak of. In fact, only minuscule traces of a white substance were observed that were far too small to be collected or analysed. Thus, it must be concluded that this strategy failed to produce the desired target structure of a nominally microporous network with additional mesoporosity generated by virtue of a template.

## CONCLUSION

In the discussion of the reasons why the experiments were abortive the focus is set on the subject as to where the reaction takes place. To ensure that the monolithic silica template does indeed accommodate the polymerisation reaction the dry-approach was devised (*cf.* **Figure 41**). That the silica pieces were properly soaked through could be witnessed during work-up when the addition of hydrochloric acid in order to quench the Yamamoto reaction causes the brownish tinge of the reaction to fade away to give rise to a lighter appearance (**Figure 43**). It is apparent that the colour starts to fade at the outer rim with the centre still displaying a darker shade. This observation propounds that the reaction components are inside the template material. Inside the pores, however, diffusion can be expected to be severely hampered due to spatial constraints casting a scenario in which reactive components might not be able to get in as close a contact as necessary. Likewise, polymer might be formed but preferably just outside the pores, that is to say at the entrance. In such an event the entrance of a pore might become blocked by polymer thereby further reducing the already adversely affected diffusion of reagents into the pores. This can be pictured especially in the case of the PBPTMOS-functionalised silica that presents groups at its surface that participate in the reaction. Such a constellation foreshadows covalent attachment of polymer to the surface. Polymer that gets attached in such a manner at the entrance of a pore will inevitably shield the pore from incoming reagents.

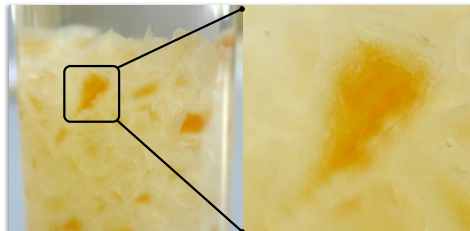


**Figure 43.** Photograph of reaction vessel utilising the dry-approach during work-up with aqueous hydrochlorid acid. The typical fading of the dark colour during quenching can be discerned to start from the outer rim of the monolithic silica pieces and proceeds to its centre. This confirms that the template has been properly impregnated with reaction medium.



# CHAPTER 3

## LIGHT

The final chapter of this thesis presents results of the incorporation of the light-responsive molecules diarylethenes (DAEs) and azobenzenes (Azos), into architectures of microporous polymers. Microporous materials are very sensitive to changes in their structure as regards for instance rigidity, contortion or geometry of building blocks. For this reason, it is expected that successful isomerisation of the photochromic moieties translates into an observable alteration in the material's properties such as surface area, pore volume, affinity for probe gases, and gas permeability.

### PHOTOCHROMISM

The key feature for a compound to be labelled photochromic is a reversible transformation  $A \rightarrow B$  in its molecular structure with a concomitant change in the UV-vis absorption spectrum upon exposure to an electromagnetic stimulus. Reversibility is of crucial importance and depending on whether the reverse reaction  $B \rightarrow A$  is triggered by heat or by light, a compound is designated t-type or p-type chromophore, respectively. It has to be mentioned, though, that thermally stable usually refers to stable at room temperature and means that the formed isomer will not relapse to the initial form at room temperature in the dark. The most frequently used chromophores are fulgides,<sup>[182-185]</sup> azobenzenes,<sup>[186-187]</sup> spiropyranes,<sup>[188-189]</sup> and diarylethenes<sup>[190-191]</sup> and the transformation in their molecular structure is of varying nature (**Figure 44**).<sup>[192]</sup>

Azobenzenes, for instance, perform a marked geometrical change by flipping around one half of the molecule to the other side of the central  $N=N$  double bond thereby switching between the (*E*)- and (*Z*)-isomer. When completed, there are no additional or missing bonds. As for spiropyranes, the hybridisation state of the spiro carbon changes from  $sp^3$  to  $sp^2$  under cleavage of an adjacent bond thereby shifting the geometry of the molecule from tetrahedral and rigid to more planar and

flexible. In addition, the molecule becomes zwitterionic and gains an increased conjugation of  $\pi$ -electrons. Azobenzenes and spiropyranes are classified as t-type chromophores since their isomers formed under UV illumination are thermally unstable and revert to the initial isomer in the dark at room temperature. Fulgides and diarylethenes show a structural motif different from the

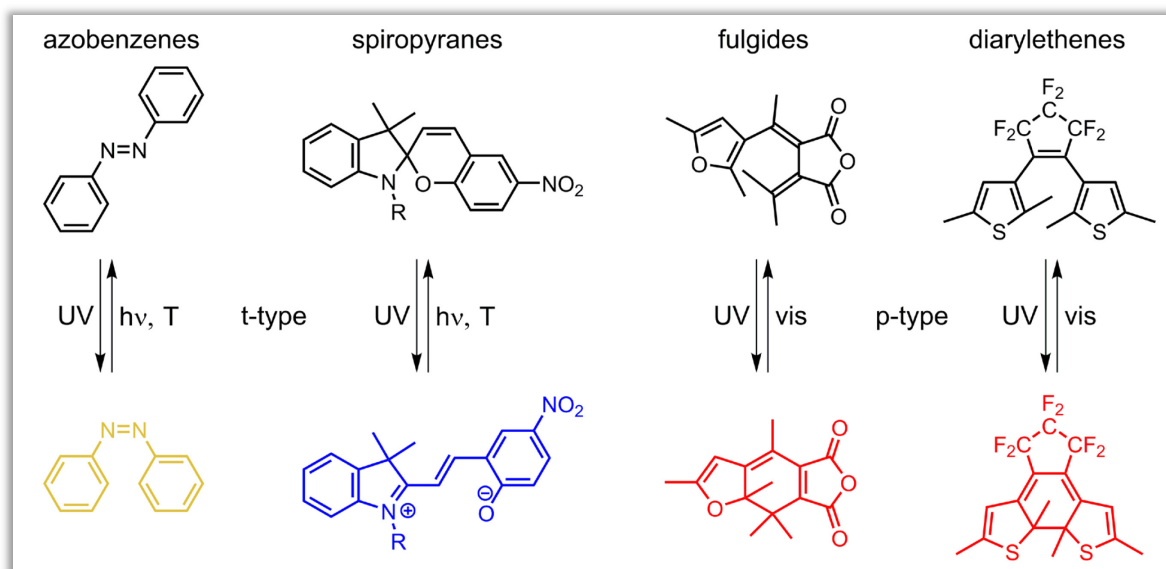


**Figure 44.** Members of different classes of photochromic compounds and their switching patterns. Azobenzenes and spiropyranes are designated t-type chromophores and the examples depicted here turn from pale yellow to orange and from colourless to blue, respectively. Fulgides and diarylethenes are designated p-type chromophores and the representatives depicted here both turn from colourless to red. This scheme shall only provide a basic overview of switching patterns and has no pretension to three-dimensionally correct arrangement of molecular moieties but simply shows flat structures (adapted from reference 193).

aforementioned but similar to each other. A central  $\pi$ -electron sextet executes a photochemically induced pericyclic ring closing reaction by concerted flipping of  $\pi$ -bonds. The result is a minor geometrical change and a stiffer molecule as well as a vastly enhanced conjugation of  $\pi$ -electrons. Fulgides and diarylethenes are classified as p-type chromophores. Azobenzenes do not undergo a large change in conjugation of  $\pi$ -electrons as can be witnessed by a barely noticeable colour change from pale yellow to orange. Conversely, spiropyranes, fulgides, and diarylethenes exhibit an increased conjugation of  $\pi$ -electrons as a result of the switching event as depicted in **Figure 44**. This is reflected in a very noticeable change in colour of those compounds from colourless to blue, red, and red, respectively. The increased conjugation causes the band gap to narrow due to which the molecules start to absorb light of lower energy than before, now lying in the visible region of the electromagnetic spectrum.

From those four classes of photochromic compounds, azobenzenes and diarylethenes have been selected to be employed in the experiments because these are most profoundly studied in literature. In addition, the high degree of symmetry that traverses their structures facilitates utilisation in polymer synthesis. These two classes of photochromic molecules will be introduced by virtue of a brief historical survey on their discovery as well as by an account of their characteristics in terms of photochemical switching.

## AZOBENZENES

Azobenzenes are a very popular class of photochromic compounds and all but new to chemistry. Over 180 years ago in 1834, Eilhard Mitscherlich published findings on a substance that he obtained as red crystals soluble in ether and alcohol but insoluble in hot water. By means of elemental analysis he found an elemental composition remarkably close to theoretical values for azobenzene and correctly figured a molecular formula of  $C_{12}H_{10}N_2$ .<sup>[186]</sup> Although it has been agreed upon that the N=N double bond gives rise to two possible isomeric forms, (*E*) and (*Z*), photochromism of azobenzene has not been a matter of concern in those early days and came to the fore only over a century later. In 1937, Hartley shed some light on this issue and, indeed, azobenzene when in the course of experiments to determine the solubility of azobenzene he was puzzled by inconsistencies in the light absorption of standard solutions that showed changes upon inadvertent exposure to light in a “north-lit room.”<sup>[187]</sup> By thoughtfully conducted solvent extraction experiments, he was able to isolate (*Z*)-azobenzene and could trace the observed inconsistencies in absorption spectra to the fact of differing absorption behaviours of (*E*)- and (*Z*)-azobenzene. Ever since, a great amount of research has been devoted to illuminate and influence the process of photochemical switching. The vast

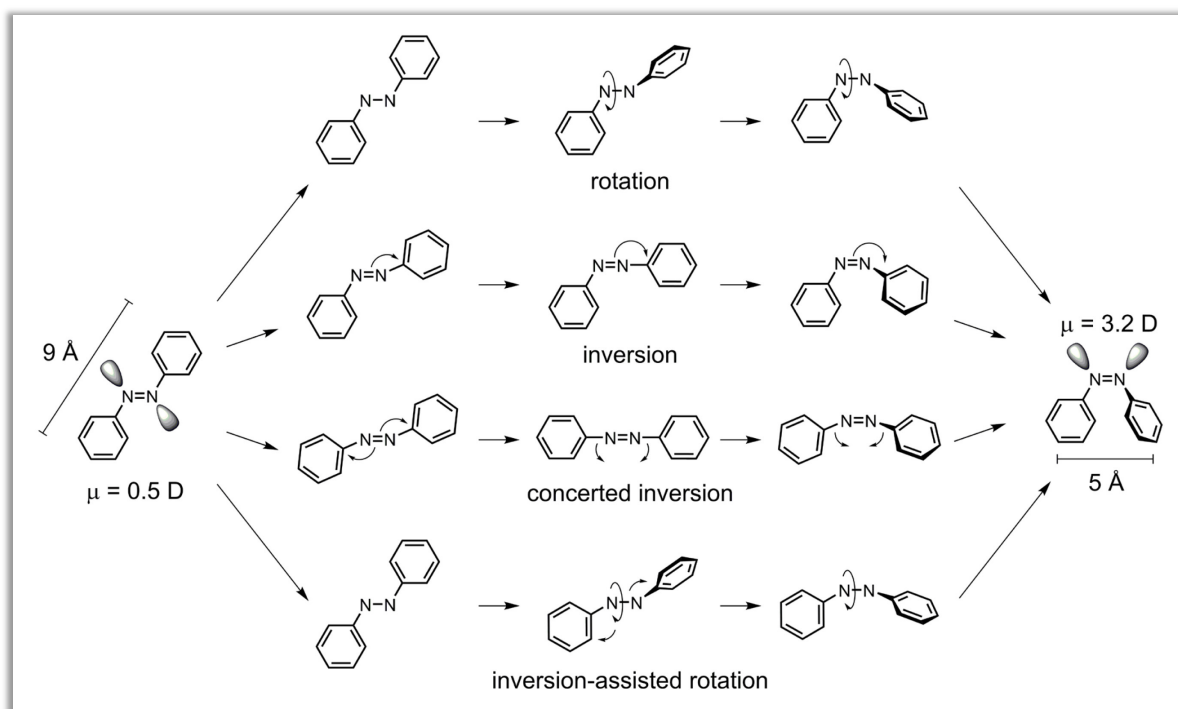


**Figure 45.** Summary of possible mechanisms for photochemically induced (*E*) → (*Z*) isomerisation of azobenzene and the associated change in molecular spatial dimension and dipole moment (adapted from reference 194).

change in geometry of the two isomers of azobenzene implicates pronounced differences in physicochemical properties. Unsubstituted (*E*)-azobenzene is thermodynamically more stable by approximately  $50 \text{ kJ}\cdot\text{mol}^{-1}$ .<sup>[195]</sup> This value, however, can experience large variations upon attachment of functional groups to the phenyl rings. Whereas (*E*)-azobenzene adopts a near planar geometry

with  $C_{2h}$  symmetry and a dipole moment near zero Debye, the (*Z*)-isomer is distinctly non-planar with one phenyl ring rotated out of plane. This leads to  $C_2$  symmetry with repercussions for the dipole moment that increases to three Debye and is associated with enhanced hydrophilicity.<sup>[194,196]</sup> Concurrently, hauling around one half of the molecule to the other side, reduces the distance between the 4 and 4' carbon atoms of the phenyl rings from 9 to 5 Å for (*E*)- and (*Z*)-azobenzene, respectively.

Investigation of azobenzene and its derivatives has elicited thorough understanding of how to influence the switching process and alter absorption maxima. However, the workings behind isomerisation remain elusive. Two mechanisms have been identified to underlie the process: rotation, involving cleavage of the  $\pi$ -bond between the nitrogen atoms, and inversion with all bonds remaining intact. Variations and combinations of these two model concepts are also discussed in literature.<sup>[194,197]</sup> **Figure 45** provides a survey of the debated mechanisms. The nature of the switching event is of interest when considering structures that incorporate azobenzenes as rotation and inversion proceed *via* different molecular motions one of which might be favoured over the other depending on the host system.

Coming back to what Hartley observed well over three quarters of a century ago, the optoelectronic properties of azobenzene and how these vary in the two isomers shall now be examined. As mentioned above, the change in colour upon switching is not as pronounced as in other photochromic molecules. Nevertheless, it can be unequivocally followed in UV-vis spectra that for both isomers show absorption patterns that are overlapping yet distinct. The upcoming discussion will refer to a spectrum not of unsubstituted azobenzene but of 3,3',4,4'-tetrafluoroazobenzene (**Figure 46**). The UV-vis spectrum of the (*E*)-isomer is dominated by three absorption events.

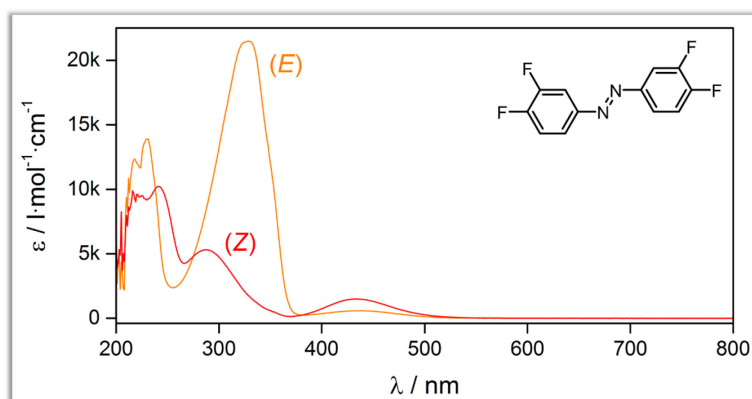


**Figure 46.** UV-vis absorption spectra of 3,3',4,4'-tetrafluoroazobenzene before (*E*) and after (*Z*) illumination with UV light at 366 nm (solvent: dichloromethane,  $c = 5 \cdot 10^{-5} \text{ mol} \cdot \text{l}^{-1}$ ).

At 225 nm, a  $\pi$ - $\pi^*$  transition is excited that is localised at the phenyl rings. At 330 nm, the strongest absorption can be witnessed hailing from a  $\pi$ - $\pi^*$  transition delocalised throughout the molecule. Finally, at 434 nm, a  $n$ - $\pi^*$  transition localised at the central nitrogen atoms takes place.<sup>[198]</sup> After illumination with UV light (366 nm, 260 s), the (*E*)- transforms into the (*Z*)-isomer, which features three absorption events as well but at different wavelength and intensities. In the UV region,

absorption is of lower magnitude and takes place at 230 and 288 nm. Higher absorption intensity can be witnessed in the visible range at 438 nm.

Since absorption properties of a molecule are intimately associated with its electronic properties, substituents at the phenyl rings exert a big influence. As a result, azobenzenes have been categorised into three classes: azobenzenes (AB), aminoazobenzenes (aAB), and pseudostilbenes (pSB). The difference is the kind of substituents and their position at the phenyl rings (**Figure 47**).<sup>[194,199]</sup> AB-type molecules show  $\pi$ - $\pi^*$  and  $n$ - $\pi^*$  transitions sufficiently different in energy

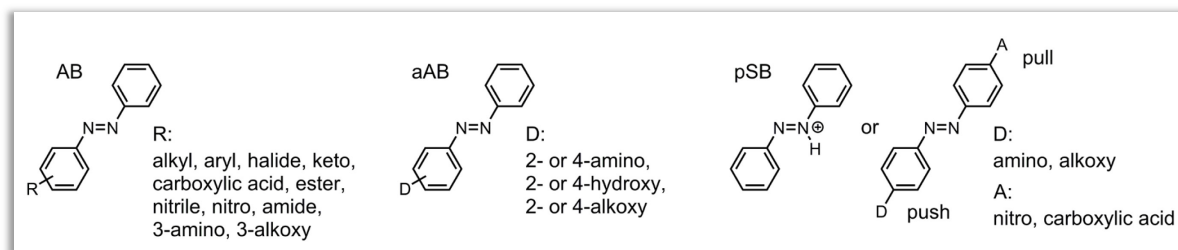


**Figure 47.** Different classes of azobenzenes (adapted from reference 194).

to yield well separated UV-vis bands (*cf.* **Figure 46**), a feature these molecules have in common with unsubstituted azobenzene. On the other hand, electron donating substituents as in aAB-type molecules infuse the system with additional electron density causing the  $\pi$ - $\pi^*$  transition to demand less energy. As a result, it occurs at higher wavelength the corollary of which are overlapping absorption bands for  $\pi$ - $\pi^*$  and  $n$ - $\pi^*$  transition. In push-pull systems realised in pSB-type compounds, the two transitions are nearly degenerate in energy and cannot be distinguished in the UV-vis spectrum.

In summary, isomerisation of azobenzene gives rise to a tremendous geometrical change. This has been exploited to block ion channels,<sup>[200]</sup> shield reactive centres,<sup>[201]</sup> or influence aggregation behaviour of biomolecules.<sup>[202-205]</sup> In addition, molecular machines were designed where the electromagnetic input is transformed into mechanical work conducted by the system.<sup>[206-208]</sup> Drawing on the change in dipole moment, the viscosity of polymers with integrated azobenzene units could be influenced by light stimulus, the so-called photoviscosity effect.<sup>[209-210]</sup>

## DIARYLETHENES

The only class of photochromic molecules that can be expected to catch up with azobenzenes in terms of scientific interest devoted to it is the class of diarylethenes (DAEs). In spite of being extremely intriguing molecules with a vast array of applications DAEs have not been rationally designed in a straightforward approach but were rather “serendipitously discovered during the course of study on photo-responsive polymers a quarter of a century ago” as Masahiro Irie, one of the father of DAEs, frames it in a comprehensive review article.<sup>[193]</sup> According to his account, in an attempt to influence a polymer’s properties by light stimuli, various photoactive molecules have been incorporated into the polymeric structure amongst others stilbene. Stilbene was known to

perform (*E*)/(*Z*) isomerisation upon light exposure in a comparable manner as described earlier for azobenzenes. However, in the presence of oxygen, stilbene reacts further when (*Z*)-configured and undergoes an irreversible annulation reaction under elimination of hydrogen to form phenanthrene, a thermodynamic trap. The scientists then pondered over how to avoid that problem and thought about replacing the hydrogens prone to elimination by methyl groups eventually leading to 2,3-dimesitylbuta-1,3-diene to serve as monomer for a radical 1,4-polymerisation, in the course of which a central C=C double bond is formed. Yet, that monomer could not be synthesised due to the too cumbersome mesitylene groups. For successful synthesis of a suitable monomer steric demand needed to be reduced and mesitylene was replaced by 2,5-dimethylthiophene yielding 2,3-bis(2',5'-dimethylthien-3'-yl)buta-1,3-diene that was successfully polymerised. To the surprise of the researchers, the resulting polymer was not interesting for an (*E*)/(*Z*) conformational change of its constituents but for a photochromic reaction evidenced by a tremendous colour change upon light exposure. More importantly, the colour did not vanish even at 100 °C but only when irradiated with visible light. It was soon figured out that the thiophene units, bridged by a C=C double bond, were responsible for this behaviour.

From the outset it was clear that the exclusive p-type character of DAEs rendered them ideal candidates for optical data storage, a potential application for organic molecules pioneered by Yehuda Hirshberg in the year of 1956.<sup>[211]</sup> In spite of DAEs having been discovered rather accidentally, the rationale behind the nowadays most frequently used structure of diarylethenes

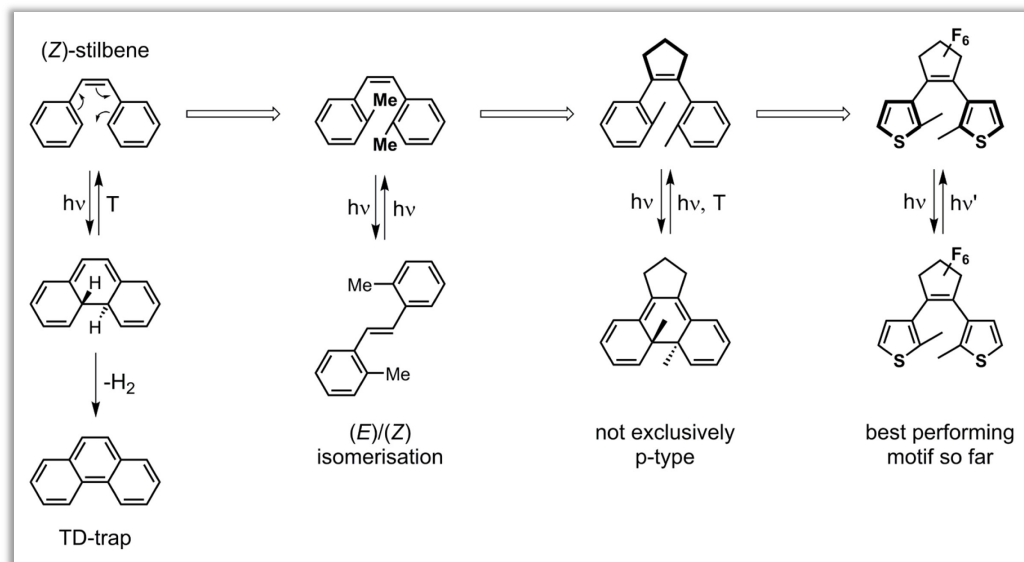


**Figure 48.** Influence of different structural characteristics on the switching behaviour of the molecular unit that eventually evolves into the DAE motif currently used. Newly introduced molecular design elements are shown in bold.

starting from its structural ancestor stilbene is adumbrated in **Figure 48**. Apart from (*E*)/(*Z*) isomerisation, stilbene can also perform a pericyclic ring closing reaction. Methyl groups prevent the molecule from falling into the thermodynamic trap *via* phenanthrene formation. To make ring

closure the only possible reaction triggered by light, (*E*)/(*Z*) isomerisation is forestalled by bridging the ethylene linker between the aromatic rings.

The reason for thienyl groups being a superior choice over phenyl moieties is rooted in the fact that benzene possesses a higher aromatic stabilisation energy than thiophene, the values amounting to 116 and 20 kJ·mol<sup>-1</sup>, respectively. That this is of importance can be fathomed when taking a closer look at the structures at hand to reveal that upon switching, aromaticity in the aromatic moieties is sacrificed to an overall extended conjugation of  $\pi$ -electrons. The higher a molecule's aromatic stabilisation energy, the more it is energetically unfavourable to lose the aromatic state. In other words, phenyl substituents are not eager to undergo a switching process and want to revert to their initial aromatic state. Therefore, the back reaction, cycloreversion, can be triggered thermally for phenyl but not for thienyl groups as the latter do not forego nearly as much energy as the former for ring closure.<sup>[193,212]</sup> Presence of two aromatic units in the structure even doubles the difference.

It was also elaborated on the size of the ring that bridges the ethylene linker and established that ring size controls planarity of the system and therefore the extent of delocalisation of  $\pi$ -electrons.<sup>[213-215]</sup> Six-membered rings were found to exhibit the highest cyclisation quantum yield but in combination with the absorption maximum of the closed ring form, five-membered rings were judged to perform best overall. Perfluorination of the central ring is attributed better spectral splitting between open and closed form as well as improved fatigue resistance.<sup>[191]</sup>

The singular most important structural feature of diarylethenes is an integrated  $\pi$ -electron sextet that endows the system with the capability to perform a cyclisation isomerisation. As such, DAEs adhere to the Woodward-Hoffmann rules for pericyclic reactions stipulating that for a 6  $\pi$ -electron system a ring closing reaction can be induced either thermally when disrotatory or *via* electromagnetic stimulus when conrotatory.<sup>[216]</sup> These two situations presuppose different molecular arrangements as depicted in **Figure 49**. The two thienyl groups in a DAE molecule can

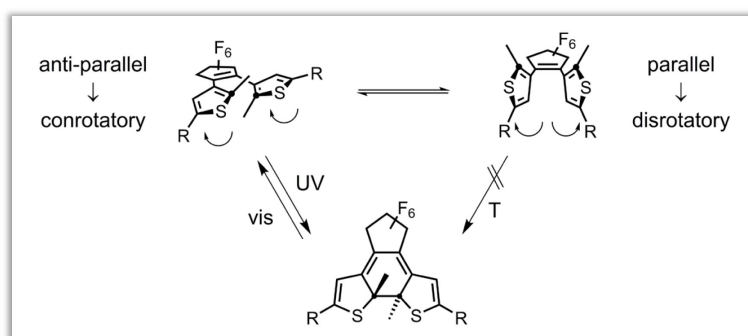


**Figure 49.** The desired photochemical isomerisation can only proceed out of anti-parallel conformation in conrotatory mode. Theoretically, parallel conformation gives rise to disrotatory isomerisation that is induced thermally. Disrotatorily, however, the methyl groups in 2 and 2' position will experience considerable sterical repulsion making this process energetically unfavourable. Reactive carbons are emphasised.

assume parallel or anti-parallel orientation towards each other. Only the anti-parallel conformation yields a conrotatory ring closure and in so doing satisfies the precondition for a light-induced isomerisation. In solution anti-parallel and parallel conformation are in dynamic equilibrium and

generally populated in a 1:1 ratio setting the upper limit of cyclisation quantum yield to 0.5. Consequently in order to increase the quantum yield, strategies have been devised to enhance anti-parallel population such as introduction of bulky substituents or long alkyl chains at reactive carbons 2 and 2', trapping DAEs in cyclodextrin cavities, incorporate DAEs covalently into polymers, introduction of pyridinium cations on both sides to exploit coulomb repulsion,<sup>[217]</sup> bridging of the thienyl rings, and, finally, introduction of intramolecular multiple non-covalent interactions<sup>[218]</sup> all of which have been dealt with in more depth elsewhere.<sup>[193]</sup>

Parallel orientation of the thienyl moieties necessitates these to move disrotatorily. A disrotatory ring closure is in principle allowed and is stimulated by thermal energy. This, however, is not desired, for DAEs to be p-type chromophores they should not show thermally induced reactions but respond exclusively to electromagnetic stimuli. In that regard, the methyl groups at the reactive carbons of the thienyl rings perform two vital tasks. Firstly, they prevent hydrogen elimination from those positions once and for all thereby avoiding the thermodynamic trap mentioned earlier. Secondly, they thwart disrotatory ring closure by inflicting steric repulsion on the system. In disrotatory motion, ground state ( $S_0$ ) orbitals of open (o) and closed (c) form are of the same symmetry thus entitled to interact with each other. However, the ground state orbital of the closed isomer  $S_0(c)$  has a far higher energy already with hydrogen in 2-position. Substituting methyl for hydrogen increases the energy of  $S_0(c)$  even further making it utterly untenable for the system to perform the ring closure in disrotatory fashion.<sup>[212]</sup>

In conrotatory mode a different orbital situation is encountered with  $S_0(o)$  and  $S_0(c)$  closer in energy. More importantly,  $S_0(c)$  is now of different symmetry than  $S_0(o)$  prohibiting direct interaction between these two orbitals. This circumstance exacts a prize from the system to be paid in form of an activation energy barrier that needs to be overcome when performing cycloreversion, *i.e.* ring opening, in ground state, *i.e.* thermally. The electronic ground state sets the stage for thermally induced reactions and the energy barrier in the ground state is the origin of the p-type character of DAEs in preventing ring closing and opening reactions that are induced thermally. However, the system can evade the ground state by resorting to electronically excited states. Those states are the stages of electromagnetically induced reactions. In excited states, orbitals are found that correspond in both symmetry and energy. Thus, ring closure and opening can be achieved by light stimuli, as desired. **Figure 50** provides a succinct account of the orbital situation present in DAEs and is a two-dimensional simplification of the three-dimensional potential energy surfaces described elsewhere.<sup>[219-221]</sup> As mentioned earlier, the energy barrier in ground state  $S_0$  will usually not be overcome at room temperature rendering the system not amenable to thermally induced isomerisation. The open ring isomer can be excited by light into excited state  $S_1$  with a subsequent relaxation of the system to the conical intersection that provides the passage from  $S_1$  to  $S_0$ . The favoured outcome is a relaxation of the molecule to the closed ring isomer's ground state  $S_0(c)$ . Basically, the same is true for cycloreversion but one important difference can be witnessed within the diagram. In  $S_1$  there is an activation barrier on the side of the closed ring isomer. Thus, for cycloreversion to take place, the excited closed ring isomer must overcome an energy barrier in  $S_1$ . This peculiarity sets the cycloreversion process in stronger competition with the relaxation process

to  $S_0(c)$  and makes it dependent on temperature and wavelength with higher conversion rates being achieved by increasing the former and reducing the latter.<sup>[222]</sup> The absence of an energy barrier in  $S_1$  on the side of the open isomer renders the cyclisation process independent from those two factors.

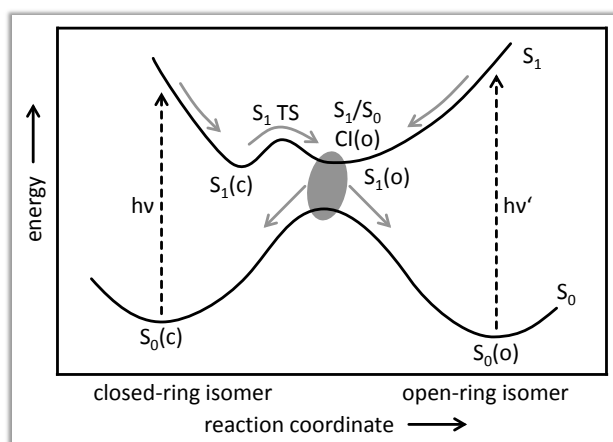


**Figure 50.** Energy diagram for ring closing and ring opening reactions in diarylethenes. Letters o and c in round brackets refer to open and closed isomer, respectively. Furthermore: TS = transition state, CI = conical intersection, and  $h\nu$  = light stimulus. The energy barrier in  $S_0$  prevents the system from performing thermally induced isomerisation. An interesting feature can be found in  $S_1$  with an energy barrier present on the side of the closed ring isomer (adapted from reference 221).

As suggested in **Figure 44**, compared to azobenzenes DAEs show a much more noticeable colour change upon switching, a manifestation of a more comprehensively altered electronic situation. **Figure 51** portrays the influence of switching on UV-vis absorption of a simple DAE derivative in direct juxtaposition with spectra from an azobenzene derivative (cf. **Figure 46**). Extinction coefficients give proof that the compared species absorb light on a similar scale. In open state, DAE shows strong absorption at 242 nm accompanied by minor events at shorter (220 nm) and longer (310 nm) wavelengths. Noticeably, no absorption is recorded within the visible range rendering the molecule colourless. After illumination with UV light (254 nm, 60 s), a striking colour change can be observed

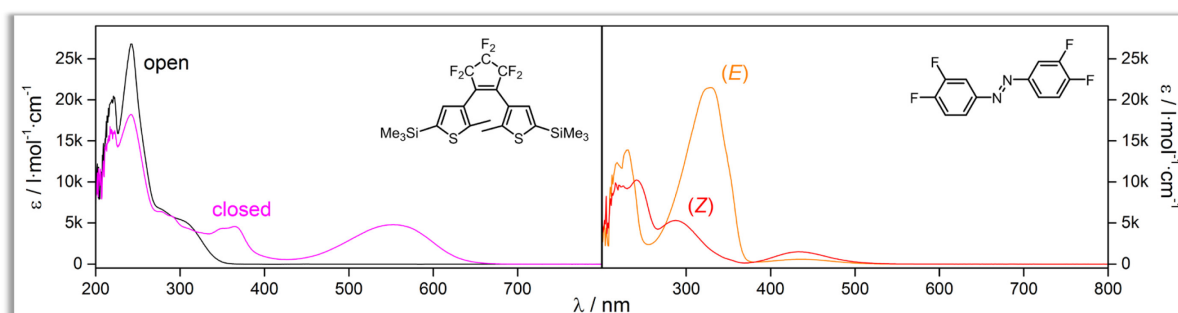


**Figure 51.** UV-vis absorption spectra of DAE 1,2-bis(2'-methyl-5'-trimethylsilylthien-3'-yl)hexafluorocyclopent-1-ene before (open) and after (closed) illumination with UV light at 254 nm (left; solvent: dichloromethane,  $c = 4.29 \cdot 10^{-5} \text{ mol} \cdot \text{l}^{-1}$ ) in comparison with **Figure 46** (right).

with the molecule turning violet. In closed state,  $\pi$ -conjugation is much more pronounced indicative of a narrowed bandgap allowing the molecule to absorb visible light around 553 nm. The UV bands

get somewhat diminished but are still clearly discernible as broad bands at 365 and 285 nm and more resolved signals at 242 and 220 nm.

Another important difference between azobenzenes and diarylethenes is the extent of geometrical change upon isomerisation that in the case of DAEs is comparably small. This forfeits any application in which a certain site needs to be blocked or shielded as described for azobenzenes. On the other hand, that drawback turns into a benefit as the very minor molecular motion occurring during ring closure/opening allows DAEs to perform isomerisation not merely in solution but also in solid state giving rise to single crystals that not only change colour but also, quite exceptionally, macroscopic shape.<sup>[223]</sup> In addition, single crystals of mixed DAE derivatives could be obtained and their constituent species were addressed individually as to allow the system to assume more than two states—typical for contemporary computers—thereby offering exciting prospects for multi-state computational systems with three-dimensional architecture.<sup>[224-225]</sup>

In that regard it is imperative to mention the key subject of fatigue resistance as it is vital for a photo-switch, especially when conceived as data storage device, to perform at least thousands of switching cycles without showing degradation. DAEs are known to irreversibly form by-products, a circumstance that leads to a diminution of photoactive molecules.<sup>[226-232]</sup> However, when appropriately designed with suitable functional groups attached, DAEs can indeed satisfy the requirement for a high number of switching cycles.<sup>[191,233]</sup>

In summary, it can be said that diarylethenes have elicited vast interest in materials chemistry, and rightfully so. Appropriately designed, they meet all demands for an efficient photoswitch: p-type character of both isomers, ring closing and opening cycles can be repeated more than 10,000 times, cyclisation quantum yield is nearly quantitative, cyclisation and cycloreversion take place on a picosecond time scale, and, finally, many DAEs perform isomerisation in solid state. The tremendous change in electronic properties prompted DAEs to serve as light-triggered switches for fluorescence, magnetism, spin state, electrical conductance, acidity/basicity, chemical reactivity proper, and non-covalent intermolecular interactions. Although small, the structural change gave rise to light-triggered switching of crystallinity, affinity for metal deposition, as well as viscosity all of which have been dealt with in more detail elsewhere.<sup>[193]</sup>

## LIGHT-SWITCHABLE MICROPOROUS STRUCTURES

In general, three strategies can be devised to incorporate photochromic molecules in host structures the first of which describes infiltration of a host structure with photo switchable molecules. This approach, however, does not really do justice to the concept of incorporation/integration but simply exploits mixing of two initially separate systems (**Figure 52**).<sup>[234-235]</sup>

The second and more appropriate methodology is to combine the two desired systems during synthesis to ensure covalent binding between them in such a way as to decorate the host structure with photochromic molecules as dangling groups. This approach has been widely employed in several areas of materials chemistry. For example, in 2004 Fernando and co-workers tethered

azobenzenes to polymer backbones not aiming at light-induced changes in porosity but looking for alterations in the polymer's viscosity.<sup>[210]</sup> Zink *et al.* functionalised the inner walls of porous silica with Azos in order to control accessibility of channels.<sup>[236]</sup> In 2009, Stock *et al.* developed a zeolitic imidazolate framework (ZIF) decorated with azobenzenes and although changes in UV-vis spectra were recorded upon switching no apparent change in any other physical property was reported.<sup>[237]</sup> Not so in complementing publications by the same group that described azobenzene tethered to MOFs and demonstrated a change in the latter's crystal structure upon switching.<sup>[238-239]</sup> In 2012, Zhou *et al.* published findings on reversible alteration of carbon dioxide uptake in a MOF functionalised with azobenzene<sup>[240]</sup> and one year later light-induced guest release was demonstrated by Yaghi *et al.*<sup>[241]</sup> Apart from MOFs, organic cages have also been functionalised with azobenzenes and their conformational change was shown to influence gas uptake as well as uptake and release of guest molecules.<sup>[242]</sup> Combining SAM and MOF chemistry, Wöll and co-workers capped a surface-bonded MOF (surMOF) with azobenzenes and used these to open and close the MOF thereby gaining control of light-induced release of adsorbed molecules.<sup>[243]</sup> Another example highlights Azos tethered to amorphous porous organic polymers that Zhang *et al.* designed to observe a change in gas uptake upon switching.<sup>[244]</sup>

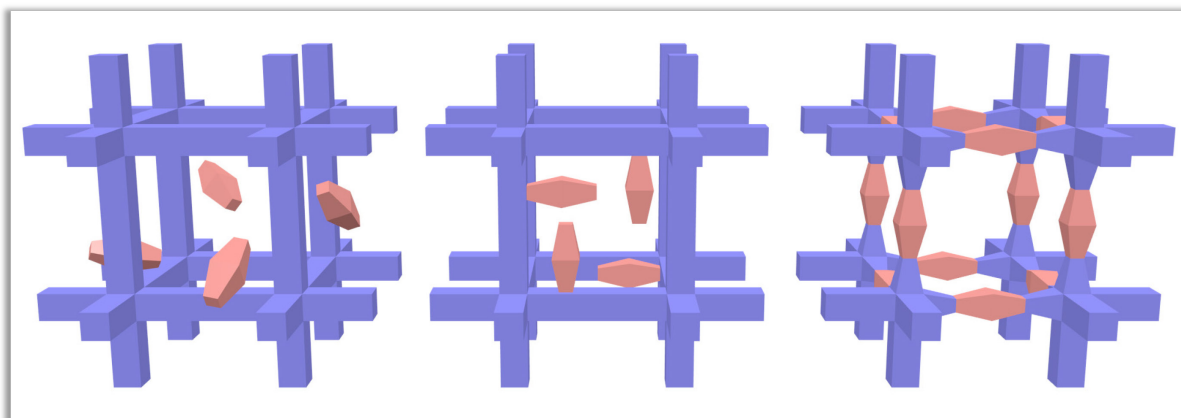


**Figure 52.** Rendering of the three concepts described. The left model shows the concept of mixing photoactive molecules (red bodies) with host compound (blue body). The centre model depicts the dangling group approach where photoactive molecules are covalently bonded to the host system by one side only. The right model portrays the methodology opted for in this work that aimed at comprehensive incorporation of light-responsive molecules into a host structures by two-fold covalent attachment thereby making DAEs or Azos a constituent part of the polymer backbone. The depicted highly ordered arrangement of the host structure does not relate to the systems used in this thesis but serves to facilitate perception.

The third approach comes closest to the concept of incorporation and relies not on tethering photochromic molecules to host structures but their complete covalent or coordinative integration into the backbone thereby making them a constituent part of the overall structure. In the case of azobenzenes the conformational change triggered by light leads to a large geometrical transformation as compared to diarylethenes. This results in the former's employment predominantly as dangling groups within host structures as described above. Conversely, diarylethenes exhibit a far less pronounced change in geometry upon conformational transformation and are

consequently more prominent protagonists of the third strategy. Again, MOFs have been the systems of choice and several studies present changes of the framework properties stimulated by light. For example by integrating a DAE in a MOF in 2014, Shustowa *et al.* showed that fluorescence of the system can be altered by incident light, *i.e.* by switching the DAE moiety.<sup>[245]</sup> In another study, Zhou and co-workers exploit the enhanced conjugation of  $\pi$ -electrons in the closed ring isomer to provide energetic levels lower in energy compared to the open ring isomer.<sup>[246]</sup> This enables formation of singlet oxygen from triplet oxygen upon irradiation with light.

### DAE-POLYMER | 3D

From the strategies delineated above, the third was embarked upon in this work to covalently incorporate light-responsive molecules into the backbone of host structures. Naturally, this concept severely constrains the degree of motional freedom for a built-in molecule and in the light of this azobenzene was ruled out to deliver satisfactory results. DAEs instead do not necessitate large motional freedom to perform isomerisation. For this reason, the envisaged three-dimensional polymer was decided to incorporate in its backbone DAEs rather than azobenzenes.

The geometrical change of DAEs upon isomerisation is negligible as compared to azobenzenes and yet it was expected to have a detectable influence on the structure of the polymer not for a pronounced rearrangement of polymer entities but for a change in stiffness of the backbone. For in open state the two thienyl moieties of a DAE are decoupled both electronically and sterically the latter aspect of which is of importance at this point. As a result, flexibility of the molecule is enhanced and since it is integrated as a linker between stiff nodes this lack of stiffness is passed on to the entire polymeric structure rendering the polymer softer and more prone to space-efficient packing. The expected outcome is a diminution in porosity.

Further reason for the preference of DAE over azobenzene is provided by the latter's ineptitude to perform isomerisation in solid state. The expected three-dimensional polymer decorated with photo switchable moieties will be a solid lacking any solubility. Thus, it is prudent to opt for a photochromic compound that is known to switch in solid state, an established fact for DAEs. That being said, this argument might be restricted right away by the peculiar nature of the envisioned structure. It is a solid indeed but light-responsive entities will be separated by node molecules hence apart from each other with the conceivable outcome that those entities amongst themselves cannot be regarded as solid such as in bulk form. More aptly, they might be considered spatially more isolated from each other as compared to bulk. And this is nothing less than a similar state as is found in solutions, save for intermingled solvent molecules. Hence, in those particular systems in which *e.g.* azobenzenes were interspersed throughout, photochromic molecules can be regarded as 'solidly dissolved or diluted'. However, even if *e.g.* azobenzene molecules did not hamper themselves in the process of switching, they are still covalently incorporated so that molecular motion is impinged by the entire polymeric structure. This might not pose a problem in—preferentially two-dimensional—crystalline systems where all photochromic entities are oriented alike. In this case azobenzenes

could perform isomerisation cooperatively, *i.e.* in the same direction and thus would not cancel out each other's motion. As the envisaged structure is not crystalline but amorphous, it cannot be expected to behave likewise and the fact remains valid that molecular movement is severely affected by the host system. This, of course, holds true for incorporated DAE molecules as well but as described above DAEs do not demand as much motional freedom for isomerisation thus, in the end, justifying their choice over azobenzenes.

Making DAEs an intrinsic part of a polymeric structure can have a beneficial side effect. DAEs can perform light-induced isomerisation only out of anti-parallel (ap) conformation (*cf.* **Figure 49**) and integration into a polymer can not only promote the molecules to adopt ap conformation but also ensnare them in this particular state. However, this cannot be guaranteed since the desired target structure is formed *via* irreversible cross-coupling reactions during which DAEs can be incorporated in parallel (p) conformation as easily. Irreversibility, then, prevents a once built-in p-DAE molecule from being released and subsequently changing its conformation to be reintegrated into the structure in ap-geometry. On the other hand, to conclude this thought, reversibility not necessarily yields a crystalline product exclusively with ap-DAE moieties. This was true only when the crystalline hence thermodynamically most stable product is formed with ap-DAEs. In the instance that incorporation of p-DAEs also gave rise to a crystalline product, competition between two crystalline products sets in. Or, in case integration of only p-DAE formed a crystalline product but that of ap-DAE did not, a structure is obtained that does not contain any light-switchable molecules and therefore embodies the opposite of what was initially intended.

According to the herein developed strategy DAEs are employed as linker molecules between stiff nodes. Bearing in mind that an extension of struts between nodes diminishes overall stiffness of the system and thus permanent porosity,<sup>[134]</sup> the node molecule was required to be of very stiff nature. A suitable candidate for an appropriate node molecule was found in 1,3,5-triethynylbenzene (1,3,5-TEB)—the archetype node motif for CMPs.

CMPs are usually accessible *via* Sonogashira-Hagihara C-C cross-coupling, a reaction scheme that satisfies the crucial demand for a reliable integration of DAE molecules in a defined and predictable way as to obtain an AB-type polymer. In contrast, a reaction protocol that relies on one functional group only such as Yamamoto cross-coupling reaction, commonly employed in the syntheses of PAFs/PPNs, cannot serve this purpose as it will promote reaction preferably between the same type of monomer species. This poses no problem when only one type of monomer is involved as is the case for PPN-4 or PPN-6 but renders this approach useless when more than one monomer species are present. Thus, the ability to form an AB-type polymer in a defined manner offered by Sonogashira-Hagihara cross-coupling reaction is emphasised here.

## RESULTS AND DISCUSSION

## DAE-CMP

The most prominent conjugated microporous polymer, CMP-1, is customarily formed from 1,3,5-triethynylbenzene (1,3,5-TEB) serving as node and 1,4-dihalobenzene functioning as strut or linker with the halogen atom being either bromine or iodine. In this work, a scheme was developed that utilises the same node molecule but substituted the linker molecule with a DAE derivative likewise bearing two functional groups. In this manner, a structure comparable to CMP-1 is envisaged with the additional benefit of incorporated light-switchable moieties that may allow of a structural alteration induced by electromagnetic stimulus. The synthesis of polymer precursors 1,2-bis(5'-iodo-2'-methylthien-3'-yl)hexafluorocyclopent-1-ene **1** and resulting DAE-CMP is outlined in **Figure 53**.

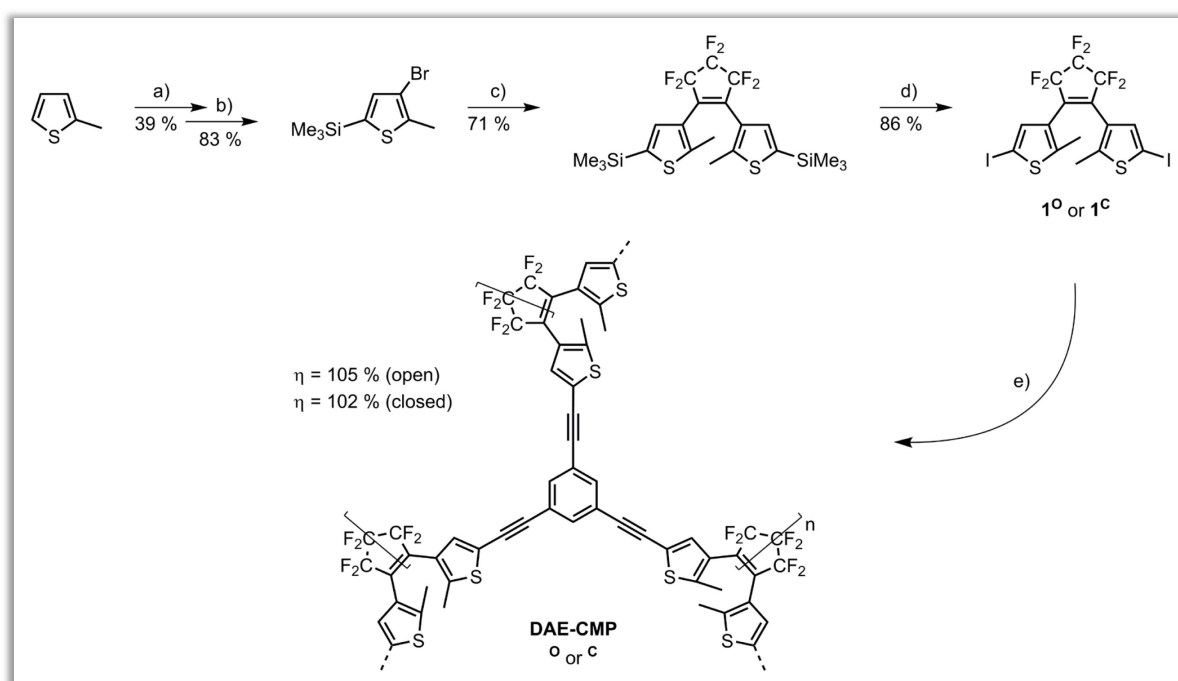


**Figure 53.** Synthesis route to DAE-CMP. a) in glacial acetic acid 2.0 eq. bromine, r.t., 5 h; b) in dry diethyl ether firstly 1.1 eq. *n*-butyllithium, -78 °C, 90 min then 2.5 eq. trimethylsilyl chloride, -78 °C, 90 min, r.t.; c) in dry tetrahydrofuran firstly 1.1 eq. *n*-butyllithium, -78 °C, 2 h then 0.45 eq. octafluorocyclopentene, -78 °C, 4 h; d) in dry chloroform 4.0 eq. iodine monochloride, 0 °C, 4.25 h. Details for DAE-CMP: Syntheses employed the DAE derivative in open (**1<sup>o</sup>**, shown) or closed (**1<sup>c</sup>**) state and 1,3,5-TEB. e) in dry DMF/TEA 0.67 eq. 1,3,5-TEB, 0.05 eq. CuI, 0.03 eq. tetrakis(triphenylphosphine)palladium(0), 100 °C, 18 h. Equivalentents are given with respect to starting material for each step being set to 1.0 eq. Percentage values denote yield for each step.

DAE component **1** was obtained starting from commercially available 2-methylthiophene that was treated with neat bromine to brominate the two most reactive sites at C<sup>3</sup> and C<sup>5</sup>. The next step comprised substitution of trimethylsilyl for bromine at C<sup>5</sup> in order to block that position's higher reactivity in the next stage that involved lithiation at C<sup>3</sup> and subsequent coupling to the bridging unit octafluorocyclopentene. The last step witnessed substitution of trimethylsilyl groups with iodine in order to obtain the appropriate functionality at C<sup>5</sup> of each thienyl moiety.

At the outset of the experiments it was pondered over why literature reports on CMPs reliably describe a 50 % excess of TEB with respect to the dihalobenzene. In order not to lose any valuable DAE monomer it was decided to purify the purchased educt 1,3,5-triethynylbenzene by means of filtration through silica thereby rendering the initially dark brown compound off-white (**Figure A6**). This finding sparked further investigation into the topic of CMP formation and the underlying mechanism and elicited a deeper understanding of these subjects.<sup>[41]</sup> Purified 1,3,5-TEB was then employed in a Sonogashira-Hagihara cross-coupling reaction together with the bifunctionalised DAE derivative in an equimolar amount with respect to functional groups. The incorporation of DAE moieties into CMP-like architectures was anticipated to endow the system with light responsiveness. In amorphous materials such as CMPs molecular entities are assembled in a disordered manner, a corollary of the irreversible nature of the cross-coupling reaction. Two implications arise from that. Firstly, a DAE molecule in open state can be built into the structure in parallel conformation, which in turn renders that moiety unreceptive to electromagnetic stimuli. Secondly, an open DAE molecule that is attached in anti-parallel conformation might be fixed by adjacent TEB units in a geometrical arrangement that prevents the two reactive carbons from approaching each other in order to perform photochemical isomerisation. Contrariwise, starting from a closed DAE isomer as monomer draws a different picture. A closed DAE has not remotely as many possible orientations in which to be incorporated into the network. As a stiff unit it compels the other network forming entities to arrange in a certain way. As a result, if the closed DAE is indeed built into the structure, it will constitute a rigid linker between two nodes. As cycloreversion does not demand any favourable orientation of molecular units, quite contrary to cyclisation, ring opening is attributed a much higher likelihood of occurrence than ring closure. Moreover, the influence that a closed, hence stiff DAE strut exerts on the orientation of other monomers will most probably not be sufficiently strong to completely alleviate the structural strain that is characteristic for a network formed by kinetically governed irreversible reaction schemes. Therefore, it is reasonable to assume that DAE units that are incorporated in closed state experience at least some strain inflicted by the network. That strain can be regarded as driving force for cycloreversion as the opening of the ring leads to assuaged stress due to higher degrees of freedom for molecular motion within the DAE entity. However, it must be pointed out that when a strained DAE is opened the stress will be relieved through reorganisation of the two thienyl moieties, very likely leading to a molecular arrangement that is detrimental to a succeeding ring closure.

Two sets of experiments were carried out. The first accords with the scheme in **Figure 53**, presenting a DAE derivative in open state. The second differs only in that it employs the DAE derivative in closed state. It has to be kept in mind, though, that one result of the ring closure is an altered electronic situation. Aromaticity of the thienyl moieties is sacrificed for an enhanced conjugation of  $\pi$ -electrons. Hence, in a closed DAE the iodine bearing carbon atoms cannot anymore be regarded as constituents of an aromatic thiophene system with possible repercussions for reactivity at these sites.

Nevertheless, quantitative yields were obtained for both protocols suggesting that the polymerisations went unimpaired. Both products were obtained as black insoluble solids. The colour

of the products cannot easily be explained. The precursor molecules were off-white 1,3,5-TEB and either colourless open DAE  $1^{\circ}$  or violet closed DAE  $1^{\text{c}}$ . The products were washed and Soxhlet extracted according to standard CMP procedure and the yields of just slightly more than 100 % bespeak little to no impurity ensnared within the final material. Typically, an extension of  $\pi$ -electron conjugation is accompanied by a narrowing of the band gap, that is to say the energy difference between the frontier orbitals HOMO and LUMO. This leads to the absorption of light of lower energy, often lying within the visible range of the electromagnetic spectrum which in turn lends a certain colour to the compound. Albeit labelled *conjugated* microporous polymers, CMPs usually do not show conjugation of  $\pi$ -electrons beyond the nodes. CMP-1, for example, exhibits conjugation only between two nodes thence it assumes a pattern of cross-conjugation. It is enough, though, to lend a pale ochre hue to CMP-1. Substituting DAE for phenyl as strut between two nodes gives rise to two different situations. In open state the thienyl units in a DAE can be treated as electronically isolated from each other. Thus, conjugation length in a CMP incorporating open DAE (DAE $^{\circ}$ -CMP) is restricted from one node to the nearest thienyl unit of a strut. The other thienyl ring of the same strut is already part of the next conjugation entity reaching to the next node (**Figure 54**). In a closed DAE-CMP (DAE $^{\text{c}}$ -CMP) the two thienyl units are electronically coupled and the entire strut is in conjugation with two nodes, one to each side. The bandgap of DAE $^{\text{c}}$ -CMP is expected to be

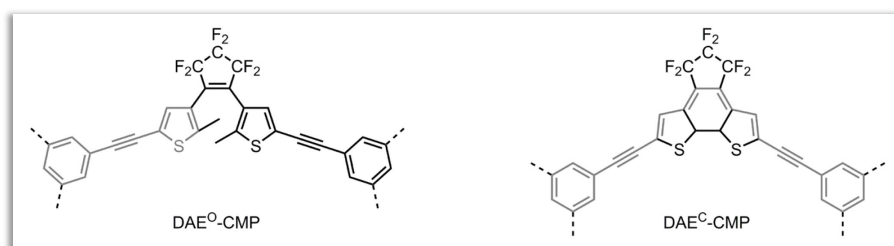


**Figure 54.** Sketch of fragments from DAE-CMPs showing different states of the strut-forming DAE moiety. Conjugation length is depicted in grey. Superscripts  $^{\circ}$  and  $^{\text{c}}$  refer to open and closed, respectively.

more narrow than that of DAE $^{\circ}$ -CMP resulting in two different colours of the overall networks. This holds true especially when considering that monomer  $1^{\text{c}}$  has a very distinct violet colour whereas  $1^{\circ}$  is colourless.

As mentioned, the two obtained polymers were of similar appearance, black. This outcome is unexpected if not for the ‘colour’ itself, which is hard to predict, then for the fact that DAE $^{\circ}$ -CMP and DAE $^{\text{c}}$ -CMP show no difference. Further investigation is warranted for example by conducting molecular calculations of the energy levels actually present in the introduced compounds.

The chemical composition of the obtained polymers was probed by virtue of elemental analysis. Experimentally obtained values accord reasonably well with theoretical figures (found for DAE $^{\circ}$ -CMP; found for DAE $^{\text{c}}$ -CMP) for  $\text{C}_{34.5}\text{H}_{15}\text{F}_9\text{S}_3$  in m-%: C 59.48 (61.61; 62.21), H 2.17 (3.26; 3.05), S 13.81 (12.15; 12.59), N 0.00 (1.20; 1.03). Apparently, both samples contain nitrogen that it is plausible to assume to hail from residual DMF and TEA that was employed during synthesis.

NMR analysis confirms successful incorporation of precursor building blocks into the final network. Signals related to ethynyl carbons, contributed by 1,3,5-TEB, are found in the spectrum of

DAE-CMP at around 90 ppm (**Figure 55**). Likewise, a signal at 12.4 ppm testifies the presence of methyl groups (♥), constituent parts of the DAE moiety. In the aromatic region the signal at 142.3 ppm can be assigned to  $sp^2$  hybridised  $C^{2,2'}$  in the thienyl units (•). The peak at 133.3 ppm has contributions from the thienyl carbons connected to the bridging unit (◊) as well as the

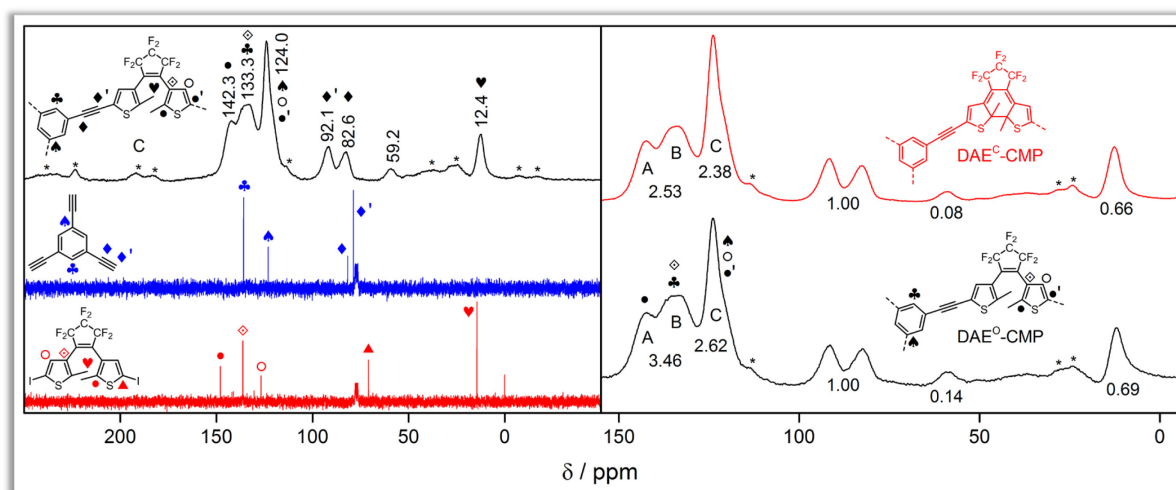


**Figure 55.** Liquid phase  $^{13}\text{C}\{^1\text{H}\}$  NMR spectra ( $\text{CDCl}_3$ , 50 MHz) of educts  $\mathbf{1}^{\text{O}}$  (left red) and 1,3,5-TEB (left blue) in comparison with solid state  $^{13}\text{C}\{^1\text{H}\}$  CP/MAS NMR spectrum ( $\nu_{\text{rot}} = 10$  kHz, spinning sidebands are marked with an asterisk) of obtained  $\text{DAE}^{\text{O}}$ -CMP (left black) and the latter in comparison with the spectrum obtained for  $\text{DAE}^{\text{C}}$ -CMP (right black and red, respectively). Solvent signals in the liquid phase spectra at 77 ppm are apodised for clarity. In the spectrum for  $\mathbf{1}^{\text{O}}$  the signal at 0 ppm originates from TMS used as stabiliser in deuterated chloroform. The numbers beneath each graph on the right-hand side denote relative integral values with respect to the integrals of the alkyne signals that were set to 1.00.

unsubstituted carbon of the benzene node (♣). At 124 ppm the most intense signal is observed with contributions from the ethynyl-substituted carbon of the benzene node (♠), the unsubstituted (○) and ethynyl substituted (•) carbon of the thienyl moieties. Notably, no signal is recorded for a carbon in a terminal, *i.e.* unsubstituted ethynyl group. Such a signal is expected at around 79 ppm (*cf.* **Figure 25**) and can clearly be witnessed in the liquid state NMR of 1,3,5-TEB (♦). Conversely, a new signal emerges at 92.1 ppm (♦') signifying successful substitution of a DAE unit for hydrogen. The absence of a signal from a terminal alkyne hints at a quantitative reaction, which is in line with the observed high yield. It should be noted that carbons of the octafluorocyclopenteny bridge do usually not produce observable signals.

The origin of the signal at 59.2 ppm is a matter of debate. It is not caused by unreacted, hence still iodine-functionalised carbon atoms because that kind of signal can be witnessed in the liquid state NMR of  $\mathbf{1}^{\text{O}}$  at 70.9 ppm (▲) thus distinctly more low-field. A possible source for the signal at 59.2 ppm is the methyl substituted carbon of the thienyl unit in a specific state. In open state, the methyl bearing carbon atoms of the thienyl units ( $C^{2,2'}$ ) are  $sp^2$ -hybridised and part of an aromatic entity thus spawning signals in the aromatic region at 142.3 ppm (•). During cyclisation those carbons change hybridisation from  $sp^2$  to  $sp^3$  with a concomitant change in chemical shift to a value of around 50 to 60 ppm, in good agreement with the observed signal. The question as to if

cyclisation actually took place during synthesis and why it may have could not be answered in the course of the investigations.

The comparison in **Figure 55** shows a difference between the carbon solid state NMR spectra of DAE<sup>O</sup>-CMP and DAE<sup>C</sup>-CMP. The relative value for the combined integrals under signals A and B is considerably higher for DAE<sup>O</sup>-CMP. The same is true for the area under signal C but not as much. Likewise, the integrals under the signal at 59.2 ppm, ascribed to sp<sup>3</sup> C<sup>2,2'</sup> of thienyl, and the peak at 12.4 ppm (♥) are slightly higher in DAE<sup>O</sup>-CMP. The higher value for the combined area under A and B can only be attributed to the DAE linker entities because integration was referenced to ethynyl signals. The ratio between ethynyl and benzene carbons is fixed since both are constituents of the same molecule. Thus, every difference in the integrals must be ascribed to DAE units because an alteration in benzene entities will inevitably be reflected in the value for ethynyl units. That change, however, is deliberately suppressed by normalising the integration to the ethynyl carbons. Now, signals A and B represent thienyl carbon C<sup>2,2'</sup> (●), C<sup>4,4'</sup> (○), and a benzene carbon (♣). As delineated above, a different value for the integral can only be effected by DAE-related carbons C<sup>2,2'</sup> and C<sup>4,4'</sup>. Amongst these two carbons only C<sup>2,2'</sup> can experience a dramatic shift in chemical environment, during cyclisation. The higher value for the area under signals A and B can thus be traced to a higher content of open ring DAE linker. However, this reasoning falls short of explaining the observed relative values for the area under the signal at 59.2 ppm that is assigned to sp<sup>3</sup>, *i.e.* closed ring C<sup>2,2'</sup>. A diminution in relative amount of sp<sup>2</sup>, *i.e.* open ring C<sup>2,2'</sup> has to take place for the benefit of sp<sup>3</sup> C<sup>2,2'</sup> implying that when the area under signals A and B decreases, the signal at 59.2 ppm should become more pronounced as a result. This is not the case. Quite contrarily, that signal is less intense in DAE<sup>C</sup>-CMP as compared to DAE<sup>O</sup>-CMP.

Alternatively, in the light of reduced integrative values for virtually all DAE-related signals in DAE<sup>C</sup>-CMP as compared to DAE<sup>O</sup>-CMP it could also be argued that the overall ratio of linker (DAE) to node (TEB) is smaller in the former. This, however, is hard to fathom when keeping in mind that the reaction protocols for both DAE<sup>O</sup>-CMP and DAE<sup>C</sup>-CMP utilised stoichiometric amounts reflecting a one to one ratio of the functional groups ethynyl and iodine. Moreover, elemental analysis does not deliver proof to substantiate that assumption and displays elemental compositions for the two discussed materials that match each other reasonably well thus attests neither a significantly higher 1,3,5-TEB content.

To ascertain whether the obtained polymers exhibit permanent porosity, nitrogen sorption experiments were carried out and a striking difference between DAE<sup>O</sup>-CMP and DAE<sup>C</sup>-CMP was disclosed. The two states of the DAE linker should precipitate very different patterns of structural integrity. For in open state the two thienyl rings are decoupled not only electronically but also sterically. As a result, they can move and rotate independently from each other but, of course, only to the extent granted by the host structure and the methyl groups at C<sup>2,2'</sup>. Giving credit to the vast amount of linker molecules throughout the material there is every reason to assume a much more flexible and less stiff structure for DAE<sup>O</sup>-CMP as compared to DAE<sup>C</sup>-CMP. That lack of stiffness in the linker entities of the entire polymeric fabric can be expected to translate into diminished permanent

porosity. Consequently, DAE<sup>C</sup>-CMP, incorporating the closed DAE isomer, is expected to display noticeably augmented permanent porosity due to a much more rigid network.

The obtained results corroborate this contemplation and show higher nitrogen uptake for DAE<sup>C</sup>-CMP yielding a  $S_{\text{ABET}}$  of  $487 \text{ m}^2 \cdot \text{g}^{-1}$  as compared to  $278 \text{ m}^2 \cdot \text{g}^{-1}$  found for DAE<sup>O</sup>-CMP (**Figure 56**). Apparently, both materials span structures sufficiently rigid to generate permanent porosity. This can primarily be attributed to the inflexible nature of the node 1,3,5-TEB. Placing linkers between these nodes that themselves show little to no flexibility—a scenario realised in DAE<sup>C</sup>-CMP—heightens the overall stiffness of the entire structure thereby spanning more pores. Pore size distribution reveals microporosity as dominant pore size domain with only minor differences between the examined specimens. A significant difference can be found in the pore volume that

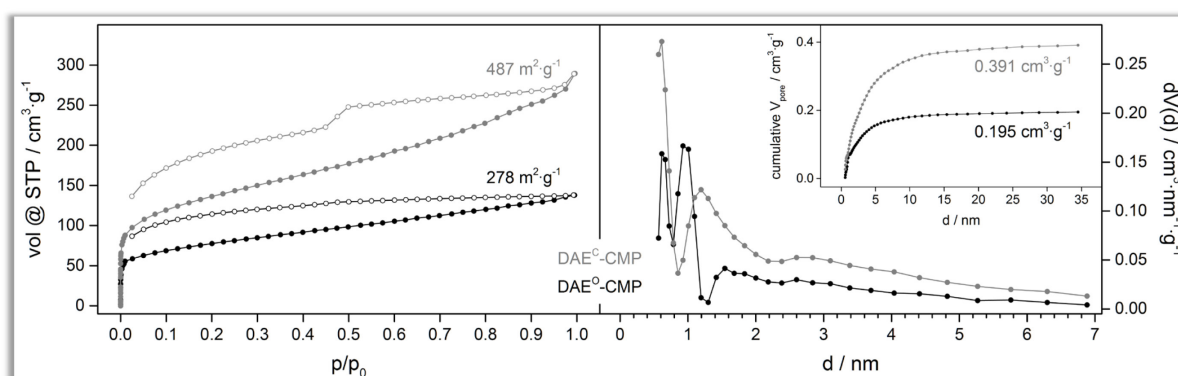


**Figure 56.** Isotherms derived from nitrogen sorption at 77 K (left, solid symbols: adsorption, empty symbols: desorption) and graphs derived from QSDFT for both PSD (right, main) and cumulative pore volume (right, inset) for DAE<sup>O</sup>-CMP (black graphs) and DAE<sup>C</sup>-CMP (grey graphs).

amounts to  $0.195$  and  $0.391 \text{ cm}^3 \cdot \text{g}^{-1}$  for DAE<sup>O</sup>-CMP and DAE<sup>C</sup>-CMP, respectively. The latter value being nearly double as high as the former supports the idea of a more extended pore system built up in the material that employed in its construction the closed ring isomer of the DAE and is in line with the recorded higher surface area. The adsorption branches of both samples show a distinct uptake at low relative pressures until an easily identifiable ‘knee’ can be observed. Thence both isotherms exhibit a steady positive slope that is higher for DAE<sup>C</sup>-CMP, which, in addition, shows a slightly enhanced uptake towards saturation pressure. A distinct difference becomes obvious during desorption. Both samples show hysteresis down to low relative pressures. However, hysteresis of DAE<sup>O</sup>-CMP is nearly featureless over the entire range probed except for a very subtle step at a relative pressure of 0.45. A very noticeable step, meanwhile, can be witnessed in DAE<sup>C</sup>-CMP at relative pressure of 0.50 indicative of the presence of mesopores. The fairly prominent step in the isotherm of DAE<sup>C</sup>-CMP is caused by a higher contribution from mesopores as compared to DAE<sup>O</sup>-CMP. This can be witnessed in the PSD in **Figure 56** (full-range in **Figure A7**) derived from quenched solid density functional theory (QSDFT) calculations.

In summary, NMR suggests that polymerisation went not as desired whereas nitrogen sorption clearly displays a marked difference between DAE<sup>O</sup>-CMP and DAE<sup>C</sup>-CMP. For this reason, the

obtained materials were tested to elicit whether or not it is possible to capitalise on the uniqueness of incorporated photo-responsive building blocks.

As described earlier,  $\text{DAE}^{\text{O}}\text{-CMP}$  and  $\text{DAE}^{\text{C}}\text{-CMP}$  are of very similar colour. This could be substantiated by means of solid state UV-vis reflectance investigations, which give rise to reflectance profiles that differ only to a small extent (**Figure 57**). For an increased contrast the compounds were blended with barium sulphate that provides for an immaculate white background. The seemingly

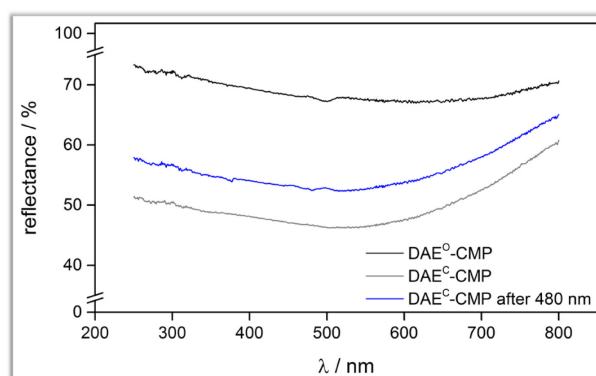


**Figure 57.** Solid state UV-vis reflectance spectra of DAE-CMPs synthesised either by employing  $\mathbf{1}^{\text{O}}$  or  $\mathbf{1}^{\text{C}}$ .

higher reflectance of  $\text{DAE}^{\text{O}}\text{-CMP}$  is not meaningful as this can arise from differences in sample packing with barium sulphate. Dissimilarities in the profile, on the other hand, are of more importance but clearly observed can be next to none other than a small bump pointing to lower reflectance values at around 500 nm in the spectrum for  $\text{DAE}^{\text{O}}\text{-CMP}$  (black line) that is absent from the graph for  $\text{DAE}^{\text{C}}\text{-CMP}$  (grey line). As outlined above, between cyclisation and cycloreversion the latter is accorded a higher probability of occurrence in the systems under discussion. For this reason, first isomerisation experiments were conducted on  $\text{DAE}^{\text{C}}\text{-CMP}$ . The sample holder was placed in a light beam at 480 nm to induce cycloreversion. Despite illumination proceeded for 60 min at high intensity, it spawned only subtle differences in the spectrum and the obtained graph (blue line) resembled the spectrum of  $\text{DAE}^{\text{C}}\text{-CMP}$  (grey line) rather than assuming the profile of the graph from  $\text{DAE}^{\text{O}}\text{-CMP}$  (black line). At around 500 nm a small bump is produced after illumination that is not visible in the grey graph but it points to higher reflectance values in contrast to the bump in the black graph that points in the opposite direction. Overall, solid state UV-vis reflectance experiments do not give any conclusive hint that cycloreversion could be triggered.

Nitrogen sorption confirms that illumination did not yield a considerably altered system as surface area as well as pore size distribution along with cumulative pore volume do not show significant differences (**Figure 58**). Full range PSD concurs with this assessment and characterises the two graphs as nearly congruent at least in the mesopore domain (see Appendix **Figure A8**). After illumination, surface area drops from 487 to 482  $\text{m}^2\cdot\text{g}^{-1}$  and pore volume from 0.391 to 0.365  $\text{cm}^3\cdot\text{g}^{-1}$ . Slight changes within the micropore region of the PSD can be observed with a reduced contribution to overall pore volume by pores the size around 0.6 and 1.2 nm whereas pores of sizes in between are more prominently present in the illuminated sample.

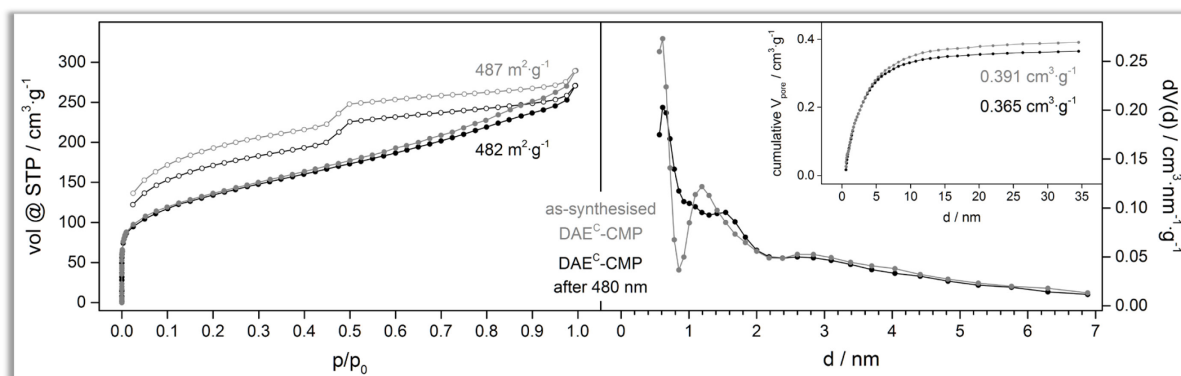


**Figure 58.** Isotherms derived from nitrogen sorption at 77 K (left, solid symbols: adsorption, empty symbols: desorption) and graphs derived from QSDFT for both PSD (right, main) and cumulative pore volume (right, inset) for DAE<sup>C</sup>-CMP (grey graphs) and DAE<sup>C</sup>-CMP after illumination (black graphs).

## CONCLUSION

Comprehensive covalent incorporation of diarylethenes in a three-dimensional CMP host structure was successful. Elemental analysis and NMR confirm the chemical composition of the obtained networks, which were produced in quantitative yields. This demonstrates the feasibility of the presented approach in terms of synthesising DAE containing three-dimensional microporous networks.

On the other hand, the main feature of light responsiveness especially with an eye towards reversible electromagnetically induced alteration of porous properties could not be observed to any satisfactory extent. There are several reasons as to why the anticipated outcome might have been thwarted. Firstly, the obtained materials were insoluble, a circumstance that, on the one hand, proves that polymerisation did proceed well while otherwise poses problems in terms of accessibility of structural entities to incident light. Only those parts of the material can be expected to respond to light that are exposed to it, *i.e.* parts that rest at the surface of the polymer particles. Those surface located regions accommodate only a minor part of the overall material making it questionable whether a sufficiently large portion of the polymer has undergone isomerisation as to trigger a detectable change in its porous properties.

Another reason that particularly applies to the case of DAE-CMP can be found in the architecture of the node-forming entities. In DAE-CMP a 1,3,5-TEB unit is surrounded by three DAE moieties. The nodal benzene ring does not establish a straight conjugation of  $\pi$ -electrons across one node but rather describes a pattern of cross-conjugation. Still, DAE units are electronically connected to each other to some extent. Ko and co-workers synthesised a star-shaped 1,3,5-triethynylbenzene molecule with one DAE attached to each triple bond.<sup>[247]</sup> Their attempts to obtain the all-closed (cc) isomer were to no avail other than was the case for a compound different only in that it incorporated vinyl rather than ethynyl groups as linkage between benzene and DAE. The molecule adopting the double bond layout can be switched from ooo to ooc, occ, and ccc. Conversely, the triple bond layout allowed only of switching from ooo to ooc and occ. Theoretical investigations by

Perrier, Jacquemin and co-workers explained why this is the case and analysed the frontier and energetically contiguous orbitals.<sup>[248-249]</sup> It was revealed that in the cco isomer the shapes of LUMO, LUMO+1, and LUMO+3 for the vinyl based structure are similar to those of their respective counterparts in the ethynyl based motif but that these orbitals contribute to differing degrees to the transition events in each molecule. In both cases LUMO+3 was identified to be the photochromic orbital, *i.e.* it shows bonding character and is located at the remaining open DAE fragment thus responsible for a potential final isomerisation to the respective ccc isomer. However, whereas this orbital contributes substantially to the transition event in the 1,3,5-trivinylbenzene based structure, transitions in the 1,3,5-triethynylbenzene based motif are devoid of any significant contribution from that very orbital and take place in molecular orbitals that are not located at the remaining open DAE moiety.

Even so, in an extended three-dimensional network it is sensible to consider two out of three switching events sufficient to effect a structural change that results in altered gas sorption properties. Moreover, the pattern of molecular orbitals in an isolated 1,3,5-triethynylbenzene molecule bearing three DAEs is probably different from that in an extended network that basically consists of that unit.

Another line of argument has at its core the nature of the polymerisation reaction. The employed reaction protocol utilised an irreversible reaction scheme governed by kinetics. As a consequence, DAE molecules that are incorporated in parallel (p) conformation, thus unresponsive to light stimuli, will retain this orientation of thienyl rings under all circumstances. Irreversibility prevents built-in units to be released and adopt anti-parallel conformation before being reintegrated into the network. On the other hand, what seems to speak in favour of reversible reactions yielding crystalline products, which have not been pursued in this work, must be subjected to scrutiny, too. Reversible reactions do provide the opportunity to release and reincorporate network-forming entities multiple times indeed. However, as long as there is no driving force for the ap-conformer of a DAE to be built in more prevalently a blend will be obtained containing both ap- and p-DAEs to similar extents. Only if the thermodynamically more stable compound is formed by incorporation of ap-DAEs, a corresponding framework will be obtained in which all DAEs are responsive to light.

Apart from the impossibility of release and reintegration of monomer entities during polymerisation, irreversibility, moreover, leads to amorphous materials. The disordered arrangement of struts and nodes, can also be imagined to foil switching events by cancelling out motions executed by individual DAE units. Although DAEs, provided they are incorporated in ap-conformation, do not demand a large degree of motional freedom to perform cyclisation it is at least conceivable that a DAE that rotates partially to undergo cyclisation is hindered in doing so by random network movement triggered by other DAE struts moving likewise to achieve the same. However, as this takes place in a setting of complete randomness of molecular arrangement it could equally be contended that a DAE is actually helped by arbitrary network movement for the same reason. Eventually, in an amorphous network with statistically arranged struts and nodes both support for and obstruction of a cyclisation event by random network movement can be argued for.

In the light of the intricacies connected with an amorphous network formed by irreversible polymerisation reactions, a prospective endeavour deals with the incorporation of DAEs into covalent organic frameworks (COFs). These are crystalline all-organic frameworks formed from reversible condensation reactions. An ordered arrangement of building blocks in a repetitive fashion can assist successful switching of DAEs because all molecules are oriented alike and will move in the same direction at the same time with no countervailing force being exerted by other light-responsive units. As a result, DAEs shall be free to perform cyclisation. Yet, this course of events can more easily be pictured in a two- rather than a three-dimensional setting the former of which is found in COF-1 or COF-5 where two-dimensional sheets stack to form a porous structure.<sup>[32]</sup> This type of architecture, when appropriately designed, might even allow of azobenzenes to be integrated and perform (*E*)/(*Z*) isomerisation prompting profound changes in the geometry of the host system.

### DAE AND AZO-POLYMERS | 1D

The high degree of cross-linking in polymers that are interconnected in a three-dimensional manner such as the aforesaid system DAE-CMP has certain detrimental ramifications the most crucial of which is insolubility of these kinds of materials. Not only are analytics severely circumscribed but also is the prospect of processability next to non-existent.

For these reasons, a different molecular architecture was framed that relies on polymers of intrinsic microporosity (PIMs).<sup>[31]</sup> Those are one-dimensional polymers evolving from reactions of monomers at least one of which must exhibit a structural kink that frustrates space-efficient packing of polymer chains (*cf.* **Figure 3**), inevitably leading to the formation of void space between those chains thereby creating pores. The one-dimensional pattern of interconnection allows PIMs to be soluble in common organic solvents hence to be processed into films or membranes. That aside, solubility opens up the prospect of addressing every single light-responsive moiety within the polymer when illuminated in dissolved state or in solid state when a transparent film or membrane is obtained.

Moreover, the severe restrictions imposed upon motional freedom of light-responsive entities in systems such as DAE-CMP do not apply in the case of materials derived from PIMs. Consequently, not only diarylethenes but also azobenzenes are suitable candidates to be incorporated into these types of polymers.

Two molecular designs have been devised, one utilising DAEs, the other Azos as light-responsive constituents. The former will hereafter be referred to as DAE-PIM whereas the latter will be designated Azo-PIM.

## RESULTS AND DISCUSSION

DAE-PIM <sup>[250]</sup>

As mentioned previously, DAEs do perform only a subtle geometrical change during isomerisation. When incorporated into the backbone of a PIM that minor alteration is expected to wield a detectable influence on the entire DAE-PIM chain more precisely on its ability to adopt a more or less contorted conformation.

The target structure was designed as to exhibit an alternating AB pattern of building blocks. For this reason, Suzuki cross-coupling reaction was opted for to form the desired DAE-PIM (**Figure 59**).

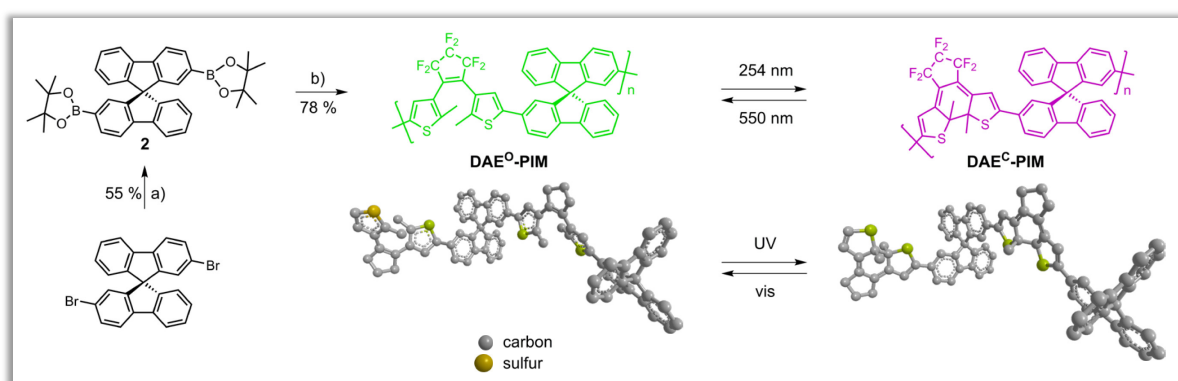


**Figure 59.** Synthesis route to DAE-PIM and isomerisation thereof. a) in dry 1,4-dioxane 2.2 eq. bis(pinacolato)diboron, 0.1 eq. 1,1'-bis(diphenylphosphino)ferrocene, 1,1'-bis(diphenylphosphino)ferrocene palladium(II)dichloride, 6.0 eq. potassium acetate, reflux, 17 h; b) in DMF/THF 1.0 eq. **1<sup>O</sup>**, 0.05 eq. tetrakis(triphenylphosphine)palladium(0), 3.85 eq. potassium carbonate, 120 °C, 20 h. Equivalents are given with respect to starting material in each step being set to 1.0 eq. 3D representations illustrate the change in the structure in DAE-PIM upon isomerisation. A detail of two repeating units is shown. Hydrogen and fluorine atoms are omitted for clarity.

Commercially available spirobifluorene bearing one bromine functionality at each fluorenyl unit was employed to guarantee that the kink of the molecule is conveyed to the entire polymer structure. By virtue of Miyaura borylation the spiro compound was functionalised with boronic ester functionalities (**2**) applicable to ensuing Suzuki cross-coupling reaction with iodinated DAE monomer **1<sup>O</sup>**. The obtained product, which is superbly soluble in THF, did not precipitate but stayed in solution and was isolated and purified by repeated precipitation from methanol. When precipitated, DAE-PIM was obtained as green powder. Conversely, when evaporated from THF the same compound formed films of very brittle nature and intense green colour (**Figure A10**). Investigations by gel permeation chromatography (GPC, polystyrene standard) revealed a molecular weight of 7179 g·mol<sup>-1</sup>, corresponding to a polymerisation degree of  $n \approx 11$ . These relatively low values are presumably responsible for the observed fragility of the films. The polydispersity index (PDI) of 3.1 is comparable to the value reported for PIM-1 and other PIMs.<sup>[31]</sup>

Elemental analysis showed discrepancies between theoretical and experimental values: calculated (found) for C<sub>40</sub>H<sub>22</sub>F<sub>6</sub>S<sub>2</sub> in m-%: C 70.58 (63.55), H 3.26 (3.95), S 9.42 (7.55), N 0.00 (0.27).

The presence of chains of differing lengths in combination with an expected presence of end groups on either type of monomer leads to deviations from the theoretical values.

NMR analysis disclosed the expected signals with sixteen protons to be found in the aromatic and six in the aliphatic region. To study the influence of isomerisation on the chemical environment within the molecule, the NMR sample solution was irradiated with either UV or visible light and spectra were recorded at different stages of the isomerisation process. In this way, it was established that isomerisation sets in motion reversible alterations within the molecule's electronic structure that are not confined to the DAE moieties but transcend well into the spiro motif evidenced by an evolution of all the signals for aromatic protons. The aliphatic region accommodates the methyl signals from the DAE and gives proof of proceeding isomerisation by the diminution of the signal at 1.77 ppm accompanied by the emergence of a new signal at 1.96 ppm (**Figure 60**). At

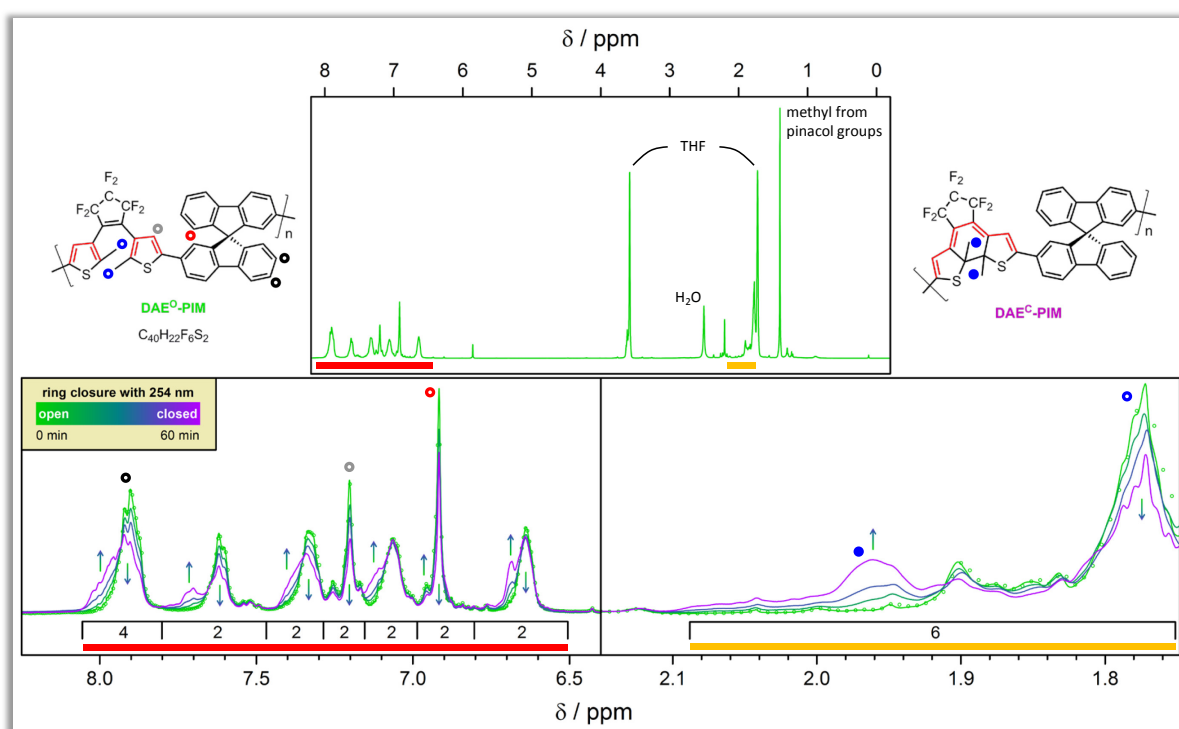


**Figure 60.** Proton NMR spectra (THF-D<sub>8</sub>, 400 MHz) of DAE<sup>0</sup>-PIM. Top plot shows initial spectrum of DAE<sup>0</sup>-PIM. Bottom plots show magnifications of the aromatic (left) and the aliphatic (right) region. During illumination with UV light, that is to say during cyclisation, the change in chemical environment can clearly be traced in the spectral evolution. After a total of 60 min of illumination time with UV light the sample was irradiated with visible light (550 nm) for 5 min and the initial spectrum (hollow circles) could be reobtained. The numbers below the signals denote the relative integral area under the respective range.

1.40 ppm an intense signal is observed that can only be explained by a rather prominent presence of methyl groups from the pinacol ester. Additional NMR studies utilising diffusion-ordered spectroscopy (DOSY) showed that the protons at 1.40 ppm have a higher mobility than both the aromatic and the DAE-methyl protons. DOSY calculates only one mobility value for each type of protons as the mean value of all mobilities, *i.e.* protons that show different mobilities, present at a

certain chemical shift. As a result, the observed protons at 1.40 ppm can hail from both loose monomer present in the sample as well as end groups of DAE-PIM chains.

Successful introduction of photochromism was revealed by UV-vis experiments conducted in solution and solid state. The obtained spectra from investigation of the dissolved compound and corresponding photographs of the solution in different states of illumination are presented in **Figure 61**. The data clearly show a change in absorption upon irradiation at 254 nm. Initially, DAE units are open and conjugation of  $\pi$ -electrons is mainly confined to the thienyl rings. As a result, nearly no absorption in the visible range is observed except for a slight absorption from 400 to 500 nm rendering the bulk compound green. DAE<sup>0</sup>-PIM does absorb in the UV region with a maximum at 337 nm accompanied by a shoulder and a minor absorption at 285 nm. Upon irradiation at 254 nm the solution turns from green to blue. This change is seen in the UV-vis spectra

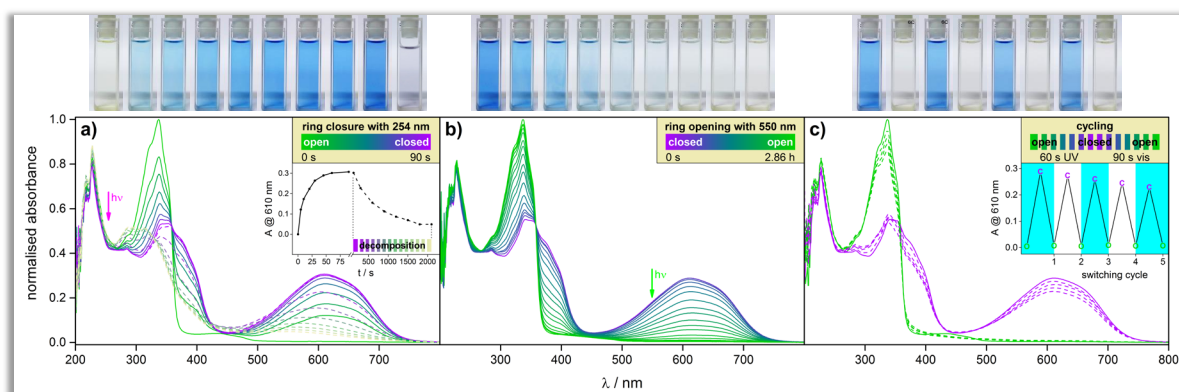


**Figure 61.** UV vis absorbance spectral evolution of DAE PIM in dissolved state (dichloromethane,  $c = 4 \cdot 10^{-5} \text{ mol} \cdot \text{l}^{-1}$ ) during illumination with 254 nm (a), 550 nm (b), and alternating exposure to either UV or visible light for cycling experiments (c). Note that for the ring opening process (b) visible light of much lower intensity was used than for the cycling experiment (c) yielding the difference in exposure time of 2.86 h as compared to only 90 s. In the insets in a) and c) focus is set on the intensity of absorbance at 610 nm.

with the emergence of a new band at 610 nm and a concomitant decrease of the bands at 285 and 337 nm. The appearance of strong absorption in the visible range is triggered by a narrowing of the molecule's bandgap induced by an augmented conjugation of  $\pi$ -electrons upon cyclisation. Noteworthy, a photo-stationary-state could not be detected. Instead, a loss of absorbance (dashed lines in **Figure 61** and inset) as well as a deviation from the isosbestic point at 358 nm is observed after irradiation times of more than 90 s, hinting at decomposition and/or side reaction induced by sustained UV irradiation. For this reason, a time of 60 s was used for irradiation with UV light in further UV-vis related experiments in solution as absorption at 610 nm reached its apex after this time already. The discussed colour change from green to blue upon irradiation with UV light could be reversed under illumination with visible light applying a wavelength of 550 nm. **Figure 61** shows the decrease in intensity of the band at 610 nm with a parallel increase of the bands at 285 and 337 nm thereby regenerating the state prior to UV illumination. Cycling experiments showed that the photo-induced switching between open and closed state is reversible, even though after five

cycles the intensity of the band at 610 nm reached only 80 % of the initial value (**Figure 61** and inset).

To verify whether DAE's capability to perform isomerisation in solid state is retained in DAE-PIM UV-vis transmission measurements were conducted on a drop-cast film. Indeed, the initially green film turns violet upon UV irradiation and reverts to its erstwhile appearance after illumination at 550 nm (**Figure 62**). Switching in the solid state was not only observed in a drop-cast *i.e.* evaporated sample, but also in the powders obtained *via* precipitation from methanol (**Figure A9**).

Importantly, when DAE<sup>C</sup>-PIM was stored in the dark at room temperature no reversion to the open isomer was observed as evinced by the intense blue colour that was retained even after weeks of storage. This behaviour confirms the p-type character of DAEs and was also observed in other systems that are related to MOFs.<sup>[235,251]</sup>

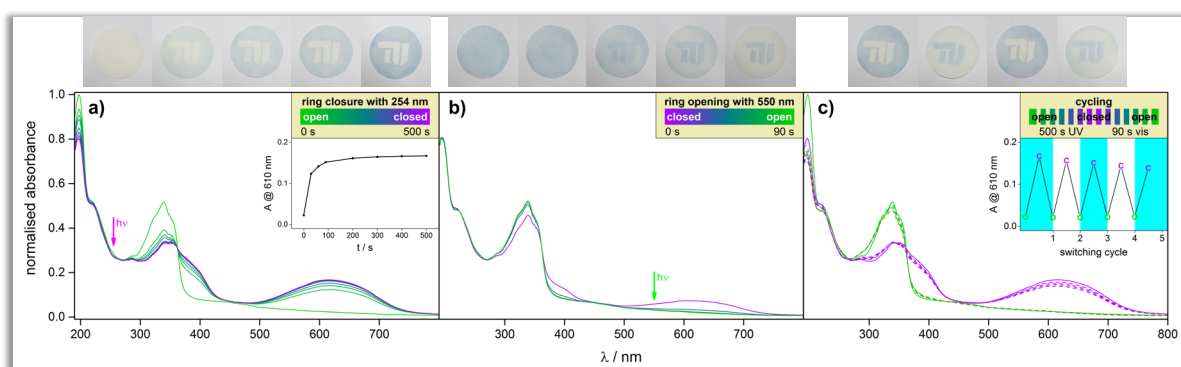


**Figure 62.** UV-vis absorbance spectral evolution of DAE-PIM in solid state during illumination with 254 nm (a), 550 nm (b) and alternating exposure to either UV or visible light for cycling experiments (c). In the insets in a) and c) focus is set on the intensity of absorbance at 610 nm.

UV-measurements on DAE-PIM in solid state indicate considerable and reversible light-triggered conversion between the open and closed state. Moreover, it can be observed that degradation of DAE moieties within the PIM is at least retarded in the solid state as compared to the polymer in solution. An investigation into the conversion rate of DAE-PIM by virtue of NMR analysis was considered unreliable as the polymeric character of the system leads to NMR signals of pronouncedly broad shape thus impeding any such inquiry (*cf.* **Figure 60**).

It has to be noted that the employed wavelength of 254 nm to induce cyclisation is not ideally suited due to its propensity to induce degradation for reasons discussed below in the concluding paragraph to this topic. Quite frequently, less hard wavelength such as 313 or 365 nm are employed to trigger cyclisation in DAEs. However, certain restrictions in terms of available equipment made it much more feasible to utilise 254 nm. This work was based on and designed as a proof of concept, a circumstance underlined by the DAE-derivative employed in this study that makes no pretensions to be fatigue resistant due to the lack of any substituents that could suppress degradation.

Porosity of DAE-PIM was investigated by means of nitrogen sorption. DAE-PIM is non-porous as film in both open and closed state (**Figure A10**). Contrarily, it shows permanent porosity when

precipitated as powder exhibiting a  $SA_{\text{BET}}$  of  $395 \text{ m}^2 \cdot \text{g}^{-1}$  for  $\text{DAE}^{\text{O}}$ -PIM. After  $\text{DAE}$ -PIM has been demonstrated to be photochromic it was of interest whether porous characteristics can be influenced by light stimulus. To minimise any unsolicited influence by externalities such as precipitation procedure  $\text{DAE}^{\text{O}}$ -PIM was switched in solid state as powder obtained *via* precipitation from methanol. UV irradiation clearly effects a change in colour of the material giving proof of proceeding isomerisation (**Figure A9**). Nitrogen sorption of the as-switched sample indeed bespeaks a distinctly altered situation with a decrease in  $SA_{\text{BET}}$  as well as a different shape of the isotherm.  $SA_{\text{BET}}$  drops from  $395$  to  $168 \text{ m}^2 \cdot \text{g}^{-1}$  for  $\text{DAE}^{\text{O}}$ -PIM and  $\text{DAE}^{\text{C}}$ -PIM, respectively (**Figure 63**). After illumination with visible light to trigger cycloreversion and regain the initial state the sample did assume its former colour and  $SA_{\text{BET}}$  did rise to  $245 \text{ m}^2 \cdot \text{g}^{-1}$ , less than the initially measured value for the open state but substantially more than the figure recorded for the closed state. It was thus shown that illumination with UV light to induce cyclisation results in a decrease in surface area that can, at least partially, be reverted by cycloreversion triggered by irradiation with visible light. That after cycloreversion  $SA_{\text{BET}}$  does not reach the value of initially measured  $\text{DAE}^{\text{O}}$ -PIM might be ascribed to degradation of  $\text{DAE}$  moieties that already took place and forestalls more comprehensive cycloreversion. The obtained isotherm for the precipitated sample shows an unusually sharp uptake of nitrogen in the region below relative pressures of  $0.1$ . As for amorphous PIMs no accumulation of

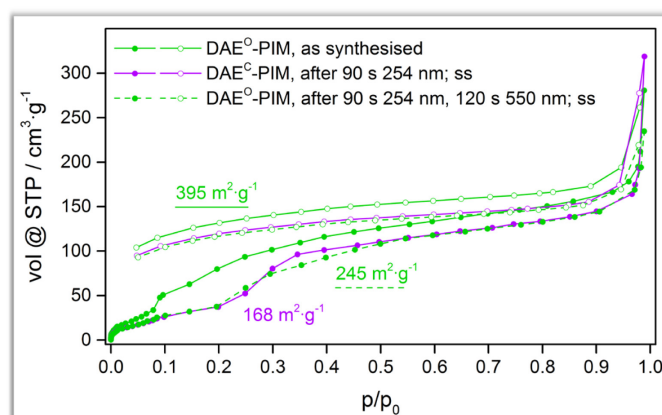


**Figure 63.** Isotherms derived from nitrogen sorption at 77 K. Plotted are isotherms from  $\text{DAE}^{\text{O}}$ -PIM (green, solid line),  $\text{DAE}^{\text{C}}$ -PIM (purple line) and  $\text{DAE}^{\text{O}}$ -PIM after reopening (green, dashed line). Switching was conducted in solid state (ss). Solid symbols: adsorption, empty symbols: desorption.

micropores with defined diameters in this region can be expected, this increase in uptake might be an intrinsic feature of the molecular structure of the compound possibly caused by a gate-pressure effect that opens up the structure thereby enhancing nitrogen uptake capacity.<sup>[252-253]</sup> The initial assumption that this bend in the isotherm might be caused by residual helium inside the pores, which is used for the calibration of the cells, could be dispelled. Measurements with pre-calibrated cells during which no helium gets in contact with the sample yielded similar results.

The reasoning for the observed decrease in  $SA_{\text{BET}}$  after cyclisation emanates from the nature of porosity prevalent in PIMs. In contrast to (micro)porous organic networks in which porosity is created within each individual polymeric (macro)molecule by a spanning of pores by highly cross-

linked struts and nodes,<sup>[15,59]</sup> PIMs can exhibit porosity only when several individual chains congregate in a space-inefficient fashion. Therefore the stiff but kinked structure of PIMs is of crucial importance for the observed inefficient chain packing and consequently determines the percolated free volume accessible to nitrogen *i.e.* microporosity of the polymer in the dry state. It was revealed that already subtle changes in the flexibility or degree of contortion of the backbone structure of PIMs can have a large influence on the finally observed porosity.<sup>[254]</sup>

Even though DAEs do not perform a large geometrical change during either cyclisation or cycloreversion, the molecule still adopts a rigid and essentially planar structure in the closed state but a slightly bent geometry in the open form. Multiplied by each repeating unit of the chain a higher degree of contortion within a polymer chain can be expected when all DEA moieties are existent in their open form, which in turn should yield a less space-efficient packing that leads to more free volume/interstitial space between the chains and thus higher  $SA_{\text{BET}}$  values.

That this material is extremely sensitive to structural changes is emphasised by the fact that, after the powder has been illuminated for 90 s at 254 nm, the conversion rate amounts to 5 % when compared to the maximal achievable conversion as evidenced by UV-vis studies (**Figure A11**).

Apart from surface area, it was examined whether gas diffusivity and permeability can be switched by light stimulus. Owing to its low molecular weight, DAE-PIM does not form a free-standing membrane on its own. However, as the compound is well soluble in various common solvents it was possible to form a composite in conjunction with Matrimid (MI), a commercially available polyimide that is commonly used in gas separation membranes (**Figure A12**). Membranes were prepared from a chloroform solution containing both polymers yielding a DAE-PIM@MI composite that consists of 5 wt% of DAE-PIM.

It was first necessary to verify whether or not DAE-PIM performs cyclisation when incorporated in the Matrimid matrix. **Figure 64** shows UV-vis transmission spectra for DAE-PIM@MI confirming that DAE-PIM does switch inside the membrane, which assumes distinct colours for the open and closed form in the process. The green curve depicts the spectrum obtained for the composite as-blended. It seems that it contains  $\text{DAE}^{\text{C}}$ -PIM to a certain extent evidenced by the band at 600 nm.

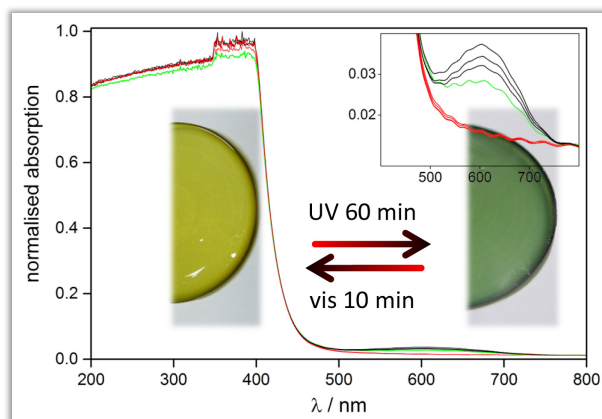


**Figure 64.** UV-vis transmission spectra for DAE-PIM@MI superimposed onto photographs of the composite in either open (left, light green) or closed (right, dark green) state.

Initial illumination was performed using visible light (550 nm) to diminish the intensity of that band and reach a steady state of DAE<sup>O</sup>-PIM@MI. Subsequently, the composite was irradiated with UV (254 nm) and visible light in an alternating fashion to conduct cycling experiments. The prolonged illumination time with UV light has to be accounted for by the applied, weak, light source (lamp for thin layer chromatography (tlc), 6 W) as well as the fact that Matrimid absorbs UV light to a considerable extent thereby drastically reducing the amount of light available to DAE-PIM inside the composite. The inset in **Figure 64** shows that although absorbance after UV cycles is lower than for the first run it stays approximately the same after that.

Diffusion coefficients (D) for oxygen and carbon dioxide were measured for DAE-PIM@MI after alternating UV and visible light illumination as well as for pure Matrimid as reference (**Figure 65**).

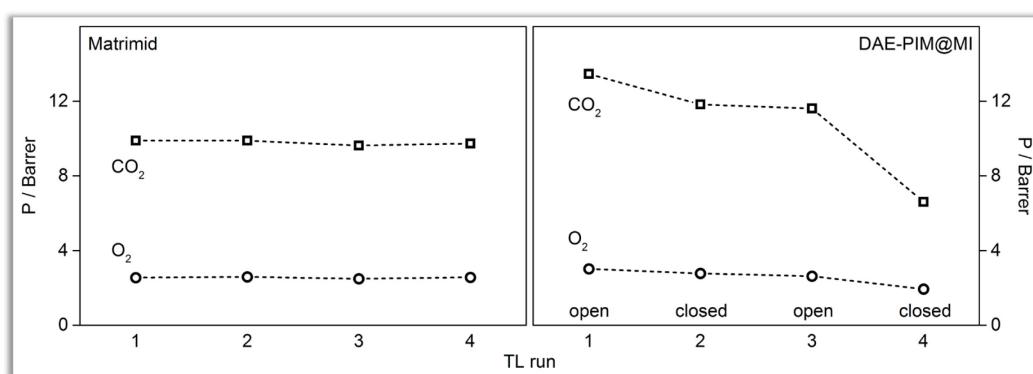


**Figure 65.** Diffusion coefficient for oxygen (circles) and carbon dioxide (squares) at 35 °C and 10 bar of pure Matrimid (left) and DAE-PIM@MI (right) for subsequent measurements in between which the composite was switched by light.

Generally, diffusion coefficients for oxygen are higher than for carbon dioxide in pure Matrimid as well as in DAE-PIM@MI membranes. This can be attributed to the kinetic or effective diameter of the gas molecules that is smaller for oxygen.<sup>[255-256]</sup> Incorporation of DAE-PIM into Matrimid leads to a slight increase in D of approximately 10 % for both oxygen and carbon dioxide. With time and an increasing number of measurements, diffusion coefficients decrease in both pure Matrimid and the composite, a manifestation of physical ageing occurring in both systems. Nonetheless, it is evident that isomerisation of DAE-PIM@MI by light stimuli has a significant influence on the diffusion coefficient of the membrane. Switching to the closed form lowers D whereas cycloreversion results in an enhancement thereof. The process can be repeated and a zigzag pattern of D can be observed with DAE<sup>O</sup>-PIM@MI exhibiting higher values than DAE<sup>C</sup>-PIM@MI.

A comparable trend is observed for the permeability of oxygen and carbon dioxide within the membranes (**Figure A13**).

## CONCLUSION

The presented results show that the light-responsive properties of diarylethenes can be transferred to a polymer of intrinsic microporosity by coupling of DAE and spirobifluorene monomers. Resulting DAE<sup>0</sup>-PIM exhibits permanent porosity with a surface area of nearly 400 m<sup>2</sup>·g<sup>-1</sup>. The polymer is soluble and isomerisation of DAE moieties could be witnessed by means of UV-vis transmission and NMR spectroscopy. Moreover, it was proven that cyclisation and cycloreversion of the DAE moieties occur in solid state, *i.e.* in films or powders of DAE-PIM. For DAE-PIM powders surface area could be altered upon isomerisation showing a decrease after cyclisation and an increase after cycloreversion. Furthermore, in combination with Matrimid a gas-permeable membrane containing DAE-PIM as light-responsive component can be formed and the properties of the membrane—most importantly the diffusion coefficient—can be switched by external light stimuli.

The proof of concept presented in here is a promising approach towards light-switchable membranes, in which diffusion and permeability of gases can be controlled by an external and non-destructive stimulus in a reversible manner. Such a system offers the benefit of circumventing the accumulation of chemical waste as is encountered in chemically switched set-ups *via* acid/base chemistry, for instance. Moreover, switching by light can be achieved over spatial distances; a circumstance that potentially provides for enhanced latitude in the construction of a respective system because the trigger—the light source—does not have to be installed in the nearest proximity of the membrane.

As the switching process is accompanied by a conspicuous colour change systems can be envisioned that exploit the colour of the membrane to determine its current state and adjust its gas separation performance accordingly. This concept is adumbrated in **Figure 66**. In one state (green) the membrane displays low permeability for incoming gas. Irradiation with an appropriate wavelength triggers isomerisation that leads to an altered permeability displayed by the other state (blueish). Thanks to the colour change the light source for switching can be connected to a detector. The latter activates or otherwise controls the lamp depending on the current state of the membrane. It can very well be feasible to not only use the two extreme states—completely open and completely closed in this case—but also conditions in between.

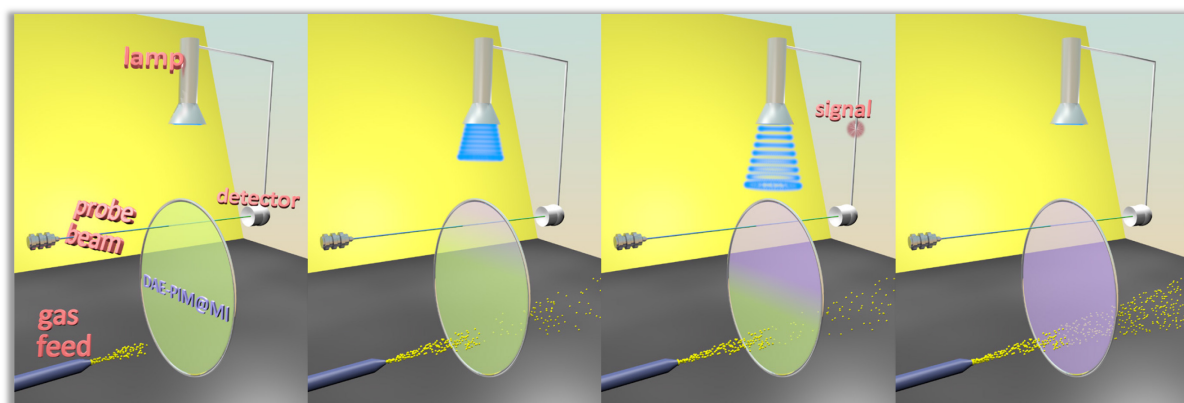


**Figure 66.** Graphical abstract outlining the concept of the application of a photo-switchable membrane.

Naturally, for this concept to work in a reliable fashion the issue of fatigue resistance has to be addressed and a DAE-monomer must be synthesised that shows no or negligible degradation upon UV irradiation. The here applied DAE derivative is certainly not optimised evidenced by the lack of any substituents that could suppress fatigue such as methyl groups in 4 and 4' position of the thienyl rings or substitution of C<sup>4</sup> with hetero atoms, approaches that have proven to be potent strategies. These and other aspects have been investigated by many groups and improvements in fatigue resistance has made great progress over the last years.<sup>[233]</sup> Additionally, the employed wavelength of 254 nm to trigger cyclisation is relatively short and it is known that such short wavelengths can lead to pronounced degradation for several reasons such as reduced penetration depth of incident light, higher spatial concentration of excited states, and a higher variety of reaction pathways that lead to by-products.<sup>[226,257]</sup> Future work has to focus on the two issues of molecular design of the DAE moiety and the utilisation of longer wavelengths such as 313 or 365 nm.

### Azo-PIM

Azobenzenes were not deemed suitable candidates to be incorporated into three-dimensional systems such as CMPs the main obstacle being the large geometrical change performed during isomerisation. However, with the utilisation of PIMs a completely new situation is encountered. Owing to their one-dimensional connection pattern PIMs are anticipated to tolerate large movements of their molecular entities.

As a result, a PIM was conceived that incorporates an azobenzene derivative as linker molecule between nodal moieties exhibiting a kink in their structure in order to generate porosity. Commercially available 5,5',6,6'-tetrahydroxy-3,3,3',3'-tetramethyl-1,1'-spirobiindane was reacted with azobenzene derivative **3**. A two-fold condensation reaction per repeating unit ensures a firm connection between linker and node leading to the formation of Azo-PIM (**Figure 67**). Formally released hydrogen fluoride is scavenged by potassium carbonate. Dissolution of all components did occur not before the reaction temperature reached 65 °C. In the course of the reaction only little

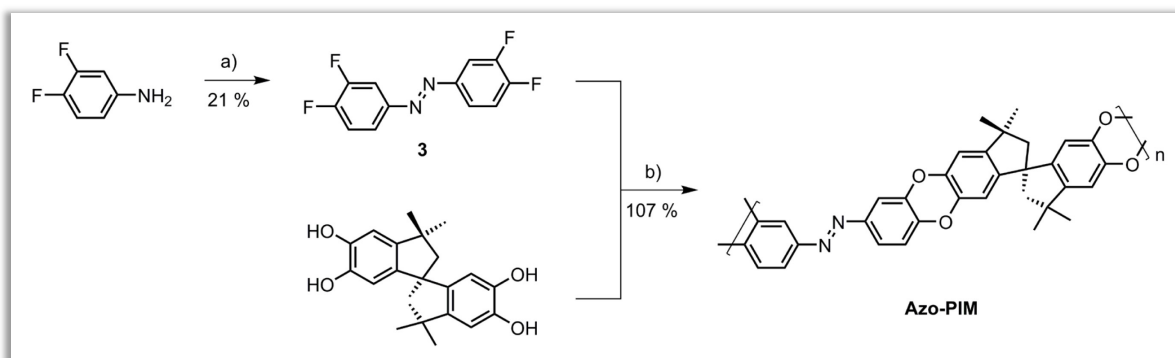


**Figure 67.** Synthesis route to Azo-PIM. a) in H<sub>2</sub>O/EtOH 1.0 eq. 3,4-difluoroaniline, 1.8 eq. potassium hydroxide, 8.0 eq. potassium hexacyanoferrate(III), reflux, 20 h; b) in dry DMF 1.0 eq. **3**, 1.0 eq. spirobiindane, 8.0 eq. potassium carbonate, 65 °C, 24 h.

precipitation was observed. The product did precipitate eventually as yellow to orange powder when the reaction batch was poured into a mixture of ice and methanol. It was observed that reaction times of 48 h yield a product that is hardly soluble. Therefore, a reaction time of 24 h was employed in order to obtain Azo-PIM with very good solubility in THF. The compound was purified by repeated precipitation from methanol. Whereas precipitation yields a powder, Azo-PIM forms an intensely coloured film of orange hue when the solvent is removed by evaporation (**Figure A14**).

GPC (polystyrene standard) revealed a molecular weight for Azo-PIM of  $9456 \text{ g}\cdot\text{mol}^{-1}$ , translating into a polymerisation degree of  $n \approx 18$ ; a figure that together with a PDI of 2.2 testifies that Azo-PIM consists of chains that are both longer and more monodisperse in length as compared to DAE-PIM with values of 11 and 3.1 for  $n$  and PDI, respectively. The enhanced chain length is expected to be responsible for the diminished fragility of the films formed by Azo-PIM, which are not remotely as brittle as is observed for DAE-PIM and stick rather firmly to the glass wall.

Elemental analysis showed good conformity of theoretical with experimental values: calculated (found) for  $\text{C}_{33}\text{H}_{26}\text{N}_2\text{O}_4$  in m-%: C 77.03 (73.71), H 5.09 (5.52), N 5.44 (4.67).

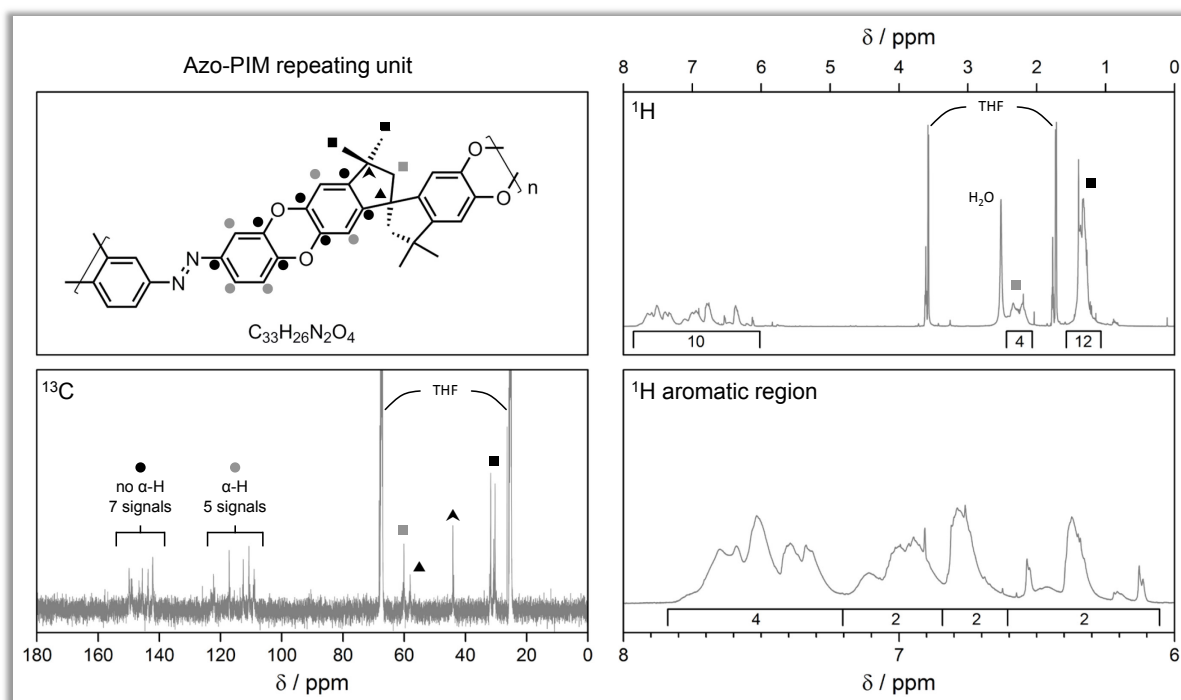


**Figure 68.** Proton (THF-D8, 500 MHz) and carbon (THF-D8, 126 MHz) NMR spectra of Azo-PIM.

Proton NMR confirms the presence of all expected hydrogens with ten hydrogens to be found in the aromatic region, four around 2.26 ppm hailing from the methylene fragments of the cyclopentane moiety, and another twelve around 1.33 ppm originating from the four methyl groups.

Carbon NMR gives rise to twelve signals in the aromatic region. According to DEPT and HSQC measurements, seven of these hail from carbon atoms that bear no hydrogen and the other five from carbon atoms with hydrogen attached. Further signals at 60.1, 58.1, and 44.1 ppm can be assigned to the methylene fragments of the cyclopentane moiety, the spiro-carbon, and the methyl

bearing carbons, respectively. Due to the methyl group's tetrahedral arrangement at the cyclopentane moiety in conjunction with a likewise tetrahedral geometry at the spiro carbon the methyl groups are exposed to differing chemical environments evidenced by the presence of two signals at 31.7 and 30.3 ppm.

The presence of fluorinated terminal groups was elucidated by fluorine NMR displaying several signals within a narrow spectral region around -135 ppm (**Figure A15**). The number of signals surpasses the expected number of fluorine species present, that is two. Measurements at an elevated temperature of 55 °C, as compared to 25 °C, did not lead to a diminution in the number of signal hence ruling out any effects originating from rotamers.

Photochromism was investigated by virtue of UV-vis absorption experiments. The monomer 3,3',4,4'-tetrafluoroazobenzene exhibits (*E*)/(*Z*) isomerisation. As mentioned earlier, azobenzene performs a vast geometrical change in the course of isomerisation and its incorporation in a PIM was expected to yield a structure that can tolerate such massive movements of its constituent parts. The results show that the target structure does indeed display photochromism. Albeit the change in colour—light orange to slightly more intense orange—is not as pronounced as was true for DAE-PIM—green to blue—UV-vis spectra unequivocally indicate reversible isomerisation. **Figure 69** contrasts UV-vis absorption spectra from Azo-PIM and the monomer 3,3',4,4'-tetrafluoroazobenzene. Both ordinate axes are set to the same scale, thus it becomes apparent that the monomer absorbs light to a much greater extent. Azo-PIM shows no noticeable absorption above 520 nm. Absorption starts at the edge of the visible region and Azo<sup>(*E*)</sup>-PIM, *i.e.* Azo-PIM with (*E*)-configured azobenzene entities, exhibits absorption events at 398, 339, 283, and 236 nm. After

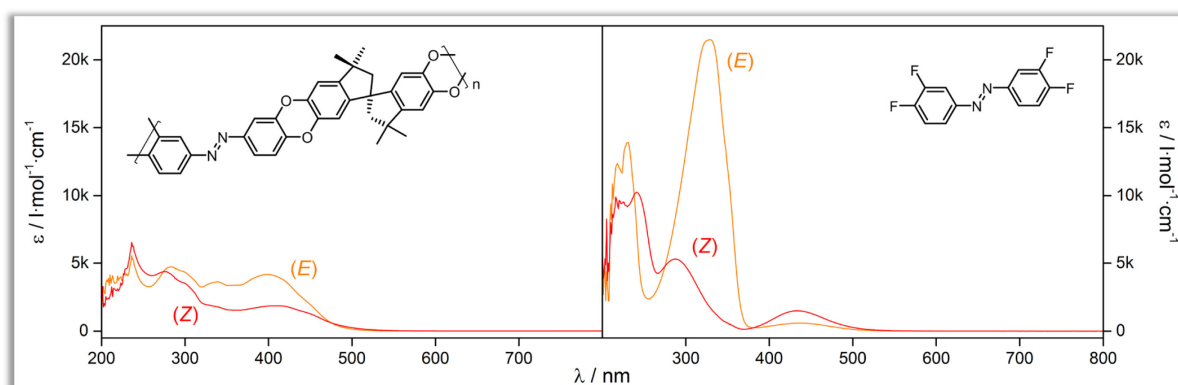


**Figure 69.** UV-vis absorption spectra for DAE-PIM (left, solvent: tetrahydrofuran,  $c = 2 \cdot 10^{-5} \text{ mol} \cdot \text{l}^{-1}$ ) and the azobenzene monomer (right, *cf.* **Figure 46**) before (*E*) and after (*Z*) illumination with UV light at 366 nm.

illumination with UV light (366 nm, 140 s) two isosbestic points could be identified at 475 and 274 nm and absorption is reduced in the entire region from the latter on to longer wavelengths. A slight increase is recorded in the peak at 236 nm. Overall, the absorption profile of Azo<sup>(*Z*)</sup>-PIM is flattened out and more featureless as compared to its (*E*)-counterpart.

Photochromism in Azo-PIM is not as straightforward an affair as **Figure 69** might suggest and was the case for DAE-PIM. Here, in an attempt to trigger (*Z*) → (*E*) isomerisation it was discovered

that the system responds in multiple ways to incoming light of different wavelengths. It appeared that depending on the employed wavelength different absorption regimes could be addressed. This peculiarity is illustrated in **Figure 70**. All three plots feature the spectra from Azo<sup>(E)</sup>-PIM (orange) and Azo<sup>(Z)</sup>-PIM (red) serving as boundaries between which spectra evolve that were obtained after varying amounts of time of illumination utilising different wavelengths. **Figure 70 a)** provides an

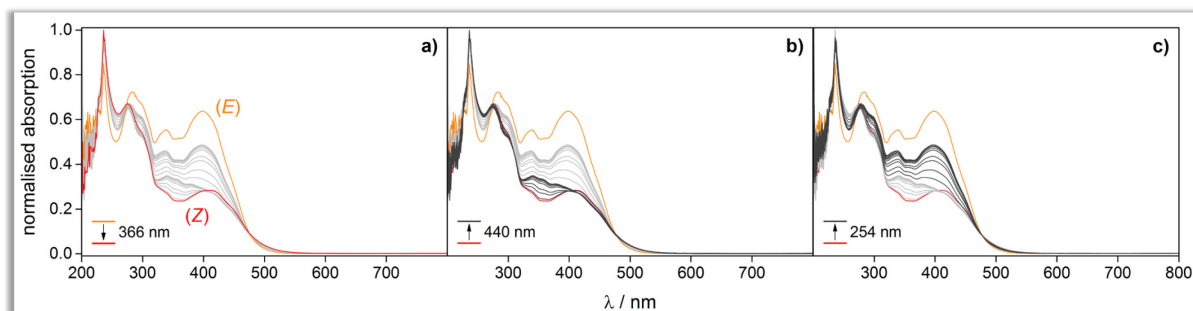


**Figure 70.** UV-vis absorption spectra from (*E*)- and (*Z*)-configured Azo-PIM (a) and in different stages of the (*Z*) → (*E*) isomerisation process either utilising 440 nm (b) or 254 nm (c) (tetrahydrofuran,  $c = 2 \cdot 10^{-5} \text{ mol} \cdot \text{l}^{-1}$ ).

overview of the obtained intermediate curves, which are rendered light grey. (*E*) → (*Z*) isomerisation was triggered by UV light (366 nm, 140 s). **Figure 70 b)** shows results from the attempt to trigger (*Z*) → (*E*) isomerisation with visible light (440 nm, 100 s). The outcome was rather surprising as only a narrow region between 300 and 400 nm was susceptible to the applied wavelength and showed a response, that is an increase in absorption, emphasised in dark grey. Thus, this procedure led to a profile that differs tremendously from the profile for Azo<sup>(E)</sup>-PIM especially when acknowledging that the major absorption band at 398 nm is not restored to any extent. Ensuing treatment with UV light (254 nm, 200 s), depicted in **c)**, led to the evolution of absorption spectra that mimic the initial profile. Whereas the shape of the spectrum from Azo<sup>(E)</sup>-PIM could be retrieved, attempts to regain the intensity where to no avail. This issue was addressed by further investigation of the monomer tetrafluoroazobenzene and a more detailed account of this can be found in the Appendix. At this point, suffice it to say that the wavelength of 440 nm opted for to trigger (*Z*) → (*E*) isomerisation affects the azobenzene moiety already when (*E*)-configured and leads to a slight diminution of the absorption intensity of Azo<sup>(E)</sup> (**Figure A16**).

The described procedure utilised 366 nm to induce (*E*) → (*Z*) isomerisation and illumination was conducted for 140 s. This duration was chosen because it was observed that a degradation process seemed to set in when the sample is overexposed to 366 nm. And although the phenomenon is not remotely as prominent as observed for DAE-PIM after sustained treatment with 254 nm (*cf.* **Figure 61**), UV-vis spectra evince a deviation from the isosbestic points at 274 and 475 nm (**Figure A17**).

The common feature amongst the aforementioned is that a wavelength of 366 nm was used to trigger (*E*) → (*Z*) isomerisation. The reverse process was stimulated by two different wavelengths, either 440 or 254 nm although only the latter seemed to yield a spectrum that mimics the initial spectrum of Azo<sup>(E)</sup>-PIM. To enhance the intricacy of the matter even further it was elaborated on

whether a wavelength other than 366 nm can be employed to induce ( $E$ )  $\rightarrow$  ( $Z$ ) isomerisation. This was considered necessary as cycling experiments showed an apparent degradation that is all but negligible when Azo-PIM is switched back and forth. This is in stark contrast to the very subtle degradation observed in **Figure A17**. However, the already described very minor degradation was observed when the sample was constantly illuminated with 366 nm in a one-way fashion. In cycling experiments, on the other hand, Azo-PIM is subjected to light of different wavelengths in an alternating fashion. In this case 366 and 254 nm were employed to foster ( $E$ )  $\rightarrow$  ( $Z$ ) and ( $Z$ )  $\rightarrow$  ( $E$ ) isomerisation, respectively. As depicted in **Figure 71 a)**, degradation becomes obvious early on. During the second cycle, absorption intensities of the supposed Azo<sup>(E)</sup>-PIM (dashed, cyan) and Azo<sup>(Z)</sup>-PIM (dashed, blue) do only match in a rough approximation the intensity recorded for the initially obtained Azo<sup>(Z)</sup>-PIM (solid, red) that demarcates the lower threshold in terms of intensity of absorption. The fourth cycle then shows intensities that are far below that boundary. Another aspect was observed regarding the influence that 254 nm exert on the sample. After having reached a fairly high intensity during ( $Z$ )  $\rightarrow$  ( $E$ ) isomerisation (solid, dark grey) further illumination leads to a decrease in absorption intensity (solid, grey) which is why for ensuing cycling experiments a time of 200 s (in **a)**, 190 s in **b)**) was chosen for treatment with 254 nm.

A different scenario unfolds when a wavelength of 415 nm is utilised for ( $E$ )  $\rightarrow$  ( $Z$ ) isomerisation (**Figure 71 b)**). In this case, even the sixth cycle of back and forth switching produces an absorption curve for Azo<sup>(E)</sup>-PIM that in the region above 350 nm is close to the one obtained after the first cycle (solid, dark grey). More strikingly, in the same region the profile for Azo<sup>(Z)</sup>-PIM remains unchanged over six cycles. Differences are encountered, though, most conspicuously in the region below

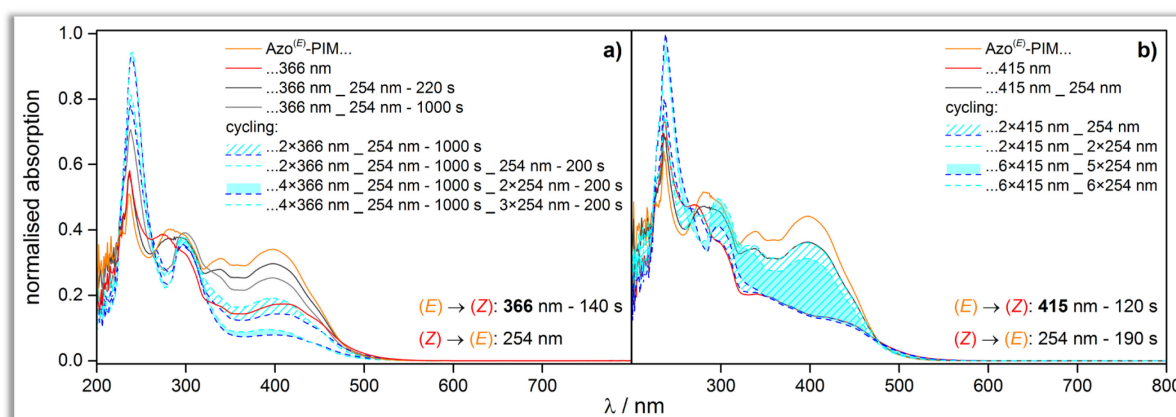


**Figure 71.** UV-vis absorption spectra for Azo-PIM where ( $E$ )  $\rightarrow$  ( $Z$ ) isomerisation is promoted either by a) 366 nm or b) 415 nm. Note that b) demonstrates a higher number of performed switching cycles as compared to a) and still displays better recoverability of the initially obtained spectrum for Azo<sup>(E)</sup>-PIM.

350 nm. In both **a)** and **b)** the isosbestic point at 274 nm is deviated from and the band at 237 nm is noticeably amplified in the course of switching between the ( $E$ )- and ( $Z$ )-isomer.

The investigations delineated above conclusively demonstrate that a PIM-like architecture can tolerate large movements of its constituent parts as Azo-PIM undoubtedly exhibits photochromism.

In summary, UV-vis investigations lead to the following conclusions:

- i) (*E*) → (*Z*) isomerisation can be promoted by either 366 or 415 nm with the latter showing much higher fatigue resistance over consecutive switching cycles.
- ii) (*Z*) → (*E*) isomerisation can be promoted by either 440 or 254 nm with the former addressing only a narrow region of the absorption spectrum leading to the assumption that this wavelength does not induce actual (*Z*) → (*E*) isomerisation. Moreover, it was discovered that 440 nm do affect the monomer Azo<sup>(E)</sup> already yielding a slight decrease in the intensity of absorption (see Appendix). Illumination with 254 nm is more appropriate to promote (*Z*) → (*E*) isomerisation.

The tacit assumption made up to this point that Azo-PIM's designation as *porous* material was wisely chosen will become more pronounced during the following paragraphs. Nitrogen sorption experiments were performed to evaluate whether or not the system displays a porous structure of permanent nature. It was discovered that the apparent surface area is heavily influenced by the number of conducted precipitation cycles with an interdependence showing increasing values for  $SA_{\text{BET}}$  with an increasing number of precipitation steps. This phenomenon can be ascribed to a higher degree of purity attained after each cycle. It has to be mentioned that as-synthesised Azo-PIM was initially precipitated twice already for the sake of purification. The material purified thusly was then precipitated again before being submitted to nitrogen sorption, *i.e.* the first isotherm in **Figure 72** was recorded on a sample that has been precipitated thrice.

The first isotherm gives rise to a  $SA_{\text{BET}}$  of  $83 \text{ m}^2 \cdot \text{g}^{-1}$ , a value that experienced a steady increase over the ensuing three precipitation cycles culminating in a figure of  $305 \text{ m}^2 \cdot \text{g}^{-1}$ . For all isotherms hysteresis is evident and the profiles are similar insofar as they exhibit a steady increase in the relative pressure region between 0.1 and 0.9 with a pronounced uptake towards saturation pressure. One difference is that this final uptake is commensurate with the number of precipitation cycles. As mentioned in the introductory chapter, such an increase is usually attributed to either macropore filling or textural porosity. In the case of PIMs consisting of individual chains the notion of macropore formation is a *non sequitur* leaving only textural porosity to serve as explanation for the observed uptake. In fact, due to the intrinsic morphology of PIMs and the structural prerequisite to avoid space-efficient packing, textural porosity is the sole sort of porosity available to PIMs. Another difference between the isotherms is obvious at low relative pressures where an augmented gas uptake in the micropore domain is responsible for higher  $SA_{\text{BET}}$  values for samples that have been precipitated more frequently.

As can be drawn from **Figure 72**,  $SA_{\text{BET}}$  seems to level out after Azo-PIM has been precipitated a fourth time. However, to substantiate that assessment further precipitation steps are certainly warranted. As of this writing, due to time constraints any such enquiry to advance elucidation of that matter has to be stalled for the time being.

Likewise, research into the switching behaviour of Azo-PIM is of very preliminary nature. First attempts employed a sample that has been precipitated twice after synthesis. The apparent surface area of that Azo<sup>(E)</sup>-PIM specimen accrues to 33 m<sup>2</sup>·g<sup>-1</sup>. In order to exclude any influence from precipitation procedures, which is evidently very prominent, (E) → (Z) isomerisation was tried to be triggered within the sorption tube. UV-vis experiments were instrumental in that regard, as the option was opened to induce (E) → (Z) isomerisation not only by UV but also visible light. The

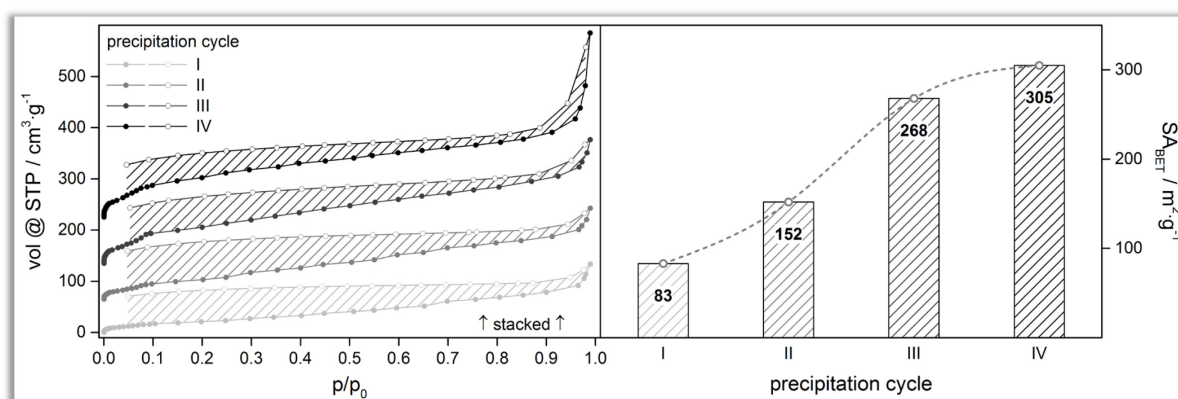


**Figure 72.** Isotherms derived from nitrogen sorption at 77 K after consecutive precipitation cycles of Azo-PIM (left). The plots are stacked along the ordinate axis for clarity. A steady increase in SA<sub>BET</sub> can be noticed with regard to an increasing number of precipitation cycles (right). Solid symbols: adsorption, empty symbols: desorption. Note that for all isotherms multi-point BET analysis was performed consistently by selection of the same five points.

sorption tube is made of glass that is not transmissive to UV-light. Visible light, however, passes unimpeded rendering light with a wavelength of 415 nm a suitable choice. When illuminating the sample within the sorption tube a caveat needs to be kept in mind. Sorption analyses as performed here are run on solid state samples, a condition that is not conducive to successful isomerisation so far as azobenzenes are concerned. Azobenzenes perform large movements upon isomerisation and cannot be expected to isomerise in the solid state. Nevertheless, the described experiment might be viewed as a confirmation of this circumstance. Indeed, after illumination with 415 nm no noticeable change could be witnessed and the compared isotherms look virtually alike (**Figure A18**).

## CONCLUSION

It was demonstrated that azobenzene in conjunction with a kinked molecule—a spirobiindane motif—yield a polymer of intrinsic microporosity. Within the polymer azobenzene units retain the capability to respond to electromagnetic stimuli and perform (E) → (Z) isomerisation in a reversible manner. It can be fathomed that the more central Azo-units, *i.e.* the one closer to the middle of the chain, have to exert more force to perform isomerisation due to the higher molecular mass that is tethered to those units as compared to the more peripheral ones. It is expected that isomerisation of the inner Azo-units is not adversely affected by this situation as it is established that azobenzenes

can exert considerable force as shown in numerous publications describing the influence of (*E*)/(*Z*) isomerisation on the structural arrangement of proteins or exploitation of the isomerisation process to operate molecular machines.<sup>[198,202,207-208,258]</sup>

UV-vis absorption shows that isomerisation in Azo-PIM is a complex matter. To elaborate upon this issue more comprehensively in order to *e.g.* explain why for (*Z*) → (*E*) isomerisation 440 nm do address only a narrow region of the absorption spectrum whereas 254 nm lead to a restoration of the initial profile, save for the intensity, (*cf.* **Figure 70**) or why switching cycles employing 366 nm for (*E*) → (*Z*) isomerisation display rapid degradation as compared to when 415 nm are utilised (*cf.* **Figure 71**), further investigations are needed. In particular, theoretical calculations should be exploited to buttress further research as it is feasible to have an idea about dipole moments, structural arrangements and (frontier) orbital as well as transition state energies prevalent in the two isomers of Azo-PIM.

Permanent porosity was proven by nitrogen sorption with a  $SA_{\text{BET}}$  of  $305 \text{ m}^2 \cdot \text{g}^{-1}$  for a sample that has been precipitated four times (six times when adding the initial two cycles that are considered 'raw purification'). The most interesting phenomenon of an (reversible) alteration of surface area induced by light stimulus could not be addressed in any sufficient detail. Nevertheless, some thoughts on this are to be outlined here. As already noted, azobenzenes do not isomerise in solid state, a circumstance illustrated in **Figure A18**. This means that isomerisation needs to be conducted in solution followed by evaporation of solvent and precipitation to obtain Azo-PIM in form of a powder as PIMs in general tend to exhibit no porosity when obtained as film. The problem that arises is that precipitation evidently has a considerable influence on surface area making it partially fruitless to perform isomerisation in the first place as an enhanced surface area cannot unequivocally be attributed to the presence of the other isomer but must be considered a repercussion of the precipitation event. On the other hand, a significant drop in surface area after successful isomerisation could quite convincingly be attributed to the presence of the other isomer as the revealed considerable influence that precipitation has did show a clear propensity towards higher surface area values. However, the following step would comprise the proof of reversibility with an anticipated increase in surface area so that the problem adumbrated above presents itself anew. One way out of this predicament is to develop a methodology according to which surface area remains constant after at least two consecutive precipitation steps *e.g.* by substitution of another solvent mixture from which precipitation occurs.

Moreover, the partial *t*-type character of azobenzenes poses problems in terms of handling. When (*Z*)-configured, thermal relaxation to the (*E*)-isomer is to be thwarted by conducting investigations at reduced temperatures unless an azobenzene derivative is employed that features an appropriate substitution pattern as to exhibit a reduced proclivity towards thermally triggered (*Z*) → (*E*) isomerisation.<sup>[196]</sup>

The inability of Azo-PIM to isomerise in solid state restricts its prospective utilisation in any sort of device such as indicated in **Figure 66** for DAE-PIM. This notwithstanding, it might be possible to incorporate Azo-PIM in a matrix to circumvent that problem in the following manner. When solidly diluted in a matrix individual Azo-PIM chains are spatially separated from each other thereby

avoiding mutual hindrance of isomerisation. Naturally, the space between Azo-PIM chains must be occupied by other matter—the matrix. Now, the success of this scenario severely depends on whether or not a matrix can be found that consists of *e.g.* polymeric or probably even better oligomeric chains that are flexible and mobile enough to rearrange swiftly and recoil from Azo-PIM chains that engage in the process of isomerisation. A matrix material of this sort might be considered quasi-solid or gelish. An endeavour to this end is very promising as the two isomers of Azo-PIM are expected to yield significantly different affinities for gases such as carbon dioxide or oxygen in particular due to the dipole moment that experiences a tremendous change upon isomerisation (*cf.* **Figure 45**). Thus, experiments regarding diffusivity and permeability are expected to yield a pattern that qualitatively should be comparable to the one obtained for DAE-PIM.

The pronouncedly higher molecular motion during isomerisation that is exerted by Azo-PIM as compared to DAE-PIM might lead to vastly enhanced deformations of the entire PIM chain. At this point, only propositions can be made as to what sort of arrangement is attained after (*E*) → (*Z*) isomerisation but a detail of two repeating units will suffice to illustrate that the Azo-PIM chain has to accommodate to the isomerisation event in a profound way (**Figure 73**). What can be discerned quite clearly is that whatever degree of linearity traverses the (*E*)-isomer is lost during isomerisation to the (*Z*)-counterpart compelling the chain to adopt a more compact and contorted geometry.

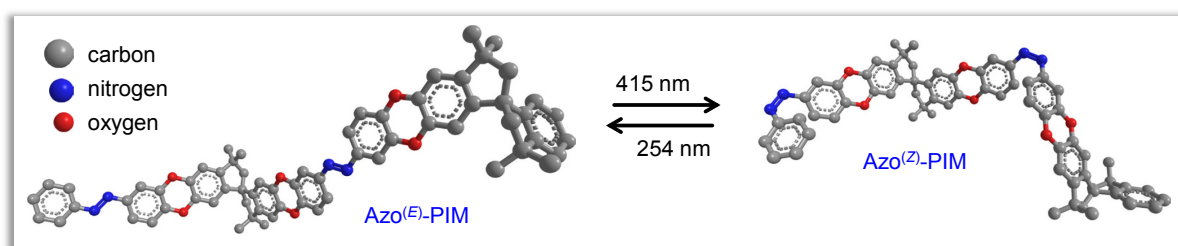


**Figure 73.** Graphical abstract of switching event in Azo-PIM shown for a detail of two repeating units. Hydrogen atoms are omitted for clarity.

Whether the outcome looks like a random coil or has some sort of order reminiscent of a helix cannot be clarified at this point in time.

# APPENDIX

## CHAPTER 1 ♦ FILMS

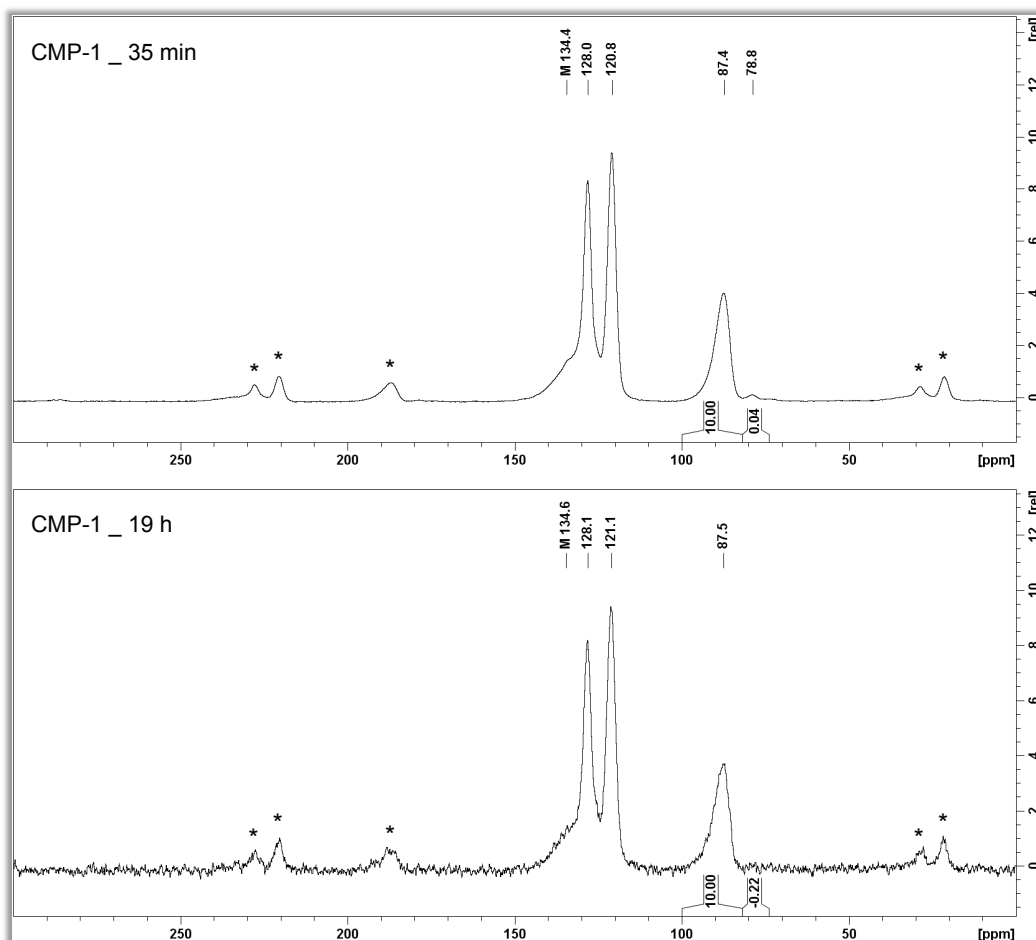


**Figure A1.**  $^{13}\text{C}$  solid-state CP-MAS NMR spectra (10 kHz) of short- (top) and long- (bottom) term CMP-1 runs. Spinning side bands are marked with an asterisk. The signal at 78.8 ppm is absent from the long-term sample.

## CHAPTER 2 ♦ SILICA

(Note: Molar masses obtained from ChemDraw Professional, v. 15.0.0.106.)

### SILICA | PRISTINE

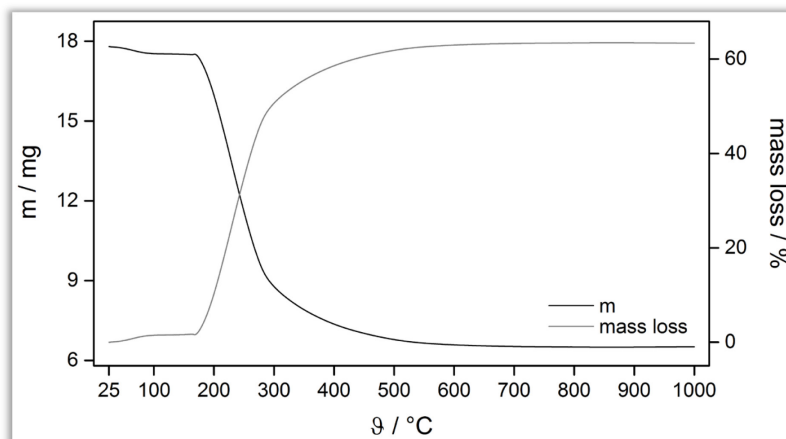


**Figure A2.** Result from TGA ( $\vartheta_{\text{start}} = 25\text{ °C}$ ,  $\vartheta_{\text{end}} = 1000\text{ °C}$ , heating rate =  $10\text{ °C}\cdot\text{min}^{-1}$ , in air) performed on an aged sample of silica formed from TEOS and P-123. The final mass loss (grey line) accumulates to 63.4 %.

#### COMMENT A: MASS OF POLYMER ANTICIPATED TO FORM INSIDE THE PORES

The silica employed for this experiment was analysed by nitrogen sorption experiments after calcination, a state denoted here as pristine. NLDFT calculation disclosed a total pore volume of  $0.561\text{ cm}^3\cdot\text{g}^{-1}$  with no contributions from micropores. This volume is the space in which the polymer PPN-6 is desired to take shape. To assess the overall pore volume available within the reaction vessel, the mass of the employed silica needs to be accounted for. Theoretically, it is advisable to refer to the mass of the silica that was used in the beginning of the reaction because at this stage the template is empty with no contributing mass fractions from polymer inside the pores. However, as it was not possible to avoid some undetermined loss of template during handling, the initially employed mass cannot be referred to as reference. For this reason, the eventually obtained mass of the supposedly infiltrated silica after workup was used for the ongoing calculation in acknowledgement that this approach suffers from the inadequacy that the final mass already contained a mass contribution from the polymer, if infiltration was successful.

Eventually, a mass of 3.57 g of supposedly infiltrated silica was gathered. Multiplied by the total pore volume of  $0.561\text{ cm}^3\cdot\text{g}^{-1}$  an overall volume of  $2.00\text{ cm}^3$  is determined. Multiplying this value with the tap density of  $0.15\text{ g}\cdot\text{cm}^{-3}$  for PPN-6<sup>[50]</sup> yields a mass of 0.300 g for PPN-6 to be formed inside the porous system of the silica template amounting to a mass fraction of 8.4 % for the polymer. Although a caveat needs to be issued on grounds of the fact that tap density does probably not reflect the packing situation of a polymer formed inside a template, this estimation still gives a rough hint for the expected mass to be found after the template has been removed.

## SILICA | FUNCTIONALISATION WITH HEXAMETHYLDISILAZANE (HMDS)

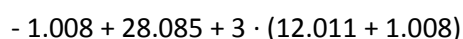
### COMMENT B: OBSERVED MASS CHANGE CAUSED BY HMDS TREATMENT

- Numbers (factors excluded) without units given in  $\text{g}\cdot\text{mol}^{-1}$ ; R refers to the surface of the silica

#### Theory

a) Transformation of silica *via* HMDS

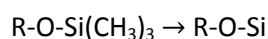
treatment:



$$= + 66.134 \quad (\triangleq 100 \%)$$

b) Decomposition of functionalised surface

during TGA:



$$= - 39.057 \quad (\triangleq 59.1 \%)$$

#### Experiment

Mass gain caused by HMDS functionalisation: 8.3 % ( $\triangleq 100 \%$ ) with respect to final mass

Mass loss according to TGA: 4.7 % ( $\triangleq 56.6 \%$ )

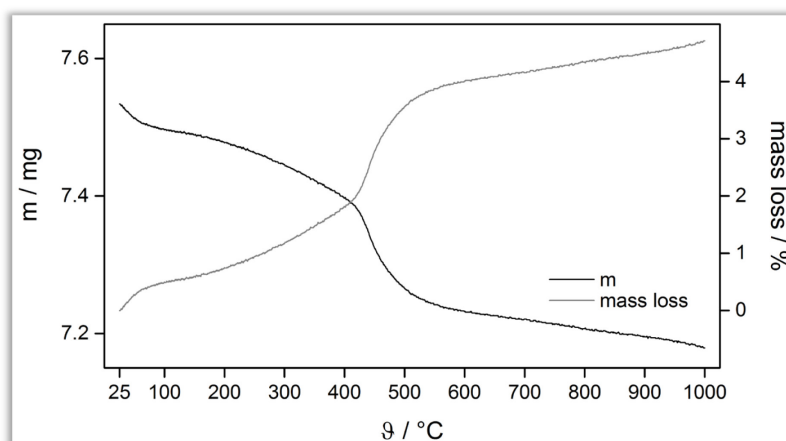


**Figure A3.** Result from TGA ( $\vartheta_{\text{start}} = 25 \text{ }^\circ\text{C}$ ,  $\vartheta_{\text{end}} = 1000 \text{ }^\circ\text{C}$ , heating rate =  $10 \text{ }^\circ\text{C}\cdot\text{min}^{-1}$ , in air) performed on a silica sample that has been calcined and subsequently functionalised with HMDS. The final mass loss (grey line) accumulates to 4.7 %.

### COMMENT C: DEGREE OF HMDS-FUNCTIONALISATION

This calculation relies on the value of 1.7 hydroxy groups per  $\text{nm}^2$  that are accessible to HMDS molecules.<sup>[181]</sup> In conjunction with Avogadro's constant a value of  $2.823 \text{ } \mu\text{mol}\cdot\text{m}^{-2}$  is determined. The employed silica template exhibited a  $\text{SA}_{\text{BET}}$  of  $595 \text{ m}^2\cdot\text{g}^{-1}$ . As 4.1957 g of pristine template were employed a total surface area of  $2496.44 \text{ m}^2$  was provided in the course of the reaction, which in turn yields a total molar amount for present hydroxy groups of  $2.823 \text{ } \mu\text{mol}\cdot\text{m}^{-2} \cdot 2496.44 \text{ m}^2 = 7.047 \text{ mmol}$ .

The observed mass gain of 0.3776 g (9.0 or 8.3 % with regard to initial or final mass, respectively) is assumed to hail exclusively from TMS groups. However, as one proton must be sacrificed for each TMS unit to bind to a silanol group a molar mass of  $72.182 \text{ g}\cdot\text{mol}^{-1}$  (TMS minus one proton) for each additional TMS group is reckoned with. As a result, the mass gain translates into a molar amount 5.231 mmol of added TMS groups. By dividing that value by the molar amount of present hydroxy groups yields a degree of functionalisation in per cent of  $5.231 \text{ mmol} \cdot (7.047 \text{ mmol})^{-1} = 74.2 \%$ .

#### COMMENT D: MASS OF POLYMER ANTICIPATED TO FORM INSIDE THE PORES

The calculation follows the same procedure as utilised under Comment A. The employed silica exhibited a pore volume of  $0.529 \text{ cm}^3\cdot\text{g}^{-1}$ . A mass of 4.2132 g of supposedly infiltrated silica was gathered. Multiplied by the total pore volume of  $0.561 \text{ cm}^3\cdot\text{g}^{-1}$  an overall volume of  $2.23 \text{ cm}^3$  is determined. Multiplying this value with the tap density of  $0.15 \text{ g}\cdot\text{cm}^{-3}$  for PPN-6<sup>[50]</sup> yields a mass of 0.3343 g for PPN-6 to be formed inside the porous system of the silica template constituting a mass fraction of 7.9 % for the polymer. This value has to be augmented by the mass loss for the HMDS-functionalised sample of 4.7 % to estimate a mass loss encountered during TGA of 12.6 %.

#### SILICA | FUNCTIONALISATION WITH PARABROMOPHENYLTRIMETHOXYSIANE (PBPTMOS)

##### COMMENT E: CORRELATION BETWEEN MASS INCREASE AND INTRODUCED PBPTMOS SPECIES

The molar amount of PBPTMOS employed in the functionalisation experiment was 16.704 mmol. The mass gain induced by functionalisation was measured to be 3.6608 g. That mass corresponds to a certain amount of introduced functional moieties. However, attention has to be paid to what species of PBPTMOS is considered to be present. PBPTMOS bears three methoxy groups each of which can but not necessarily does undergo a condensation reaction with a hydroxyl at the surface of the silica. Each condensation reaction releases one methanol molecule to give rise to a siloxane bond formation. Thus, it is important to recognise whether two, one, or none methoxy groups are kept per PBPTMOS unit after attachment to the silica. These different species will be designated  $M^2$ ,  $M^1$ , and  $M^0$  for the following consideration (**Figure A4**). As there will be different molecular weights associated with  $M^2$ ,  $M^1$ , and  $M^0$  the measured mass increase can be related to the presence of one or the other species. As every condensation reaction sacrifices formally one hydrogen atom belonging to surface hydroxyls to form methanol, the molecular weights of  $M^2$ ,  $M^1$ , and  $M^0$  need to be reduced by the molecular weight of one, two, and three hydrogen atoms, respectively.

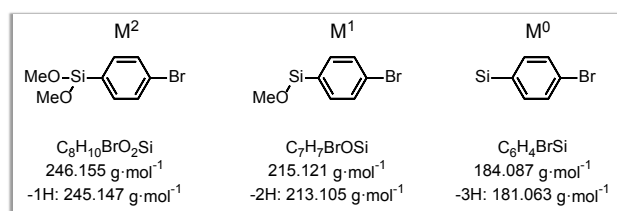


**Figure A4.** Formal chemical structures of the PBPTMOS species that can possibly contribute to the mass increase. Depending on whether one, two, or all three methoxy groups have undergone condensation reaction, two (M<sup>2</sup>), one (M<sup>1</sup>), or none (M<sup>0</sup>) methoxy groups, respectively, will be maintained in the surface bonded moiety. Formally correct charges on the silicon atom are omitted for clarity.

Results of calculations employing the different molecular weights:

$$\begin{aligned}
 n(\text{M}^x) &= m_{\text{gained}} \cdot M_{\text{PBPTMOS species}}^{-1} = n_{\text{PBPTMOS species}} \\
 n(\text{M}^2) &= 3.6608 \text{ g} \cdot 245.147 \text{ g}\cdot\text{mol}^{-1}^{-1} = 14.933 \text{ mmol} \\
 n(\text{M}^1) &= 3.6608 \text{ g} \cdot 213.105 \text{ g}\cdot\text{mol}^{-1}^{-1} = 17.178 \text{ mmol} \\
 n(\text{M}^0) &= 3.6608 \text{ g} \cdot 181.063 \text{ g}\cdot\text{mol}^{-1}^{-1} = 20.218 \text{ mmol}
 \end{aligned}$$

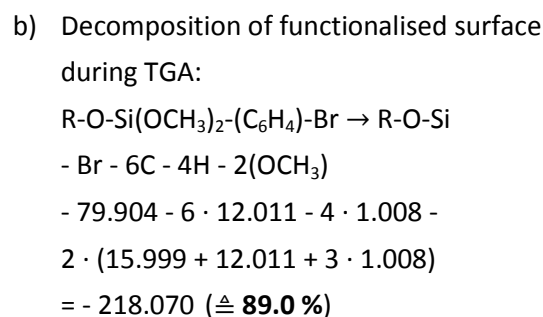
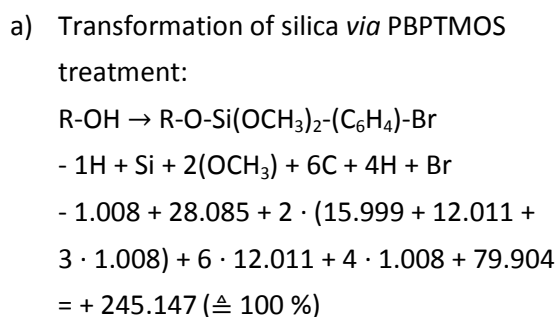
It can easily be understood that two of those reckonings do not comply with reality:  $n(\text{M}^1)$  and  $n(\text{M}^0)$ , for the simple reason that the calculated molar amount of attached PBPTMOS exceeds the amount of 16.704 mmol employed in the first place. Naturally, it is possible that combinations of the three condensation events (one-, two-, and three-fold) did occur. However, this is not part of this deliberation.

The previous reflection suggests that the functionalisation proceeded *via* one-fold condensation reaction leaving the attached parabromophenylsiloxane moiety with two remaining methoxy groups. The following will show that this hypothesis can be substantiated by TGA analysis.

#### COMMENT F: OBSERVED MASS CHANGE CAUSED BY PBPTMOS TREATMENT

- Numbers (factors excluded) without units given in g·mol<sup>-1</sup>; R refers to the surface of the silica

#### Theory



### Experiment

Mass gain caused by PBPTMOS functionalisation: 17.5 % ( $\pm$  100 %) with respect to final mass

Mass loss according to TGA: 16.1 % ( $\pm$  92.0 %)

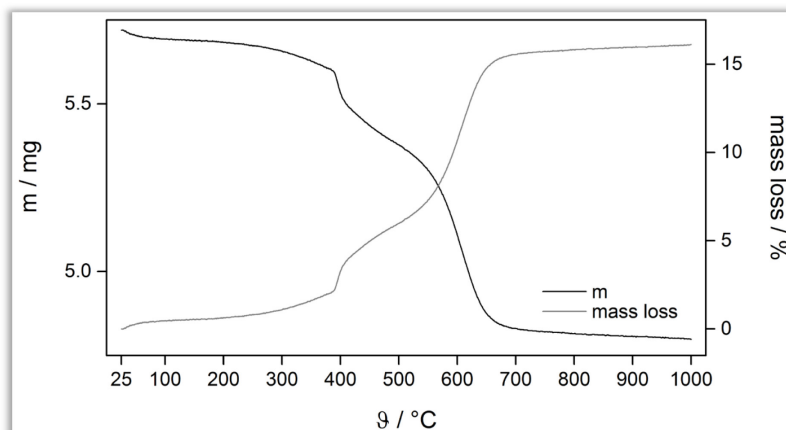


**Figure A5.** Result from TGA ( $\vartheta_{\text{start}} = 25\text{ }^{\circ}\text{C}$ ,  $\vartheta_{\text{end}} = 1000\text{ }^{\circ}\text{C}$ , heating rate =  $10\text{ }^{\circ}\text{C}\cdot\text{min}^{-1}$ , in air) performed on a silica sample that has been calcined and subsequently functionalised with PBPTMOS. The final mass loss (grey line) accumulates to 16.1 %. The sudden mass loss at around 400 °C amounts to 4.9 % and is ascribed to the loss of bromine.

Indeed, the assumption of a one-fold condensation reaction leaving two methoxy groups on the attached PBPTMOS unit produces the best result in a theoretical approach to rationalise the TGA findings. The mass loss measured by virtue of TGA amounts to 16.1 %, which constitutes 92.0 % of the mass gain. Theory predicts a ratio of mass loss to mass gain in per cent of 89.0 % when putting into relation the increase in mass observed for the transformation of a hydroxyl to a parabromophenyldimethoxysilane moiety to the mass loss experienced during TGA. Although these values differ to some extent they still are in reasonable conformity to each other.

Another hint for the legitimacy of the hypothesis of a one-fold condensation event is the plummeting mass loss observed at around 400 °C in the TGA plot (**Figure A5**). This step accumulates to a decline in mass of 4.9 % and is ascribed to the expulsion of bromine. When set into relation to the total mass loss of 16.1 %, the witnessed step accounts for 30.4 %. Bromine, on the other hand, constitutes 44.1, 37.5, and 32.6 % of the molecular weight of the parabromophenyl moieties bearing none, one, and two remaining methoxy groups, respectively. Thus, applying the molecular weight of the parabromophenyl species bearing two methoxy groups, the outcome of a one-fold condensation event, yields the result that conforms best to the experimentally obtained value.

#### COMMENT G: DEGREE OF PBPTMOS-FUNCTIONALISATION

This calculation relies on the value of 1.7 hydroxy groups per  $\text{nm}^2$ .<sup>[181]</sup> Although this value was established for hydroxyls accessible to HMDS it is still considered a valid parameter to apply albeit PBPTMOS is a bigger molecule than HMDS. If anything, that number most probably would encounter reduction since it is reasonable to argue that less surface hydroxyls are accessible to bigger

molecules as compared to the number that can be reached by smaller ones. In reducing the value of 1.7 groups per  $\text{nm}^2$ , however, the degree of functionalisation will be enhanced since in the applied fraction the denominator will be decreased while the numerator remains unchanged.

Taking the aforesaid value of 1.7 groups per  $\text{nm}^2$  into account in conjunction with Avogadro's constant a value for present hydroxyl groups of  $2.823 \mu\text{mol}\cdot\text{m}^{-2}$  is determined. The employed silica template exhibited a  $S_{\text{BET}}$  of  $486 \text{ m}^2\cdot\text{g}^{-1}$ . As 17.2205 g of pristine template were employed a total surface area of  $8369.16 \text{ m}^2$  was provided in the course of the reaction, in turn yielding a total molar amount for present hydroxy groups of  $2.823 \mu\text{mol}\cdot\text{m}^{-2} \cdot 8369.16 \text{ m}^2 = 23.626 \text{ mmol}$ .

Supposing that the incoming PBPTMOS molecules underwent a one-fold condensation reaction the observed mass gain of 3.6608 g (21.3 or 17.5 % with regard to initial or final mass, respectively) is assumed to hail exclusively from parabromophenyldimethoxysilyl (PBPDMOS) groups. However, as one proton from the surface hydroxy groups must be sacrificed for each condensation step a molar mass of  $245.147 \text{ g}\cdot\text{mol}^{-1}$  (PBPDMOS minus one proton, *cf.* **Figure A4**) for each additional PBPDMOS group is reckoned with. As a result, the mass gain translates into a molar amount  $14.933 \text{ mmol}$  of added PBPDMOS groups. By dividing that value by the molar amount of present hydroxy groups yields a degree of functionalisation in per cent of  $14.933 \text{ mmol} \cdot (23.626 \text{ mmol})^{-1} = 63.2 \%$ .

#### COMMENT H: MASS OF POLYMER ANTICIPATED TO FORM INSIDE THE PORES

The calculation follows the same procedure as applied under Comment A. The employed silica exhibited a pore volume of  $0.383 \text{ cm}^3\cdot\text{g}^{-1}$ . Masses of 9.5135 and 9.6889 g of supposedly infiltrated silica were gathered for wet- and dry-approach, respectively. Multiplied by the total pore volume of  $0.383 \text{ cm}^3\cdot\text{g}^{-1}$  overall volumes of 3.64 and  $3.71 \text{ cm}^3$  are determined that by multiplication with the tap density of  $0.15 \text{ g}\cdot\text{cm}^{-3}$  for PPN-6<sup>[50]</sup> translate into masses of 0.5466 and 0.5566 g for wet- and dry-approach, respectively, for polymer formed inside the porous system of the silica template. Both these figures lead to a mass fraction of 5.7 % for the polymer within its respective sample. In contrast to the case of the HMDS-functionalised sample this value must not be augmented by solely adding the mass loss observed during TGA of the, in this case, PBPTMOS-functionalised silica. Unlike HMDS, the PBPTMOS motif does partake in the reaction hence experiences a mass loss, the loss of bromine, upon successful tethering of polymer to the surface. This intrinsic mass loss has to be allowed for and as delineated under Comment E a one-fold condensation is presumed for the functionalisation in which case bromine accounts for 32.6 % of the mass of the surface bonded PBPTMOS moiety (*cf.* Comment F). That percentage has to be deducted on a proportionate basis from the mass loss of the PBPTMOS-functionalised silica of 16.1 % yielding a mass loss corrected for the loss of bromine of 10.9 %. That value is in good agreement with the number of 11.2 % that is obtained when subtracting the mass loss of 4.9 % observed at around 400 °C from the total mass loss of 16.1 % (*cf.* **Figure A5**). The figure of 10.9 % is relevant to be added to the calculated weight fraction for the polymer of 5.7 % leading to a theoretical mass loss induced by combustion of 16.6 %.

## CHAPTER 3 ♦ LIGHT



**Figure A6.** Photographs of 1,3,5-triethynylbenzene as-purchased and after a filtration run through silica with dichloromethane as mobile phase.

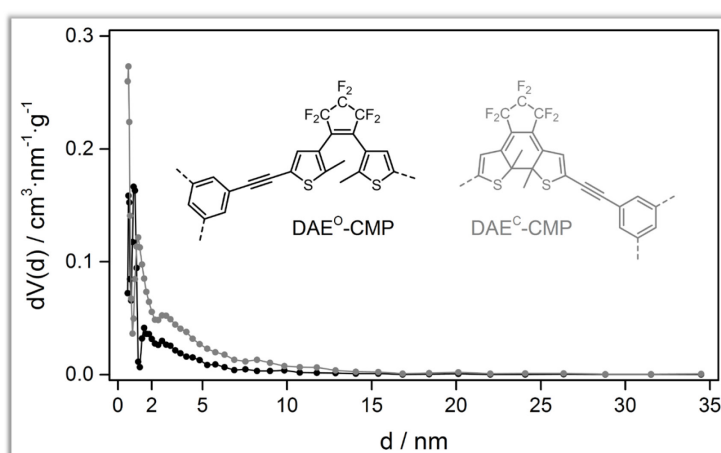


**Figure A7.** Full range pore size distribution according to QSDFT (calc. model: N2 at 77 K on carbon; slit pore, QSDFT adsorption model) for DAE<sup>O</sup>-CMP (black graph) and DAE<sup>C</sup>-CMP (grey graph).

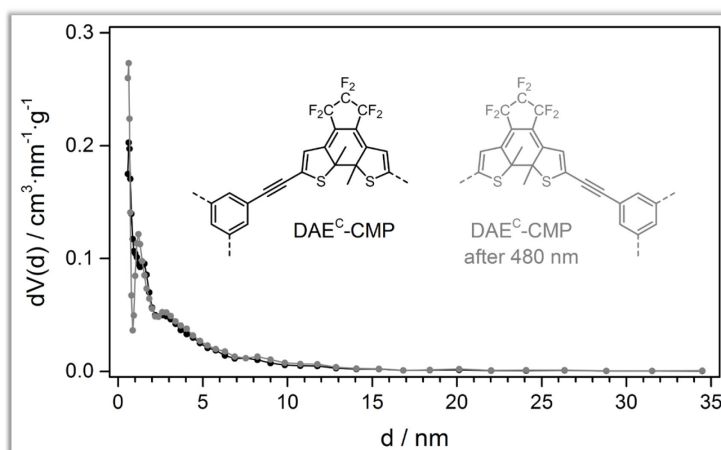


**Figure A8.** Full range pore size distribution according to QSDFT (calc. model: N2 at 77 K on carbon; slit pore, QSDFT adsorption model) for DAE<sup>C</sup>-CMP (black graph) and DAE<sup>C</sup>-CMP that underwent illumination (grey graph).

Note on QSDFT adsorption model:

The software ASiQwin (v. 3.01) that was used for the analysis did not have implemented an adsorption model for the desired method of calculation. Therefore, desorption points of the isotherm were deleted and an equilibrium model was applied to that modified isotherm. In this way an adsorption model was simulated to be applied to the isotherm—credits to Dr. Jérôme Roeser for suggesting that methodology to the author.

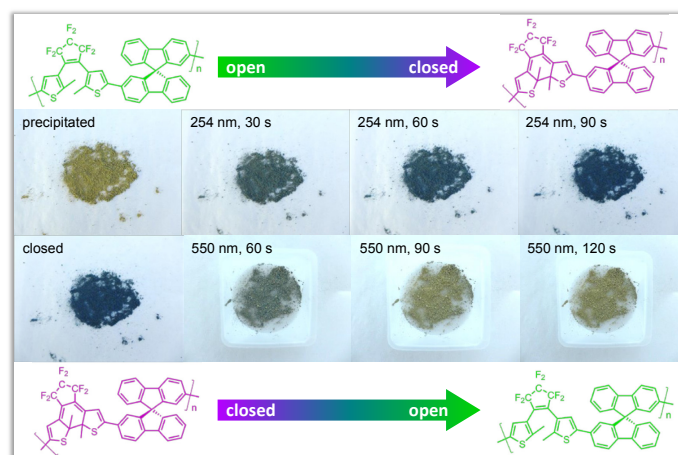


**Figure A9.** Photographs of DAE-PIM switched in solid state as powder as obtained from precipitation from methanol.

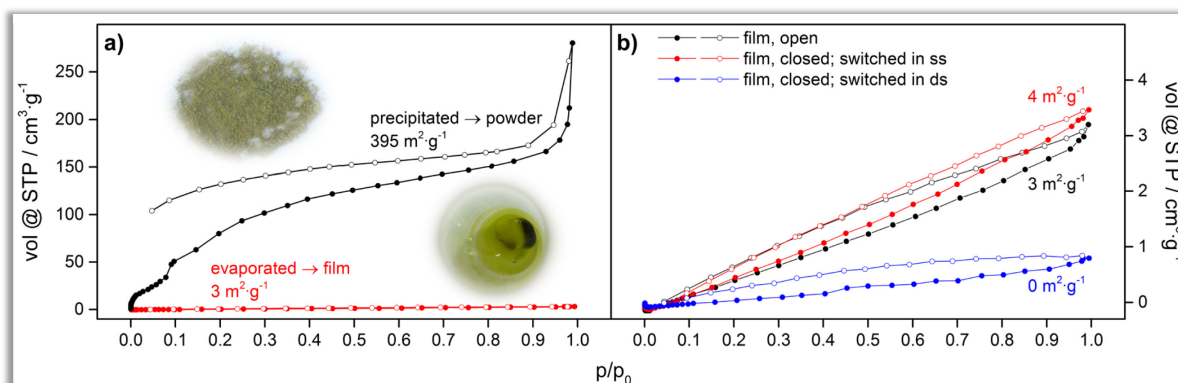


**Figure A10.** a) Isotherms derived from nitrogen sorption at 77 K for **DAE<sup>0</sup>-PIM** obtained as both powder from precipitation (black graph) and film from evaporation (red graph). b) Isotherms derived from nitrogen sorption at 77 K for DAE-PIM film-like samples obtained *via* evaporation of solvent. The lack of porosity is evident in both films that incorporate the open and films that incorporate the closed isomer of DAE-PIM irrespective of whether switching was conducted in solid state (ss) or dissolved state (ds). Solid symbols: adsorption, hollow symbols: desorption.

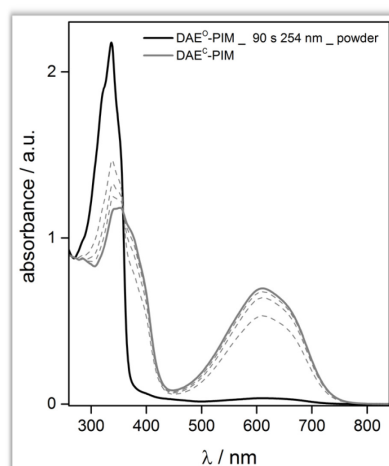


**Figure A11.** UV-vis absorbance spectrum to determine the conversion rate of the sample that shows a drop in  $SA_{\text{BET}}$  after UV-treatment. The powder sample has been illuminated with 254 nm for 90 s (black solid curve). For UV-vis measurement the as-irradiated sample was dissolved in dichloromethane and after its spectrum has been recorded that dissolved sample was treated further with 254 nm for additional intervals of illumination (dashed curves) to obtain the maximal achievable conversion (grey solid curve) after 180 s of illumination time in the dissolved state, *i.e.* a total duration of illumination of 270 s. To determine the conversion rate with regard to the maximal achievable conversion the absorbance values at 610 nm were set into relation. Such comparison between the red and blue curve yields a conversion rate of 5 %.

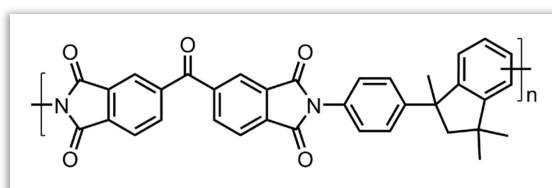


**Figure A12.** Chemical structure of Matrimid.

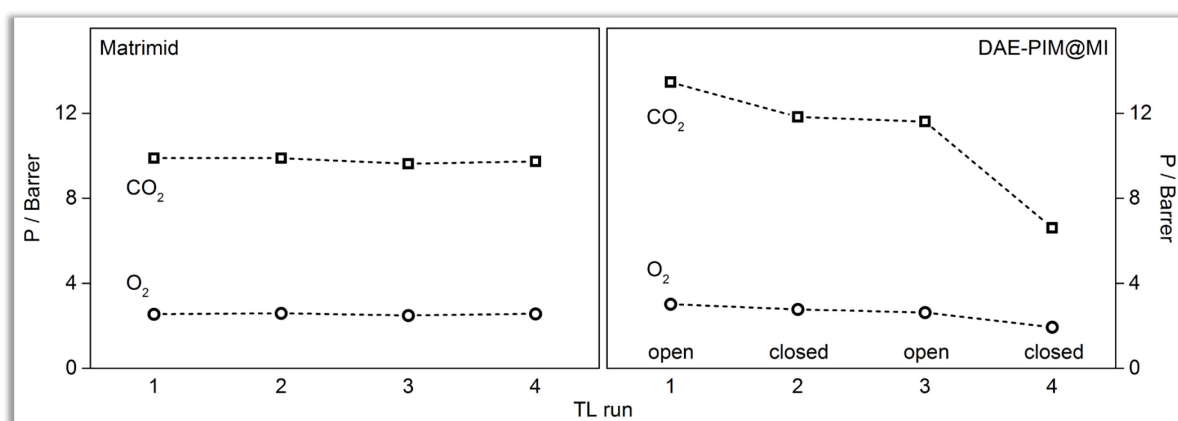


**Figure A13.** Permeability for oxygen (circles) and carbon dioxide (squares) at 35 °C and 10 bar of pure Matrimid (left) and DAE-PIM@MI (right) for subsequent measurements in between which the composite was switched by light.



**Figure A14.** Photographs of Azo-PIM obtained as powder or flakes from precipitation (left) and as film from evaporation of solvent (right).

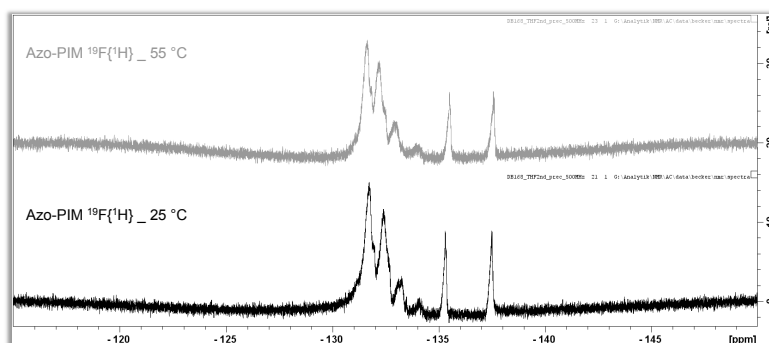


**Figure A15.** NMR spectra of Azo-PIM recorded at r.t. and elevated temperature to accelerate possible rotational movements and reduce the number of fluorine species that can be distinguished by NMR spectroscopy. As both spectra look alike, the presence of rotamers is ruled out.

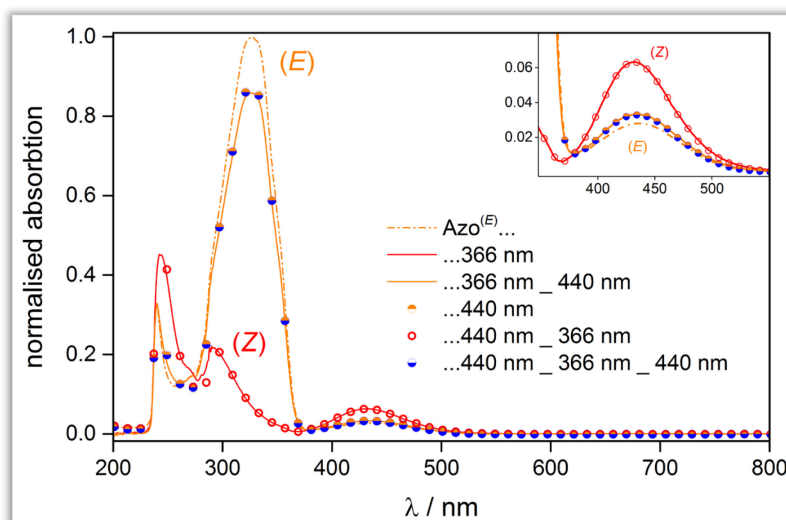


**Figure A16.** UV-vis absorption spectra of 3,3',4,4'-tetrafluoroazobenzene to illustrate the influence of 440 nm on the (*E*) isomer. The inset shows a close-up on the absorption band in the visible region. As a recurring pattern during UV-vis investigations of Azo-PIM it was observed that the intensity of UV-vis absorption after (*Z*) → (*E*) isomerisation triggered by 440 nm did not reach the initial value exhibited by Azo<sup>(*E*)</sup>-PIM. (*E*) → (*Z*) isomerisation was induced by UV light at 366 nm and the reverse process by 440 nm. As the photochromic entity in Azo-PIM is the azobenzene moiety, the monomer 3,3',4,4'-tetrafluoroazobenzene (“Azo”) was studied in more detail. It was discovered that illumination with 440 nm already exerts an influence on Azo<sup>(*E*)</sup>, *i.e.* the monomer with an (*E*)-configured N=N double bond. When irradiated with said wavelength the absorption profile for Azo<sup>(*E*)</sup> shows an evolution reminiscent of the actual (*E*) → (*Z*) isomerisation process. However, this is true only for the beginning and the process stops and yields a new photo-stationary state (PSS) close to the initial absorption pattern of the (*E*) isomer.

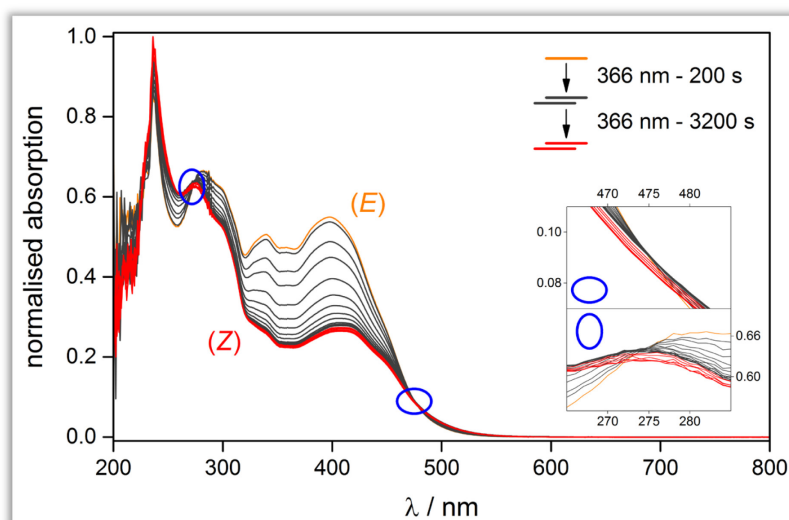


**Figure A17.** Overexposure to 366 nm. UV-vis absorption spectra of Azo-PIM recorded during ( $E$ )  $\rightarrow$  ( $Z$ ) isomerisation utilising 336 nm. After sustained illumination, a deviation from the isobestic points at 274 and 475 nm is observed (insets).

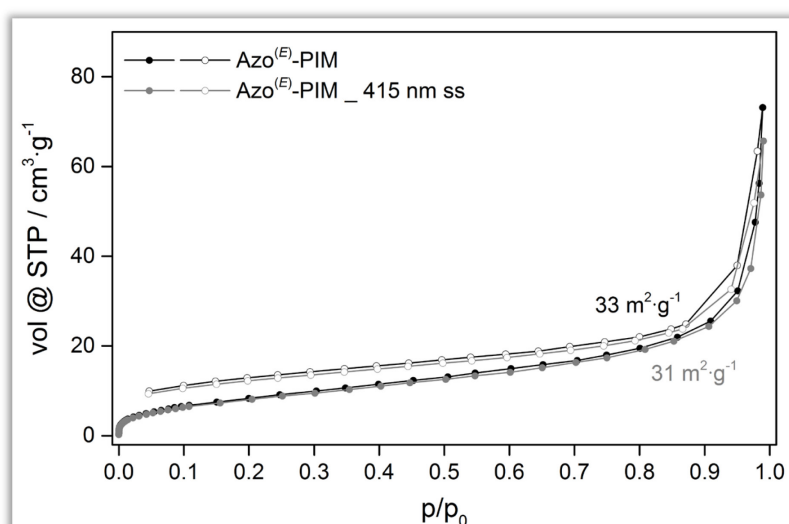


**Figure A18.** Isotherms derived from nitrogen sorption at 77 K for Azo<sup>(E)</sup>-PIM before (black) and after illumination with 415 nm in solid state (grey). Solid symbols: adsorption, hollow symbols: desorption.

#### Note on 3D renderings:

Figures 1, 3, 6 (left part), 33, 52, and 66 were conceived and produced by the author of this thesis by utilisation of the 3D software  blender<sup>™</sup>, which can be obtained free of charge from <https://www.blender.org/download/> (as of December 2016).



**EXPERIMENTAL**

**PART**

## INSTRUMENTATION

Samples for nitrogen sorption at 77 K and krypton sorption at 87 K were activated by degassing in vacuum at varying temperatures and for varying periods of time. For a detailed overview refer to appended spreadsheet. Samples measured on Quadrasorb have been activated with a MasterPrep whereas those measured on or Autosorb-iQ have been activated directly on the Autosorb machine. All devices mentioned in this paragraph were manufactured by Quantachrome Instruments. The employed software was ASiQwin (v. 3.01).

	adsorbate	machine	activation	
			$\vartheta$ /°C	t/h
PPN-6_films	Kr	Autosorb iQ	100	1
PPN-6_bulk_18 h	N <sub>2</sub>	Autosorb iQ	200	17
PPN-6_bulk_18 min	N <sub>2</sub>	Quadrasorb	110	20
PPN-6_bulk_50 min	N <sub>2</sub>	Quadrasorb	110	20
CMP-1_bulk_35 min	N <sub>2</sub>	Autosorb iQ	80	20
CMP-1_bulk_19 h	N <sub>2</sub>	Autosorb iQ	80	20
silica_pristine	N <sub>2</sub>	Quadrasorb	80	20
silica_PPN-6_1 <sup>st</sup> polym.	N <sub>2</sub>	Quadrasorb	110	20
silica_PPN-6_2 <sup>nd</sup> polym.	N <sub>2</sub>	Quadrasorb	110	20
silica_HMDS	N <sub>2</sub>	Quadrasorb	80	20
silica_HMDS_PPN-6	N <sub>2</sub>	Quadrasorb	110	20
silica_PBPTMOS	N <sub>2</sub>	Quadrasorb	80	20
silica_PBPTMOS_PPN-6_wet	N <sub>2</sub>	Quadrasorb	110	20
silica_PBPTMOS_PPN-6_dry	N <sub>2</sub>	Quadrasorb	110	20
DAE-CMP_open	N <sub>2</sub>	Autosorb iQ	70	20
DAE-PIM	N <sub>2</sub>	Quadrasorb	40	10
DAE-Azo	N <sub>2</sub>	Quadrasorb	40	10

Surface enhanced infrared absorption spectroscopy (SEIRAS)—operated by Nina Heidary at Technische Universität Berlin—for monitoring the adsorption of a 4-bromothiophenol self-assembled monolayer on a gold surface was carried out in a Kretschmann-like attenuated total reflection configuration. Details about the ATR-FTIR set-up are given elsewhere.<sup>[259-260]</sup> The removable single crystal silicon prism of the ATR cell was coated with a thin nanostructured gold film to obtain an adequate surface enhancement. FTIR spectra were recorded with a spectral resolution of 4 cm<sup>-1</sup> on a Bruker IFS66v/s IR spectrometer equipped with a photoconductive MCT detector cooled with liquid nitrogen. For each spectrum 400 scans were accumulated.

Liquid NMR analyses was conducted on a Bruker Avance II 400 MHz or 200 MHz device. Solid state NMR spectra were recorded on a Bruker Avance 400 MHz Solid State. The data were processed using the Topspin software (v. 3.2).

UV–vis analyses were carried out on a Varian Cary 300 Scan UV–visible Spectrophotometer (instrument version 10) employing a scan rate of  $600 \text{ nm}\cdot\text{min}^{-1}$  and a data interval of 1 nm with the source changeover set to 350 nm. The used software was Varian Cary WinUV Software.

Infrared spectra were acquired on a Varian 640IR spectrometer equipped with a GladiATR cell and running the Varian ResolutionsPro (v. 5.2.0) software.

SEM and EDX analyses—operated by Prof. Anna Fischer, Axel Heilemann and Dr. Amandine Guiet at Technische Universität Berlin and Albert-Ludwigs-Universität Freiburg—were acquired using either a FEG-SEM Hitachi SU8030, operated between 5 and 15 kV, equipped with a TEAM EDX-System from EDAX (30 mm<sup>2</sup> SDD) or a FEG-SEM Hitachi SU8220, operated between 5 and 15 kV, equipped with an EDX System (X-Flash and FlatQuad) from Bruker.

Elemental analyses were performed on a Thermo FlashEA 1112 Organic Elemental Analyzer using dynamic flash combustion or high-temperature pyrolysis in combination with the Eager 300 software. Note: A 'Δ' in the percentage values for certain elements, *e.g.* fluorine, denotes a value that is obtained by deduction of the other obtained measured values from 100 %.

Thermo-gravimetric analyses were conducted on a Mettler Toledo TGA1 STARe System using the STARe SOFTWARE (v. 12.10b).

Mass spectrometric measurements were obtained by employing a LTQ Orbitrap XL (atmospheric-pressure chemical ionization (APCI) and electrospray ionization (ESI)) or a MAT 95S (electron impact (EI) ionization) equipped with the Excalibur software (v. 2.10).

Powder X-ray diffraction analyses were performed on a Bruker D8 Advance using the Cu K $\alpha$  excitation wavelength of  $\lambda = 154.18 \text{ pm}$  and the DiffracSuite software package (v.2 2.2.60.0).

Gel permeation chromatography was conducted on a device from Thermo Separation Products in combination with a Shodex RI-71 detector and the PSS WinGPC UniChrom software (v. 8.0.6).

Gas diffusion experiments—operated by Nora Konnertz and Martin Böhning at Bundesanstalt für Materialforschung und -prüfung—were conducted applying the time-lag method. In a temperature-controlled set-up the dense, defect-free polymer film with a diameter of 38 mm is placed in a permeation cell on a porous metal support and sealed by a Viton O-ring. The film and the entire cell are thoroughly evacuated before the probe gas is fed into the upstream compartment. The pressure in the closed and previously evacuated downstream volume is measured with a temperature-controlled MKS Baraton gauge (128 A, 10 mbar range) and recorded as function of time.<sup>[250]</sup>

Illumination for the purpose of isomerisation was done using either a laboratory lamp usually employed for thin layer chromatography at 254 nm (6 W) for UV exposure or a Lumatec Superlite S400 at 550 nm for exposure to visible light. At one instance, a 1000 W Xe-Arc lamp (model 6271) from Newport Spectra-Physics with an optical filter to generate 480 nm was utilised in the attempt to switch open the closed form of DAE-CMP. This experiment was conducted by Dr. Alexis Goulet-Hanssens at Humboldt-Universität zu Berlin.

Glovebox: MBraun UniLAB with Siemens Panel Touch, H<sub>2</sub>O < 0.1 ppm, O<sub>2</sub> < 0.1 ppm)

Vacuum oven: Heraeus model VT6025

## MATERIALS

(chemicals were used as received unless stated otherwise; percentage values are given as wt.%)

Nitrogen and argon gas (< 2.0 ppm-mol H<sub>2</sub>O, 99.999 %) were purchased from Air Liquide.

Deionised water (0.057 µS) was home-grown with a Millipore Elix 20 with 12'' vent Ctg with CO<sub>2</sub> trap and a Q-Gard TL.

Ethanol (≥ 99.8 %), methanol (≥ 99.0 %), acetone (≥ 99.9 %), *n*-pentane (≥ 99.0 %), *n*-hexane (≥ 95.0 %), dichloromethane (≥ 99.5 %), chloroform (≥ 99.0 %), tetrahydrofuran (≥ 99.5 %), toluene (≥ 99.5 %), acetonitrile (≥ 99.9 %), diethylether (≥ 99.5 %), and acetic acid (100 %) were purchased from Carl Roth.

*N,N'*-dimethylformamide (≤ 0.005 % H<sub>2</sub>O, 99.8 %), tetrahydrofuran (≤ 0.005 % H<sub>2</sub>O, 99.5 %) were purchased from Acros Organics.

Diethylether (anh., stabiliser: BHT, ≥ 99.0 %), chloroform (anh., stabiliser: amylenes, ≥ 99.0 %), 1,4-dioxane (anh., 99.8 %) were purchased from Sigma Aldrich.

Parabromophenyltrimethoxysilane (99 %) was purchased from Gelest.

Octafluorocyclopentene (97 %) was purchased from ChemPur.

Tetraphenylmethane (96 %) was purchased from Alfa Aesar.

Sulphuric acid (98 %), hydrogen peroxide (aqueous, 30 %), silica gel (40-63 µm, 400-230 mesh), sodium hydroxide (≥ 99.0 %), hydrochloric acid (aqueous, 37 %), and sodium sulphate (≥ 99.0 %) were purchased from Carl Roth.

2,2'-dibromo-9,9'-spirobi[9*H*-fluorene] and 1,3,5-triethynylbenzene were purchased from TCI. The former was purified by column chromatography prior to use. 1,3,5-triethynylbenzene was purified by a filter column (eluent: dichloromethane).

4-iodobenzenesulphonyl chloride (97 %), bis(1,5-cyclooctadiene)nickel(0), potassium hexacyanoferrate(III) (99 %), and potassium carbonate (99 %) were purchased from Acros Organics. Potassium carbonate was dried in vacuum at 170 °C for 24 h when required.

Tetrakis(triphenylphosphine)palladium(0) (99 %), 4-bromothiophenol (95 %), bromine (99 %), triphenylphosphine (99 %), 2,2'-bipyridyl ( $\geq 99.0$  %), 1,5-cyclooctadiene ( $\geq 99.0$  %), 1,4-diiodobenzene (99 %), Pluronic-123 (100 %), tetraethyl orthosilicate (98 %), hexamethyldisilazane (99 %), 2-methylthiophene (98 %), *n*-BuLi ( $1.6 \text{ mol}\cdot\text{l}^{-1}$  and  $2.5 \text{ mol}\cdot\text{l}^{-1}$  in hexanes), chloro trimethylsilane ( $\geq 99.0$  %), iodine monochloride (100 %), triisopropyl borate (98 %), copper(I) iodide (98 %), 1,1'-bis(diphenylphosphino)ferrocene (97 %), [1,1'-bis(diphenylphosphino)ferrocene]dichloro palladium(II) (100 %), potassium acetate (100 %), bis(pinacolato)diboron (99 %), 3,5-difluoroaniline (99 %), potassium hydroxide (100 %), 5,5',6,6'-tetrahydroxy-3,3',3'-tetramethyl-1,1'-spirobiindane (96 %), triethylamine (anh.,  $\geq 99.5$  %), sodium thiosulphate ( $\geq 98.0$  %), and gold coated silicon wafers (thickness of silicon: 0.5 mm, crystalline orientation:  $\langle 100 \rangle$ , coated with titanium (99.99 %) adhesion layer to bind the gold (99.999 %, 100 nm thickness, polycrystalline with preference to  $\langle 111 \rangle$  orientation) to the silicon wafer) were purchased from Sigma Aldrich. Potassium acetate was dried in vacuum at  $170$  °C for 48 h when required.

#### GENERAL PROCEDURE FOR SAM FORMATION

Silicon wafer shards were cleaned prior to use by treatment with piranha solution for 10 min.<sup>1</sup> subsequently wafer pieces were flushed with copious amounts of water followed by ethanol and dried in a nitrogen stream whereupon the wafer shards were immersed in a  $1 \text{ mmol}\cdot\text{l}^{-1}$  ethanolic solution of the respective SAM-molecule (4-bromothiophenol or 4-iodothiophenol) in a vial. The solution was covered with argon, the vial sealed and placed in the dark for 16 h. The functionalised pieces were taken out, flushed thoroughly with ethanol and dried in a nitrogen stream.

As-prepared SAM-functionalised substrates were subjected to reaction mixture within hours until when they were stored in an argon filled vial in order to avoid adventitious adsorption of water or any organic compound ubiquitously present in a laboratory environment.<sup>[124,261]</sup>

#### GENERAL PROCEDURE FOR FILM FORMATION<sup>[122]</sup>

In order to avoid mechanical stress imposed upon the substrates by a stirrer, a scheme was conceived that enabled the silicon shards to be immersed in the solution from atop with no contact whatsoever to a stirrer inside the reaction vessel. Additionally, the applied technique permitted the immersion depth to be controlled. To achieve this, the samples were held by a crocodile clip the teeth of which were covered by several layers of PTFE thread. This proved necessary owing to the single crystalline nature of the wafer shards the anisotropy of which can lead to breakage only by the pressure that is generated by the spiky teeth of the crocodile clip. PTFE covering disposed of this

<sup>1</sup> Piranha solution (Caro's acid): conc. sulphuric acid/30 % aqueous hydrogen peroxide 2/1 (V/V).

Warning! Piranha solution is an extremely oxidising agent. Nascent oxygen will react violently with anything organic. Therefore, any organic residues, even remaining solvent in a frit, must be avoided by prior washing with polar organic solvent followed by copious amounts of water. Moreover, in order to avoid an excess of peroxide, sulphuric acid has to be allocated firstly followed by hydrogen peroxide of no more than half the allocated volume. When mixed, the solution gets boiling hot so that glass apparatuses cannot be handled barehanded.

problem as the pressure was reduced due to enhanced contact surface between the clip and the shard. The clip itself was attached to a wire (iron coated with zinc) that was pierced through a septum thus ensuring an inert atmosphere and at the same time allowing of the substrates to be immersed in the solution from atop (*cf.* **Figure 23**).

The final assembly of the reaction vessel was conducted inside a glovebox. After the solution has been prepared, the vials were sealed with a septum that accommodated the crocodile clip holding two substrates back to back. In this manner, two substrates with two different SAMs could be subjected at once to the very same reaction mixture or, for that matter, one SAM-functionalised and one blank sample. Having thus ensured an inert atmosphere, vials were taken out of the glovebox and placed for stirring inside fume hood either at room temperature (r.t.) (PPN-6 films) or at 80 °C (CMP-1 films).

### MONOLITHIC SBA-15-TYPE SILICA

In a typical synthesis a 50 ml round bottom flask was charged with block-copolymer P-123 (2.0 g) followed by ethanol (10.0 ml) and  $\text{HCl}_{(\text{aq})}$  ( $1.0 \text{ mol}\cdot\text{l}^{-1}$ , 0.4 g, 0.4 ml). The mixture was stirred until a homogeneous suspension was obtained before tetraethyl orthosilicate (TEOS) (4.16 g) was added dropwise *via* pipette. The sol was then stirred for 15 min before being poured into vessels of *e.g.* tubular shape. The sol was left ageing at r.t. for 40 h to yield a solidified, clear gel that was not entirely crack free but still retained the shape of the mold. At this stage the gels were covered with a layer of paraffin oil ca. 3 mm in thickness before being subjected to ageing at elevated temperature (60 °C, 18 h). As a result, crack formation became enhanced leading to silica blocks that fell apart yet not into powder but rather into tangible chunks.

The shape of the vessel the sol is poured into has a tremendous effect on the first ageing progress at r.t. For example, when a syringe, large (20 ml) or small (1 ml), was filled with sol and left standing with the only opening being the tip of the syringe (no needle attached), the sol would not solidify but rather display sedimentation of its components. Conversely, a 50 ml cylindrical glass vial (diameter 2.4 cm, height 9.5 cm) with an opening of ca. 2.3 cm gave the best results. The main reason is the opening of the respective vessel and how well it allows the ethanol to evaporate.

The aged silica chunks were subjected to calcination according to the following heating protocol:

- 25 °C to 550 °C in 17.5 h ( $30 \text{ }^\circ\text{C}\cdot\text{h}^{-1}$ )
- 550 °C for 6 h
- cooling to r.t. overnight

### FUNCTIONALISATION WITH HMDS

Monolithic silica chunks (4.1957 g) were dried under vacuum at 120 °C for 4 h to remove residual water before being immersed in dry toluene (30 ml). At r.t. and under argon atmosphere HMDS (18.7967 mmol, 3.0337 g, 3.9917 ml) was added *via* syringe. In order not to impair the structural integrity of the silica chunks the magnetic stirrer was operated very carefully initially before being deactivated altogether. Mixture was heated up to 70 °C and kept at this temperature for 23 h before being allowed to cool to r.t. After silica pieces were collected *via* filtration (frit, porosity 4, vacuum)

and washed with toluene, acetone, ethanol, ethanol/water (1/1, V/V), water, ethanol, acetone, *n*-pentane in that order, they were dried in vacuum at 80 °C for 15 h.

#### FUNCTIONALISATION WITH PBPTMOS

Monolithic silica chunks (17.2205 g) were dried under vacuum at 120 °C for 24 h to remove residual water before being immersed in dry toluene (60 ml). At r.t. and under argon atmosphere PBPTMOS (16.7039 mmol, 4.6301 g, 2.8371 ml) was added *via* syringe. Without stirring mixture was refluxed overnight before being allowed to cool to r.t.

After silica pieces were collected *via* filtration (frit, porosity 4, vacuum) and washed with copious amounts of dichloromethane, they were dried in vacuum at 80 °C for 20 h.

#### PPN-6 FORMATION | WET-APPROACH

The procedure was carried out in a glove box. A flame-dried glass vial was charged with bis(1,5-cyclooctadiene)-nickel(0) (4.6258 eq., 0.6020 mmol, 0.1656 mg), 2,2'-bipyridyl (4.6028 eq., 0.5990 mmol, 0.0936 mg), dry DMF (12.5 ml) and dry THF (10.5 ml). The mixture was stirred until a solution was obtained. 1,5-cyclooctadiene (4.6575 eq., 0.6061 mmol, 0.0656 mg, 0.0745 ml) was added *via* Eppendorf pipette and solution stirred for a 1 min. Monomer tetrakis(4-bromophenyl)methane (1.0000 eq., 0.1301 mmol, 0.0828 g) dissolved in THF (2 ml) was added *via* pipette and complemented reaction mixture stirred for 0.5 min. PBPTMOS-functionalised silica pieces (9.8700 g) were transferred into reaction vial and without stirring reaction proceeded for 18 h after which aqueous hydrochloric acid (6 mol·l<sup>-1</sup>, 8.1 ml). Mixture was slightly moved to ensure proper mixing and left standing for ca. 2 h until colour changed from brownish-red to blueish-green. Bulk polymer floated at top of liquid phase whereas silica pieces rested at bottom. Bulk PPN-6 could be removed *via* pipette. Silica pieces were filtered off (frit, porosity 4, vacuum), washed with water and methanol thrice each and THF once before being Soxhlet extracted (THF, overnight) and subsequently dried in vacuum (110 °C, 26 h).

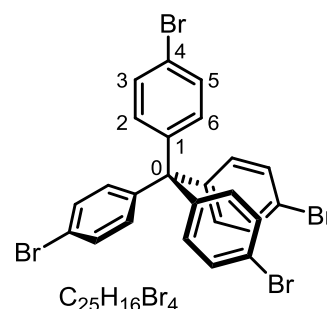
#### PPN-6 FORMATION | DRY-APPROACH

The procedure equals the protocol described above for the wet-approach up until the point where the silica pieces are introduced into the reaction vial. After that has been achieved the heterogeneous mixture was left standing for 5 min before the reaction mixture was withdrawn *via* pipette yielding the silica pieces bereft of surplus reaction medium but properly impregnated (*cf.* **Figure 41**). Quenching with HCl<sub>(aq)</sub> necessitated prior addition of THF (25 ml) in order generate a liquid environment. After silica pieces turned from brownish-red to blueish-green (ca. 2 h) the procedure again equals the one described in the wet-approach.

#### TETRAKIS(4-BROMOPHENYL)METHANE<sup>[262]</sup>

A 50 ml two-neck round bottom flask—equipped with a Dimroth reflux condenser to accommodate and alleviate bromine fumes—was charged with bromine (20.0 eq., 125.7841 mmol, 20.1013 g, 6.4795 ml). At r.t., tetraphenylmethane (1.0 eq., 6.2892 mmol, 2.0152 g) was added under stirring as

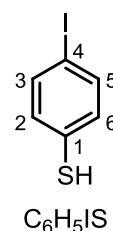
solid in small portions. With the flask left open, the heterogeneous mixture was stirred for 45 min and then cooled to  $-78\text{ }^{\circ}\text{C}$  (solid  $\text{CO}_2/\text{acetone}$ ) to add ethanol (excess, 15.7 ml) dropwise. The reaction mixture was allowed to warm to r.t. overnight. The solid was filtered off (frit, porosity 5, vacuum) and washed with aqueous sodium thiosulphate solution ( $0.5\text{ mol}\cdot\text{l}^{-1}$ , 200 ml) and water (400 ml) to yield a brown-yellowish solid that was thoroughly dried in the frit. The solid was then dissolved in THF (60 ml) and sodium sulphate added to remove residual water. Solution filtered off (folded filter, gravity) and evaporated to dryness to yield the crude product as pale yellow solid in quantitative yield. The crude product was purified by column chromatography (silica, crude product infused on silica, V/V (*n*-pentane/DCM) 93/7  $\rightarrow$  90/10) to yield the clean product as white solid (3.4507 g, 86 %).



**NMR- $^1\text{H}$**  200 MHz,  $\text{CDCl}_3$ ,  $\delta$  / ppm: 7.39 (d,  $J = 8.7\text{ Hz}$ , 8 H,  $\text{H}^{3,5}$ ), 7.01 (d,  $J = 8.7\text{ Hz}$ , 8 H,  $\text{H}^{2,6}$ )  
**NMR- $^{13}\text{C}$**  50 MHz,  $\text{CDCl}_3$ ,  $\delta$  / ppm: 144.6 ( $\text{C}^1$ ), 132.5 ( $\text{C}^{3,5}$ ), 131.2 ( $\text{C}^{2,6}$ ), 121.0 ( $\text{C}^4$ ), 63.9 ( $\text{C}^0$ )

#### 4-iodothiophenol<sup>[263]</sup>

A flame-dried 250 ml Schlenk flask equipped with robust stirrer was charged with 4-iodobenzenesulphonyl chloride ('pipsyl chloride', 1.0 eq., 19.8351 mmol, 6.0003 g). Dry toluene (100 ml) was added under argon atmosphere *via* syringe to yield a suspension. At r.t., triphenylphosphine (3.0 eq., 59.5053 mmol, 15.6077 g) was added under vigorous stirring in small portions under argon flow which causes the mixture to warm up. The obtained foamy suspension of yellowish colour was kept stirring for 10 min without additional external heating followed by stirring for an additional 10 min at  $60\text{ }^{\circ}\text{C}$  by means of external heating. Then, suspension was allowed to cool to  $50\text{ }^{\circ}\text{C}$  whereupon water (25 ml) was slowly added and mixture stirred for 30 min. Aqueous layer (AL) was discarded, organic layer (OL) extracted with  $\text{NaOH}_{(\text{aq})}$  (10 w-%,  $2 \times 100\text{ ml}$ ) to deprotonate render hydrophilic the thiol. The obtained alkaline AL was washed with toluene (3  $\times$ ) and acidified with  $\text{HCl}_{(\text{aq})}$  ( $4\text{ mol}\cdot\text{l}^{-1}$ ) until pH plummeted from above 11 to below 2, which consumed approximately 120 ml of  $\text{HCl}_{(\text{aq})}$ . When aqueous medium turns acidic, the thiol gets reprotonated thus insoluble in water evidenced by an observed precipitation of white solid accompanied by the emergence of a distinct odour reminiscent of that of 4-bromothiophenol. Acidic AL was extracted with DCM (3  $\times$ ) causing the precipitate to dissolve rapidly. Merged OLs dried over sodium sulphate, filtered off (folded filter, gravity) and evaporated to dryness to yield a white crystalline solid that was purified by sublimation (overnight,  $1\text{E}-3\text{ mbar}$ ,  $\vartheta_{\text{oil bath}} = 50\text{ }^{\circ}\text{C}$ ,  $\vartheta_{\text{coolant (water)}} = 10\text{ }^{\circ}\text{C}$ ) to yield the clean product as white crystalline solid (3.9801 g, 85 %).



**NMR  $^1\text{H}$**  200 MHz,  $\text{CDCl}_3$ ,  $\delta$  / ppm: 7.54 (d,  $J = 8.4\text{ Hz}$ , 2 H,  $\text{H}^{3,5}$ ), 7.01 (d,  $J = 8.5\text{ Hz}$ , 2 H,  $\text{H}^{2,6}$ ), 3.42 (s, S-H)

**NMR  $^{13}\text{C}$**  50 MHz,  $\text{CDCl}_3$ ,  $\delta$  / ppm: 138.2 ( $\text{C}^{3,5}$ ), 131.3 ( $\text{C}^{2,6}$ ), 131.1 ( $\text{C}^1$ ), 90.3 ( $\text{C}^4$ )

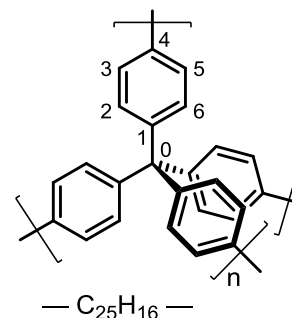
**PPN-6 FILMS**<sup>[50,122]</sup>

A flame-dried 50 ml vial equipped with triangular stirrer was charged with 2,2'-bipyridyl (4.6028 eq., 0.5999 mmol, 0.0937 g) and bis(1,5-cyclooctadiene)nickel(0) (4.6258 eq., 0.6029 mmol, 0.1658 g). Addition of dry DMF (12.53 ml) and dry THF (10.53 ml) ensued upon which a deep violet mixture was obtained that was stirred for 5 min at r.t. to dissolve components. 1,5-cyclooctadiene (4.6575 eq., 0.6071 mmol, 0.0657 g, 0.075 ml) was added and solution stirred shortly. In a separate vial, flame-dried beforehand, monomer tetrakis(4-bromophenyl)methane (1.0000 eq., 0.1303 mmol, 0.0829 g) was dissolved in 2 ml of dry THF in order to ensure proper mixing of the components from the very beginning. Immediately after dissolved monomer was added to the prepared reaction solution, silicon wafer pieces were subjected to the reaction. It lasted only minutes to observe a colour change from violet to brown. Reactions were quenched after varying amounts of time (18 or 50 min, 18 or 20 h) by careful addition of  $\text{HCl}_{(\text{aq})}$  ( $6 \text{ mol}\cdot\text{l}^{-1}$ , 8.1 ml) followed by stirring for approximately 2 h until reaction mixture turned from brown over reddish to blueish-green with white bulk polymer floating at the top of the phase boundary. Silicon wafer pieces were then taken out and rinsed with ample amounts of water, methanol, chloroform and THF. Bulk polymer was filtered off (frit, porosity 4, vacuum) and washed accordingly before both silicon shards and bulk polymer were Soxhlet extracted from THF overnight. Silicon substrates dried in vacuum at  $80^\circ\text{C}$  overnight and bulk polymer dried in vacuum at  $110^\circ\text{C}$  overnight. The short-term experiment applying 18 min and 50 min reaction time yielded 0.0363 g (87 %) and 0.0396 g (95 %), respectively. The long-term trial, surprisingly, yielded only 78 %.

Analytical data for bulk polymer:

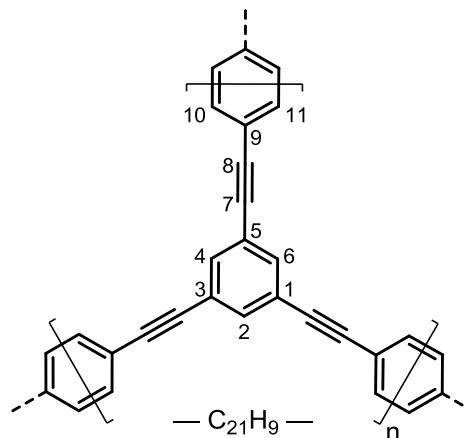
**NMR**  $^{13}\text{C}$  solid state, CP-MAS,  $\nu_{\text{rot}} = 10 \text{ kHz}$ ,  $\delta / \text{ppm}$ : 143.9 ( $\text{C}^4$ ), 137.3 ( $\text{C}^1$ ), 128.8 ( $\text{C}^{2,6}$ ), 123.0 ( $\text{C}^{3,5}$ ), 62.2 ( $\text{C}^0$ ). At 27.7 ppm an additional signal protrudes the side band which can be ascribed to residual THF.

**EA** calculated (found) for  $\text{C}_{25}\text{H}_{16}^{4*}$  in m-%: C 94.90 (92.70), H 5.10 (6.18).

**CMP-1 FILMS**

A flame-dried 50 ml vial equipped with triangular stirrer was charged with 1,3,5-triethynylbenzene (0.67 eq., 0.0926 mmol, 0.0139 g), 1,4-diodobenzene (1.00 eq., 0.1388 mmol, 0.0458 g) and tetrakis(triphenylphosphine)-palladium(0) (0.013 eq., 0.0018 mmol, 0.0021 g). Addition of dry TEA (16.68 ml) and dry DMF (8.84 ml) ensued and mixture was stirred for 5 min until solution was obtained. Vial sealed with septum that accommodated the clip holding two substrates. Reaction vessel was taken out from glovebox and placed in a pre-heated oil bath ( $80^\circ\text{C}$ ).

Reaction solution remained colourless for the first 10 min thenceforth assumed a yellow tinge but



stayed clear for ensuing 15 min. Subsequently, solution turned turbid hinting at beginning precipitation. Thanks to low concentration of  $0.00555 \text{ mol}\cdot\text{l}^{-1}$  (1,4-diiodobenzene) everything was kept in motion for the entire duration of the reaction that was aborted after periods of time of 35 min and 19 h. Resultant precipitate was filtered off (frit, porosity 4, vacuum) and washed with methanol, THF and DCM. Silicon wafer substrates were washed accordingly and both bulk polymer and substrates were Soxhlet extracted (methanol, overnight). Bulk polymer was dried in vacuum oven ( $80 \text{ }^\circ\text{C}$ , overnight) to yield CMP-1 as pale yellow powder in quantities of 0.0227 g (63 %, 35 min trial) and 0.0263 g (72 %, 19 h trial).

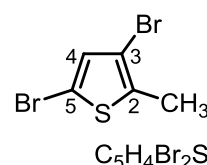
Analytical data for bulk polymer:

**NMR**  $^{13}\text{C}$  solid state, CP-MAS,  $\nu_{\text{rot}} = 10 \text{ kHz}$ ,  $\delta / \text{ppm}$ : 134.4 ( $\text{C}^{2,4,6}$ ), 128.0 ( $\text{C}^{10,11}$ ), 120.8 ( $\text{C}^{1,3,5}$ ), 87.4 ( $\text{C}^{7,8}$ ). At 78.8 ppm a signal is observed that hails from residual unreacted terminal alkyne groups.

**EA** calculated (found) for  $\text{C}_{21}\text{H}_9$ <sup>9\*</sup> in m-%: C 96.53 (92.53), H 3.47 (3.71).

### 3,5-DIBROMO-2-METHYLTHIOPHENE<sup>[264-266]</sup>

To glacial acetic acid (154 ml) allocated in a 500 ml flask 2-methylthiophene (1.0 eq., 76.8720 mmol, 7.5462 g, 7.398 ml) was added and solution stirred. Flask was placed in water bath to avoid too rapid temperature rise in next step. However, cooling to  $0 \text{ }^\circ\text{C}$  as described in literature is not recommended since glacial acetic acid melts at  $16 \text{ }^\circ\text{C}$ . Dropwise addition of bromine (2.0 eq., 153.7440 mmol, 24.5695 g, 7.920 ml) *via* dropping funnel ensued whereupon solution turned orange-brown. After stirring at r.t. for 5 h, solution transferred into a beaker and aqueous saturated solution of sodium bicarbonate was added carefully (120 ml). Solution extracted with chloroform (5  $\times$ , tlc check for UV-active substance). Organic layer (OL) washed with water (5  $\times$ ) and dried over sodium sulphate, then filtered off (folded filter, gravity) and evaporated to yield crude product as brown liquid (16.3098 g, 83 %). Purification by column chromatography (silica, *n*-hexane 100 %) yielded pure product as pale yellow liquid (7.7404 g, 39 %).



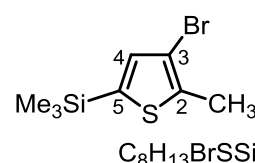
**NMR**  $^1\text{H}$  400 MHz,  $\text{CDCl}_3$ ,  $\delta / \text{ppm}$ : 6.85 (s, 1 H,  $\text{H}^4$ ), 2.34 (s, 3 H,  $\text{CH}_3$ )

**NMR**  $^{13}\text{C}$  100 MHz,  $\text{CDCl}_3$ ,  $\delta / \text{ppm}$ : 136.1 ( $\text{C}^2$ ), 132.0 ( $\text{C}^4$ ), 108.8 ( $\text{C}^5$ ), 108.6 ( $\text{C}^3$ ), 15.0 ( $\text{CH}_3$ )

**MS** APCI, M/Z calculated (found) for  $[\text{M}]$ : 253.83950 (253.83925)

### 3-BROMO-2-METHYL-5-TRIMETHYLSILYLTHIOPHENE<sup>[264-266]</sup>

A flame-dried 3-neck 500 ml flask equipped with dropping funnel was charged with 3,5-dibromo-2-methylthiophene (1.0 eq., 30.2411 mmol, 7.7404 g) under Ar flow. Dry diethyl ether (130 ml) was added. Mixture was stirred and cooled to  $-78 \text{ }^\circ\text{C}$  (solid  $\text{CO}_2$ /acetone) to add *n*-BuLi ( $1.6 \text{ mol}\cdot\text{l}^{-1}$  in *n*-hexane, 1.1 eq., 33.2652 mmol, 2.1308 g, 20.791 ml) dropwise *via* dropping funnel whereupon solution turned yellow and warmed up. After complete addition, mixture was stirred for 90 min at  $-78 \text{ }^\circ\text{C}$  followed by slow addition of trimethylsilyl chloride (2.5 eq., 75.6026 mmol, 8.2136 g, 9.663 ml) *via* syringe. After a further 90 min stirring at  $-78 \text{ }^\circ\text{C}$  cooling was removed and solution allowed to cool to r.t. Reaction mixture poured into water (150 ml) and layers were separated.



Aqueous layer extracted with diethyl ether (3 ×) and merged organic layers dried over sodium sulphate, filtered off (folded filter, gravity) and evaporated to yield crude product as yellow-brownish liquid (7.0981 g, 94 %). Column chromatography (silica, *n*-hexane) gave rise to purified product as colourless clear liquid (6.2375 g, 83 %).

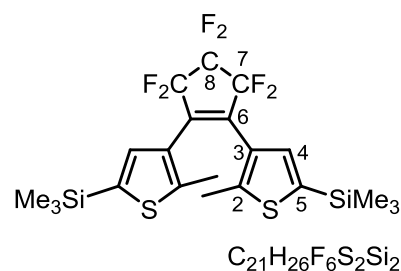
**NMR**  $^1\text{H}$  200 MHz,  $\text{CDCl}_3$ ,  $\delta$  / ppm: 7.03 (s, 1 H,  $\text{H}^4$ ), 2.43 (s, 3 H,  $\text{C}^2\text{-CH}_3$ ), 0.30 (s, 9 H,  $\text{Si-(CH}_3)_3$ )

**NMR**  $^{13}\text{C}$  100 MHz,  $\text{CDCl}_3$ ,  $\delta$  / ppm: 139.5 ( $\text{C}^2$ ), 137.9 ( $\text{C}^4$ ), 136.5 ( $\text{C}^5$ ), 110.8 ( $\text{C}^3$ ), 14.9 ( $\text{C}^2\text{-CH}_3$ ), -0.2 ( $\text{Si-(CH}_3)_3$ )

**MS** APCI, M/Z calculated (found) for [M]: 247.96851 (247.96840)

### 1,2-BIS(2'-METHYL-5'-TRIMETHYLSILYLTHIEN-3'-YL)HEXAFLUOROCYCLOPENT-1-ENE<sup>[264-266]</sup>

A flame-dried 500 ml 2-neck Schlenk flask equipped with dropping funnel was charged with dry THF (215 ml) followed by 3-bromo-2-methyl-5-trimethylsilylthiophene (1.00 eq., 24.4577 mmol, 6.0959 g) *via* syringe. Solution was cooled to  $-78\text{ }^\circ\text{C}$  (solid  $\text{CO}_2$ /acetone) to add *n*-BuLi ( $1.6\text{ mol}\cdot\text{l}^{-1}$  in *n*-hexane, 1.10 eq., 26.9034 mmol, 1.7233 g, 16.815 ml) dropwise *via* dropping funnel. After addition was completed,



mixture was stirred at  $-78\text{ }^\circ\text{C}$  for 2 h whereupon octafluorocyclopentene was added at  $-78\text{ }^\circ\text{C}$  slowly *via* canula as follows: A separate flame-dried 25 ml Schlenk flask was charged with of dry THF (10 ml) and cooled to  $-78\text{ }^\circ\text{C}$  (solid  $\text{CO}_2$ /acetone). Octafluorocyclopentene (0.45 eq., 11.0060 mmol, 2.3337 g, 1.477 ml) was taken from the freezer and readily added to the separate flask *via* syringe (caution: compound is extremely volatile,  $\vartheta_{\text{boil}} = 27\text{ }^\circ\text{C}$ , and evaporates instantaneously out of the syringe because of which the tip of the needle needs to be placed inside the allocated and cooled THF layer). Dissolved octafluorocyclopentene was transferred to the prepared reaction mixture *via* cannula and small flask flushed with dry THF ( $2 \times 10\text{ ml}$ ). Addition of octafluorocyclopentene caused reaction mixture to assume a red-brownish colour. After addition was completed, solution was stirred at  $-78\text{ }^\circ\text{C}$  for 4 h, then cooling was removed and solution stirred for another 18 h. Reaction was quenched by addition of  $\text{HCl}_{(\text{aq})}$  ( $0.1\text{ mol}\cdot\text{l}^{-1}$ , 100 ml) and mixture stirred for 5 min whereupon the red organic layer (OL) was separated. Aqueous layer (AL) was extracted once with diethyl ether, which was merged with THF-OL. Merged OLs dried over sodium sulphate, filtered (folded filter, gravity) and evaporated to obtain crude product as red liquid (6.6088 g, 117 %), that solidified in refrigerator. Column chromatography (silica, *n*-hexane) in combination with recrystallisation (*n*-hexane, fridge) of mixed fractions yielded clean product as waxy, white solid (3.9865 g, 71 %).

**NMR**  $^1\text{H}$  200 MHz,  $\text{CDCl}_3$ ,  $\delta$  / ppm: 7.05 (s, 2 H,  $\text{H}^4$ ), 1.90 (s, 6 H,  $\text{C}^2\text{-CH}_3$ ), 0.27 (s, 18 H,  $\text{Si-(CH}_3)_3$ )

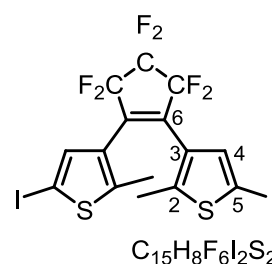
**NMR**  $^{13}\text{C}$  100 MHz,  $\text{CDCl}_3$ ,  $\delta$  / ppm: 146.9, 138.9, 134.1, 133.5 ( $\text{C}^6$ ), 126.7 ( $\text{C}^4$ ), 121.4 ( $\text{C}^7$ ), 109.1 ( $\text{C}^8$ ), 14.2 ( $\text{C}^2\text{-CH}_3$ ), -0.1 ( $\text{Si-(CH}_3)_3$ ).

**MS** APCI, M/Z calculated (found) for [M]: 512.09132 (512.09015)

**EA** calculated (found) for  $\text{C}_{21}\text{H}_{26}\text{F}_6\text{S}_2\text{Si}_2$  in m-%: C 49.19 (49.06), H 5.11 (5.35), S 12.51 (11.97), N 0.00 (0.16)

**1,2-BIS(5'-IODO-2'-METHYLTHIEN-3'-YL)HEXAFLUOROCYCLOPENT-1-ENE**<sup>[264-266]</sup> (**1**)

In a flame-dried 500 ml Schlenk flask 1,2-bis(2'-methyl-5'-trimethylsilylthien-3'-yl)hexafluorocyclopent-1-ene (1.0 eq., 3.9008 mmol, 2.0000 g) was dissolved in dry chloroform (153 ml). Solution was cooled to 0 °C (crushed ice/water) before iodine monochloride (4.0 eq., 15.6032 g, 2.5333 g) was added in one portion under Ar flow causing the solution to assume a red colour. Solution was stirred at 0 °C for 4.25 h after which the cooling was removed and solvent evaporated. Obtained residue redissolved in chloroform (300 ml) and washed with aqueous sodium thiosulphate solution (0.5 mol·l<sup>-1</sup>, 2 ×). Each aqueous layer (AL) was extracted with chloroform twice. Merged organic layers (OLs) were washed with water twice and each resulting AL extracted with chloroform once. Merged OLs dried over sodium sulphate, filtered off (folded filter, gravity) and evaporated to give crude product as red, highly viscous oil (2.5942 g, 107 %) that solidifies partially in refrigerator. Column chromatography (silica, *n*-pentane/DCM 98/2 (V/V)) yielded clean product as pink, highly viscous substance (2.0825 g, 86 %).



**NMR** <sup>1</sup>H 200 MHz, CDCl<sub>3</sub>, δ / ppm: 7.18 (s, 2 H, H<sup>4</sup>), 1.90 (s, 6 H, C<sup>2</sup>-CH<sub>3</sub>)

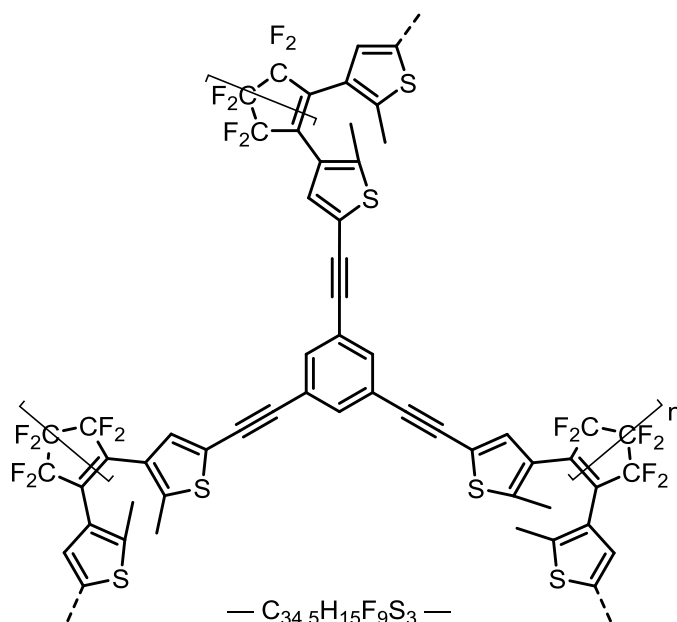
**NMR** <sup>13</sup>C 100 MHz, CDCl<sub>3</sub>, δ / ppm: 147.8 (C<sup>2</sup>), 136.2, 126.7, 70.9 (C<sup>5</sup>), 14.5 (C<sup>2</sup>-CH<sub>3</sub>)

**MS** EI, M/Z calculated (found) for [M]<sup>+</sup>: 619.80555 (619.80599)

**EA** calculated (found) for C<sub>15</sub>H<sub>8</sub>F<sub>6</sub>I<sub>2</sub>S<sub>2</sub> in m-%: C 29.05 (28.93), H 1.30 (1.47), S 10.34 (9.71), N 0.00 (0.11)

**DAE-CMP**

An oven-dried Schlenk-tube with thick glass wall was charged with **1** (1.00 eq., 0.3225 mmol, 0.2000 g) and purified 1,3,5-triethynylbenzene (0.67 eq., 0.2150 mmol, 0.0323 g). Dry TEA (2.443 ml) and dry DMF (2.443 ml) were added and mixture stirred until solution was obtained. Schlenk-tube sealed with screw cap and heated up to 100 °C before a slurry of tetrakis(triphenylphosphine)palladium(0) (0.0288 eq., 0.0093 mmol, 0.0108 g) and copper(I) iodide (0.0525 eq., 0.0169 mmol, 0.0032 g) in dry DMF



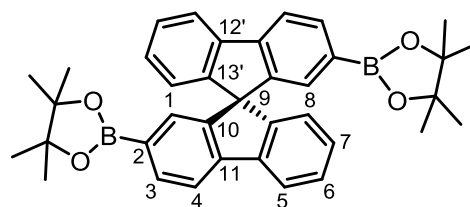
(0.212 ml) was added under argon flow. Schlenk-tube was resealed and mixture stirred at 100 °C for 18 h. Formed blackish coloured solid was filtered off (frit, porosity 4, vacuum) and washed with chloroform, water, methanol and acetone (3 × each). Soxhlet extraction (methanol, 18 h) and consecutive drying in vacuum (70 °C, 18 h) yielded a black insoluble solid (0.1578 g, 105 %).

**NMR**  $^{13}\text{C}$  solid state, CP-MAS,  $\nu_{\text{rot}} = 10$  kHz,  $\delta$  / ppm: 142.3, 133.3, 124.0, 113.9 (sh), 92.1 (C≡C), 82.6 (C≡C), 59.2, 12.4 (CH<sub>3</sub>)

**EA** calculated (found) for C<sub>34.5</sub>H<sub>15</sub>F<sub>9</sub>S<sub>3</sub> in m-%: C 59.48 (61.61), H 2.17 (3.26), S 13.81 (12.15), F(Δ) 24.54 (21.79), N 0.00 (1.20)

**2,2'-BIS(4,4,5,5-TETRAMETHYL-1,3,2-DIOXABOROLAN-2-YL)-9,9'-SPIROBIFLUORENE**<sup>[267]</sup> (**2**)

A flame-dried 250 ml Schlenk flask equipped with reflux condenser was charged with 2,2'-dibromo-9,9'-spirobi[9H-fluorene] (1.0 eq., 4.1937 mmol, 1.9886 g), bis(pinacolato)diboron (2.2 eq., 9.2262 mmol, 2.3429 g), 1,1'-bis(diphenylphosphino)ferrocene (0.1 eq., 0.4194 mmol, 0.2325 g), 1,1'-bis(diphenylphosphino)-



C<sub>37</sub>H<sub>38</sub>B<sub>2</sub>O<sub>4</sub>

ferrocene palladium(II)dichloride (0.1 eq., 0.4194 mmol, 0.3069 g) and anhydrous potassium acetate (6.0 eq., 25.1622 mmol, 2.4695 g). The solids were degassed in vacuum with consecutive refilling with argon for four times. Dry 1,4-dioxane (84 ml) was added *via* syringe and mixture refluxed for 20 h (reaction progress checked by means of tlc). After cooling to r.t., DCM and water were added to separate organic layer (OL). Aqueous layer was extracted with DCM (3 ×) and merged OLs washed with water (2 ×), dried over sodium sulphate, filtered off (folded filter, gravity) and evaporated to dryness to yield a black solid as crude product. Purification by column chromatography (silica, *n*-pentane/ethyl acetate 99/1 → 90/10 (V/V)) yielded clean product as white solid (1.3101 g, 55 %).

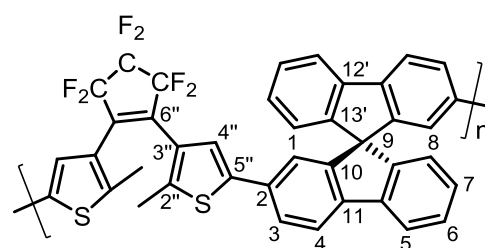
**NMR**  $^1\text{H}$  200 MHz, CDCl<sub>3</sub>,  $\delta$  / ppm: 7.91-7.80 (m, 6 H, H<sup>Ar</sup>), 7.35 (t,  $J = 7.5$  Hz, 2 H, H<sup>Ar</sup>), 7.17 (s, 2 H, H<sup>Ar</sup>), 7.09 (dt,  $J = 7.6, 0.9$  Hz, 2 H, H<sup>Ar</sup>), 6.66 (d,  $J = 7.6$  Hz, 2 H, H<sup>Ar</sup>), 1.26 (s, 24 H, 8 × CH<sub>3</sub>)

**NMR**  $^{13}\text{C}$  50 MHz, CDCl<sub>3</sub>,  $\delta$  / ppm: 149.7, 147.7, 145.2, 141.6, 134.9, 130.6, 128.4, 127.7, 124.2, 120.6, 119.5, 83.8 (C<sup>quat,ethylene</sup>), 66.07 (C<sup>q</sup>), 25.0 (CH<sub>3</sub>)

**MS** APCI, M/Z calculated (found) for [M+H]<sup>+</sup>: 569.30290 (569.30310)

**DEA-PIM**

A 250 ml Schlenk flask equipped with reflux condenser was evacuated and refilled with argon three times before being charged with **1** (1.0 eq., 1.9350 mmol, 1.2000 g), **2** (1.0 eq., 1.9350 mmol, 1.0997 g) and tetrakis(triphenylphosphine)palladium(0) (0.05 eq., 0.0968 mmol, 0.1118 g). Reaction vessel degassed and backfilled with argon thrice. A mixture of DMF



— C<sub>40</sub>H<sub>22</sub>F<sub>6</sub>S<sub>2</sub> —

(14.885 ml) and THF (14.885 ml), degassed by three freeze-thaw-cycles, was added to yield a suspension. Aqueous potassium carbonate solution (2 mol·l<sup>-1</sup>, 3.85 eq., 7.4425 mmol, 1.0286 g in 3.721 ml water) was added, reaction vessel sealed by screw cap and solution again degassed by three freeze-thaw cycles. Solution heated up to 120 °C under argon atmosphere with no reflux condenser attached and stirred at that temperature for 42 h. Afterwards, solvent was evaporated to add a small amount of THF to dissolve soluble compounds. Solution dropped into methanol (300 ml)

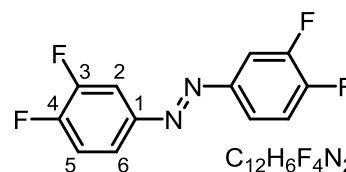
causing precipitation of an olive green powder that was filtered off (frit, porosity 5, vacuum), then within the frit redissolved in THF to dispose with any insoluble residues. The as-such obtained solution was evaporated to dryness then redissolved in THF (3 ml) and reprecipitated from methanol (150 ml). Precipitate filtered off (frit, porosity 5, vacuum) to yield an olive green solid (1.0333 g, 78 %). Alternatively, to obtain the product as powder rather than as film reprecipitation was repeated but the precipitate was collected by means of centrifugation (4000 rpm, 20 min).

**NMR**  $^1\text{H}$  400 MHz, THF-D8,  $\delta$  / ppm: 8.03-7.79 (m, 4 H,  $\text{H}^{\text{Spiro}}$ ), 7.72-7.45 (m, 2 H,  $\text{H}^{\text{Spiro}}$ ), 7.33 (s, 2 H,  $\text{H}^{\text{Spiro}}$ ), 7.28-7.14 (m, 2 H,  $\text{H}^{\text{Spiro}}$ ), 7.06 (s, 2 H,  $\text{H}^{\text{Spiro}}$ ), 6.92 (s, 2 H,  $\text{H}^{\text{Spiro}}$ ), 6.64 (s, 2 H,  $\text{H}^{\text{Ar,DAE}}$ ), 1.93-1.75 (m, 6 H,  $\text{H}^{\text{Me}}$ )

**NMR**  $^{13}\text{C}$  101 MHz, THF-D8,  $\delta$  / ppm: 150.3, 149.8, 143.2, 142.9, 142.1, 142.0, 138.2 ( $\text{C}^2$  with pinacol residue), 134.0, 129.0, 128.8, 126.6, 125.9 ( $\text{C}^1$ ), 124.7, 123.2 ( $\text{C}^{4''}$ ), 121.6, 121.5, 121.1, 67.9 ( $\text{C}^9$ ), 35.1 ( $\text{C}^{\text{quat,pinacol}}$ ), 30.7 ( $\text{CH}_3^{\text{pinacol}}$ ), 26.4, 14.5 ( $\text{CH}_3^{\text{DAE}}$ )

### 3,3',4,4'-Tetrafluoroazobenzene<sup>[268]</sup> (3)

To a solution of water (188 ml) and ethanol (188 ml) allocated in a 1000 ml 3-neck flask equipped with reflux condenser 3,4-difluoroaniline (1.0 eq., 37.6133 mmol, 4.8562 g, 3.730 ml) was added. It is recommended to use a strong stirrer or on that scale even a KPG stirring unit. Under vigorous stirring potassium hydroxide (1.8 eq., 67.7040 mmol, 3.7986 g) and potassium hexacyanoferrate(III) (8.0 eq., 300.9065 mmol, 99.0728 g) were added. Reaction mixture was refluxed for 20 h, then cooled to r.t. whereupon mixture was filtered (frit, porosity 4, vacuum) to remove undissolved oxidant that was extracted within the frit thrice with DCM. Obtained filtrate was deep violet in colour and was evaporated until DCM and ethanol vanished. Oily remnant was redissolved in a small amount of ethanol and water added to extract crude product with DCM (5  $\times$ ). Organic layers merged and washed with water (3  $\times$ ), dried over sodium sulphate, filtered off (folded filter, gravity) and evaporated to yield an intensely violet solid as crude product (3.9702 g, 83 %). Filtration through silica (*n*-pentane 100 %) yielded clean product as orange, crystalline solid (0.9951 g, 21 %).



**NMR**  $^1\text{H}$  700 MHz, acetone-D6,  $\delta$  / ppm: 7.96-7.86 (m, 2 H,  $\text{H}^{2\text{ or }6}$ ), 7.86-7.75 (m, 2 H,  $\text{H}^{2\text{ or }6}$ ), 7.59 (ddd,  $J = 17.4, 8.5 \text{ Hz}, 1.8 \text{ Hz}, 2 \text{ H}, \text{H}^5$ )

**NMR**  $^{13}\text{C}\{^1\text{H}\}$  50 MHz, acetone-D6,  $\delta$  / ppm: 153.2 (dd,  $J = 253.0, 13.3 \text{ Hz}, \text{C}^{3\text{ or }4}$ ), 151.7 (dd,  $J = 249.6, 14.1 \text{ Hz}, \text{C}^{3\text{ or }4}$ ), 149.8 (m,  $\text{C}^1$ ), 123.1 (dd,  $J = 7.2, 3.2 \text{ Hz}, \text{C}^6$ ), 118.9 (d,  $J = 18.8 \text{ Hz}, \text{C}^5$ ), 110.5 (d,  $J = 18.5 \text{ Hz}, \text{C}^2$ )

**NMR**  $^{13}\text{C}\{^{19}\text{F}\}$  176 MHz, acetone-D6,  $\delta$  / ppm: 153.2 (m,  $\text{C}^{3\text{ or }4}$ ), 151.6 (t,  $J = 7.2 \text{ Hz}, \text{C}^{3\text{ or }4}$ ), 149.8 (m,  $\text{C}^1$ ), 123.2 (dd,  $J = 16.8, 6.6 \text{ Hz}, \text{C}^6$ ), 118.9 (d,  $J = 167.8 \text{ Hz}, \text{C}^5$ ), 110.5 (dd,  $J = 167.6, 6.6 \text{ Hz}, \text{C}^2$ )

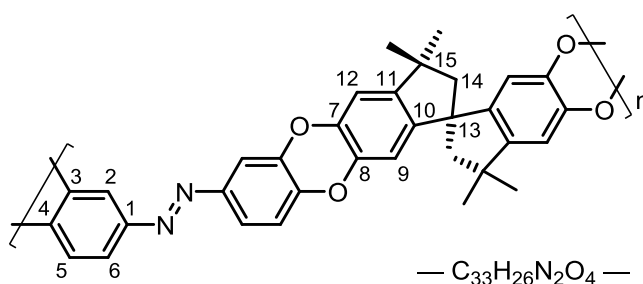
**NMR**  $^{19}\text{F}$  188 MHz, acetone-D6,  $\delta$  / ppm: -134.6 (m, 1 F), -137.5 (m, 1 F)

**MS** EI, M/Z calculated (found) for  $[\text{M}]^-$ : 254.04616 (254.04544)

**EA** calculated (found) for  $\text{C}_{12}\text{H}_6\text{F}_4\text{N}_2$  in m-%: C 56.70 (56.80), H 2.38 (2.41), N 11.02 (10.90), F( $\Delta$ ) 29.90 (29.90)

**Azo-PIM**

A flame-dried 20 ml Schlenk tube made of thick glass was charged with **3** (1.0 eq., 1.1215 mmol, 0.2851 g), 5,5',6,6'-tetrahydroxy-3,3',3',3'-tetramethyl-1,1'-spirobi-indane (1.0 eq., 1.1215 mmol, 0.3818 g) and dry potassium carbonate (8.0 eq., 8.9723 mmol, 1.2400 g). Solid components



were degassed by means of vacuum and refilling with argon three times. Dry DMF (5.608 ml) was added *via* syringe, reaction vessel sealed with screw cap and mixture heated up to 65 °C. After 24 h, reaction mixture was poured into a mixture of crushed ice (100 g) and methanol (100 ml) whereupon an orange solid precipitated. Mixture was stirred to ensure dissolution of potassium carbonate and potassium fluoride, then filtered off (frit, pore 4, vacuum) to yield an orange-red solid that was washed with water (3 ×) and methanol (cooled by ice water). Drying yielded crude product as orange solid, that forms film upon evaporation of solvent. For purification, compound was dissolved in THF (3 ml) and reprecipitated from methanol (58 ml). Precipitate filtered off (frit, pore 4, vacuum) and washed with methanol (cooled by ice water, 2 × 20 ml). The procedure was repeated once to yield the purified product as orange solid (0.6158 g, 107 %). To obtain the product as powder rather than as film reprecipitation was repeated but the precipitate was collected by means of centrifugation (4000 rpm, 20 min).

**NMR** <sup>1</sup>H 500 MHz, THF-D8, δ / ppm: 7.83-7.20 (m, 4 H, H<sup>5,6</sup>), 7.20-6.84 (m, 2 H, H<sup>9 or 12</sup>), 6.84-6.59 (m, 2 H, H<sup>2</sup>), 6.59-6.04 (m, 2 H, H<sup>9 or 12</sup>), 2.49-2.07 (m, 4 H, H<sup>14</sup>), 1.49-1.13 (m, 12 H, 4 × CH<sub>3</sub>)

**NMR** <sup>13</sup>C{<sup>1</sup>H} 126 MHz, THF-D8, δ / ppm: 149.9 (C<sup>1 or 3</sup>), 149.2 (C<sup>1 or 3</sup>), 149.0 (C<sup>11</sup>), 146.7 (C<sup>4 or 7 or 8</sup>), 145.5 (C<sup>4 or 7 or 8</sup>), 143.6 (C<sup>10</sup>), 142.1 (C<sup>4 or 7 or 8</sup>), 122.3 (C<sup>6</sup>), 117.2 (C<sup>9 or 12</sup>), 112.6 (C<sup>9 or 12</sup>), 110.7 (C<sup>2</sup>), 109.0 (C<sup>5</sup>), 60.1 (C<sup>14</sup>), 58.1 (C<sup>13</sup>), 44.1 (C<sup>15</sup>), 31.7 (CH<sub>3</sub>), 30.3 (CH<sub>3</sub>)



# ABBREVIATIONS

ALPO	Aluminophosphate
AMOCO	American Oil Company
APCI	Atmospheric Pressure Chemical Ionisation (MS technique)
ATR	Attenuated Total Reflection
BDC	benzenedicarboxylate
BET	Brunauer, Emmet, Teller (scientists, formulated a theory on adsorption)
BHT	2,6-di- <i>tert</i> -butyl-4-methylphenol (stabiliser in THF and diethylether)
BJH	Barrett, Joyner, Halenda (scientists, formulated a theory for the calculation of PSD)
CAU	Christian-Albrechts-Universität
CMP	Conjugated Microporous Polymer
COF	Covalent Organic Framework
COSY	Correlated Spectroscopy (NMR technique)
CP/MAS	Cross-Polarisation/Magic Angle Spinning
CTF	Covalent Triazine-based Framework
DEPT	Distortionless Enhancement by Polarisation Transfer (NMR technique)
DIB	diiodobenzene
DCM	dichloromethane
DH	Dollimore, Heal (scientists, advanced BJH theory)
DMF	N,N'-dimethylformamide
DOE	Department of Energy
DOSY	Diffusion-Ordered Spectroscopy (NMR technique)
EI	Electron Impact (MS technique)
EOF	Elemental Organic Framework
eq.	equivalent(s)
ESI	Electrospray Ionisation (MS technique)
FDU	Fudan University
FT	Fourier Transform
GPC	Gel Permeation Chromatography
HCP	Hyper Cross-Linked Polymer
HKUST	Hong Kong University of Science and Technology
HMBC	Heteronuclear Multiple Bond Correlation (NMR technique)
HOMO	Highest Occupied Molecular Orbital
HSQC	Heteronuclear Single Quantum Coherence (NMR technique)
HTC	Hydrothermal Carbonisation

---

IM	Intrinsic Microporosity
IMFV	Internal Molecular Free Volume
IR	Infrared
IRMOF	Isorecticular Metal Organic Framework
ITO	Indium Tin Oxide
KIT	Korean Institute of Technology
LUMO	Lowest Unoccupied Molecular Orbital
MCM	Mobile Corporation Material, Mobil Catalytic Material, <sup>[2]</sup> or Mobil Composition of Matter <sup>[269]</sup>
MIL	Matériaux Institute Lavoisier
MOF	Metal Organic Framework
MOP	Microporous Organic Polymer
MPN	Microporous Polymer Network
MS	Mass Spectrometry
NLDFT	Non-Local Density Functional Theory
NMR	Nuclear Magnetic Resonance
NU	Northwestern University
on.	overnight
PAE	poly(aryleneethynylene)
PAF	Porous Aromatic Framework
PALS	Positron Annihilation Lifetime Spectroscopy
PCBM	phenyl-C61-butyric acid methyl ester
(P)CP	(Porous) Coordination Polymer
PIM	Polymer of Intrinsic Microporosity
PMD	Periodic Mesoporous Dendrisilicas
PMO	Periodic Mesoporous Organosilanes
PPB	poly(phenylene butadiynylene)
PPN	Porous Polymer Network
PPV	poly(phenylenevinylene)
PSD	Pore Size Distribution
PSN	Poly(organosiloxane) Network
$p/p_0$	relative pressure
PXRD	Powder X-Ray Diffraction
QSDFT	Quenched Solid Density Functional Theory
r.t.	room temperature
SA	Surface Area
SAM	Self-Assembled Monolayer
SAPO	Silicon Aluminium Phosphate
SAXS	Small X-Ray Angle Scattering
SEIRAS	Surface Enhanced Infrared Absorption Spectroscopy

---

SEM	Scanning Electron Microscopy
SERS	Surface Enhanced Raman Spectroscopy
SBA	Santa Barbara
SCMP	Soluble Microporous Conjugated Network
SCP	Surface Coordination Polymer
SDA	Structure Directing Agent
SOCONY	Standard Oil Company of New York
SPCP	Surface Porous Coordination Polymer
SURMOF	Surface MOF
TEA	triethylamine
TEB	1,3,5-triethynylbenzene
TGA	Thermo-Gravimetric Analysis
THF	tetrahydrofuran
UMCM	University of Michigan Crystalline Material
ZIF	Zeolitic Imidazolid Framework
ZSM	Zeolite Socony Mobil



# LITERATURE REFERENCES

- [1] "Manual of Symbols and Terminology for Physicochemical Quantities and Units, Appendix II: Definitions, Terminology and Symbols in Colloid and Surface Chemistry", D. H. Everett, *Pure Appl. Chem.* **1972**, 31, 577-638, DOI: 10.1351/pac197231040577
- [2] *Handbook of Porous Solids*, F. Schlüth, K. S. W. Sing, J. Weitkamp, 1, Wiley-VCH, **2008**.
- [3] "An Account of Some Experiments Shown before the Royal Society; With an Enquiry into the Cause of the Ascent and Suspension of Water in Capillary Tubes. By James Jurin, M. D. and R. Soc. S", J. Jurin, *Philos. Trans.* **1717**, 30, 739-747, DOI: 10.1098/rstl.1717.0026
- [4] "An Essay on the Cohesion of Fluids", T. Young, *Philos. Trans. R. Soc. London, A* **1805**, 95, 65-87, DOI: 10.1098/rstl.1805.0005
- [5] P. S. de Laplace, *Traité de mécanique céleste*, Paris, **1805**.
- [6] "On the Equilibrium of Vapour at a Curved Surface of Liquid", W. Thomson, *Philos. Mag. J. Sci.* **1871**, 42, 448-452, DOI:
- [7] "The nucleus in and the growth of hygroscopic droplets", H. Köhler, *Transactions of the Faraday Society* **1936**, 32, 1152-1161, DOI: 10.1039/TF9363201152
- [8] "The Kelvin versus the Raoult Term in the Köhler Equation", H. Wex, F. Stratmann, D. Topping, G. McFiggans, *J. Atmos. Sci.* **2008**, 65, 4004-4016, DOI: 10.1175/2008jas2720.1
- [9] "Über die Struktur des Gels der Kieselsäure. Theorie der Entwässerung", R. Zsigmondy, *Z. Anorg. Chem.* **1911**, 71, 356-377, DOI: 10.1002/zaac.19110710133
- [10] S. S. Kistler, *Nature* **1931**, 127, 741-741, DOI:
- [11] "The Sorption of Polar and Non-Polar Gases by Zeolites", R. M. Barrer, *Proc. R. Soc. London, A* **1938**, 167, 392-420, DOI: 10.1098/rspa.1938.0138
- [12] "Structure of synthetic zeolite ZSM-5", G. T. Kokotailo, S. L. Lawton, D. H. Olson, W. M. Meier, *Nature* **1978**, 272, 437-438, DOI:
- [13] "A new family of mesoporous molecular sieves prepared with liquid crystal templates", J. S. Beck, J. C. Vartuli, W. J. Roth, M. E. Leonowicz, C. T. Kresge, K. D. Schmitt, C. T. W. Chu, D. H. Olson, E. W. Sheppard, S. B. McCullen, J. B. Higgins, J. L. Schlenker, *J. Am. Chem. Soc.* **1992**, 114, 10834-10843, DOI: 10.1021/ja00053a020
- [14] "Hard Templates for Soft Materials: Creating Nanostructured Organic Materials †", A. Thomas, F. Goettmann, M. Antonietti, *Chem. Mater.* **2008**, 20, 738-755, DOI: 10.1021/cm702126j
- [15] "Functional materials: from hard to soft porous frameworks", A. Thomas, *Angew. Chem., Int. Ed. Engl.* **2010**, 49, 8328-8344, DOI: 10.1002/anie.201000167

- [16] "Macronet isoporous gels through crosslinking of dissolved polystyrene", V. A. Davankov, S. V. Rogoshin, M. P. Tsyurupa, *J. Polym. Sci.: Polym. Symp.* **1974**, 47, 95-101, DOI: 10.1002/polc.5070470113
- [17] "Structure and properties of hypercrosslinked polystyrene—the first representative of a new class of polymer networks", V. A. Davankov, M. P. Tsyurupa, *React. Polym.* **1990**, 13, 27-42, DOI: 10.1016/0923-1137(90)90038-6
- [18] "Design and construction of a new class of scaffolding-like materials comprising infinite polymeric frameworks of 3D-linked molecular rods. A reappraisal of the zinc cyanide and cadmium cyanide structures and the synthesis and structure of the diamond-related frameworks  $[N(CH_3)_4][CuI ZnII(CN)_4]$  and  $CuI[4,4',4'',4''']$ -tetracyanotetraphenylmethane]BF<sub>4</sub>.x C<sub>6</sub>H<sub>5</sub>NO<sub>2</sub>", B. F. Hoskins, R. Robson, *J. Am. Chem. Soc.* **1990**, 112, 1546-1554, DOI: 10.1021/ja00160a038
- [19] "Preparation, Clathration Ability, and Catalysis of a Two-Dimensional Square Network Material Composed of Cadmium(II) and 4,4'-Bipyridine", M. Fujita, Y. J. Kwon, S. Washizu, K. Ogura, *J. Am. Chem. Soc.* **1994**, 116, 1151-1152, DOI: 10.1021/ja00082a055
- [20] "Assembly of porphyrin building blocks into network structures with large channels", B. F. Abrahams, B. F. Hoskins, D. M. Michail, R. Robson, *Nature* **1994**, 369, 727-729, DOI: 10.1038/369727a0
- [21] "Zeolite-like Behavior of a Coordination Network", D. Venkataraman, G. B. Gardner, S. Lee, J. S. Moore, *J. Am. Chem. Soc.* **1995**, 117, 11600-11601, DOI: 10.1021/ja00151a034
- [22] "Three-Dimensional Framework with Channeling Cavities for Small Molecules:  $\{[M_2(4, 4'$ -bpy)<sub>3</sub>(NO<sub>3</sub>)<sub>4</sub>·xH<sub>2</sub>O]<sub>n</sub> (M = Co, Ni, Zn)", M. Kondo, T. Yoshitomi, K. Seki, H. Matsuzaka, S. Kitagawa, *Angew. Chem., Int. Ed. Engl.* **1997**, 36, 1725-1727, DOI: 10.1002/anie.199717251
- [23] "Selective binding and removal of guests in a microporous metal-organic framework", O. M. Yaghi, G. Li, H. Li, *Nature* **1995**, 378, 703-706, DOI:
- [24] "Design and synthesis of an exceptionally stable and highly porous metal-organic framework", H. Li, M. Eddaoudi, M. O'Keeffe, O. M. Yaghi, *Nature* **1999**, 402, 276-279, DOI: 10.1038/46248
- [25] "Impact of Preparation and Handling on the Hydrogen Storage Properties of Zn<sub>4</sub>O(1,4-benzenedicarboxylate)<sub>3</sub> (MOF-5)", S. S. Kaye, A. Dailly, O. M. Yaghi, J. R. Long, *J. Am. Chem. Soc.* **2007**, 129, 14176-14177, DOI: 10.1021/ja076877g
- [26] "Gases in Multimolecular Layers", S. Brunauer, P. H. Emmett, E. Teller, *J. Am. Chem. Soc.* **1938**, 60, 309-309, DOI: 10.1021/ja01269a023
- [27] "Design and its limitations in the construction of bi- and poly-nuclear coordination complexes and coordination polymers (aka MOFs): a personal view", R. Robson, *Dalton Trans.* **2008**, 5113-5131, DOI: 10.1039/B805617J
- [28] "A chromium terephthalate-based solid with unusually large pore volumes and surface area", G. Férey, C. Mellot-Draznieks, C. Serre, F. Millange, J. Dutour, S. Surblé, I. Margiolaki, *Science* **2005**, 309, 2040-2042, DOI: 10.1126/science.1116275

- [29] "A Porous Coordination Copolymer with over 5000 m<sup>2</sup>/g BET Surface Area", K. Koh, A. G. Wong-Foy, A. J. Matzger, *J. Am. Chem. Soc.* **2009**, *131*, 4184-4185, DOI: 10.1021/ja809985t
- [30] "Metal-organic framework materials with ultrahigh surface areas: is the sky the limit?", O. K. Farha, I. Eryazici, N. C. Jeong, B. G. Hauser, C. E. Wilmer, A. A. Sarjeant, R. Q. Snurr, S. T. Nguyen, A. Ö. Yazaydin, J. T. Hupp, *J. Am. Chem. Soc.* **2012**, *134*, 15016-15021, DOI: 10.1021/ja3055639
- [31] "Polymers of intrinsic microporosity (PIMs): robust, solution-processable, organic nanoporous materials", P. M. Budd, B. S. Ghanem, S. Makhseed, N. B. McKeown, K. J. Msayib, C. E. Tattershall, *Chem. Commun. (Cambridge, U. K.)* **2004**, 230-231, DOI: 10.1039/b311764b
- [32] "Porous, crystalline, covalent organic frameworks", A. P. Côté, A. I. Benin, N. W. Ockwig, M. O'Keeffe, A. J. Matzger, O. M. Yaghi, *Science* **2005**, *310*, 1166-1170, DOI: 10.1126/science.1120411
- [33] "Molecular tectonics. Use of the hydrogen bonding of boronic acids to direct supramolecular construction", J.-H. Fournier, T. Maris, J. D. Wuest, W. Guo, E. Galoppini, *J. Am. Chem. Soc.* **2003**, *125*, 1002-1006, DOI: 10.1021/ja0276772
- [34] "Designed Synthesis of 3D Covalent Organic Frameworks", H. M. El-Kaderi, J. R. Hunt, J. L. Mendoza-Cortés, A. P. Côté, R. E. Taylor, M. O'Keeffe, O. M. Yaghi, *Science (New York, N.Y.)* **2007**, *316*, 268-272, DOI: 10.1126/science.1139915
- [35] "A Crystalline Imine-Linked 3-D Porous Covalent Organic Framework", F. J. Uribe-Romo, J. R. Hunt, H. Furukawa, C. Klöck, M. O'Keeffe, O. M. Yaghi, *J. Am. Chem. Soc.* **2009**, *131*, 4570-4571, DOI: 10.1021/ja8096256
- [36] "Crystalline Covalent Organic Frameworks with Hydrazone Linkages", F. J. Uribe-Romo, C. J. Doonan, H. Furukawa, K. Oisaki, O. M. Yaghi, *J. Am. Chem. Soc.* **2011**, *133*, 11478-11481, DOI: 10.1021/ja204728y
- [37] "Covalent organic frameworks", X. Feng, X. Ding, D. Jiang, *Chem. Soc. Rev.* **2012**, *41*, 6010-6022, DOI: 10.1039/c2cs35157a
- [38] "Covalent organic frameworks (COFs): from design to applications", S.-Y. Ding, W. Wang, *Chem. Soc. Rev.* **2013**, *42*, 548-568, DOI: 10.1039/c2cs35072f
- [39] "On the road towards electroactive covalent organic frameworks", M. Dogru, T. Bein, *Chem. Commun. (Cambridge, U. K.)* **2014**, *50*, 5531-5546, DOI: 10.1039/C3CC46767H
- [40] "Conjugated microporous poly(aryleneethynylene) networks", J.-X. Jiang, F. Su, A. Trewin, C. D. Wood, N. L. Campbell, H. Niu, C. Dickinson, A. Y. Ganin, M. J. Rosseinsky, Y. Z. Khimyak, A. I. Cooper, *Angew. Chem., Int. Ed. Engl.* **2007**, *46*, 8574-8578, DOI: 10.1002/anie.200701595
- [41] "Copper-Free Sonogashira Coupling for High-Surface-Area Conjugated Microporous Poly(aryleneethynylene) Networks", M. Trunk, A. Herrmann, H. Bildirir, A. Yassin, J. Schmidt, A. Thomas, *Chem. - Eur. J.* **2016**, *22*, 7179-7183, DOI: 10.1002/chem.201600783
- [42] "High surface area amorphous microporous poly(aryleneethynylene) networks using tetrahedral carbon- and silicon-centred monomers", E. Stockel, X. Wu, A. Trewin, C. D. Wood, R. Clowes, N. L. Campbell, J. T. A. Jones, Y. Z. Khimyak, D. J. Adams, A. I. Cooper, *Chem. Commun. (Cambridge, U. K.)* **2009**, 212-214, DOI: 10.1039/B815044C

- [43] "Soluble conjugated microporous polymers", G. Cheng, T. Hasell, A. Trewin, D. J. Adams, A. I. Cooper, *Angew. Chem., Int. Ed. Engl.* **2012**, *51*, 12727-12731, DOI: 10.1002/anie.201205521
- [44] "Porous, covalent triazine-based frameworks prepared by ionothermal synthesis", P. Kuhn, M. Antonietti, A. Thomas, *Angew. Chem., Int. Ed. Engl.* **2008**, *47*, 3450-3453, DOI: 10.1002/anie.200705710
- [45] "Covalent triazine frameworks as heterogeneous catalysts for the synthesis of cyclic and linear carbonates from carbon dioxide and epoxides", J. Roeser, K. Kailasam, A. Thomas, *ChemSusChem* **2012**, *5*, 1793-1799, DOI: 10.1002/cssc.201200091
- [46] "Solid catalysts for the selective low-temperature oxidation of methane to methanol", R. Palkovits, M. Antonietti, P. Kuhn, A. Thomas, F. Schüth, *Angew. Chem., Int. Ed. Engl.* **2009**, *48*, 6909-6912, DOI: 10.1002/anie.200902009
- [47] "Targeted synthesis of a porous aromatic framework with high stability and exceptionally high surface area", T. Ben, H. Ren, S. Ma, D. Cao, J. Lan, X. Jing, W. Wang, J. Xu, F. Deng, J. M. Simmons, S. Qiu, G. Zhu, *Angew. Chem., Int. Ed. Engl.* **2009**, *48*, 9457-9460, DOI: 10.1002/anie.200904637
- [48] "Conjugated Microporous Polymer Networks via Yamamoto Polymerization", J. Schmidt, M. Werner, A. Thomas, *Macromolecules (Washington, DC, U. S.)* **2009**, *42*, 4426-4429, DOI: 10.1021/ma9005473
- [49] "Amorphous PAF-1: Guiding the Rational Design of Ultraporous Materials", J. M. H. Thomas, A. Trewin, *J. Phys. Chem. C* **2014**, *118*, 19712-19722, DOI: 10.1021/jp502336a
- [50] "Sulfonate-grafted porous polymer networks for preferential CO<sub>2</sub> adsorption at low pressure", W. Lu, D. Yuan, J. P. Sculley, D. Zhao, R. Krishna, H.-C. Zhou, *J. Am. Chem. Soc.* **2011**, *133*, 18126-18129, DOI: 10.1021/ja2087773
- [51] "Dianin's compound as a zeolitic sorbent", R. M. Barrer, V. H. Shanson, *J. Chem. Soc., Chem. Commun.* **1976**, 1976, 333-334, DOI: 10.1039/c39760000333
- [52] "One-pot synthesis of a shape-persistent endo-functionalised nano-sized adamantoid compound", M. Mastalerz, *Chem. Commun. (Cambridge, U. K.)* **2008**, 4756-4758, DOI: 10.1039/B808990F
- [53] "One-Pot, 18-Component Synthesis of an Octahedral Nanocontainer Molecule", X. Liu, Y. Liu, G. Li, R. Warmuth, *Angew. Chem., Int. Ed.* **2006**, *45*, 901-904, DOI: 10.1002/anie.200504049
- [54] "Porous organic cages", T. Tozawa, J. T. A. Jones, S. I. Swamy, S. Jiang, D. J. Adams, S. Shakespeare, R. Clowes, D. Bradshaw, T. Hasell, S. Y. Chong, C. Tang, S. Thompson, J. Parker, A. Trewin, J. Bacsá, A. M. Z. Slawin, A. Steiner, A. I. Cooper, *Nat. Mater.* **2009**, *8*, 973-978, DOI: 10.1038/nmat2545
- [55] "Rational construction of an extrinsic porous molecular crystal with an extraordinary high specific surface area", M. Mastalerz, I. M. Oppel, *Angew. Chem., Int. Ed. Engl.* **2012**, *51*, 5252-5255, DOI: 10.1002/anie.201201174
- [56] "A Salicylbisimine Cage Compound with High Surface Area and Selective CO<sub>2</sub>/CH<sub>4</sub> Adsorption", M. Mastalerz, M. W. Schneider, I. M. Oppel, O. Presly, *Angew. Chem., Int. Ed. Engl.* **2011**, *50*, 1046-1051, DOI: 10.1002/anie.201005301

- [57] "Organic cage compounds--from shape-persistency to function", G. Zhang, M. Mastalerz, *Chem. Soc. Rev.* **2014**, *43*, 1934-1947, DOI: 10.1039/c3cs60358j
- [58] "Chemical functionalization strategies for carbon dioxide capture in microporous organic polymers", R. Dawson, A. I. Cooper, D. J. Adams, *Polym. Int.* **2013**, *62*, 345-352, DOI: 10.1002/pi.4407
- [59] "Nanoporous organic polymer networks", R. Dawson, A. I. Cooper, D. J. Adams, *Prog. Polym. Sci.* **2012**, *37*, 530-563, DOI: 10.1016/j.progpolymsci.2011.09.002
- [60] "Highly stable porous polymer networks with exceptionally high gas-uptake capacities", D. Yuan, W. Lu, D. Zhao, H.-C. Zhou, *Adv. Mater. (Deerfield Beach, Fla.)* **2011**, *23*, 3723-3725, DOI: 10.1002/adma.201101759
- [61] "Target Explanation Document: Onboard Hydrogen Storage for Light-Duty Fuel Cell Vehicles", Office of Energy Efficiency & Renewable Energy, **2015**, Revised May 2015, p. 7, U.S. Department of Energy, Washington DC, [http://energy.gov/sites/prod/files/2015/05/f22/fcto\\_targets\\_onboard\\_hydro\\_storage\\_explanation.pdf](http://energy.gov/sites/prod/files/2015/05/f22/fcto_targets_onboard_hydro_storage_explanation.pdf)
- [62] "Nanoporous Polymers Containing Stereocontorted Cores for Hydrogen Storage", S. Yuan, S. Kirklin, B. Dorney, D.-J. Liu, L. Yu, *Macromolecules* **2009**, *42*, 1554-1559, DOI: 10.1021/ma802394x
- [63] "High capacity carbon dioxide adsorption by inexpensive covalent organic polymers", H. A. Patel, F. Karadas, A. Canlier, J. Park, E. Deniz, Y. Jung, M. Atilhan, C. T. Yavuz, *J. Mater. Chem.* **2012**, *22*, 8431-8437, DOI: 10.1039/C2JM30761H
- [64] "Gas storage in porous aromatic frameworks (PAFs)", T. Ben, C. Pei, D. Zhang, J. Xu, F. Deng, X. Jing, S. Qiu, *Energy Environ. Sci.* **2011**, *4*, 3991-3999, DOI: 10.1039/c1ee01222c
- [65] "Amine-oxide hybrid materials for acid gas separations", P. Bollini, S. A. Didas, C. W. Jones, *J. Mater. Chem.* **2011**, *21*, 15100-15120, DOI: 10.1039/C1JM12522B
- [66] "FTIR Study of CO<sub>2</sub> Adsorption on Amine-Grafted SBA-15: Elucidation of Adsorbed Species", A. Danon, P. C. Stair, E. Weitz, *J. Phys. Chem. C* **2011**, *115*, 11540-11549, DOI: 10.1021/jp200914v
- [67] "Microporous organic polymers for carbon dioxide capture", R. Dawson, E. Stockel, J. R. Holst, D. J. Adams, A. I. Cooper, *Energy Environ. Sci.* **2011**, *4*, 4239-4245, DOI: 10.1039/C1EE01971F
- [68] "Mechanism and Kinetics of CO<sub>2</sub> Adsorption on Surface Bonded Amines", M. W. Hahn, M. Steib, A. Jentys, J. A. Lercher, *J. Phys. Chem. C* **2015**, *119*, 4126-4135, DOI: 10.1021/jp512001t
- [69] "Tuning porosity and activity of microporous polymer network organocatalysts by copolymerisation", J. Schmidt, D. S. Kundu, S. Blechert, A. Thomas, *Chem. Commun. (Cambridge, U. K.)* **2014**, *50*, 3347-3349, DOI: 10.1039/c3cc49220f
- [70] "An Anionic Microporous Polymer Network Prepared by the Polymerization of Weakly Coordinating Anions", S. Fischer, J. Schmidt, P. Strauch, A. Thomas, *Angew. Chem., Int. Ed. Engl.* **2013**, *52*, 12174-12178, DOI: 10.1002/anie.201303045

- [71] "A photoconductive thienothiophene-based covalent organic framework showing charge transfer towards included fullerene", M. Dogru, M. Handloser, F. Auras, T. Kunz, D. Medina, A. Hartschuh, P. Knochel, T. Bein, *Angew. Chem., Int. Ed. Engl.* **2013**, *52*, 2920-2924, DOI: 10.1002/anie.201208514
- [72] "An Ambipolar Conducting Covalent Organic Framework with Self-Sorted and Periodic Electron Donor-Acceptor Ordering", X. Feng, L. Chen, Y. Honsho, O. Saengsawang, L. Liu, L. Wang, A. Saeki, S. Irle, S. Seki, Y. Dong, D. Jiang, *Adv. Mater.* **2012**, *24*, 3026-3031, DOI: 10.1002/adma.201201185
- [73] "THE ADSORPTION OF GASES ON PLANE SURFACES OF GLASS, MICA AND PLATINUM", I. Langmuir, *J. Am. Chem. Soc.* **1918**, *40*, 1361-1403, DOI: 10.1021/ja02242a004
- [74] J. Rouquerol, P. Llewellyn, F. Rouquerol, in *Is the BET equation applicable to microporous adsorbents?*, Volume 160(Eds.: F. R.-R. J. R. P.L. Llewellyn, N. Seaton), Elsevier, **2007**, pp. 49-56.
- [75] "Applicability of the BET method for determining surface areas of microporous metal-organic frameworks", K. S. Walton, R. Q. Snurr, *J. Am. Chem. Soc.* **2007**, *129*, 8552-8556, DOI: 10.1021/ja071174k
- [76] "Evaluation of the BET method for determining surface areas of MOFs and zeolites that contain ultra-micropores", Y.-S. Bae, A. O. Yazaydin, R. Q. Snurr, *Langmuir* **2010**, *26*, 5475-5483, DOI: 10.1021/la100449z
- [77] "Reporting physisorption data for gas/solid systems with special reference to the determination of surface area and porosity (Recommendations 1984)", K. S. W. Sing, D. H. Everett, R. A. W. Haul, L. Moscou, R. A. Pierotti, J. Rouquérol, T. Siemieniowska, *Pure Appl. Chem.* **1985**, *57*, 603-619, DOI: 10.1351/pac198557040603
- [78] "Physical Adsorption on Non-Uniform Surfaces", G. Halsey, *J. Chem. Phys.* **1948**, *16*, 931-937, DOI: 10.1063/1.1746689
- [79] "Thet-curve of multimolecular N<sub>2</sub>-adsorption", J. H. de Boer, B. C. Lippens, B. G. Linsen, J. C. P. Broekhoff, A. van den Heuvel, T. J. Osinga, *J. Colloid Interface Sci.* **1966**, *21*, 405-414, DOI: 10.1016/0095-8522(66)90006-7
- [80] "Evaluation of the External Surface Area of Carbon Black by Nitrogen Adsorption", R. W. Magee, *Rubber Chem. Technol.* **1995**, *68*, 590-600, DOI: doi:10.5254/1.3538760
- [81] "The Determination of Pore Volume and Area Distributions in Porous Substances. I. Computations from Nitrogen Isotherms", E. P. Barrett, L. G. Joyner, P. P. Halenda, *J. Am. Chem. Soc.* **1951**, *73*, 373-380, DOI: 10.1021/ja01145a126
- [82] "An improved method for the calculation of pore size distribution from adsorption data", D. Dollimore, G. R. Heal, *Journal of Applied Chemistry* **1964**, *14*, 109-114, DOI: 10.1002/jctb.5010140302
- [83] "Experimental Confirmation of Different Mechanisms of Evaporation from Ink-Bottle Type Pores: Equilibrium, Pore Blocking, and Cavitation", P. I. Ravikovitch, A. V. Neimark, *Langmuir* **2002**, *18*, 9830-9837, DOI: 10.1021/la026140z

- [84] "Adsorption Hysteresis of Nitrogen and Argon in Pore Networks and Characterization of Novel Micro- and Mesoporous Silicas", M. Thommes, B. Smarsly, M. Groenewolt, P. I. Ravikovitch, A. V. Neimark, *Langmuir* **2006**, *22*, 756-764, DOI: 10.1021/la051686h
- [85] "The effect of pore space connectivity on the hysteresis of capillary condensation in adsorption—desorption isotherms", G. Mason, *J. Colloid Interface Sci.* **1982**, *88*, 36-46, DOI: 10.1016/0021-9797(82)90153-9
- [86] "The determination of pore-size distributions from sorption isotherms and mercury penetration in interconnected pores: The application of percolation theory", G. C. Wall, R. J. C. Brown, *J. Colloid Interface Sci.* **1981**, *82*, 141-149, DOI: 10.1016/0021-9797(81)90132-6
- [87] "Development of the capillary condensation and desorption theory in mesoporous adsorbents based on the porous structure lattice models", A. V. Neimark, *Dokl. Akad. Nauk SSSR* **1983**, *273*, 384-388, DOI: -
- [88] "A Microporous Binol-Derived Phosphoric Acid", D. S. Kundu, J. Schmidt, C. Bleschke, A. Thomas, S. Blechert, *Angew. Chem., Int. Ed. Engl.* **2012**, *51*, 5456-5459, DOI: 10.1002/anie.201109072
- [89] "Nanoporous Polymers: Bridging the Gap between Molecular and Solid Catalysts?", M. Rose, *ChemCatChem* **2014**, *6*, 1166-1182, DOI: 10.1002/cctc.201301071
- [90] "Light-harvesting conjugated microporous polymers: rapid and highly efficient flow of light energy with a porous polyphenylene framework as antenna", L. Chen, Y. Honsho, S. Seki, D. Jiang, *J. Am. Chem. Soc.* **2010**, *132*, 6742-6748, DOI: 10.1021/ja100327h
- [91] "Terephthalonitrile-derived nitrogen-rich networks for high performance supercapacitors", L. Hao, B. Luo, X. Li, M. Jin, Y. Fang, Z. Tang, Y. Jia, M. Liang, A. Thomas, J. Yang, L. Zhi, *Energy Environ. Sci.* **2012**, *5*, 9747-9751, DOI: 10.1039/C2EE22814A
- [92] "An Energy Storage Principle using Bipolar Porous Polymeric Frameworks", K. Sakaushi, G. Nickerl, F. M. Wisser, D. Nishio-Hamane, E. Hosono, H. Zhou, S. Kaskel, J. Eckert, *Angew. Chem., Int. Ed. Engl.* **2012**, *51*, 7850-7854, DOI: 10.1002/anie.201202476
- [93] "Room Temperature Synthesis of Heptazine-Based Microporous Polymer Networks as Photocatalysts for Hydrogen Evolution", K. Kailasam, J. Schmidt, H. Bildirir, G. Zhang, S. Blechert, X. Wang, A. Thomas, *Macromol. Rapid Commun.* **2013**, *34*, 1008-1013, DOI: 10.1002/marc.201300227
- [94] "A 2D Mesoporous Imine-Linked Covalent Organic Framework for High Pressure Gas Storage Applications", M. G. Rabbani, A. K. Sekizkardes, Z. Kahveci, T. E. Reich, R. Ding, H. M. El-Kaderi, *Chem.--Eur. J.* **2013**, *19*, 3324-3328, DOI: 10.1002/chem.201203753
- [95] "Cationic microporous polymer networks by polymerisation of weakly coordinating cations with CO<sub>2</sub>-storage ability", S. Fischer, A. Schimanowitz, R. Dawson, I. Senkovska, S. Kaskel, A. Thomas, *J. Mater. Chem. A* **2014**, *2*, 11825-11829, DOI: 10.1039/C4TA02022G
- [96] "Polyamine-tethered porous polymer networks for carbon dioxide capture from flue gas", W. Lu, J. P. Sculley, D. Yuan, R. Krishna, Z. Wei, H.-C. Zhou, *Angew. Chem., Int. Ed. Engl.* **2012**, *51*, 7480-7484, DOI: 10.1002/anie.201202176

- [97] "Microporous Polycarbazole with High Specific Surface Area for Gas Storage and Separation", Q. Chen, M. Luo, P. Hammershøj, D. Zhou, Y. Han, B. W. Laursen, C.-G. Yan, B.-H. Han, *J. Am. Chem. Soc.* **2012**, *134*, 6084-6087, DOI: 10.1021/ja300438w
- [98] "Accessing functionalized porous aromatic frameworks (PAFs) through a de novo approach", S. J. Garibay, M. H. Weston, J. E. Mondloch, Y. J. Colón, O. K. Farha, J. T. Hupp, S. T. Nguyen, *CrystEngComm* **2013**, *15*, 1515-1519, DOI: 10.1039/c2ce26595h
- [99] "A Belt-Shaped, Blue Luminescent, and Semiconducting Covalent Organic Framework", S. Wan, J. Guo, J. Kim, H. Ihee, D. Jiang, *Angew. Chem., Int. Ed. Engl.* **2008**, *47*, 8826-8830, DOI: 10.1002/anie.200803826
- [100] "Conjugated organic framework with three-dimensionally ordered stable structure and delocalized  $\pi$  clouds", J. Guo, Y. Xu, S. Jin, L. Chen, T. Kaji, Y. Honsho, M. A. Addicoat, J. Kim, A. Saeki, H. Ihee, S. Seki, S. Irle, M. Hiramoto, J. Gao, D. Jiang, *Nat. Commun.* **2013**, *4*, art.2736, DOI: 10.1038/ncomms3736
- [101] "A Tetrathiafulvalene (TTF)-Conjugated Microporous Polymer Network", H. Bildirir, J. P. Paraknowitsch, A. Thomas, *Chem.--Eur. J.* **2014**, *20*, 9543-9548, DOI: 10.1002/chem.201402278
- [102] "Fluorescent nanoparticles based on a microporous organic polymer network: fabrication and efficient energy transfer to surface-bound dyes", A. Patra, J.-M. Koenen, U. Scherf, *Chem. Commun. (Cambridge, U. K.)* **2011**, *47*, 9612-9614, DOI: 10.1039/C1CC13420E
- [103] "Oriented 2D covalent organic framework thin films on single-layer graphene", J. W. Colson, A. R. Woll, A. Mukherjee, M. P. Levendorf, E. L. Spitler, V. B. Shields, M. G. Spencer, J. Park, W. R. Dichtel, *Science* **2011**, *332*, 228-231, DOI: 10.1126/science.1202747
- [104] "Synthesis and characterization of pyrrole-containing microporous polymeric networks", Y. Yang, Q. Zhang, J. Zheng, S. Zhang, *Polymer* **2013**, *54*, 3254-3260, DOI: 10.1016/j.polymer.2013.04.038
- [105] "Porous conjugated polymer nanotip arrays for highly stable field emitter", L. Zhang, K. Wang, X. Qian, H. Liu, Z. Shi, *ACS Appl. Mater. Interfaces* **2013**, *5*, 2761-2766, DOI: 10.1021/am4004914
- [106] "Polymer Carpets", I. Amin, M. Steenackers, N. Zhang, A. Beyer, X. Zhang, T. Pirzer, T. Hugel, R. Jordan, A. Götzhäuser, *Small* **2010**, *6*, 1623-1630, DOI: 10.1002/smll.201000448
- [107] "High thermal stability of cross-linked aromatic self-assembled monolayers: Nanopatterning via selective thermal desorption", A. Turchanin, M. El-Desawy, A. Götzhäuser, *Appl. Phys. Lett.* **2007**, *90*, 053102-053101 - 053102-053103, DOI: 10.1063/1.2437091
- [108] "Fully cross-linked and chemically patterned self-assembled monolayers", A. Beyer, A. Godt, I. Amin, C. T. Nottbohm, C. Schmidt, J. Zhao, A. Götzhäuser, *Phys. Chem. Chem. Phys.* **2008**, *10*, 7233-7238, DOI: 10.1039/b809787a
- [109] "One Nanometer Thin Carbon Nanosheets with Tunable Conductivity and Stiffness", A. Turchanin, A. Beyer, C. T. Nottbohm, X. Zhang, R. Stosch, A. Sologubenko, J. Mayer, P. Hinze, T. Weimann, A. Götzhäuser, *Adv. Mater.* **2009**, *21*, 1233-1237, DOI: 10.1002/adma.200803078

- [110] "Microporous Conjugated Poly(thienylene arylene) Networks", J. Schmidt, J. Weber, J. D. Epping, M. Antonietti, A. Thomas, *Adv. Mater. (Weinheim, Ger.)* **2009**, *21*, 702-705, DOI: 10.1002/adma.200802692
- [111] "Electrochemical route to fabricate film-like conjugated microporous polymers and application for organic electronics", C. Gu, Y. Chen, Z. Zhang, S. Xue, S. Sun, K. Zhang, C. Zhong, H. Zhang, Y. Pan, Y. Lv, Y. Yang, F. Li, S. Zhang, F. Huang, Y. Ma, *Adv. Mater. (Deerfield Beach, Fla.)* **2013**, *25*, 3443-3448, DOI: 10.1002/adma.201300839
- [112] "Controlled Synthesis of Conjugated Microporous Polymer Films: Versatile Platforms for Highly Sensitive and Label-Free Chemo- and Biosensing", C. Gu, N. Huang, J. Gao, F. Xu, Y. Xu, D. Jiang, *Angew. Chem., Int. Ed. Engl.* **2014**, *53*, 4850-4855, DOI: 10.1002/anie.201402141
- [113] "Comparison of electrolyte effects for poly(3,4-ethylenedioxythiophene) and poly(3-octylthiophene) by electrochemical impedance spectroscopy and polymerization parameters with morphological analyses on coated films", M. Ates, T. Karazehir, F. Arican, N. Eren, *J. Coat. Technol. Res.* **2013**, *10*, 317-330, DOI: 10.1007/s11998-012-9448-0
- [114] "Production of Nanostructured Conjugated Polymers by Electropolymerization of Tailored Tetrahedral Precursors", A. Yassin, R. Mallet, P. Leriche, J. Roncali, *ChemElectroChem* **2014**, *1*, 1219-1225, DOI: 10.1002/celec.201402007
- [115] "Selective nucleation and growth of metal-organic open framework thin films on patterned COOH/CF<sub>3</sub>-terminated self-assembled monolayers on Au(111)", S. Hermes, F. Schröder, R. Chelmoski, C. Wöll, R. A. Fischer, *J. Am. Chem. Soc.* **2005**, *127*, 13744-13745, DOI: 10.1021/ja053523l
- [116] "Oriented growth of the metal organic framework Cu<sub>3</sub>(BTC)<sub>2</sub>(H<sub>2</sub>O)<sub>3</sub>.xH<sub>2</sub>O tunable with functionalized self-assembled monolayers", E. Biemmi, C. Scherb, T. Bein, *J. Am. Chem. Soc.* **2007**, *129*, 8054-8055, DOI: 10.1021/ja0701208
- [117] "Step-by-step route for the synthesis of metal-organic frameworks", O. Shekhah, H. Wang, S. Kowarik, F. Schreiber, M. Paulus, M. Tolan, C. Sternemann, F. Evers, D. Zacher, R. A. Fischer, C. Wöll, *J. Am. Chem. Soc.* **2007**, *129*, 15118-15119, DOI: 10.1021/ja076210u
- [118] "Thin films of metal-organic frameworks", D. Zacher, O. Shekhah, C. Wöll, R. A. Fischer, *Chem. Soc. Rev.* **2009**, *38*, 1418-1429, DOI: 10.1039/b805038b
- [119] "Oriented growth of the functionalized metal-organic framework CAU-1 on -OH- and -COOH-terminated self-assembled monolayers", F. M. Hinterholzinger, C. Scherb, T. Ahnfeldt, N. Stock, T. Bein, *Phys. Chem. Chem. Phys.* **2010**, *12*, 4515-4520, DOI: 10.1039/b924657f
- [120] "Implementing chemical functionality into oriented films of metal-organic frameworks on self-assembled monolayers", C. Scherb, J. J. Williams, F. M. Hinterholzinger, S. Bauer, N. Stock, T. Bein, *J. Mater. Chem.* **2011**, *21*, 14849-14856, DOI: 10.1039/c0jm04526h
- [121] "Preparation of Ultrathin Films of Molecular Networks through Layer-by-Layer Cross-Linking Polymerization of Tetrafunctional Monomers", M. Kim, M. Byeon, J.-S. Bae, S.-Y. Moon, G. Yu, K. Shin, F. Basarir, T.-H. Yoon, J.-W. Park, *Macromolecules* **2011**, *44*, 7092-7095, DOI: 10.1021/ma201480t

- [122] "Microporous polymer network films covalently bound to gold electrodes", D. Becker, N. Heidary, M. Horch, U. Gernert, I. Zebger, J. Schmidt, A. Fischer, A. Thomas, *Chem. Commun. (Cambridge, U. K.)* **2015**, 51, 4283-4286, DOI: 10.1039/C4CC09637A
- [123] "Spontaneously Organized Molecular Assemblies. 4. Structural Characterization of n-Alkyl Thiol Monolayers on Gold by Optical Ellipsometry, Infrared Spectroscopy, and Electrochemistry", M. D. Porter, T. B. Bright, D. L. Allara, C. E. D. Chidsey, *J. Am. Chem. Soc.* **1987**, 109, 3559-3568, DOI: 10.1021/ja00246a011
- [124] "Formation of monolayer films by the spontaneous assembly of organic thiols from solution onto gold", C. D. Bain, E. B. Troughton, Y.-T. Tao, J. Evall, G. M. Whitesides, R. G. Nuzzo, *J. Am. Chem. Soc.* **1989**, 111, 321-335, DOI: 10.1021/ja00183a049
- [125] "Surface-enhanced infrared ATR spectroscopy for in situ studies of electrode/electrolyte interfaces", M. Osawa, K.-i. Ataka, K. Yoshii, T. Yotsuyanagi, *J. Electron Spectrosc. Relat. Phenom.* **1993**, 64-65, 371-379, DOI: 10.1016/0368-2048(93)80099-8
- [126] "Benzenethiol: Thermodynamic Properties in the Solid, Liquid and Vapor States; Internal Rotation of the Thiol Group 1", D. W. Scott, J. P. McCullough, W. N. Hubbard, J. F. Messerly, I. A. Hossenlopp, F. R. Frow, G. Waddington, *J. Am. Chem. Soc.* **1956**, 78, 5463-5468, DOI: 10.1021/ja01602a002
- [127] "Theoretical and experimental studies on the adsorption behavior of thiophenol on gold nanoparticles", S. Li, D. Wu, X. Xu, R. Gu, *J. Raman Spectrosc.* **2007**, 38, 1436-1443, DOI: 10.1002/jrs1791
- [128] "Analyzing the vibrational signatures of thiophenol adsorbed on small gold clusters by DFT calculations", C. G. Tetsassi Feugmo, V. Liégeois, *ChemPhysChem* **2013**, 14, 1633-1645, DOI: 10.1002/cphc.201201077
- [129] "Reflection Method for Obtaining the Infrared Spectrum of a Thin Layer on a Metal Surface", R. G. Greenler, *J. Chem. Phys.* **1969**, 50, 1963-1968, DOI: 10.1063/1.1671315
- [130] "Possible Importance of a "Metal-Surface Selection Rule" in the Interpretation of the Infrared Spectra of Molecules Adsorbed on Particulate Metals; Infrared Spectra from Ethylene Chemisorbed on Silica-Supported Metal Catalysts", H. A. Pearce, N. Sheppard, *Surf. Sci.* **1976**, 59, 205-217, DOI:
- [131] "Surface Enhanced Infrared Spectroscopy: The Origin of the Absorption Enhancement and Band Selection Rule in the Infrared Spectra of Molecules Adsorbed on Fine Metal Particles", M. Osawa, K.-i. Ataka, K. Yoshii, Y. Nishikawa, *Appl. Spectrosc.* **1993**, 47, 1497-1502, DOI:
- [132] M. Osawa, in *Handbook of Vibrational Spectroscopy*, (Eds.: J. M. Chalmers, P. Griffiths), **2001**, pp. 785-799.
- [133] "Surface-enhanced infrared absorption spectroscopy (SEIRAS) to probe monolayers of membrane proteins", K.-i. Ataka, S. T. Stripp, J. Heberle, *Biochim. Biophys. Acta, Biomembr.* **2013**, 1828, 2283-2293, DOI: 10.1016/j.bbamem.2013.04.026
- [134] "Synthetic control of the pore dimension and surface area in conjugated microporous polymer and copolymer networks", J.-X. Jiang, F. Su, A. Trewin, C. D. Wood, H. Niu, J. T. A. Jones, Y. Z. Khimyak, A. I. Cooper, *J. Am. Chem. Soc.* **2008**, 130, 7710-7720, DOI: 10.1021/ja8010176

- [135] "Conjugated microporous poly(phenylene butadiynylene)s", J.-X. Jiang, F. Su, H. Niu, C. D. Wood, N. L. Campbell, Y. Z. Khimyak, A. I. Cooper, *Chem. Commun. (Cambridge, U. K.)* **2008**, 486-488, DOI: 10.1039/b715563h
- [136] "High Surface Area Conjugated Microporous Polymers: The Importance of Reaction Solvent Choice", R. Dawson, A. Laybourn, Y. Z. Khimyak, D. J. Adams, A. I. Cooper, *Macromolecules* **2010**, *43*, 8524-8530, DOI: 10.1021/ma101541h
- [137] "Band gap engineering in fluorescent conjugated microporous polymers", J.-X. Jiang, A. Trewin, D. J. Adams, A. I. Cooper, *Chem. Sci.* **2011**, *2*, 1777-1781, DOI: 10.1039/c1sc00329a
- [138] "Shedding Light on Structure–Property Relationships for Conjugated Microporous Polymers: The Importance of Rings and Strain", M. A. Zwijnenburg, G. Cheng, T. O. McDonald, K. E. Jelfs, J.-X. Jiang, S. Ren, T. Hasell, F. Blanc, A. I. Cooper, D. J. Adams, *Macromolecules* **2013**, *46*, 7696-7704, DOI: 10.1021/ma401311s
- [139] "Network formation mechanisms in conjugated microporous polymers", A. Laybourn, R. Dawson, R. Clowes, T. Hasell, A. I. Cooper, Y. Z. Khimyak, D. J. Adams, *Polym. Chem.* **2014**, *5*, 6325-6333, DOI: 10.1039/C4PY00647J
- [140] "Gold compounds as efficient co-catalysts in palladium-catalysed alkynylation", L. A. Jones, S. Sanz, M. Laguna, *Catal. Today* **2007**, *122*, 403-406, DOI: 10.1016/j.cattod.2007.01.045
- [141] "On the catalytic duo PdCl<sub>2</sub>(PPh<sub>3</sub>)<sub>2</sub>/AuCl(PPh<sub>3</sub>) that cannot effect a Sonogashira-type reaction: a correction", B. Panda, T. K. Sarkar, *Tetrahedron Lett.* **2010**, *51*, 301-305, DOI: 10.1016/j.tetlet.2009.11.003
- [142] "Gold and palladium combined for the Sonogashira-type cross-coupling of arenediazonium salts", B. Panda, T. K. Sarkar, *Chem. Commun. (Cambridge, U. K.)* **2010**, *46*, 3131-3133, DOI: 10.1039/C001277G
- [143] "Unlikelihood of Pd-Free Gold(I)-Catalyzed Sonogashira Coupling Reactions", T. Lauterbach, M. Livendahl, A. Rosellón, P. Espinet, A. M. Echavarren, *Org. Lett.* **2010**, *12*, 3006-3009, DOI: 10.1021/ol101012n
- [144] "Gold catalyzes the Sonogashira coupling reaction without the requirement of palladium impurities", A. Corma, R. Juarez, M. Boronat, F. Sanchez, M. Iglesias, H. Garcia, *Chem. Commun. (Cambridge, U. K.)* **2011**, *47*, 1446-1448, DOI: 10.1039/C0CC04564K
- [145] "Identity of the Active Site in Gold Nanoparticle-Catalyzed Sonogashira Coupling of Phenylacetylene and Iodobenzene", S. K. Beaumont, G. Kyriakou, R. M. Lambert, *J. Am. Chem. Soc.* **2010**, *132*, 12246-12248, DOI: 10.1021/ja1063179
- [146] "Sonogashira Coupling on an Extended Gold Surface in Vacuo: Reaction of Phenylacetylene with Iodobenzene on Au(111)", V. K. Kanuru, G. Kyriakou, S. K. Beaumont, A. C. Papageorgiou, D. J. Watson, R. M. Lambert, *J. Am. Chem. Soc.* **2010**, *132*, 8081-8086, DOI: 10.1021/ja1011542
- [147] "Coordination chemistry of metal surfaces. 2. Chemistry of acetonitrile and methyl isocyanide on nickel surfaces", C. M. Friend, J. Stein, E. L. Muetterties, *J. Am. Chem. Soc.* **1981**, *103*, 767-772, DOI: 10.1021/ja00394a007

- 
- [148] "Adsorption of alkanenitriles and alkanedinitriles on gold and copper", U. B. Steiner, W. R. Caseri, U. W. Suter, *Langmuir* **1992**, *8*, 2771-2777, DOI: 10.1021/la00047a031
- [149] "Interaction of mono- and diisocyanoozulenenes with gold surfaces: first examples of self-assembled monolayer films involving azulenic scaffolds", D. L. DuBose, R. E. Robinson, T. C. Holovics, D. R. Moody, E. C. Weintrob, C. L. Berrie, M. V. Barybin, *Langmuir* **2006**, *22*, 4599-4606, DOI: 10.1021/la0532050
- [150] "Surface-enhanced Raman spectroscopy as a probe of adsorbate-surface bonding: simple alkenes and alkynes adsorbed at gold electrodes", M. L. Patterson, M. J. Weaver, *J. Phys. Chem.* **1985**, *89*, 5046-5051, DOI: 10.1021/j100269a032
- [151] "Theoretical study of ethynylbenzene adsorption on Au(111) and implications for a new class of self-assembled monolayer", M. J. Ford, R. C. Hoft, A. McDonagh, *J. Phys. Chem. B* **2005**, *109*, 20387-20392, DOI: 10.1021/jp053238o
- [152] "Ethynylbenzene monolayers on gold: a metal-molecule binding motif derived from a hydrocarbon", A. M. McDonagh, H. M. Zareie, M. J. Ford, C. S. Barton, M. Ginic-Markovic, J. G. Matison, *J. Am. Chem. Soc.* **2007**, *129*, 3533-3538, DOI: 10.1021/ja064297y
- [153] "The Preparation of Alkyltriethylammonium-Kaneinite Complexes and Their Conversion to Microporous Materials", T. Yanagisawa, T. Shimizu, K. Kuroda, C. Kato, *Bull. Chem. Soc. Jpn.* **1990**, *63*, 988-992, DOI: 10.1246/bcsj.63.988
- [154] "Ordered mesoporous molecular sieves synthesized by a liquid-crystal template mechanism", C. T. Kresge, M. E. Leonowicz, W. J. Roth, J. C. Vartuli, J. S. Beck, *Nature* **1992**, *359*, 710-712, DOI: 10.1038/359710a0
- [155] "Triblock Copolymer Syntheses of Mesoporous Silica with Periodic 50 to 300 Angstrom Pores", D. Zhao, J. Feng, Q. Huo, N. Melosh, G. H. Fredrickson, B. F. Chmelka, G. D. Stucky, *Science* **1998**, *279*, 548-552, DOI: 10.1126/science.279.5350.548
- [156] "Nonionic Triblock and Star Diblock Copolymer and Oligomeric Surfactant Syntheses of Highly Ordered, Hydrothermally Stable, Mesoporous Silica Structures", D. Zhao, Q. Huo, J. Feng, B. F. Chmelka, G. D. Stucky, *J. Am. Chem. Soc.* **1998**, *120*, 6024-6036, DOI: 10.1021/ja974025i
- [157] "Assembly of large-area, highly ordered, crack-free inverse opal films", B. Hatton, L. Mishchenko, S. Davis, K. H. Sandhage, J. Aizenberg, *Proc. Natl. Acad. Sci. U. S. A.* **2010**, *107*, 10354-10359, DOI: 10.1073/pnas.1000954107
- [158] "Fabrication of Polymer - Nanoparticle Composite Inverse Opals by a One-Step Electrochemical Co-deposition Process", A. Yu, F. Meiser, T. Cassagneau, F. Caruso, *Nano Lett.* **2004**, *4*, 177-177, DOI: 10.1021/nl0348443
- [159] "Semiconducting Polymer Inverse Opals Prepared by Electropolymerization", T. Cassagneau, F. Caruso, *Adv. Mater. (Weinheim, Ger.)* **2002**, *14*, 34-38, DOI: 10.1002/1521-4095(20020104)14:1<34::AID-ADMA34>3.0.CO;2-M
- [160] "Bottom-up assembly of photonic crystals", G. von Freymann, V. Kitaev, B. V. Lotsch, G. A. Ozin, *Chem. Soc. Rev.* **2013**, *42*, 2528-2554, DOI: 10.1039/C2CS35309A
- [161] "Photonic crystals: putting a new twist on light", J. D. Joannopoulos, P. R. Villeneuve, S. Fan, *Nature* **1997**, *386*, 143-149, DOI: 10.1038/386143a0
-

- [162] "Large-scale synthesis of a silicon photonic crystal with a complete three-dimensional bandgap near 1.5 micrometres", A. Blanco, E. Chomski, S. Grabtchak, M. Ibisate, S. John, S. W. Leonard, C. Lopez, F. Meseguer, H. Miguez, J. P. Mondia, G. A. Ozin, O. Toader, H. M. van Driel, *Nature* **2000**, 405, 437-440, DOI: 10.1038/35013024
- [163] "Cubic Ia3d large mesoporous silica: synthesis and replication to platinum nanowires, carbon nanorods and carbon nanotubes", F. Kleitz, S. Hei Choi, R. Ryoo, *Chem. Commun. (Cambridge, U. K.)* **2003**, 2136-2137, DOI: 10.1039/B306504A
- [164] "Characterization of MCM-48 Materials", K. Schumacher, P. I. Ravikovitch, A. Du Chesne, A. V. Neimark, K. K. Unger, *Langmuir* **2000**, 16, 4648-4654, DOI: 10.1021/la991595i
- [165] "Generalized synthesis of periodic surfactant/inorganic composite materials", Q. Huo, D. I. Margolese, U. Ciesla, P. Feng, T. E. Gier, P. Sieger, R. Leon, P. M. Petroff, F. Schuth, G. D. Stucky, *Nature* **1994**, 368, 317-321, DOI:
- [166] "Synthesis and Pore Size Control of Cubic Mesoporous Silica SBA-1", M. J. Kim, R. Ryoo, *Chem. Mater.* **1999**, 11, 487-491, DOI: 10.1021/cm980691m
- [167] "Highly ordered large caged cubic mesoporous silica structures templated by triblock PEO-PBO-PEO copolymer", C. Yu, Y. Yu, D. Zhao, *Chem. Commun. (Cambridge, U. K.)* **2000**, 575-576, DOI: 10.1039/B000603N
- [168] "The Plumber's Nightmare:1 A New Morphology in Block Copolymer-Ceramic Nanocomposites and Mesoporous Aluminosilicates", A. C. Finnefrock, R. Ulrich, G. E. S. Toombes, S. M. Gruner, U. Wiesner, *J. Am. Chem. Soc.* **2003**, 125, 13084-13093, DOI: 10.1021/ja0355170
- [169] "Pore Size Analysis of MCM-41 Type Adsorbents by Means of Nitrogen and Argon Adsorption", A. V. Neimark, P. I. Ravikovitch, M. Grün, F. Schüth, K. K. Unger, *J. Colloid Interface Sci.* **1998**, 207, 159-169, DOI: <http://dx.doi.org/10.1006/jcis.1998.5748>
- [170] "Direct Imaging of Surface Topology and Pore System of Ordered Mesoporous Silica (MCM-41, SBA-15, and KIT-6) and Nanocast Metal Oxides by High Resolution Scanning Electron Microscopy", H. Tüysüz, C. W. Lehmann, H. Bongard, B. Tesche, R. Schmidt, F. Schüth, *J. Am. Chem. Soc.* **2008**, 130, 11510-11517, DOI: 10.1021/ja803362s
- [171] "Control of the microporosity within the pore walls of ordered mesoporous silica SBA-15", K. Miyazawa, S. Inagaki, *Chem. Commun. (Cambridge, U. K.)* **2000**, 2121-2122, DOI: 10.1039/B005128O
- [172] "Characterization of the Porous Structure of SBA-15", M. Kruk, M. Jaroniec, C. H. Ko, R. Ryoo, *Chem. Mater.* **2000**, 12, 1961-1968, DOI: 10.1021/cm000164e
- [173] "Characterization of Micro- and Mesoporosity in SBA-15 Materials from Adsorption Data by the NLDFT Method", P. I. Ravikovitch, A. V. Neimark, *J. Phys. Chem. B* **2001**, 105, 6817-6823, DOI: 10.1021/jp010621u
- [174] "Evidence for General Nature of Pore Interconnectivity in 2-Dimensional Hexagonal Mesoporous Silicas Prepared Using Block Copolymer Templates", S. H. Joo, R. Ryoo, M. Kruk, M. Jaroniec, *J. Phys. Chem. B* **2002**, 106, 4640-4646, DOI: 10.1021/jp013583n

- [175] "Microporosity and connections between pores in SBA-15 mesostructured silicas as a function of the temperature of synthesis", A. Galarneau, H. Cambon, F. Di Renzo, R. Ryoo, M. Choi, F. Fajula, *New J. Chem.* **2003**, 27, 73-79, DOI: 10.1039/B207378C
- [176] "Consecutive Generation of Mesopores and Micropores in SBA-15", C.-M. Yang, B. Zibrowius, W. Schmidt, F. Schüth, *Chem. Mater.* **2003**, 15, 3739-3741, DOI: 10.1021/cm031109j
- [177] "Facile synthesis of high quality mesoporous SBA-15 with enhanced control of the porous network connectivity and wall thickness", M. Choi, W. Heo, F. Kleitz, R. Ryoo, *Chem. Commun. (Cambridge, U. K.)* **2003**, 1340-1341, DOI: 10.1039/B303696K
- [178] "Microporosity in Ordered Mesoporous Aluminosilicates Characterized by Catalytic Probing Reactions", Y. Sun, Y. Han, L. Yuan, S. Ma, D. Jiang, F.-S. Xiao, *J. Phys. Chem. B* **2003**, 107, 1853-1857, DOI: 10.1021/jp027656u
- [179] "Structure and diffusion characterization of SBA-15 materials", V.-T. Hoang, Q. Huang, M. Eić, T.-O. Do, S. Kaliaguine, *Langmuir* **2005**, 21, 2051-2057, DOI: 10.1021/la048349d
- [180] "A Fast Way for Preparing Crack-Free Mesostructured Silica Monolith", H. Yang, Q. Shi, B. Tian, S. Xie, F. Zhang, B. Tu, D. Zhao, *Chem. Mater.* **2003**, 15, 536-541, DOI: 10.1021/cm020135z
- [181] "Quantification of silanol sites for the most common mesoporous ordered silicas and organosilicas: total versus accessible silanols", M. Ide, M. El-Roz, E. De Canck, A. Vicente, T. Planckaert, T. Bogaerts, I. Van Driessche, F. Lynen, V. Van Speybroeck, F. Thybault-Starzyk, P. Van Der Voort, *Phys. Chem. Chem. Phys.* **2013**, 15, 642-650, DOI: 10.1039/C2CP42811C
- [182] "Phototropieerscheinungen bei Fulgiden und anderen Stoffen", H. Stobbe, *Justus Liebigs Ann. Chem.* **1908**, 359, 1-48, DOI: 10.1002/jlac.19083590102
- [183] "Die Fulgide", H. Stobbe, *Justus Liebigs Ann. Chem.* **1911**, 380, 1-2, DOI: 10.1002/jlac.19113800102
- [184] "I. Beziehungen zwischen Farbe und Konstitution der Fulgide", H. Stobbe, *Justus Liebigs Ann. Chem.* **1911**, 380, 2-17, DOI: 10.1002/jlac.19113800103
- [185] "II. Thermochromieerscheinungen", H. Stobbe, *Justus Liebigs Ann. Chem.* **1911**, 380, 17-26, DOI: 10.1002/jlac.19113800104
- [186] "Ueber das Stickstoffbenzid", E. Mitscherlich, *Ann. Pharm. (Lemgo, Ger.)* **1834**, 12, 311-314, DOI: 10.1002/jlac.18340120282
- [187] "The cis-form of azobenzene", G. S. Hartley, *Nature* **1937**, 281-281, DOI: 10.1038/140281a0
- [188] "Formation of Coloured Forms of Spirans by Low-Temperature Irradiation", E. Fischer, Y. Hirshberg, *Journal of the Chemical Society (Resumed)* **1952**, 4522-4524, DOI:
- [189] "Sur la double phototropie de certains spiranes", O. Chaudé, P. Rumpf, *C. R. Seances Acad. Sci.* **1953**, 236, 697-699, DOI:
- [190] "Thermally irreversible photochromic systems. Reversible photocyclization of diarylethene derivatives", M. Irie, M. Mohri, *J. Org. Chem.* **1988**, 53, 803-808, DOI: 10.1021/jo00239a022

- [191] "Diarylethenes for Memories and Switches", M. Irie, *Chem. Rev. (Washington, DC, U. S.)* **2000**, *100*, 1685-1716, DOI: 10.1021/cr980069d
- [192] "Phototropy (or Photochromism)", R. Exelby, R. Grinter, *Chem. Rev. (Washington, DC, U. S.)* **1965**, *65*, 247-260, DOI: 10.1021/cr60234a005
- [193] "Photochromism of Diarylethene Molecules and Crystals: Memories, Switches, and Actuators", M. Irie, T. Fukaminato, K. Matsuda, S. Kobatake, *Chem. Rev. (Washington, DC, U. S.)* **2014**, *114*, 12174-12277, DOI: 10.1021/cr500249p
- [194] "Photoisomerization in different classes of azobenzene", H. M. D. Bandara, S. C. Burdette, *Chem. Soc. Rev.* **2012**, *41*, 1809-1825, DOI: 10.1039/c1cs15179g
- [195] "Enthalpies of formation of cis-azobenzene and trans-azobenzene", A. R. Dias, M. E. Minas Da Piedade, J. A. Martinho Simões, J. A. Simoni, C. Teixeira, H. P. Diogo, Y. Meng-Yan, G. Pilcher, *J. Chem. Thermodyn.* **1992**, *24*, 439-447, DOI: 10.1016/S0021-9614(05)80161-2
- [196] "Quantum Chemical Investigation of Thermal Cis-to-Trans Isomerization of Azobenzene Derivatives: Substituent Effects, Solvent Effects, and Comparison to Experimental Data", J. Dokić, M. Gothe, J. Wirth, M. V. Peters, J. Schwarz, S. Hecht, P. Saalfrank, *J. Phys. Chem. A* **2009**, *113*, 6763-6773, DOI: 10.1021/jp9021344
- [197] "On the rotation-inversion controversy on photoisomerization of azobenzenes. Experimental proof of inversion", H. Rau, E. Lueddecke, *J. Am. Chem. Soc.* **1982**, *104*, 1616-1620, DOI: 10.1021/ja00370a028
- [198] "Azobenzenes—synthesis and carbohydrate applications", F. Hamon, F. Djedaini-Pilard, F. Barbot, C. Len, *Tetrahedron* **2009**, *65*, 10105-10123, DOI: 10.1016/j.tet.2009.08.063
- [199] H. Rau, *Photochromism: Molecules and Systems*, H. Dürr, H. Bouas-Laurent, Elsevier, Amsterdam, revised edn., **2003**.
- [200] "Light-activated ion channels for remote control of neuronal firing", M. Banghart, K. Borges, E. Isacoff, D. Trauner, R. H. Kramer, *Nat. Neurosci.* **2004**, *7*, 1381-1386, DOI: 10.1038/nn1356
- [201] "Photoswitching of Basicity", M. V. Peters, R. S. Stoll, A. Kühn, S. Hecht, *Angew. Chem., Int. Ed. Engl.* **2008**, *47*, 5968-5972, DOI: 10.1002/anie.200802050
- [202] "Structure-Based Approach to the Photocontrol of Protein Folding", F. Zhang, A. Zarrine-Afsar, M. S. Al-Abdul-Wahid, R. S. Prosser, A. R. Davidson, G. A. Woolley, *J. Am. Chem. Soc.* **2009**, *131*, 2283-2289, DOI: 10.1021/ja807938v
- [203] "Photo-control of helix content in a short peptide", J. R. Kumita, O. S. Smart, G. A. Woolley, *Proc. Natl. Acad. Sci.* **2000**, *97*, 3803-3808, DOI: 10.1073/pnas.97.8.3803
- [204] "Photoswitchable Molecular Glue for DNA", C. Dohno, S.-n. Uno, K. Nakatani, *J. Am. Chem. Soc.* **2007**, *129*, 11898-11899, DOI: 10.1021/ja074325s
- [205] "Azobenzene photoswitches for biomolecules", A. A. Beharry, G. A. Woolley, *Chem. Soc. Rev.* **2011**, *40*, 4422-4437, DOI: 10.1039/c1cs15023e

- [206] "A Light-Driven Molecular Shuttle Based on a Rotaxane", H. Murakami, A. Kawabuchi, K. Kotoo, M. Kunitake, N. Nakashima, *J. Am. Chem. Soc.* **1997**, *119*, 7605-7606, DOI: 10.1021/ja971438a
- [207] "Light-Driven Molecular Hinge: A New Molecular Machine Showing a Light-Intensity-Dependent Photoresponse that Utilizes the Trans-Cis Isomerization of Azobenzene", Y. Norikane, N. Tamaoki, *Org. Lett.* **2004**, *6*, 2595-2598, DOI: 10.1021/ol049082c
- [208] "Mechanical twisting of a guest by a photoresponsive host", T. Muraoka, K. Kinbara, T. Aida, *Nature* **2006**, *440*, 512-515, DOI: 10.1038/nature04635
- [209] "THE PHOTOVISCOSITY EFFECT", R. Lovrien, *Proc. Natl. Acad. Sci. U. S. A.* **1967**, *57*, 236-242, DOI: -
- [210] "Synthesis of Azobenzene-Based Polymers and the in-Situ Characterization of Their Photoviscosity Effects", M. Moniruzzaman, C. J. Sabey, G. F. Fernando, *Macromolecules* **2004**, *37*, 2572-2577, DOI: 10.1021/ma049905d
- [211] "Reversible Formation and Eradication of Colors by Irradiation at Low Temperatures. A Photochemical Memory Model", Y. Hirshberg, *J. Am. Chem. Soc.* **1956**, *78*, 2304-2312, DOI: 10.1021/ja01591a075
- [212] "Thermally irreversible photochromic systems. A theoretical study", S. Nakamura, M. Irie, *J. Org. Chem.* **1988**, *53*, 6136-6138, DOI: 10.1021/jo00261a035
- [213] "Viscosity dependence of fluorescence quantum yields", S. Sharafy, K. A. Muszkat, *J. Am. Chem. Soc.* **1971**, *93*, 4119-4125, DOI: 10.1021/ja00746a004
- [214] "1,2-Diphenylcycloalkenes: electronic and geometric structures in the gas phase, solution, and solid state", G. Hohlneicher, M. Mueller, M. Demmer, J. Lex, J. H. Penn, L. X. Gan, P. D. Loesel, *J. Am. Chem. Soc.* **1988**, *110*, 4483-4494, DOI: 10.1021/ja00222a001
- [215] "Models for stilbene photoisomerization: experimental and theoretical studies of the excited-state dynamics of 1,2-diphenylcycloalkenes", J. H. Frederick, Y. Fujiwara, J. H. Penn, K. Yoshihara, H. Petek, *J. Phys. Chem.* **1991**, *95*, 2845-2858, DOI: 10.1021/j100160a040
- [216] "Stereochemistry of Electrocyclic Reactions", R. B. Woodward, R. Hoffmann, *J. Am. Chem. Soc.* **1965**, *87*, 395-397, DOI: 10.1021/ja01080a054
- [217] "Very High Cyclization Quantum Yields of Diarylethene Having Two N-Methylpyridinium Ions", K. Matsuda, Y. Shinkai, T. Yamaguchi, K. Nomiyama, M. Isayama, M. Irie, *Chem. Lett.* **2003**, *32*, 1178-1179, DOI: 10.1246/cl.2003.1178
- [218] "Photon-Quantitative Reaction of a Dithiazolylarylene in Solution", S. Fukumoto, T. Nakashima, T. Kawai, *Angew. Chem., Int. Ed. Engl.* **2011**, *50*, 1565-1568, DOI: 10.1002/anie.201006844
- [219] "Can Diarylethene Photochromism Be Explained by a Reaction Path Alone? A CASSCF Study with Model MMVB Dynamics", M. Boggio-Pasqua, M. Ravaglia, M. J. Bearpark, M. Garavelli, M. A. Robb, *J. Phys. Chem. A* **2003**, *107*, 11139-11152, DOI: 10.1021/jp036862e

- [220] "Theoretical Study on the Photochromic Cycloreversion Reactions of Dithienylethenes; on the Role of the Conical Intersections", Y. Asano, A. Murakami, T. Kobayashi, A. Goldberg, D. Guillaumont, S. Yabushita, M. Irie, S. Nakamura, *J. Am. Chem. Soc.* **2004**, *126*, 12112-12120, DOI: 10.1021/ja035035o
- [221] "Photoirradiation wavelength dependence of cycloreversion quantum yields of diarylethenes", T. Sumi, Y. Takagi, A. Yagi, M. Morimoto, M. Irie, *Chem. Commun. (Cambridge, U. K.)* **2014**, *50*, 3928-3930, DOI: 10.1039/C4CC00396A
- [222] "Femtosecond Laser Photolysis Studies on Temperature Dependence of Cyclization and Cycloreversion Reactions of a Photochromic Diarylethene Derivative", Y. Ishibashi, T. Umesato, S. Kobatake, M. Irie, H. Miyasaka, *J. Phys. Chem. C* **2012**, *116*, 4862-4869, DOI: 10.1021/jp2107632
- [223] "Rapid and reversible shape changes of molecular crystals on photoirradiation", S. Kobatake, S. Takami, H. Muto, T. Ishikawa, M. Irie, *Nature* **2007**, *446*, 778-781, DOI: 10.1038/nature05669
- [224] "Multicolor Photochromism of Two- and Three-Component Diarylethene Crystals", M. Morimoto, S. Kobatake, M. Irie, *J. Am. Chem. Soc.* **2003**, *125*, 11080-11087, DOI: 10.1021/ja035277o
- [225] "Photochromism of Mixed Crystals Containing Bisthieryl-, Bisthiazolyl-, and Bisoxazolylolethene Derivatives", S. Takami, L. Kuroki, M. Irie, *J. Am. Chem. Soc.* **2007**, *129*, 7319-7326, DOI: 10.1021/ja068786+
- [226] "Fatigue resistant properties of photochromic dithienylethenes: by-product formation", M. Irie, T. Lifka, K. Uchida, S. Kobatake, Y. Shindo, *Chem. Commun. (Cambridge, U. K.)* **1999**, 747-750, DOI: 10.1039/A809410A
- [227] "Fatigue Mechanism of Photochromic 1,2-Bis(3-thienyl)perfluorocyclopentene", K. Higashiguchi, K. Matsuda, T. Yamada, T. Kawai, M. Irie, *Chem. Lett.* **2000**, *29*, 1358-1359, DOI: 10.1246/cl.2000.1358
- [228] "Limited photochromism in covalently linked double 1,2-dithienylethenes", A. Peters, N. R. Branda, *Adv. Mater. Opt. Electron.* **2000**, *10*, 245-249, DOI: 10.1002/1099-0712(200011/12)10:6<245::AID-AMO422>3.0.CO;2-O
- [229] "Photochromic properties of tetrakis(2-methylthien-3-yl)ethene and its tetrakis(methylthio) derivative", H. Ikeda, A. Sakai, A. Kawabe, H. Namai, K. Mizuno, *Tetrahedron Lett.* **2008**, *49*, 4972-4976, DOI: 10.1016/j.tetlet.2008.05.080
- [230] "Selective photoconversion of photochromic diarylethenes and their properties", H.-h. Liu, Y. Chen, *New J. Chem.* **2012**, *36*, 2223-2227, DOI: 10.1039/C2NJ40377C
- [231] "Thermal bleaching reactions of photochromic diarylethenes with thiophene-S,S-dioxide for a light-starting irreversible thermosensor", H. Shoji, S. Kobatake, *Chem. Commun. (Cambridge, U. K.)* **2013**, *49*, 2362-2364, DOI: 10.1039/C3CC00053B
- [232] "Formation of Two-dimensionally Ordered Diarylethene Annulated Isomer at the Liquid/HOPG Interface upon In Situ UV Irradiation", T. Sakano, Y. Imaizumi, T. Hirose, K. Matsuda, *Chem. Lett.* **2013**, *42*, 1537-1539, DOI: 10.1246/cl.130705

- [233] "Improving the Fatigue Resistance of Diarylethene Switches", M. Herder, B. M. Schmidt, L. Grubert, M. Pätzel, J. Schwarz, S. Hecht, *J. Am. Chem. Soc.* **2015**, *137*, 2738-2747, DOI: 10.1021/ja513027s
- [234] "Tunable Photodynamic Switching of DArE@PAF-1 for Carbon Capture", R. Lyndon, K. Konstas, R. A. Evans, D. J. Keddie, M. R. Hill, B. P. Ladewig, *Adv. Funct. Mater.* **2015**, *25*, 4405-4411, DOI: 10.1002/adfm.201502069
- [235] "Photo-responsive MOFs: light-induced switching of porous single crystals containing a photochromic diarylethene", I. M. Walton, J. M. Cox, J. A. Coppin, C. M. Linderman, D. G. D. Patel, J. B. Benedict, *Chem. Commun. (Cambridge, U. K.)* **2013**, *49*, 8012-8014, DOI: 10.1039/c3cc44119a
- [236] "Dual-controlled nanoparticles exhibiting AND logic", S. Angelos, Y.-W. Yang, N. M. Khashab, J. F. Stoddart, J. I. Zink, *J. Am. Chem. Soc.* **2009**, *131*, 11344-11346, DOI: 10.1021/ja9042752
- [237] "[Zn(C<sub>3</sub>H<sub>3</sub>N<sub>2</sub>)(C<sub>3</sub>H<sub>2</sub>N<sub>2</sub>-N=N-C<sub>6</sub>H<sub>5</sub>)], a Mixed-Linker ZIF Containing a Photo-switchable Phenylazo Group", S. Bernt, M. Feyand, A. Modrow, J. Wack, J. Senker, N. Stock, *Eur. J. Inorg. Chem.* **2011**, *2011*, 5378-5383, DOI: 10.1002/ejic.201100789
- [238] "The first porous MOF with photoswitchable linker molecules", A. Modrow, D. Zargarani, R. Herges, N. Stock, *Dalton Trans.* **2011**, *40*, 4217-4222, DOI: 10.1039/c0dt01629b
- [239] "Introducing a photo-switchable azo-functionality inside Cr-MIL-101-NH<sub>2</sub> by covalent post-synthetic modification", A. Modrow, D. Zargarani, R. Herges, N. Stock, *Dalton Trans.* **2012**, *41*, 8690-8696, DOI: 10.1039/c2dt30672g
- [240] "Reversible alteration of CO<sub>2</sub> adsorption upon photochemical or thermal treatment in a metal-organic framework", J. Park, D. Yuan, K. T. Pham, J.-R. Li, A. Yakovenko, H.-C. Zhou, *J. Am. Chem. Soc.* **2012**, *134*, 99-102, DOI: 10.1021/ja209197f
- [241] "Photophysical pore control in an azobenzene-containing metal-organic framework", J. W. Brown, B. L. Henderson, M. D. Kiesz, A. C. Whalley, W. Morris, S. Grunder, H. Deng, H. Furukawa, J. I. Zink, J. F. Stoddart, O. M. Yaghi, *Chem. Sci.* **2013**, *4*, 2858-2864, DOI: 10.1039/c3sc21659d
- [242] "Azobenzene-functionalized metal-organic polyhedra for the optically responsive capture and release of guest molecules", J. Park, L.-B. Sun, Y.-P. Chen, Z. Perry, H.-C. Zhou, *Angew. Chem., Int. Ed. Engl.* **2014**, *53*, 5842-5846, DOI: 10.1002/anie.201310211
- [243] "Photoswitching in two-component surface-mounted metal-organic frameworks: optically triggered release from a molecular container", L. Heinke, M. Cakici, M. Dommaschk, S. Grosjean, R. Herges, S. Bräse, C. Wöll, *ACS Nano* **2014**, *8*, 1463-1467, DOI: 10.1021/nn405469g
- [244] "Reversible tuning of pore size and CO<sub>2</sub> adsorption in azobenzene functionalized porous organic polymers", Y. Zhu, W. Zhang, *Chem. Sci.* **2014**, *5*, 4957-4961, DOI: 10.1039/C4SC02305F
- [245] "Energy Transfer on Demand: Photoswitch-Directed Behavior of Metal-Porphyrin Frameworks", D. E. Williams, J. A. Rietman, J. M. Maier, R. Tan, A. B. Greytak, M. D. Smith, J. A. Krause, N. B. Shustova, *J. Am. Chem. Soc.* **2014**, *136*, 11886-11889, DOI: 10.1021/ja505589d

- [246] "Photochromic Metal–Organic Frameworks: Reversible Control of Singlet Oxygen Generation", J. Park, D. Feng, S. Yuan, H.-C. Zhou, *Angew. Chem., Int. Ed. Engl.* **2015**, *54*, 430-435, DOI: 10.1002/anie.201408862
- [247] "Synthesis and photochromic reactivity of diarylethene trimers bridged by ethenyl and ethynyl unit", H. Choi, I. Jung, K. H. Song, K. Song, D.-S. Shin, S. O. Kang, J. Ko, *Tetrahedron* **2006**, *62*, 9059-9065, DOI: 10.1016/j.tet.2006.06.095
- [248] "TD-DFT simulations of the electronic properties of star-shaped photochromes", D. Jacquemin, E. A. Perpète, F. Maurel, A. Perrier, *Phys. Chem. Chem. Phys.* **2010**, *12*, 7994-8000, DOI: 10.1039/b927323a
- [249] "Single molecule multiphotochromism with diarylethenes", A. Perrier, F. Maurel, D. Jacquemin, *Acc. Chem. Res.* **2012**, *45*, 1173-1182, DOI: 10.1021/ar200214k
- [250] "Light-Switchable Polymers of Intrinsic Microporosity", D. Becker, N. Konnertz, M. Böhning, J. Schmidt, A. Thomas, *Chem. Mater.* **2016**, *28*, 8523-8529, DOI: 10.1021/acs.chemmater.6b02619
- [251] "Photoswitching CO<sub>2</sub> Capture and Release in a Photochromic Diarylethene Metal–Organic Framework", F. Luo, C. B. Fan, M. B. Luo, X. L. Wu, Y. Zhu, S. Z. Pu, W.-Y. Xu, G.-C. Guo, *Angew. Chem., Int. Ed. Engl.* **2014**, *53*, 9298-9301, DOI: 10.1002/anie.201311124
- [252] "Novel Expansion/Shrinkage Modulation of 2D Layered MOF Triggered by Clathrate Formation with CO<sub>2</sub> Molecules", A. Kondo, H. Noguchi, S. Ohnishi, H. Kajiro, A. Tohdoh, Y. Hattori, W.-C. Xu, H. Tanaka, H. Kanoh, K. Kaneko, *Nano Lett.* **2006**, *6*, 2581-2584, DOI: 10.1021/nl062032b
- [253] "Kinetic Gate-Opening Process in a Flexible Porous Coordination Polymer", D. Tanaka, K. Nakagawa, M. Higuchi, S. Horike, Y. Kubota, T. C. Kobayashi, M. Takata, S. Kitagawa, *Angew. Chem., Int. Ed.* **2008**, *47*, 3914-3918, DOI: 10.1002/anie.200705822
- [254] "Exploring Polymers of Intrinsic Microporosity – Microporous, Soluble Polyamide and Polyimide", J. Weber, Q. Su, M. Antonietti, A. Thomas, *Macromol. Rapid Commun.* **2007**, *28*, 1871-1876, DOI: 10.1002/marc.200700346
- [255] D. W. Breck, *Zeolite Molecular Sieves: Structure, Chemistry and Use*, John Wiley & Sons, Chichester, 1st, **1974**.
- [256] "Correlation aspects of the selective gas permeabilities of polymeric materials and membranes", V. Teplyakov, P. Meares, *Gas Separation & Purification* **1990**, *4*, 66-74, DOI: [http://dx.doi.org/10.1016/0950-4214\(90\)80030-O](http://dx.doi.org/10.1016/0950-4214(90)80030-O)
- [257] "Femtosecond Dynamics of the Ring Closing Process of Diarylethene: A Case Study of Electrocyclic Reactions in Photochromic Single Crystals", H. Jean-Ruel, R. R. Cooney, M. Gao, C. Lu, M. A. Kochman, C. A. Morrison, R. J. D. Miller, *J. Phys. Chem. A* **2011**, *115*, 13158-13168, DOI: 10.1021/jp205818h
- [258] "Photocontrolling Peptide  $\alpha$  Helices", G. A. Woolley, *Acc. Chem. Res.* **2005**, *38*, 486-493, DOI: 10.1021/ar040091v

- [259] "Electrochemically Induced Surface-Enhanced Infrared Difference Absorption (SEIDA) Spectroscopy of a Protein Monolayer", K. Ataka, J. Heberle, *J. Am. Chem. Soc.* **2003**, *125*, 4986-4987, DOI: 10.1021/ja0346532
- [260] "Monitoring Catalysis of the Membrane-Bound Hydrogenase from *Ralstonia eutropha* H16 by Surface-Enhanced IR Absorption Spectroscopy", N. Wisitruangsakul, O. Lenz, M. Ludwig, B. Friedrich, F. Lenzian, P. Hildebrandt, I. Zebger, *Angew. Chem., Int. Ed.* **2009**, *48*, 611-613, DOI: 10.1002/anie.200802633
- [261] "Self-assembled monolayers of thiolates on metals as a form of nanotechnology", J. C. Love, L. A. Estroff, J. K. Kriebel, R. G. Nuzzo, G. M. Whitesides, *Chem. Rev. (Washington, DC, U. S.)* **2005**, *105*, 1103-1169, DOI: 10.1021/cr0300789
- [262] "Porous Polymer Networks: Synthesis, Porosity, and Applications in Gas Storage/Separation", W. Lu, D. Yuan, D. Zhao, C. I. Schilling, O. Plietzsch, T. Muller, S. Bräse, J. Guenther, J. Blümel, R. Krishna, Z. Li, H.-C. Zhou, *Chem. Mater.* **2010**, *22*, 5964-5972, DOI: 10.1021/cm1021068
- [263] "Synthesis of Oligo(phenyleneethynylene)s with Vertically Disposed Tetrathiafulvalene Units", K. Jennum, M. Vestergaard, A. H. Pedersen, J. Fock, J. Jensen, M. Santella, J. J. Led, K. Kilså, T. Bjørnholm, M. B. Nielsen, *Synthesis* **2011**, *2011*, 539-548, DOI: 10.1055/s-0030-1258385
- [264] "Conductance switching and mechanisms in single-molecule junctions", C. Jia, J. Wang, C. Yao, Y. Cao, Y. Zhong, Z. Liu, Z. Liu, X. Guo, *Angew. Chem., Int. Ed. Engl.* **2013**, *52*, 8666-8670, DOI: 10.1002/anie.201304301
- [265] "Photochromism of Dithienylethenes with Electron-Donating Substituents", M. Irie, K. Sakemura, M. Okinaka, K. Uchida, *J. Org. Chem.* **1995**, *60*, 8305-8309, DOI: 10.1021/jo00130a035
- [266] "New fast synthesis route for symmetric and asymmetric phenyl-substituted photochromic dithienylethenes bearing functional groups such as alcohols, carboxylic acids, or amines", S. Hermes, G. Dassa, G. Toso, A. Bianco, C. Bertarelli, G. Zerbi, *Tetrahedron Lett.* **2009**, *50*, 1614-1617, DOI: 10.1016/j.tetlet.2009.01.102
- [267] "Synthesis of Enantiomerically Pure Dissymmetric 2,2'-Disubstituted 9,9'-Spirobifluorenes", F. Thiemann, T. Piehler, D. Haase, W. Saak, A. Lützen, *Eur. J. Org. Chem.* **2005**, *2005*, 1991-2001, DOI: 10.1002/ejoc.200400796
- [268] "Oxidation of fluoroanilines to fluoroazobenzenes with potassium ferricyanide and KOH", E. Leyva, E. Monreal, C. Medina, S. Leyva, *Tetrahedron Lett.* **1997**, *38*, 7847-7848, DOI: 10.1016/S0040-4039(97)10131-9
- [269] "Ordered mesoporous materials in catalysis", A. Taguchi, F. Schüth, *Microporous Mesoporous Mater.* **2005**, *77*, 1-45, DOI: <http://dx.doi.org/10.1016/j.micromeso.2004.06.030>